

AD-765 383

FRESNEL DIFFRACTION OF RF WAVEFRONTS

George P. Bein

Calspan Corporation

Prepared for:

Federal Aviation Administration

February 1973

DISTRIBUTED BY:

NTIS

National Technical Information Service
U. S. DEPARTMENT OF COMMERCE
5285 Port Royal Road, Springfield Va. 22151

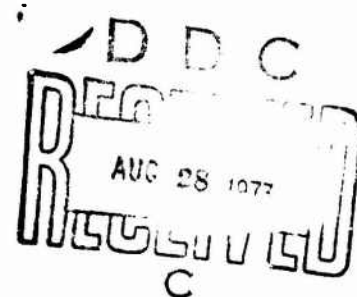
FRESNEL DIFFRACTION OF RF WAVEFRONTS

AD 765383

George P. Bein
Calspan Corporation
(Formerly Cornell Aeronautical Laboratory, Inc.)
Buffalo, New York 14221



Reproduced by
NATIONAL TECHNICAL
INFORMATION SERVICE
U.S. Department of Commerce
Springfield VA 22151



February 1973
FINAL REPORT

Availability is unlimited. Document may be released to the
National Technical Information Service, Springfield, Virginia
22151, for sale to the public.

Prepared for

DEPARTMENT OF TRANSPORTATION
FEDERAL AVIATION ADMINISTRATION
Systems Research & Development Service
Washington, D.C. 20591

188

ACCESSION for	
NTIS	White Section <input checked="" type="checkbox"/>
DDO	Buff Section <input type="checkbox"/>
UNANNOUNCED	<input type="checkbox"/>
JUSTIFICATION	
BY	
DISTRIBUTION/AVAILABILITY CODES	
Dist.	Avail. and/or SPECIAL
A	

THE CONTENTS OF THIS REPORT REFLECT THE VIEWS OF CALSPAN CORPORATION, WHICH IS RESPONSIBLE FOR THE FACTS AND THE ACCURACY OF THE DATA PRESENTED HEREIN. THE CONTENTS DO NOT NECESSARILY REFLECT THE OFFICIAL VIEWS OR POLICY OF THE DEPARTMENT OF TRANSPORTATION. THIS REPORT DOES NOT CONSTITUTE A STANDARD, SPECIFICATION OR REGULATION.

1. Report No. FAA-RD-73-34	2. Government Accession No.	3. Recipient's Catalog No.	
4. Title and Subtitle FRESNEL DIFFRACTION OF RF WAVEFRONTS		5. Report Date February 1973	
		6. Performing Organization Code	
7. Author(s) George P. Bein		8. Performing Organization Report No. AG-5082-E-1	
9. Performing Organization Name and Address Calspan Corporation Advanced Technology Center P.O. Box 235 Buffalo, New York 14221		10. Work Unit No. 213-620	
		11. Contract or Grant No. DOT-FA72WA-2782	
12. Sponsoring Agency Name and Address Department of Transportation Federal Aviation Administration Systems Research and Development Service Washington, D.C. 20591		13. Type of Report and Period Covered Final Report December 1971 to February 1973	
		14. Sponsoring Agency Code	
15. Supplementary Notes Details of Illustrations in this document may be better studied on microfiche			
16. Abstract The objective of this program was to develop the necessary mathematics including a computer program to predict and define the RF and geometric shadow of any proposed (or existing) obstruction in the coverage volume of airspace of radar facilities operating in appropriate aeronautical service bands. The RF shadow calculation includes the effects of Fresnel diffraction by a perfectly-conducting rectangular obstruction through the use of Geometric Diffraction Theory. Both the line-of-sight (geometrical-optic) shadow and Fresnel diffraction effects are calculated by the computer program for arbitrary incidence and observation angles relative to the obstacle. Signal degradation relative to the obstacle-free field, and for desired combinations of transmit and receive polarizations, was described by providing plots of arbitrarily chosen dB levels at chosen observation planes behind the obstruction. Circularly cylindrical, spherical, and convex polyhedron obstructions were also considered but only to determine geometric shadowing. A flight test program was conducted to experimentally validate the computer program utilizing a rectangular obstruction at three different viewing angles. The experimental results were in good agreement with predicted values.			
17. Key Words Fresnel Diffraction Rectangular Buildings Radar Shadowing		18. Distribution Statement Document is available to the Public through the National Technical Informa- tion Service, Springfield, Virginia 22151	
19. Security Classif. (of this report) Unclassified	20. Security Classif. (of this page) Unclassified	21. No. of Pages 200	22. Price

PREFACE

The research described in the report is the result of significant work by many individuals at Calspan Corporation. The author wishes to acknowledge their contributions and thank them for their participation.

Marley Bechtel and Dr. R.A. Ross developed the analytical approach for describing diffraction from a rectangular building. The major computer programming effort was accomplished by George Gaidasz. Computer program design and certain geometric-optical descriptions were initially developed by William Fryer. Ted Wojcinski provided assistance in regard to conversion of the computer program from the IBM system to other type computers.

The flight test program was performed with the able assistance of William Mahar, Charles Wolf and Hendrik Prinsen. Richard Blum performed antenna pattern measurements pertinent to the choice of an appropriate receive antenna configuration. Photographic services during the test were provided by Ralph Jones, Fred Thornton and Cecil LaGrange.

Calspan wishes to thank Prior Aviation Service, Inc., Buffalo, N.Y., for their assistance and cooperation in the use of their helicopter; the helicopter pilots, Jack B. Prior and Gerry Cheselka, are thanked for a job well done.

George Sargis coordinated efforts in the publication of this and other project reports. Other documentation associated with this project consists of:

Calspan Report No. AG-5082-E-2, "Computer Operator's Manual,"

Calspan Report No. AG-5082-E-3, "Computer Programmer's Manual."

The author wishes to thank Robert E. Kell and Dr. Stephen N. Andre for reviewing this report and for providing pertinent suggestions for improvement.

Preceding page blank

CONTENTS

<u>Section</u>	<u>page</u>
1 INTRODUCTION AND SUMMARY	1
2 THEORETICAL DISCUSSION	5
2.1 Background	5
2.1.1 General	5
2.1.2 Scattering Center Concept	6
2.1.3 Polarization Matrix	7
2.2 Diffraction by an Infinitely Long Edge	9
2.2.1 Geometrical Diffraction Theory	9
2.2.2 Sommerfeld's Half-Plane Result	14
2.2.3 Combined Formulation	16
2.3 Diffraction by a Finite Length Edge	19
2.3.1 Introduction	19
2.3.2 Analysis	20
2.3.3 Combined Formulation	25
2.3.4 Preliminary Calculation of the Total Field Around a Finite-Length Right-Angle Edge	26
2.3.5 Modification to Half-Plane Formulas in the Illuminated Region	28
2.4 Diffraction by a Rectangular Building	32
2.4.1 Geometrical Considerations	32
2.4.2 Sample Calculations for Isolated Edges	42
2.4.3 Sample Calculation Considering All Contributing Edges	50
2.5 Geometrical-Optic Shadowing	50
3 FLIGHT TEST VALIDATION	51
3.1 General Discussion	51
3.1.1 Preliminary Considerations	52
3.1.2 Experimental Procedures	53
3.1.3 Instrumentation	53
3.1.4 Tracking	59
3.2 Diffraction from a Spherical Obstruction	65
3.2.1 Description of Experimental Layout	65
3.2.2 Scope of Tests Performed	65
3.2.3 Experimental Results	68
3.2.4 Conclusions	83

Preceding page blank

CONTENTS (continued)

<u>Section</u>	<u>page</u>
3.3 Diffraction from a Cylindrical Obstruction	84
3.3.1 Description of Experimental Layout	84
3.3.2 Scope of Tests Performed	84
3.3.3 Experimental Results	88
3.3.4 Conclusions	93
3.4 Diffraction from a Rectangular Obstruction	95
3.4.1 Comparison Between Theory and Experiment . .	99
3.4.2 Conclusions	163
4 CONCLUSIONS	165
REFERENCES	167
Appendix	
I EVALUATION OF THE Q-FACTOR	169
II REFORMULATION OF BISECTOR COMPUTATION	187

ILLUSTRATIONS

<u>Figure</u>	<u>page</u>
1 Diffraction from a Point on the Edge of a Two-Dimensional Wedge	10
2 Shadow Boundaries	13
3 Half Plane Geometry	15
4 U_{TOTAL} for 90°-Wedge: Vertical Polarization	17
5 U_{TOTAL} for 90°-Wedge: Horizontal Polarization	18
6 Edge Geometry for Mid-Point Simplification	24
7 Geometry for Preliminary Calculation	27
8 Preliminary Total Field Calculation	29
9 Effect of Incorporating Modified Formulas	31
10 Rectangular Building: Node Numbering Scheme	33
11 Spherical Triangle for Incidence Angle	36
12 Spherical Triangle for Observation Angle	38
13 Incidence Orientation Angle	41
14 Observation Orientation Angle	41
15 Plan View of Layout for Rectangular Building	43
16 Theoretically Calculated Total Field Scattered from Finite Vertical Edge	44
17 Plan View of Layout for Rectangular Building	46
18 Theoretically Calculated Total Field Scattered from Finite Vertical Edge	47
19 Side View of Square Obstacle	48
20 Theoretically Calculated Total Field Scattered from a Horizontal Edge	49
21 Conceptual Plan View of Test Site; Typical Test Profiles	54

ILLUSTRATIONS (continued)

<u>Figure</u>		<u>page</u>
22	S-Band Transmitting System (Mounted on Plywood Board) . . .	55
23	S-Band Transmitting System (being Installed in Helicopter). . .	55
24	S-Band Transmitting System (Helicopter Installation)	55
25	S-Band Transmitting System (Front View)	55
26	Block Diagram of Equipment Layout	57
27	S-Band Receive Antennas	58
28	Receiving Equipment	58
29	Receiving Equipment	58
30	Recording Equipment	58
31	VHF Receiving Antenna	60
32	VHF Receiving Antenna	60
33	Movie Camera and LED	61
34	Experimental Set-Up for Sphere Diffraction Study	65
35	Spherical Water Tank used as Test Object (Located in East Aurora, New York)	66
36	Relative Signal Strength vs Distance from Test Centerline for Spherical Water Tank; $d_1 = 891$ ft, $d_2 = 2650$ ft, Altitude = 540 ft	69
37	Relative Signal Strength vs Distance from Test Centerline for Spherical Water Tank; $d_1 = 891$ ft, $d_2 = 2650$ ft, Altitude = 500 ft	70
38	Relative Signal Strength vs Distance from Test Centerline for Spherical Water Tank; $d_1 = 891$ ft, $d_2 = 2650$ ft, Altitude = 290 ft	71
39	Relative Signal Strength vs Distance from Test Centerline for Spherical Water Tank; $d_1 = 891$ ft, $d_2 = 2650$ ft, Altitude = 437 ft	72

ILLUSTRATIONS (continued)

<u>Figure</u>		<u>page</u>
40	Relative Signal Strength vs Distance from Test Centerline for Spherical Water Tank; $d_1 = 891$ ft, $d_2 = 5700$ ft, Altitude = 700 ft	73
41	Relative Signal Strength vs Distance from Test Centerline for Spherical Water Tank; $d_1 = 891$ ft, $d_2 = 5700$ ft, Altitude = 921 ft	75
42	Relative Signal Strength vs Distance from Test Centerline for Spherical Water Tank; $d_1 = 891$ ft, $d_2 = 5700$ ft, Altitude = 532 ft	76
43	Relative Signal Strength vs Distance from Test Centerline for Spherical Water Tank; $d_1 = 891$ ft, $d_2 = 10,600$ ft, Altitude = 1545 ft	77
44	Relative Signal Strength vs Distance from Test Centerline for Spherical Water Tank; $d_1 = 891$ ft, $d_2 = 10,600$ ft, Altitude = 1325 ft	78
45	Relative Signal Strength vs Distance from Test Centerline for Spherical Water Tank; $d_1 = 891$ ft, $d_2 = 10,600$ ft, Altitude = 1000 ft	79
46	Cylindrical Water Tank Used as Test Object (Located in Corfu, New York)	85
47	Cylindrical Water Tank (Two Views)	86
48	Experimental Setup for Cylinder Diffraction Study	84
49	Relative Signal Strength vs Distance from Test Centerline for Cylindrical Water Tank; $d_1 = 962$ ft, $d_2 = 6300$ ft, Altitude = 1125 ft	89
50	Relative Signal Strength vs Distance from Test Centerline for Cylindrical Water Tank; $d_1 = 962$ ft, $d_2 = 6300$ ft, Altitude = 7715 ft	90
51	Relative Signal Strength vs Distance from Test Centerline for Cylindrical Water Tank; $d_1 = 962$ ft, $d_2 = 6300$ ft, Altitude = 390 ft	92
52	Relative Signal Strength vs Distance from Test Centerline for Cylindrical Water Tank; $d_1 = 962$ ft, $d_2 = 13,300$ ft, Altitude = 1000 ft	94

ILLUSTRATIONS (continued)

<u>Figure</u>		<u>page</u>
53	Aerial View of Niagara Intake Gate Buildings Looking Northwest	97
54	Aerial View of Niagara Intake Gate Buildings Looking Southeast	97
55	Bridge and Towers: Possible Sources of VHF Multipath	97
56	Photograph of Niagara Intake Gate Buildings	97
57	Photograph of Niagara Intake Gate Buildings	97
58	Photograph of Niagara Intake Gate Buildings	97
59	Photograph of Niagara Intake Gate Buildings	97
60	Experimental Layout for B-Series	100
61	Flight Paths, B1X1-Series, S-Band, Vertical Polarization . . .	103
62	Flight Paths, B1X2-Series, S-Band, Horizontal Polarization	104
63	Flight Paths, B1XY-Series, VHF, Vertical Polarization	105
64	Flight Paths, B2X1-Series, S-Band, Vertical Polarization . . .	106
65	Flight Paths, B2X2-Series, S-Band, Vertical Polarization . . .	107
66	Flight Paths, B2XY-Series, VHF, Vertical Polarization	108
67	Comparison Between Theory and Experiment, Relative Signal Strength vs Distance from Test Centerline, Runs B111 and B112; $d_1 = 650$ ft, $d_2 \approx 4200$, Altitude ≈ 655 ft . .	109
68	Comparison Between Theory and Experiment, Relative Signal Strength vs Distance from Test Centerline, Runs B121 and B122; $d_1 = 650$ ft, $d_2 \approx 4200$ ft, Altitude ≈ 950 ft	110
69	Comparison Between Theory and Experiment, Relative Signal Strength vs Distance from Test Centerline, Runs B131 and B132; $d_1 = 650$ ft, $d_2 \approx 4200$ ft, Altitude ≈ 400 ft	111

ILLUSTRATIONS (continued)

<u>Figure</u>		<u>page</u>
70	Comparison Between Theory and Experiment, Relative Signal Strength vs Distance from Test Centerline, Runs B211 and B212; $d_1 = 650$ ft, $d_2 \approx 8500$ ft, Altitude ≈ 1150 ft	113
71	Comparison Between Theory and Experiment, Relative Signal Strength vs Distance from Test Centerline, Runs B221 and B222; $d_1 = 650$ ft, $d_2 \approx 8500$ ft, Altitude ≈ 1650 ft	115
72	Comparison Between Theory and Experiment, Relative Signal Strength vs Distance from Test Centerline, Runs B231 and B232; $d_1 = 650$ ft, $d_2 \approx 8500$ ft, Altitude ≈ 650 ft	117
73	Level Variation as a Function of Range, B1X1-Series	120
74	Level Variation as a Function of Range, A1X1-Series	121
75	Level Variation as a Function of Range, N2X1-Series	122
76	Experimental Layout for A-Series	124
77	Flight Paths, A1X1-Series, S-Band, Vertical Polarization . . .	127
78	Flight Paths, A1X2-Series, S-Band, Horizontal Polarization. .	128
79	Flight Paths, A1XY-Series, VHF, Vertical Polarization	129
80	Flight Paths, A2X1-Series, S-Band, Vertical Polarization . . .	130
81	Flight Paths, A2X2-Series, S-Band, Vertical Polarization . . .	131
82	Flight Paths, A2XY-Series, VHF, Vertical Polarization	132
83	Comparison Between Theory and Experiment, Relative Signal Strength vs Distance from Test Centerline, Runs A111 and A112; $d_1 = 412$ ft, $d_2 \approx 3300$ ft, Altitude ≈ 1500 ft	133
84	Comparison Between Theory and Experiment, Relative Signal Strength vs Distance from Test Centerline, Runs A121 and A122, $D_1 = 412$ ft, $d_2 \approx 3300$ ft, Altitude ≈ 900 ft	134

ILLUSTRATIONS (continued)

<u>Figure</u>		<u>page</u>
85	Comparison Between Theory and Experiment, Relative Signal Strength vs Distance from Test Centerline, Runs A131 and A132; $d_1 = 412$ ft, $d_2 \approx 3300$ ft, Altitude ≈ 400 ft	135
86	Comparison Between Theory and Experiment, Relative Signal Strength vs Distance from Test Centerline, Runs A211 and A212; $d_1 = 412$ ft, $d_2 \approx 6850$ ft, Altitude ≈ 2200 ft	136
87	Comparison Between Theory and Experiment, Relative Signal Strength vs Distance from Test Centerline, Runs A221 and A222; $d_1 = 412$ ft, $d_2 \approx 6850$ ft, Altitude ≈ 1000 ft	137
88	Comparison Between Theory and Experiment, Relative Signal Strength vs Distance from Test Centerline, Runs A231 and A232; $d_1 = 412$ ft, $d_2 \approx 6850$ ft, Altitude ≈ 500 ft	139
89	Experimental Layout for N-Series	143
90	Flight Paths, N1X1-Series, S-Band, Vertical Polarization	146
91	Flight Paths, N1X2-Series, S-Band, Horizontal Polarization	147
92	Flight Paths, N1XY-Series, VHF, Vertical Polarization	148
93	Flight Paths, N2X1-Series, S-Band, Vertical Polarization	149
94	Flight Paths, N2X2-Series, S-Band, Horizontal Polarization	150
95	Flight Paths, N2XY-Series, VHF, Vertical Polarization	151
96	Comparison Between Theory and Experiment, Relative Signal Strength vs Distance from Test Centerline, Runs N111 and N112; $d_1 = 496$ ft, $d_2 \approx 3300$ ft, Altitude ≈ 991 ft	152
97	Comparison Between Theory and Experiment, Relative Signal Strength vs Distance from Test Centerline, Runs N121 and N122; $d_1 = 496$ ft, $d_2 \approx 3300$ ft, Altitude ≈ 755 ft	153
98	Comparison Between Theory and Experiment, Relative Signal Strength vs Distance From Test Centerline, Runs N131 and N132; $d_1 = 496$ ft, $d_2 \approx 3300$ ft, Altitude ≈ 400 ft	155

ILLUSTRATIONS (continued)

<u>Figure</u>		<u>page</u>
99	Comparison Between Theory and Experiment, Relative Signal Strength vs Distance from Test Centerline, Runs N211 and N212; $d_1 = 496$ ft, $d_2 \approx 8000$ ft, Altitude ≈ 2200 ft	157
100	Comparison Between Theory and Experiment, Relative Signal Strength vs Distance from Test Centerline, Runs N221 and N222; $d_1 = 496$ ft, $d_2 \approx 8000$ ft, Altitude ≈ 1670 ft	158
101	Comparison Between Theory and Experiment, Relative Signal Strength vs Distance from Test Centerline, Runs N231 and N232; $d_1 = 496$ ft, $d_2 \approx 8000$ ft, Altitude ≈ 888 ft	161
102	Basic Edge Geometry	170
103	Subdivision of Edge into Shorter Segments	172
104	Flow Diagram for Subroutine QQ1	177
105	Flow Diagram for Subroutine QQ2	182
106	Example of Continuity of Q at Transition Between Equations 62 and 66	185

TABLES

<u>Table</u>	<u>page</u>
I Spherical Obstruction Scope of Tests Performed	67
II Cylindrical Obstruction Scope of Tests Performed	87
III Rectangular Obstruction, B-Series Scope of Tests Performed	101
IV Rectangular Obstruction, A-Series Scope of Tests Performed	126
V Rectangular Obstruction, N-Series Scope of Tests Performed	145
VI Comparison of Computed Q Values with Far-Zone Approximation	184

Section 1

INTRODUCTION AND SUMMARY

Under Contract No. DOT-FA72WA-2782 with the Federal Aviation Administration, Calspan Corporation has been studying the shadowing effects of presently existing or proposed obstructions in the near vicinity of FAA radar and navigational facility antennas. Commercial real estate developers who propose construction work exceeding certain criteria contained in FAR, Part 77, must submit the details of this potential obstruction to the FAA. The FAA, in turn, must determine whether the proposed obstruction constitutes a hazard to air navigation. FAA engineers must determine the potential derogation of ASR, ARSR, ACTCBS and other facilities by examining the limits of the "no detection" zone or "shadowing" which would be caused by the proposed construction. Political and economic factors related to such major construction projects dictate that these engineering predictions be as accurate as possible.

The objective of this program was to develop the necessary mathematics, including a computer program, to predict and define the RF and geometrical shadow of any proposed obstruction in the airspace coverage volume of radar facilities operating in appropriate aeronautical service bands. The RF shadow calculation includes the effects of Fresnel diffraction by the obstacle through the use of Geometrical Diffraction Theory (GDT).

The basic obstacle shape considered was a finite, perfectly conducting rectangular cylinder. Both the line-of-sight (geometrical-optic) shadow and Fresnel diffraction effects are calculated by the computed program for arbitrary incidence and observation angles relative to the obstacle and desired combinations of transmit and receive polarizations. The total field in the presence of the obstruction was determined at a matrix of points on an observation plane at a chosen distance behind the obstruction. Single degradation, relative to the obstacle-free field, was described by providing contour plots of arbitrarily chosen dB levels for that observation plane.

Circularly cylindrical, spherical, and convex polyhedron obstructions were also considered, but only to determine the geometrical shadowing. Such obstruction types are amenable to diffraction theory analysis but the analysis of such effects was not within the scope of the contract.

For all cases, it was assumed that the radar and obstruction were situated on smooth, curved earth having an effective radius equal to four-thirds that of the true radius of the earth.

Details of the computer program, which was delivered to the FAA in July 1972, are contained in previously published reports.* The program, containing 42 subprograms, was written utilizing Calspan's IBM 370 computer; certain modifications were then made to allow the program to run on a CDC 6400 computer.

There are two separate versions of the program: a batch version which employs a card reader and a high-speed printer, and an interactive version which utilizes a teletypewriter to provide input and output data.

Plots of signal degradation levels (e.g., -3 dB, -6 dB, -10 dB, etc.), caused by an obstruction, are obtained from both a print-plot routine and from a contour plotter (such as a CALCOMP machine). In addition, the printout includes both the normalized complex field and the normalized field magnitude (in dB) as a two-dimensional matrix of observation points.

A flight test program was planned and conducted by Calspan for the Federal Aviation Administration to experimentally validate the computer program developed in the analytical phase of the project. The validation was performed using a rectangular obstruction at three different viewing angles. A helicopter was utilized to simultaneously transmit both S-band (3000 MHz) and VHF (123 MHz) signals to a ground receive terminal as it traversed selected flight paths behind the obstacles. The helicopter position was monitored with a moving picture camera. A single time-reference was inserted on both the received signal strength recording and the movie frames to relate helicopter position to the appropriate signal level.

* Report No. AG-5082-E-2, "Computer Operator's Manual" and Report No. AG-5082-E-3, "Computer Programmer's Manual," George Gaidasz and George P. Bein, Calspan Corporation, Buffalo, New York 14221.

The flight test data was reduced to provide the RF signal attenuation, due to presence of the obstacle in the line-of-sight, relative to the signal obtained at approximately the same range but without the obstacle. This data was compared with the computer predictions of RF attenuation, due to the presence of the obstacle, relative to the free-space signal level. Agreement between the experimental S-band flight test data and predicted behavior of signal levels was very good, generally within about 2 dB of each other. One discrepancy, in S-band comparisons, was that predicted peaks of about 7 dB in signal level at points localized near the shadow boundaries were not experimentally observed. Although there are physical arguments which deem the appearance of these peaks credible, it is also possible that they result from the use of certain approximate methods utilized in providing transition between shadow boundary and geometric diffraction theory analytic formulations. The discrepancy might also be attributed to differences between the idealized theoretical model and the actual building utilized for the tests.

The easiest and fastest way of resolving this would be to conduct a scale model experiment where there would be no differences between assumed and actual obstacle properties. If the peaks still do not appear, the more involved procedure of reevaluating the analytical procedures should be undertaken.

The VHF signal exhibited scalloping and other level changes which it is felt, were not caused by diffraction from the obstacle under test. These signal variations are attributed to ground refractions, other multipath phenomena, and possibly, a nonomnidirectional airborne VHF antenna pattern. Because the recorded VHF signal was not constant, even for helicopter positions far from the obstacles, it was sometimes difficult to determine the no-perturbation or 0 dB reference level. In many cases, good agreement between theory and experiment can be obtained by merely uniformly shifting the reference level assumed in the data reduction by an appropriate amount.

The effects of ground reflections and antenna pattern effects can be incorporated into the computer program; this would provide a more accurate model of the electromagnetic configuration.

Measurements of S-band and VHF signals were also made utilizing spherical and cylindrical obstructions. No theoretical predictions were made for these cases, other than simple geometric optics as provided in the computer. Interestingly, peaks in signal level appeared near the shadow boundaries for many of the sphere tests; they were absent for the cylinder. For both the sphere and cylinder, S-band signal level perturbations (on the order of from 2 to 4 dB, one-way) extended out to approximately twice the distance of the shadow boundary projection. Within the shadow region, the signal level was generally much less than the free-space field, although for both the sphere and cylinder a signal peak of typically -3 dB was present over a fairly large region in the center of the geometric shadow. In summary, geometric-optical predictions based on the line-of-sight overestimate the signal loss within the shadow and underestimate the loss outside the shadow.

A study program can be performed to develop appropriate theories that would accurately take into account diffraction contributions for spherical and cylindrical obstructions. Such theories could be easily incorporated into the present computer program. Theoretical predictions could be compared with the experimental results already obtained.

The theoretical analysis of diffraction from a rectangular building, utilizing geometrical diffraction theory, is contained in Section 2 of this report. In Section 3, the flight test validation program is described; results are presented which compare predicted signal levels with the corresponding experimental outcomes. In subsections 3.2.4, 3.3.4 and 3.4.2, dealing with spherical, cylindrical and rectangular obstructions, respectively, conclusions and recommendations for additional study are presented.

Section 2

THEORETICAL DISCUSSION

2.1 BACKGROUND

2.1.1 General

Perturbation of an electromagnetic field by obstacles placed within the field has been a central topic of continuous experimental and analytical investigation at Calspan for many years. There exists, at present, both detailed theoretical treatments and suitable engineering approximations for handling many problems. This experience which permits the development of engineering approximations and assessment of their accuracy is of fundamental importance in the present study because the rigorous description of the perturbation effects is very complicated. Although this detailed, complex field must be sufficiently understood to permit estimation of field reduction or enhancement effects, the exact, three-dimensional spatially-varying vector field is much too complex to be practically utilized for engineering purposes. It is noted that the interference phenomena which give rise to the local field maxima and minima are sensitive to obstacle geometry, obstacle material, RF wavelength, polarization, orientation relative to the RF transmitting antenna, and distances both from the obstacle and from the antenna.

A portion of this investigation was directed toward development of a computer program to predict the total field distribution due to an intervening rectangular building. One component of the total field distribution is estimated by geometric optics (i.e., unity incident field in the illuminated region; zero incident field in the shadow region). Of course, geometric optics is valid only in the limit of vanishing wavelength. In practical situations, a second component describing diffraction by the obstacle is added to the geometric optics term to obtain a representation of the total field distribution which corresponds with observations. For example, diffraction accounts for non-zero fields observed in the shadow region.

To make the analytical problem tractable, it has been assumed that the building can be modeled by a finite, perfectly-conducting rectangular cylinder. Diffracted fields arise when the incident field illuminates an edge

on the rectangular building. The best description of edge-diffracted fields is Keller's geometrical diffraction theory (GDT). However, GDT diffraction formulas are asymptotic in nature with singularities occurring at the reflection and forward scattering directions. Because the total field distribution at and near the forward scattering direction was also of interest in this program, a second theory was required as well. A modified form of Sommerfeld's half-plane solution was chosen for this situation.

The diffraction results described above apply to two-dimensional obstacles with edges. The fact that a building is three-dimensional had to be included in the theory to obtain reasonably accurate results; that is, the finite edges on the building were assumed to be illuminated by a spherical wave rather than a plane wave. A major portion of the analysis concerns transformation of well-known two-dimensional formulas for application to the three-dimensional problem. By summing the resultant fields diffracted at contributing finite edges on the building and by including the geometric optics field, the total field distribution beyond the obstacle can be estimated.

2.1.2 Scattering Center Concept

One of the most important concepts that has been applied in recent investigations of short wavelength scattering is that the diffracted fields appear to have localized sources (scattering centers) on the target. In terms of formal electromagnetic theory, each scattering center is identified with a mathematical discontinuity in the Chu-Stratton radiation integral* - that is to say, with a corresponding physical location on the target at the place where the discontinuity occurs. Simplification of the diffraction interaction in terms of scattering centers rests largely upon the cancellation properties of an integral with oscillating integrand and upon preservation of mathematical continuity except at the recognized geometric discontinuities. Thus, although a surface remote from a discontinuity is assumed to produce a net contribution of zero to the total diffracted field, truncation of the surface could introduce a pronounced discontinuity, and, so, generate a new scattering center. A smooth surface, then, plays a very important, although largely hidden, role in the description of the diffraction interaction.

* See Stratton, J.A., "Electromagnetic Theory," McGraw-Hill Book Co., Inc., pp. 464-470.

According to the scattering center concept, the field reradiated from each center on the target depends primarily upon the local dimensions and the surface conditions of the target. Secondary effects involve interactions between the various centers on the target. The first step in the analysis is to take a body of complex shape and find its individual scattering centers. Next, an analytical theory which accounts for aspect, frequency, polarization, and bistatic dependence is used to estimate the total diffracted field (primary and secondary contributions) reradiated from individual scattering centers. Finally, the vector and phasor sum of these contributions allows estimation of diffracted fields.

The major simplification attendant upon applications of the scattering center concept is that by treating only a small number of localized regions on the body (the discontinuities), obstacle diffraction can be estimated. Thus, the difficulty of the computation of high frequency diffraction is unrelated to the actual size of the target and depends only upon the number of important scattering centers (edges). Although large smooth surfaces on the target cannot be ignored when they support specular scattering, appropriate modification of scattering center formulations in these instances does not appreciably complicate the computations.

The scattering center concept is inherent in the geometrical theory of diffraction, which will be discussed in subsection 2.2.

2.1.3 Polarization Matrix

It is well known that the total field depends upon the obstacle shape and material, source-obstacle and obstacle - observation point separations, the incidence and observation angles at which the building is viewed, the frequency of the source, and the polarization of the source and receiving antennas. In particular, if an obstacle is viewed at specific ranges, angles, and with a single frequency, the total field depends upon polarization.

The total field may be expressed as an explicit function of polarization when matrices are defined which describe the polarization properties of antennas and obstacle. Consider an arbitrarily polarized transmitting antenna; the polarization of this antenna can be represented by the expression

$$\hat{q} = \begin{bmatrix} \cos \gamma_t \\ e^{j\delta_t} \sin \gamma_t \end{bmatrix} \quad (1)$$

where \hat{q} is a unit column matrix defining the polarization of the transmitted wave; γ_t is an angle which denotes the orientation of the linear polarization that results if δ_t is zero, referred to the horizontal plane; δ_t is a phase angle which can vary from 0 to 2π radians. Any wave polarization is thus specified when γ, δ and the direction of propagation are known. Since the geometric optics contribution ($u_{g.o.}$) is simply the incident field in the illuminated region,* its polarization is specified by \hat{q} above.

Next consider a receiving antenna, at the observation point, represented by a row matrix p :

$$\hat{p} = [\cos \gamma_r \ e^{j\delta_r} \sin \gamma_r] \quad (2)$$

It is assumed that "polarization" of a receiving antenna means the polarization of that antenna when it is used as a transmitting antenna. The observed geometric optics field is $u_{g.o.} \cdot \hat{p} \cdot \hat{q}$.

The diffracted contribution of the total field measured at the observation point is also a function of the polarization matrix S of the obstacle. The polarization matrix S of an arbitrary obstacle may be expressed as a 2×2 matrix provided the following two assumptions are valid:

1. The distances between source, obstacle and observation point are large compared to the wavelength and to the dimensions of the building, and
2. The material of the obstacle and intervening medium are such that there are linear relationships between field quantities at every point, whatever the incident field.

Furthermore, a great simplification obtains when the obstacle presents a horizontal plane of symmetry; the polarization matrix is then diagonalized. Thus, for the rectangular buildings considered in this report, we may write

* $u_{g.o.} = 0$ in shadow region.

$$S = \begin{bmatrix} u_{dH} & 0 \\ 0 & u_{dV} \end{bmatrix} \quad (3)$$

where u_d is the sum of fields diffracted by scattering centers (edges) on the building. It is evident in Equation 3 that u_{dH} is the complex diffraction contribution to the total field when source and receiving antennas are linearly polarized with horizontal orientation (i.e., $\gamma_t = \gamma_r = 0$; $\delta_t = \delta_r = 0$). Similarly, u_{dV} is the corresponding quantity for the vertical polarization case. It is common practice to refer to u_{dH} and u_{dV} as the principal polarization diffracted fields.

In the diffraction analyses in this report we work with principal polarization diffracted fields. Total fields for arbitrary combination of source- and receiving-antenna polarizations may be determined from the relative orientation of the building and the relation

$$u_{total} = u_{G.O.} \hat{p} \cdot \hat{q} + \hat{p} S \hat{q} \quad (4)$$

In the following sections we shall see how $u_{G.O.}$ and S are calculated.

2.2 DIFFRACTION BY AN INFINITELY LONG EDGE

2.2.1 Geometrical Diffraction Theory

Consider a plane electromagnetic wave incident upon a perfectly conducting wedge of infinite extent. Figure 1 illustrates the coordinate convention employed in describing the diffraction phenomenon. An X-Y-Z coordinate system has been chosen such that the Z-axis is coincident with the edge of a two-dimensional wedge having interior angle $2\alpha_k$. The Y-axis is the bisector of the interior wedge angle, and the X-Y plane is normal to the edge at the point of diffraction p .

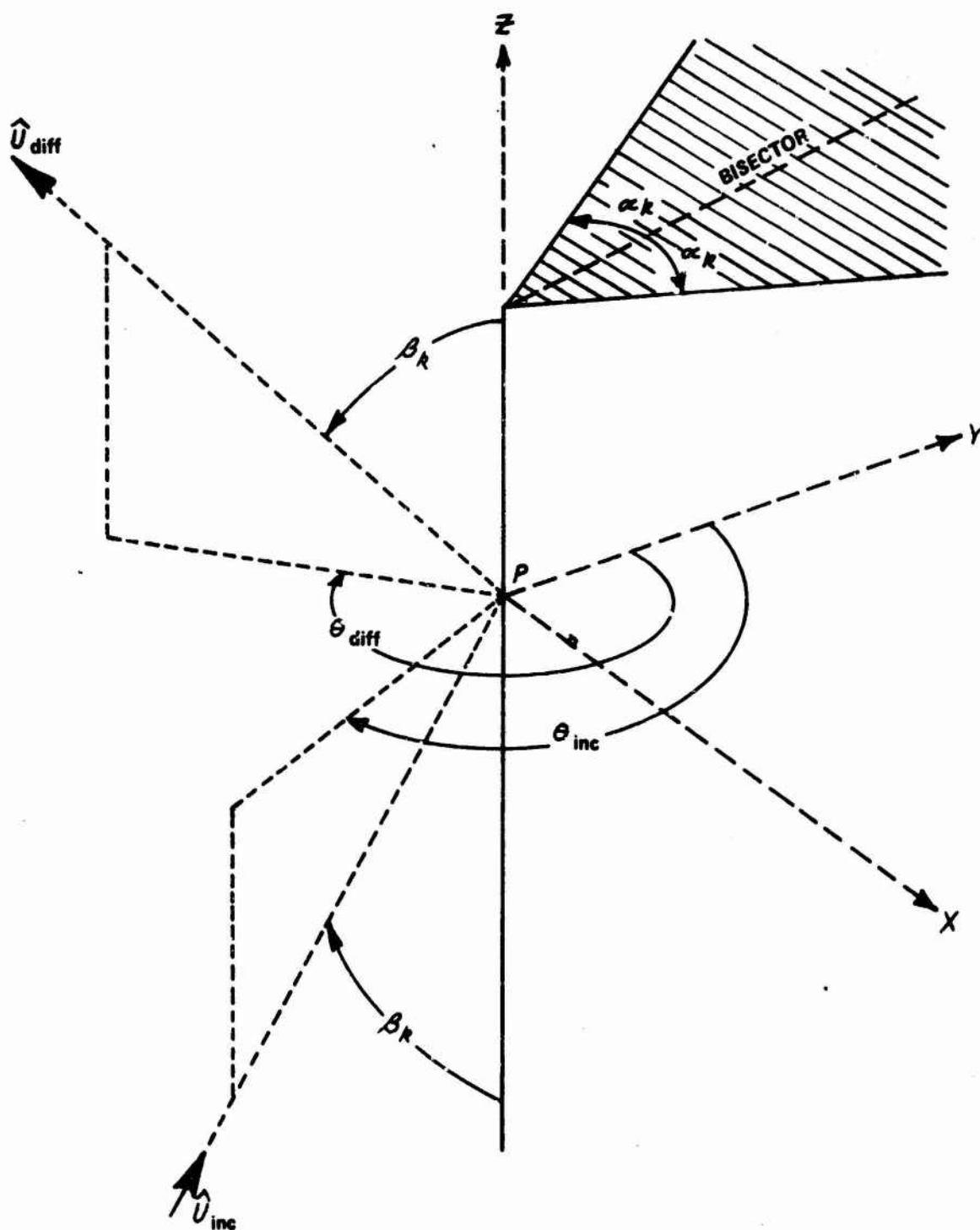


Figure 1 DIFFRACTION FROM A POINT ON THE EDGE OF A TWO-DIMENSIONAL WEDGE

The vector μ_{inc} represents the sense and arbitrary direction on an incident ray. The angle between the incident ray and the positive tangent to the edge (negative Z-axis) is denoted by β_k . The angle between the projection of the direction of incidence in the plane normal to the edge at the point of diffraction (X-Y or normal plane) and the bisector of the interior wedge angle (Y-axis) is denoted by θ_{inc} . According to the law of edge diffraction, the family of rays diffracted at the edge point p lie on the surface of a cone with apex coincident with the point of diffraction, and with half-cone angle β_k . One member of this family of diffracted rays is illustrated by the vector \hat{u}_{diff} . Here the projection of \hat{u}_{diff} in the normal plane makes an angle θ_{diff} with the Y-axis.

A comprehensive discussion of geometrical diffraction theory (GDT) is given in Reference 3. Briefly, GDT assumes that the diffracted field u_{diff} arising at point p on an edge is proportional to the incident field $u_{inc}(p)$ evaluated at that point. Two factors of proportionality called the divergence factor and the diffraction coefficient must be evaluated. For plane wave incidence on a two-dimensional wedge, the divergence factor is $(s_{po})^{-\frac{1}{2}}$ where s_{po} is the separation between point p on the edge and the observation point 0. Similarly, the diffraction coefficient is obtained from the first term in the asymptotic expansion of the corresponding boundary value solution for the wedge. The resultant expression for the edge diffracted field at the observation point is

$$u_{diff} = u_{inc_p}(p) \frac{e^{-iks_{po} - i\frac{\pi}{4}}}{\sqrt{2\pi ks_{po}}} \frac{\sin \frac{\pi}{n}}{n \sin \beta_k} \left[\left\{ \cos \frac{\pi}{n} - \cos \frac{\theta_{diff} - \theta_{inc}}{n} \right\}^{-1} \right. \\ \left. \mp \left\{ \cos \frac{\pi}{n} + \cos \frac{2\pi - \theta_{diff} - \theta_{inc}}{n} \right\}^{-1} \right] \quad (5)$$

$$\text{when} \quad \alpha_k \leq \theta_{diff}, \quad \theta_{inc} \leq 2\pi - \alpha_k$$

$$= 0 \quad \text{when} \quad \begin{cases} \theta_{inc}, \theta_{diff} \leq \alpha_k \\ \theta_{inc}, \theta_{diff} \geq 2\pi - \alpha_k \end{cases}$$

where

$u_{inc,p}(\rho)$ is the incident plane wave $e^{ikr \cos(\theta_{diff} - \theta_{inc})}$
calculated at the edge p

s_{po} is the separation between edge and observation point

θ_{inc} is the angle of incidence

θ_{diff} is the angle of diffraction

$n = \frac{2\pi - 2\alpha_k}{\pi}$ ($2\alpha_k$ being the interior wedge angle)

β_k is the angle between the incidence ray and the positive
tangent to the edge

and k is the wave number ($k = 2\pi/\lambda$, λ the wavelength).

A rectangular cylinder is modeled by right-angle wedges ($2\alpha_k = \pi/2$), so that n equals $3/2$. The choice of signs in Equation 5 relates to the polarization convention: use the upper sign for vertical polarization (E-vectors parallel to the edge of the wedge) and use the lower sign for horizontal polarization (E-vectors perpendicular to the edge). Finally, the angular restrictions on Equation 5 exclude contributions from rays which pass through the interior of the obstacle.

The diffracted field has the form of a cylindrical wave emanating from the edge. Due to its asymptotic relation to exact theory, u_{diff} is accurate provided $ks_{po} \sin \frac{\delta}{2}$ is large. Here δ is an angle which becomes zero on the reflection ($\theta_{diff} = \pi + 2\alpha - \theta_{inc}$) and forward scattering ($\theta_{diff} = \pi + \theta_{inc}$) shadow boundaries (see Figure 2). This failing of GDT is apparent in Equation 5, where u_{diff} is singular along the forward scattering direction due to the polarization independent term.

Accurate estimates of wedge diffraction in the forward scattering region are crucial in the present investigation of obstacle shadowing effects. In the next subsection, we introduce an alternate formulation which is valid in this limited aspect region.

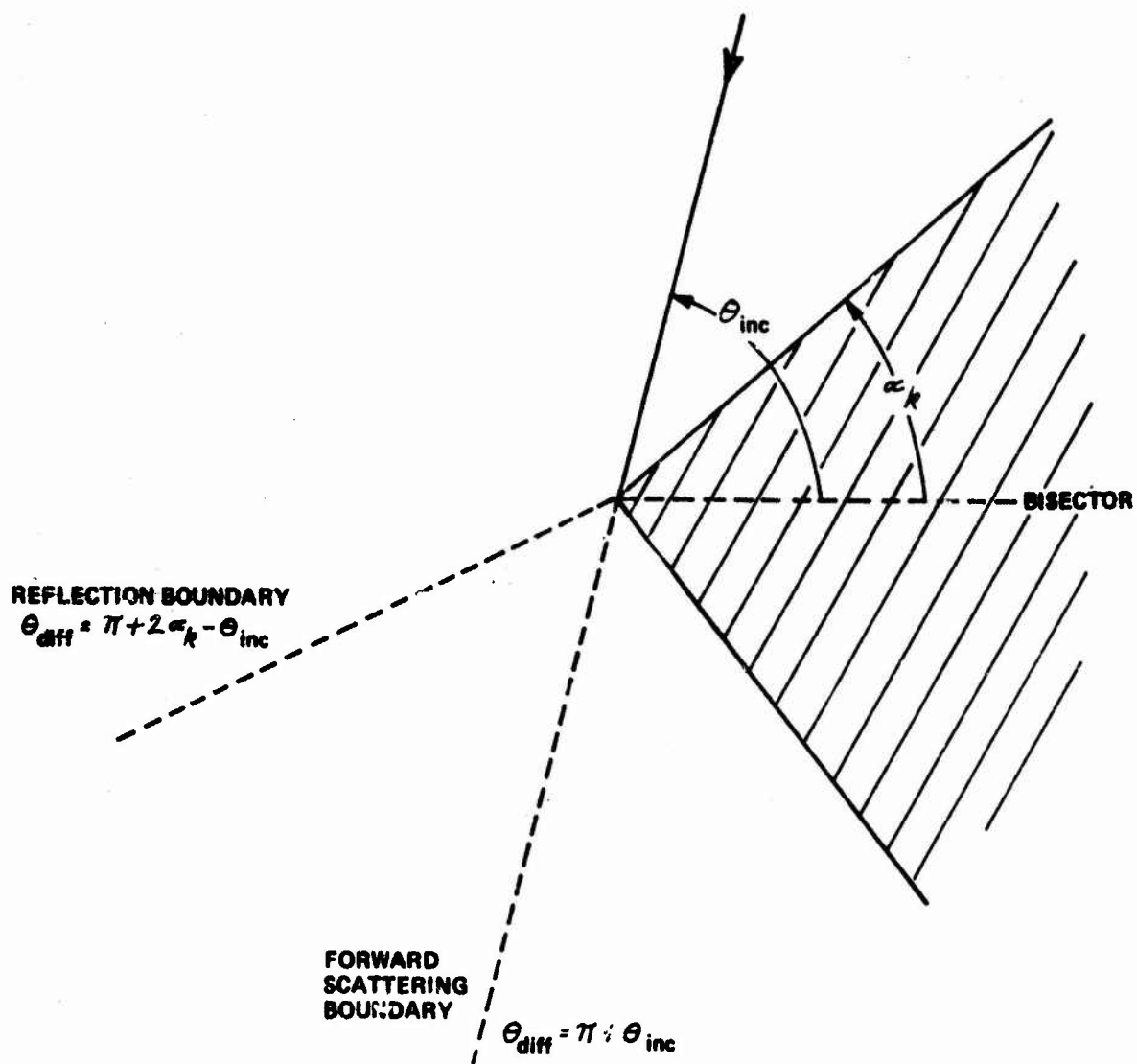


Figure 2 SHADOW BOUNDARIES

2.2.2 Sommerfeld's Half-Plane Result

At and near the forward scattering direction, estimates of the total field around a right-angle wedge could be based upon a relatively complicated summation of hypergeometric functions. However, the diffraction process is known to be insensitive to wedge angle in this region. When the wedge is collapsed to a half-plane, the corresponding result for the diffracted field (Sommerfeld's solution) is a simple combination of Fresnel integrals.

A half-plane is depicted in Figure 3 in terms of the circular cylindrical coordinates (r, θ, ϕ) by $\theta = 0$ (upper surface) and $\theta = 2\pi$ (lower surface). The primary source is a plane wave propagating in the plane perpendicular to the z -axis at an angle θ_{inc} where $\theta \leq \theta_{inc} \leq \pi$ is assumed without loss of generality. We are interested in principal polarization values of the total field u_{total} for small values of $\delta = \pi - (\theta_{diff} - \theta_{inc})$. Sommerfeld's famous result* is

$$u_{total} = u_{inc\rho}(0) \left\{ \left[\frac{1}{2} + \frac{1+i}{2} \left\{ C\left(\frac{\pi}{2}\rho_d^2\right) - iS\left(\frac{\pi}{2}\rho_d^2\right) \right\} \operatorname{sgn}(\rho_d) \right] \mp \left[\frac{1}{2} + \frac{1+i}{2} \left\{ C\left(\frac{\pi}{2}\rho_s^2\right) - iS\left(\frac{\pi}{2}\rho_s^2\right) \right\} \operatorname{sgn}(\rho_s) \right] \right\} \quad (6)$$

where

$u_{inc\rho}(0)$ is the incident plane wave $e^{iks_{po}\cos(\theta_{diff} - \theta_{inc})}$ evaluated at the observation point

$$\rho_s = 2\sqrt{\frac{ks_{po}}{\pi}} \sin\left(\theta_{inc} - \frac{\delta}{2}\right)$$

$$\rho_d = 2\sqrt{\frac{ks_{po}}{\pi}} \sin\frac{\delta}{2}$$

s_{po} is the separation between the edge and the observation point

and $C(x), S(x)$ are the real, imaginary parts of the Fresnel integral.

As we approach the forward scattering direction ($\delta = 0$) from either the illuminated or shadow side, $u_{total} \rightarrow \frac{1}{2} u_{inc\rho}(0)$ which is a well known characteristic of the half-plane solution.

* A. Sommerfeld, Optics, Academic Press, New York, 1954, Chapter V.

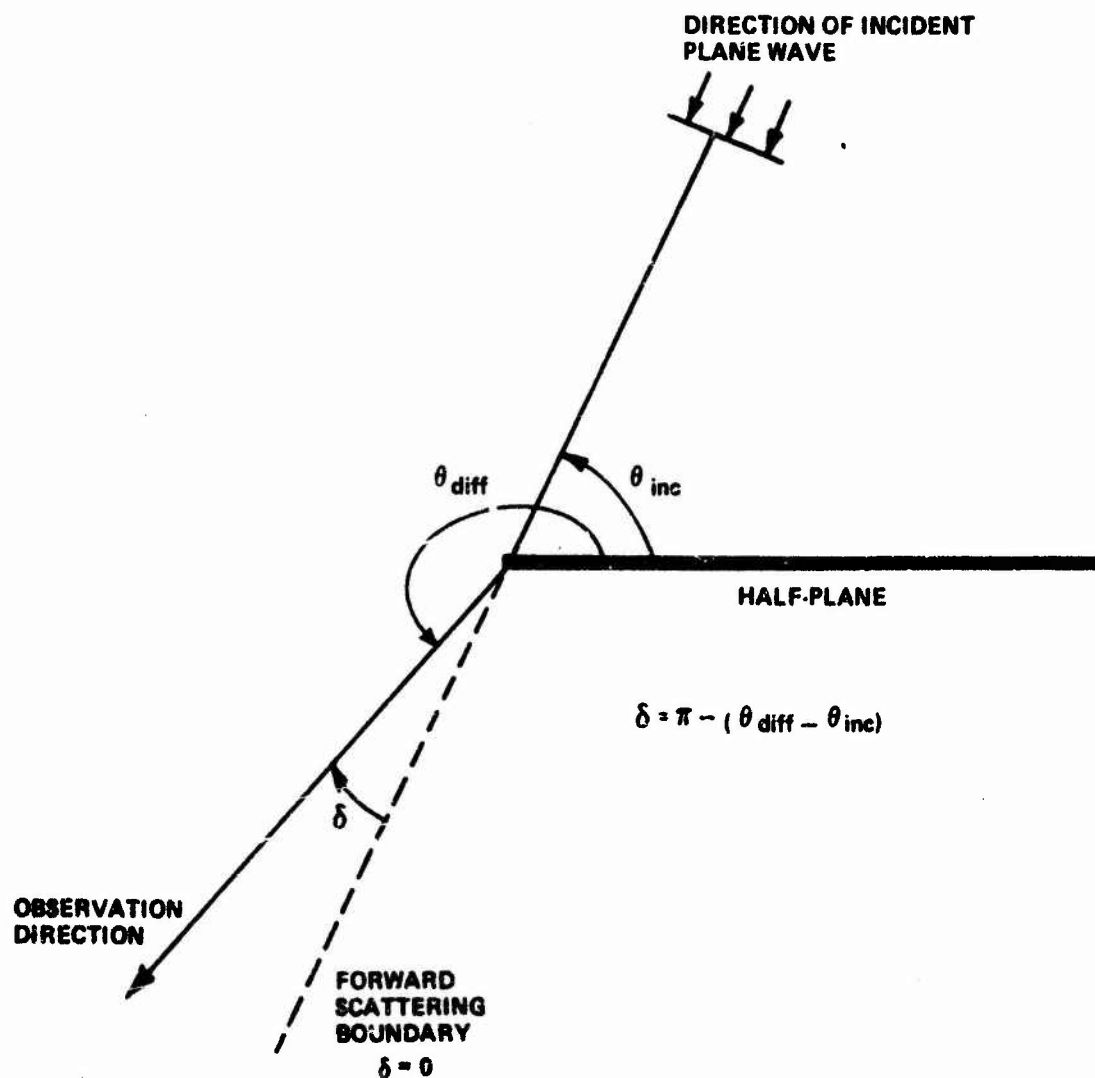


Figure 3 HALF-PLANE GEOMETRY

2.2.3 Combined Formulation

Away from the forward scattering direction, geometric optics plus geometric diffraction theory is a valid representation of the total field

$$u_{total} = u_{G.O.} + u_{diff} \quad (7)$$

For plane wave incidence on an infinitely long right-angle wedge, u_{diff} is given by Equation 5 with $n = 3/2$. Similarly, $u_{G.O.}$ is the incident field evaluated at the observation point O .

$$u_{G.O.} = C_1 e^{iks_{po} \cos(\theta_{diff} - \theta_{inc})} \quad (8)$$

where

$$C_1 = 1; \theta_{diff} \leq \pi + \theta_{inc}$$

$$= 0; \theta_{diff} > \pi + \theta_{inc}$$

The factor C_1 in Equation 8 is an explicit reminder of shadowing effects in any geometric optics description.

Sommerfeld's result (Equation 6) gives the total field due to plane wave incidence on an infinite half-plane. It also approximates the total field around a right-angle wedge provided observation is close to the forward scattering direction.

Here we evaluate the utility of a combined formulation for the total field about a right-angle wedge. Specifically, we seek a suitable range/ observation angle parameter at which the switch between the two analytical descriptions preserves continuity in predicted fields. Figures 4 and 5 show principal polarization calculations for normal incidence ($\beta_k = \pi/2$) with $\theta_{inc} = \pi/2$ and $ks_{po} = 1000$. The dashed curves exhibit the failure of GDT predictions near the forward scattering direction ($\delta = 0$) due to the singularity contained in the diffraction term u_{diff} . The solid curves show that Sommerfeld's half-plane result is well-behaved in the forward-scattering region, and that it is in essential agreement with asymptotic theory for $|\delta| \geq 4$ degrees. The switch-over point corresponds to $|\rho_d| = 1.25$, where ρ_d is given in Equation 6: Therefore, for $|\rho_d| \geq 1.25$, use the asymptotic representation given by Equation 5; for $|\rho_d| < 1.25$, use the half-plane result (Equation 6).

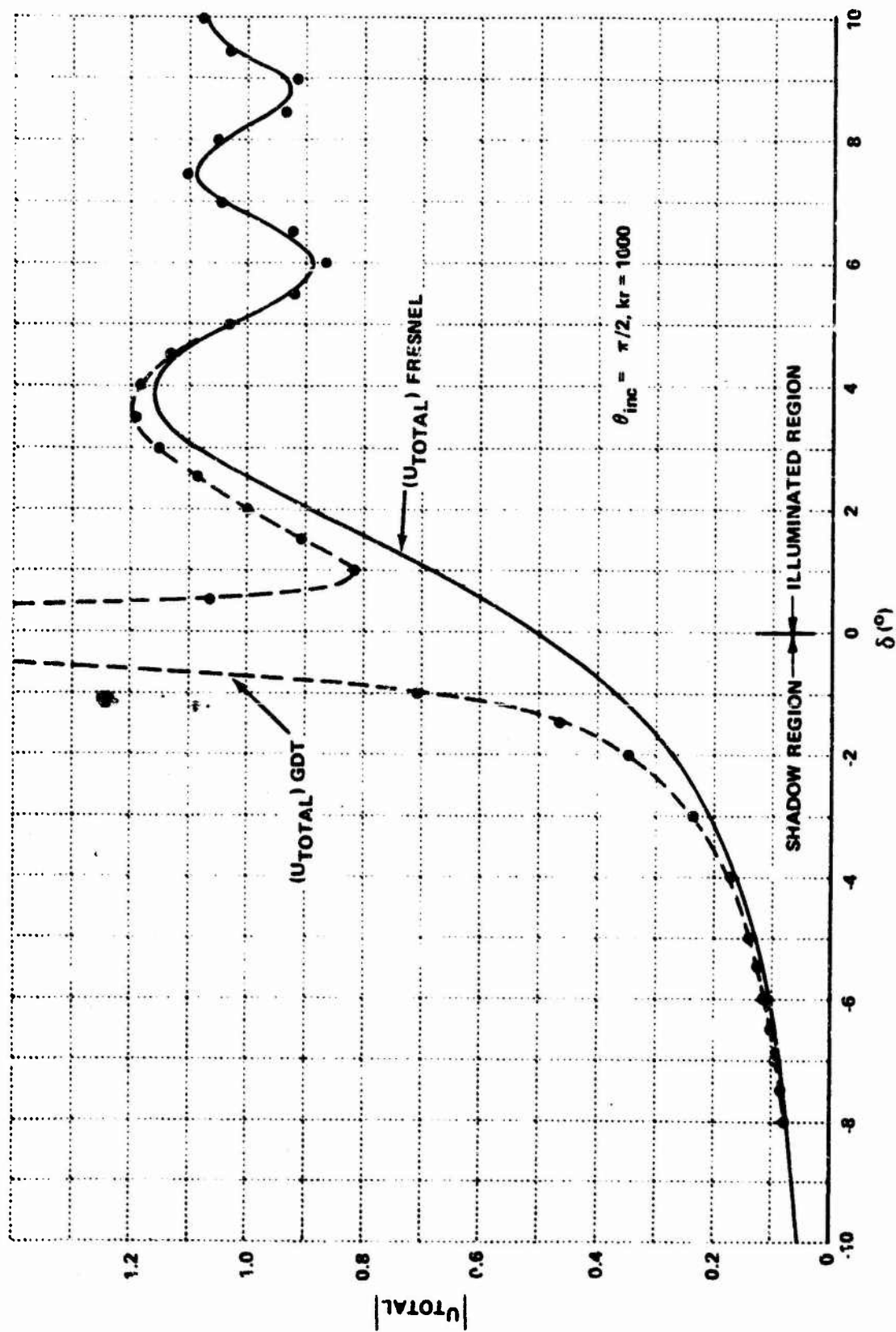


Figure 4 U_{TOTAL} FOR 90° WEDGE: VERTICAL POLARIZATION

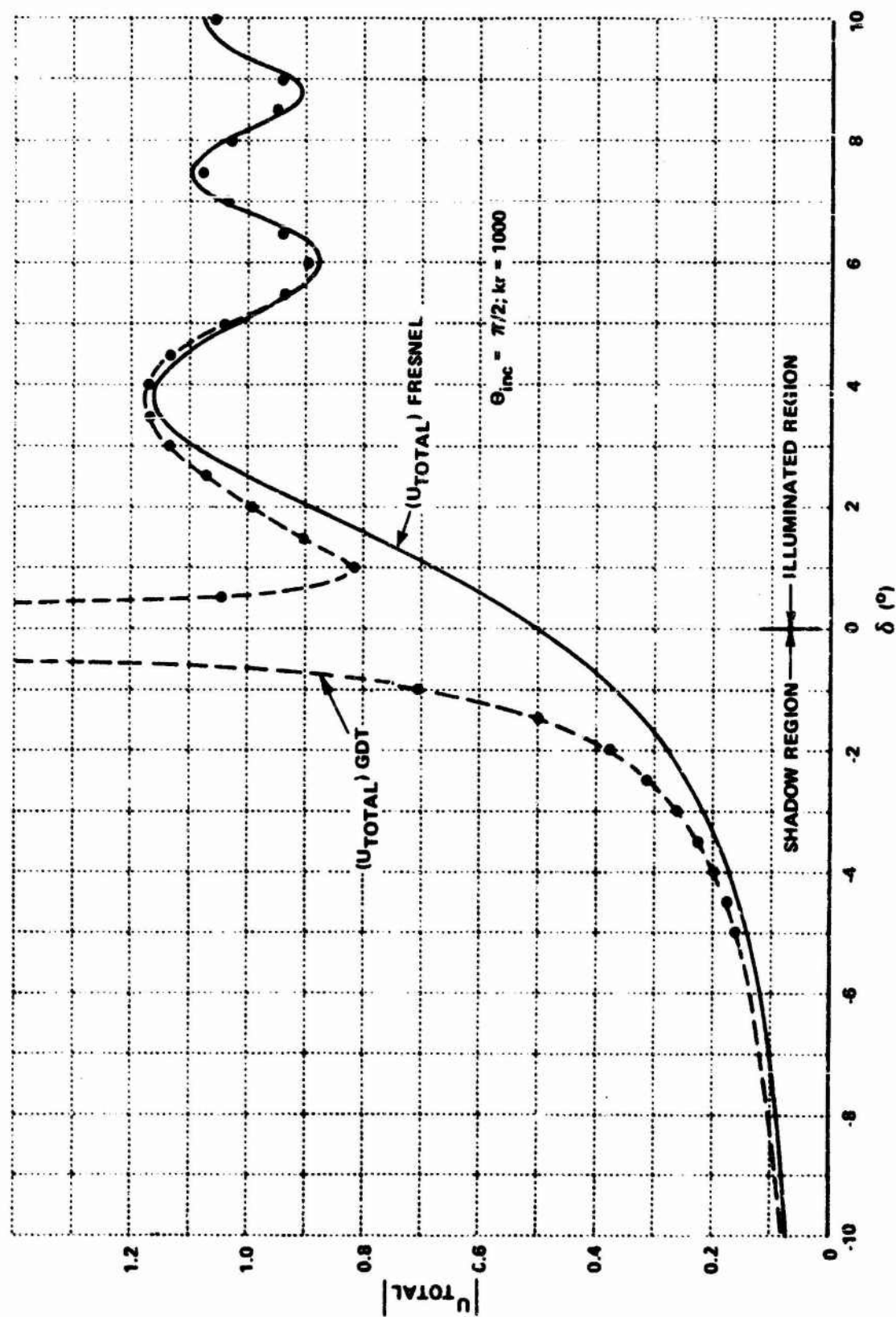


Figure 5 U_{TOTAL} FOR 90° WEDGE: HORIZONTAL POLARIZATION

2.3 DIFFRACTION BY A FINITE LENGTH EDGE

2.3.1 Introduction

A problem in the development of suitable expressions for the present diffraction program arose from the fact that the building producing the diffracted fields of interest is modeled by edges of finite length which may be illuminated at angles other than normal and may, in addition, be illuminated and observed from distances small enough to invalidate the usual plane-wave (flat-phase-front) approximation.

When the edge has finite length, diffraction occurs in many directions in addition to those satisfied by the law of edge diffraction. Thus, although maximum diffraction can be expected along the cone of diffracted rays in Figure 1, an edge of finite length will produce nonzero fields propagating in other directions.

In the present application, we are interested in nonnormal incidence by waves that may have curved phase fronts because of the relatively long diffracting edges of buildings that may not be extremely great distances from the source of illumination or the point of observation.

It is therefore desirable to establish a simple formalism that can be used to approximate diffracted fields in practical situations. To apply Equation 5 directly to an edge of finite length would be extremely time-consuming: the field diffracted by an edge, u_{edge} , would be the integral of u_{diff} at a point on the edge, evaluated over the length of the edge. In the usual situation, the separations between source-obstacle and obstacle-observation point will be many hundreds of wavelengths. Then certain aspects of edge diffraction are well approximated by the behavior at the mid-point of the edge. Specifically, angles and ranges can be assigned those values corresponding to the mid-point, but phase variation along the edge must be retained. On this basis, a simple relation can be derived which transforms the two-dimensional analysis of Section 2.2 to the three-dimensional case of interest.

2.3.2 Analysis

Here we consider the relationship between two-dimensional and three-dimensional fields, i.e., between diffraction from an infinitely long and from a finite edge. First we treat the normal plane case, and then expand this result for nonnormal incidence.

i) Normal Plane Case

The procedure and notation to be used for the simple normal plane case is largely that used by van de Hulst (Reference 1). For the infinitely long cylinder, he gives (Reference 1, page 302) the two-dimensional diffracted field, u_2 , as

$$u_2 = \sqrt{\frac{2}{\pi k R}} T(\theta) e^{-i\frac{3\pi}{4} - ikR} \quad (9)$$

where

k = wave number

$T(\theta)$ = angular scattering pattern.

It is assumed here that illumination is by a plane wave traveling normal to the axis of the cylinder. Van de Hulst uses a straightforward but relatively complicated way to obtain the diffracted field when a section of length ℓ of the cylinder becomes the scatterer (Reference 1, page 305). The field of the resulting three-dimensional wave is

$$u_3 = \frac{\ell}{i\pi R} T(\theta) e^{-ikR} \quad (10)$$

By taking the ratio of u_3 and u_2 , we can establish the relationship between two-dimensional and three-dimensional fields, i.e., between the diffraction from an infinitely long and from a finite cylinder. We get

$$u_3 = u_2 \left[\frac{e^{+i\frac{\pi}{4}}}{\sqrt{R\lambda}} \right] \ell \quad (11)$$

Equation 11 also relates two- and three-dimensional results for diffraction by an edge. In this case the azimuthal angular scattering pattern is determined by comparing Equations 5 and 9. We find that

$$\tau(\theta) = \frac{e^{i\frac{\pi}{2}}}{2} \frac{\sin \frac{\pi}{n}}{n} \left[\left\{ \cos \frac{\pi}{n} - \cos \frac{\theta_{diff} - \theta_{inc}}{n} \right\}^{-1} \right. \\ \left. + \left\{ \cos \frac{\pi}{n} + \cos \frac{2\pi - \theta_{diff} - \theta_{inc}}{n} \right\}^{-1} \right] \quad (12)$$

with all parameters in Equation 12 defined with Equation 5.

In the following development we treat nonnormal incidence of spherical waves on an edge.

ii) Nonnormal Case

The method used by Van de Hulst to get Equation 10 above becomes quite cumbersome when more complicated scattering geometries are to be treated. In particular, we are interested in nonnormal incidence by spherical waves that may have curved phase fronts because of the relatively long diffracting edges of buildings that may not be extremely great distances from the source of illumination or the point of observation. It is therefore desirable to establish a simpler formalism that can be used to approximate the diffracted field.

It is very reasonable to assume that the current flowing along the diffracting edge is determined to a large extent by the local incident field, provided the edge is much longer than a wavelength so that resonance effects are unimportant. It is also reasonable to assume that the field observed at a point distant from the edge is determined by radiation from the current elements along the edge. Under these assumptions we can write the field at the observation point as

$$u_{edge} = p \int_{-L/2}^{L/2} u_{inc}(z) e^{-ik(r_{sz} + s_{po})} dz \quad (13)$$

where

$$u_{edge} = \text{field diffracted from a finite length edge,}$$

$$u_{inc}(z) = \text{incident field at a point } z \text{ on edge,}$$

$$r_{sz} = \text{distance from source points to a point } z \text{ on edge,}$$

$$s_{zo} = \text{distance to observation point } O \text{ from a point } z \text{ on edge,}$$

$$l = \text{length of edge}$$

$$V = \sin \beta_k \sin \beta_s \quad \text{where } \beta_k (\beta_s) \text{ is the angle between the incident (observed) ray and the edge}$$

and

$$P = \text{constant, to be determined.}$$

The unknown constant P must take into account the azimuthal scattering pattern of the edge and the divergence of the spherical wave from the edge.

We can most easily obtain this constant by assuming plane-wave incidence normal to the edge. Next we compare this form of Equation 13 with the more rigorous result of Van de Hulst (Equation 10) to obtain

$$P = \frac{T(\theta)}{i\pi S_{po}} \quad (14)$$

where $T(\theta)$ is the azimuthal scattering pattern associated with the normal-incidence, two-dimensional edge diffraction solution.

It remains to interpret Equation 13 when u_{inc} is a spherical wave emanating from a point source,

$$u_{inc_s}(z) = \frac{e^{-ikr_{sz}}}{\sqrt{4\pi} r_{sz}} \quad (15)$$

where r_{sz} is the distance from the source to a point z on the finite edge. Substituting Equations 14 and 15 into Equation 13, the result is

$$u_{edge} = \left[\frac{T(\theta)}{i\pi S_{po}} \right] \left[\frac{1}{\sqrt{4\pi} r_{sz}} \right] V \int_{-\frac{l}{2}}^{\frac{l}{2}} e^{-ik(r_{sz} + s_{zo})} dz \quad (16)$$

In summary, knowledge of the two-dimensional solution of diffraction by an infinite edge (which provides $T(\theta)$) followed by application of Equation 16 provides our estimate of three-dimensional diffraction due to spherical wave illumination of a finite edge.

We now introduce the mid-point simplification discussed in subsection 2.3.1. Equation 16 applies for the point source and edge (having finite length l) depicted in Figure 6. It is convenient to consider the edge coincident with the Z-axis with mid-point p located at $z = 0$. First we make the usual assumption that ranges in the amplitude factors of Equation 16 (i.e., r_{sz}, s_{zo}) can be replaced by the mid-point values (i.e., r_{sp}, s_{po}). Second, we retain phase-curvature effects by expanding the z-dependent ranges about the mid-point range

$$\begin{aligned}
 r_{sz} &\sim r_{sp} + z \cos \beta_k + \frac{1}{2} \left(\frac{z^2}{r_{sp}} \right) \sin^2 \beta_k - \frac{1}{2} \left(\frac{z^3}{r_{sp}^2} \right) \cos \beta_k \sin^2 \beta_k \\
 &\quad - \frac{1}{8} \left(\frac{z^4}{r_{sp}^3} \right) \sin^2 \beta_k (1 - 5 \cos^2 \beta_k) + \dots \\
 &\sim r_{sp} + r(z) \\
 s_{zo} &\sim s_{po} + z \cos \beta_s + \frac{1}{2} \left(\frac{z^2}{s_{po}} \right) \sin^2 \beta_s - \frac{1}{2} \left(\frac{z^3}{s_{po}^2} \right) \cos \beta_s \sin^2 \beta_s \\
 &\quad - \frac{1}{8} \left(\frac{z^4}{s_{po}^3} \right) \sin^2 \beta_s (1 - 5 \cos^2 \beta_s) + \dots \\
 &\sim s_{po} + s(z)
 \end{aligned} \tag{17}$$

Equation 17 above is substituted when range appears in a phase term of Equation 16, since any such range term which changes by a significant fraction of a wavelength will have an effect on the integration necessary to determine the diffracted field u_{edge} . Reflecting the above considerations into our previous result we obtain

$$u_{edge} = \left[\frac{T(\theta)}{i\pi s_{po}} \right] \left[\frac{1}{\sqrt{4\pi} r_{sp}} \right] e^{-ik(r_{sp} + s_{po})} Q \tag{18}$$

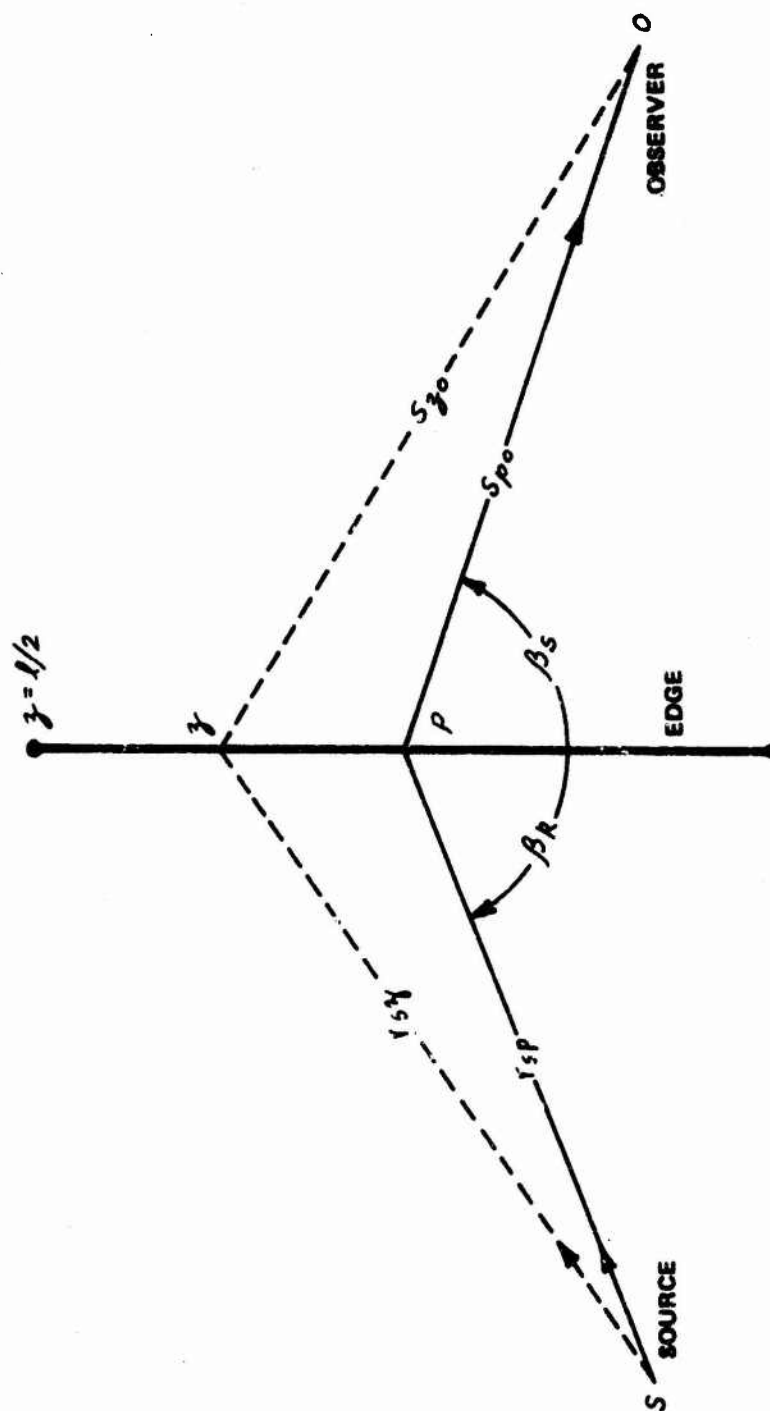


Figure 6 EDGE GEOMETRY FOR MID-POINT SIMPLIFICATION

where

$$Q = \sqrt{\int_{-\frac{1}{2}}^{\frac{1}{2}} e^{-ik[r(z)+s(z)]} dz} \quad (19)$$

Efforts to evaluate the integral Q of Equation 19 suggest that a direct integration for phase functions involving powers of z greater than the second is impractical. It appears that the best way to handle excessively large amounts of phase curvature is to break up the edge into shorter sections, each of them short enough so that phase terms through only second order need be incorporated. Then we can evaluate Q as a sum of integrals, each of which permits expression in terms of Fresnel integrals. The details of the evaluation of Q in this manner are presented in Appendix I.

2.3.3 Combined Formulation

Collecting results presented in subsections 2.2 and 2.3, we can now present our formulas for estimating diffraction by a finite-length edge illuminated by a spherical wave at nonnormal incidence.

In the aspect region away from the forward scattering direction, simple GDT formulas provide an accurate estimate of edge diffracted fields. From Equations 13 and 18 we have

$$(u_{GDT})_{edge} = \left[\frac{e^{-ikr_{sp}}}{\sqrt{4\pi r_{sp}}} \right] \left[\frac{e^{-iks_{po}}}{i\pi s_{po}} \right] T(\theta) Q \quad (20)$$

The first bracketed term in Equation 20 represents the incident spherical wave evaluated at the edge. The second bracketed term accounts for spherical wave diffraction from the edge. $T(\theta)$ is the azimuthal angular scattering pattern given by Equation 12. Finally, Q is the integral given by Equation 19 which incorporates phase curvature effects across a finite edge.

In the aspect region near and at the forward scattering direction, Sommerfeld's half-plane solution is substituted for GDT to avoid the singular behavior of the latter formulation. In this limited region, the two-dimensional total field $(u_s)_{total}$ is given by Equation 6. To construct the equivalent

diffracted field $(u_s)_{diff}$ we subtract the incident plane wave. The two-dimensional result is

$$(u_s)_{diff_{2-D}} = u_{inc_p}(0) \left[(u_s)_{total} - C_1 \right] \quad (21)$$

Finally, Equation 21 is modified according to Equation 11 for our application

$$(u_s)_{diff} = \left[\frac{e^{-ikr_{sp}}}{\sqrt{4\pi r_{sp}}} \right] e^{i\frac{\pi}{4}} \sqrt{\frac{k}{2\pi s_{po}}} \left[(u_s)_{diff_{2-D}} \right] \quad (22)$$

Equation 22 applies for $|\rho_d| \leq 1.25$ as stated in subsection 2.2.3.

2.3.4 Preliminary Calculation of the Total Field Around a Finite-Length Right-Angle Edge

Figure 7 depicts the source, edge and observation plane in a typical case. The spherical source is located at a height z_s above a flat earth (x-y plane) at a distance D_2 from the center of the obstacle. A vertical edge extends a finite length ℓ above the earth with mid-point elevation denoted by z_{mp} . Observation points $O(x_o, y_o, z_o)$ are constrained to lie on a vertical observation plane which is oriented perpendicular to the line through the source and center of the obstacle. We wish to calculate the total field at the observation plane at a height $z_o = z_s$.

The total field u_{total} is expressed as

$$u_{total} = u_{G.O.} + u_{diff}$$

where $u_{G.O.}$ is the geometric optics field (equal to u_{inc} in the illuminated region and zero in the shadow region) and u_{diff} for spherical wave incidence on a finite edge is given by Equations 20 or 22. In order to spotlight a remaining difficulty in the analysis, we purposely choose the following combination of parameters: low frequency ($\lambda = 1.09$ feet), short separations ($D_1 = D_2 = 1000$ feet), long edge ($\ell = 100$ feet). For simplicity, we choose $z_s = z_o = z_{mp} = 50$ feet, so that calculations are made in a plane as a function of distance along the Y-axis.

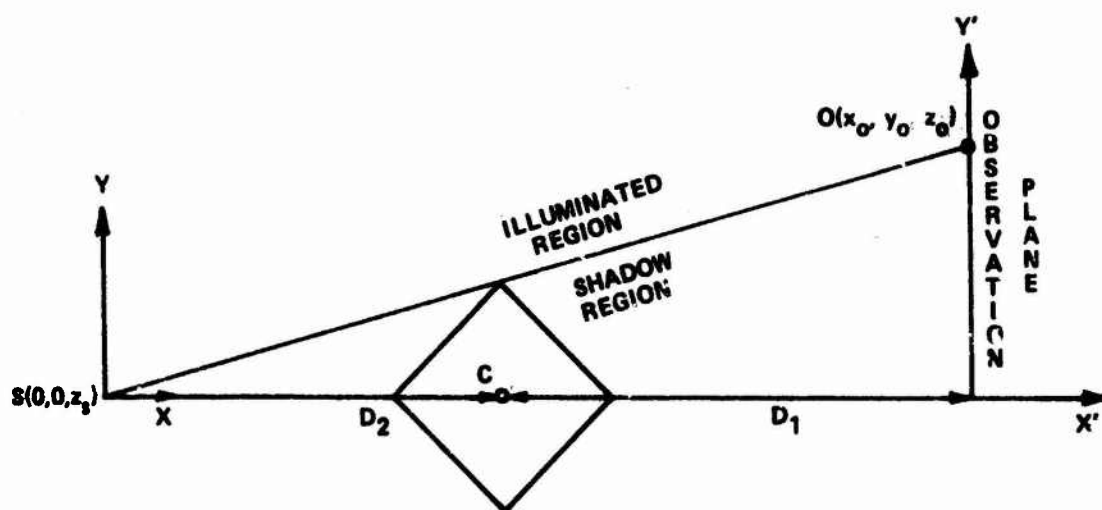


Figure 7 GEOMETRY FOR PRELIMINARY CALCULATION

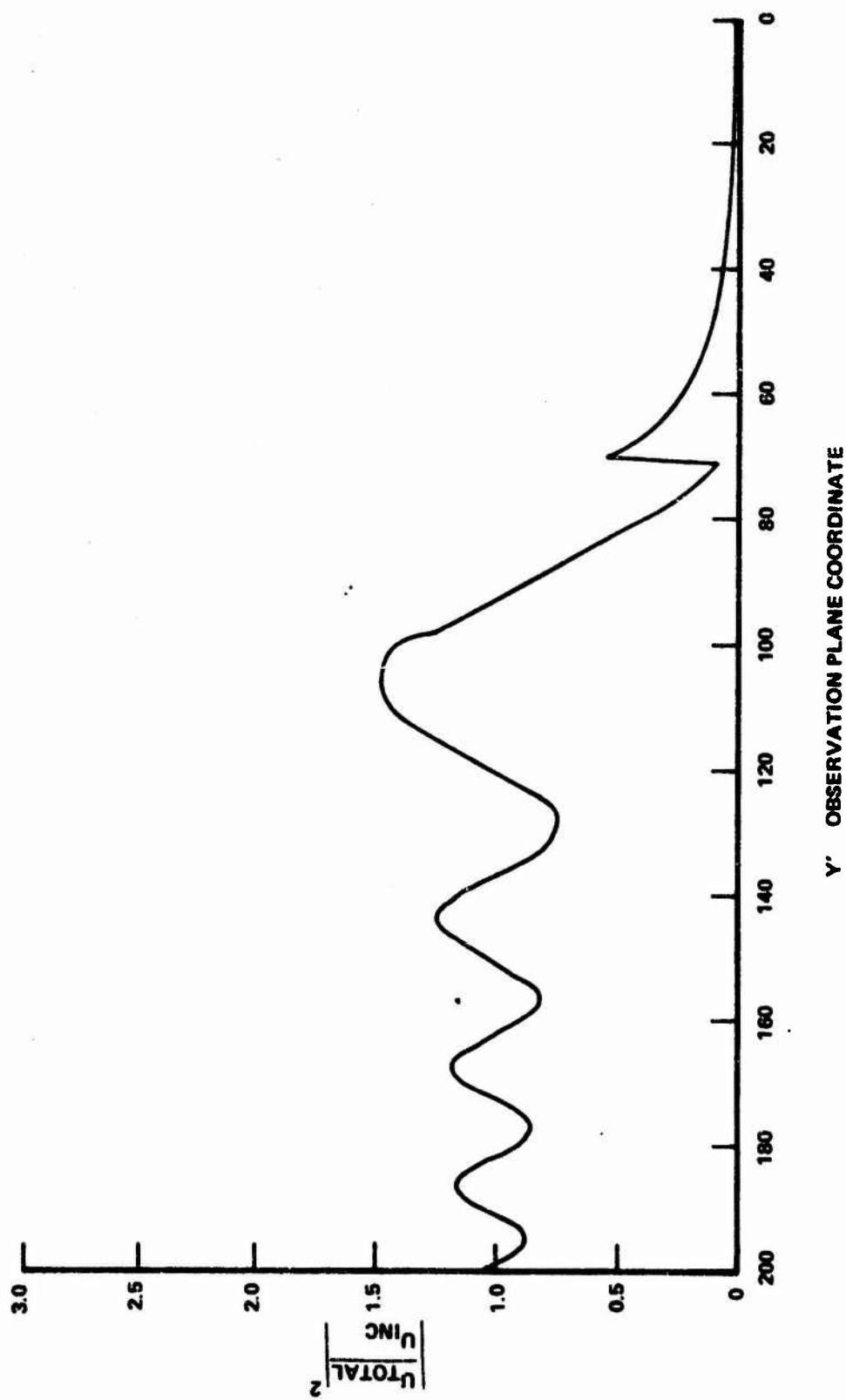
Figure 8 is a plot of the square of the absolute value of the normalized total field (vertical polarization) evaluated along the Y-axis at the observation plane. At the point farthest into the shadow region ($Y = 0$), calculations are based upon GDT. The shadow field is continuous at $Y = 18$ meters, where the switch is made to half-plane formulas. The forward scattering direction corresponds to $Y = 72$ meters, where a sharp discontinuity is observed. Half-plane formulas are used out to $Y = 100$ meters, where the GDT approximation enters, and the latter formulation is employed for all larger values of Y .

Based upon previous experience, we can state that predictions based upon GDT are accurate. Similarly, half-plane estimates in the shadow region are well founded. Therefore, the half-plane estimates in the illuminated region shown in Figure 8 must be in error. The proper behavior of the fields under question should provide continuity with adjacent fields. In the next subsection we identify the cause of error and introduce a compensating modification which improves upon present field estimates based upon the half-plane solution in the illuminated region.

2.3.5 Modification to Half-Plane Formulas in the Illuminated Region

The fictitious discontinuity occurring at the forward scattering direction in Figure 8 can be traced to the equivalent diffracted field defined according to Equation 17. There the half-plane diffracted field has a discontinuity which is exactly cancelled by the discontinuity in the geometric optics field (in the half-plane solution, the geometric optics field is the incident plane wave in the illuminated region). The resultant three-dimensional diffracted field given by Equation 21 cannot be continuous at the shadow boundary since now a spherical wave is added to obtain the total field.

More realistic estimates of the total field in the illuminated region based upon the half-plane formulas must provide continuity at the forward scattering boundary. This can be achieved by reducing the role of the geometrics optics fields near the shadow boundary. Towards this end, we have introduced the following modifications.



Y' OBSERVATION PLANE COORDINATE

PRELIMINARY TOTAL FIELD CALCULATION

Figure 8

Recall that the field predictions in the illuminated region switch from the half-plane solution to GDT for $\rho_d = 1.25$. Denoting this transition value as ρ_{dT} , we employ Equation 6 to determine the transition angle δ_T measured from the shadow boundary

$$\delta_T \sim \frac{\rho_{dT}}{\sqrt{\frac{k s p_0}{\pi}}} \quad (23)$$

Next we form the ratio δ/δ_T , which is zero on the shadow boundary and unity at the transition direction.

First we apply the factor δ/δ_T to Equation 21 to obtain total field estimates near the shadow line in a two-dimensional analysis

$$(u_s)_{diff_{2-D}} = u_{inc_p}(0) \left[(u_s)_{total} - C_1 \frac{\delta}{\delta_T} \right] \quad (24)$$

Next we reduce the role of the geometric optics term (spherical wave) at the shadow boundary by assuming

$$u_{total} = u_{g.o.} \frac{\delta}{\delta_T} + u_{diff} \quad (25)$$

Comparison of results shown in Figures 8 and 9 shows the effect of incorporating the modified formulas (Equations 24 and 25). Notice the field predictions are essentially continuous through the forward scattering directions. Near the transition point ($y = 100$), our formulation underestimates the expected behavior, which is indicated by the dashed curve. However, the suspect predictions are confined to a region less than 10 meters in extent on the observation plane and the error is less than 0.5 dB. Thus, the modified formulation in its present form was employed. It is noted that additional analysis could be fruitful in applications which require more precise estimates.

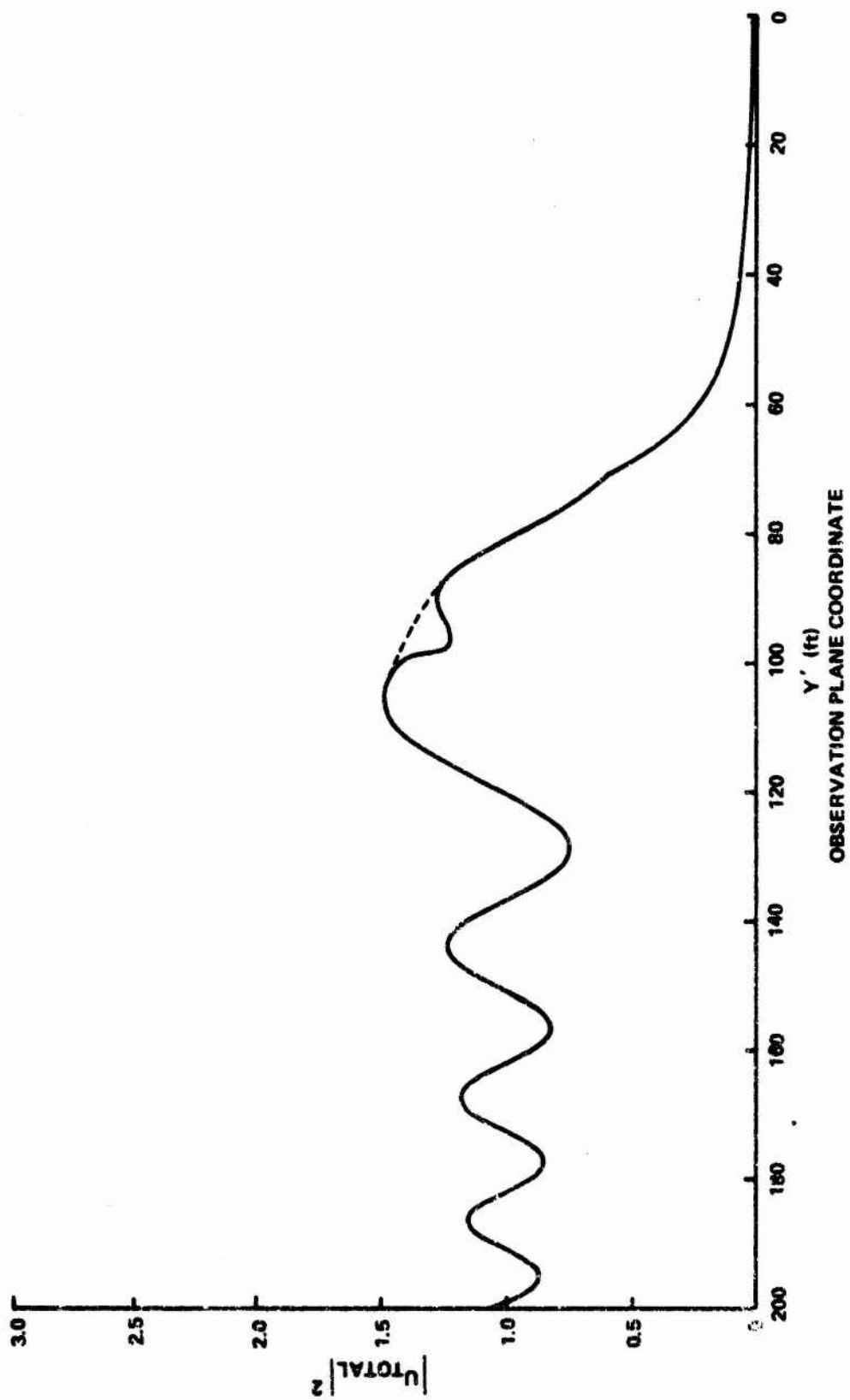


Figure 9 EFFECT OF INCORPORATING MODIFIED FORMULAS

2.4 DIFFRACTION BY A RECTANGULAR BUILDING

2.4.1 Geometrical Considerations

This section contains the derivation of geometrical parameters required in applying diffraction formulae to the edges of the finite cylinder. These parameters include specification of source, edge and observation locations, incidence and observation angles, and polarization. The mid-point simplification introduced in subsection 2.3.2 is employed at each edge.

Figure 10 illustrates the source, S , rectangular building and observation point, O . An arbitrary numbering scheme for corners is shown. The hidden node labelled 8 is flagged in the computer so that edges involving this corner are automatically screened from further consideration. In addition, horizontal edges joining nodes at the ground will be excluded. To illustrate the computation procedure, the geometric parameters associated with edge are derived below.

First calculate the length of edge E_{15}

$$L_{15} = \sqrt{(x_1 - x_5)^2 + (y_1 - y_5)^2 + (z_1 - z_5)^2} \quad (26)$$

and the coordinates of the mid-point on the edge

$$P_{15} = \left(\frac{x_1 + x_5}{2}, \frac{y_1 + y_5}{2}, \frac{z_1 + z_5}{2} \right) = (x_{P15}, y_{P15}, z_{P15}) \quad (27)$$

Taking the source coordinates as $S(0, 0, z_s)$ and observation coordinates as $O(x_o, y_o, z_o)$, compute the mid-point ranges

$$r_{sp} = \sqrt{(x_{P15})^2 + (y_{P15})^2 + (z_{P15})^2} \quad (28)$$

$$s_{po} = \sqrt{(x_{P15} - x_o)^2 + (y_{P15} - y_o)^2 + (z_{P15} - z_o)^2} \quad (29)$$

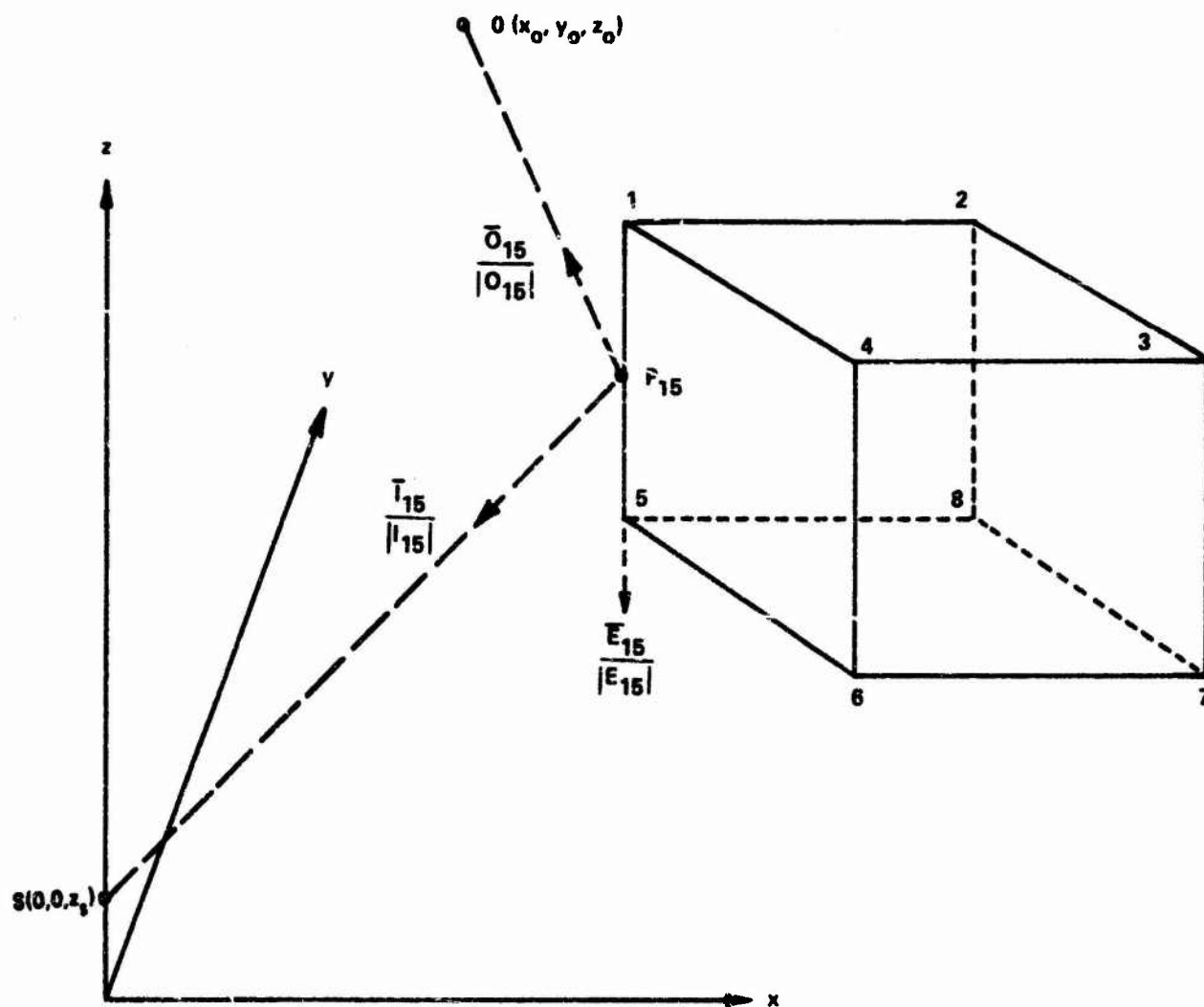


Figure 30 RECTANGULAR BUILDING: NODE NUMBERING SCHEME

To calculate the angles β_k , β_s , θ_{inc} and θ_{diff} for edge E_{15} using the mid-point simplification, consider the properties of incident, observation and edge vectors. According to the convention depicted in Figure 10, the incidence vector \bar{I}_{15} joins p_{15} to S and the observation vector \bar{O}_{15} joins p_{15} to O . The edge vector \bar{E}_{15} originates at the mid-point p_{15} with sense determined by node ranges r_1 and r_5 . Assume $r_5 \leq r_1$. Then points in the direction of node 5. Working with the direction cosines (l, m, n) of these vectors we have

$$\frac{\bar{I}_{15}}{|\bar{I}_{15}|} = \frac{(-x_{p_{15}})\hat{i}_x + (-y_{p_{15}})\hat{i}_y + (z_5 - z_{p_{15}})\hat{i}_z}{r_{sp}}$$

$$\equiv (l_{I_{15}}, m_{I_{15}}, n_{I_{15}})$$
(30)

$$\frac{\bar{O}_{15}}{|\bar{O}_{15}|} = \frac{(x_0 - x_{p_{15}})\hat{i}_x + (y_0 - y_{p_{15}})\hat{i}_y + (z_0 - z_{p_{15}})\hat{i}_z}{s_{p0}}$$

$$\equiv (l_{O_{15}}, m_{O_{15}}, n_{O_{15}})$$
(31)

$$\frac{\bar{E}_{15}}{|\bar{E}_{15}|} = \frac{(x_5 - x_{p_{15}})\hat{i}_x + (y_5 - y_{p_{15}})\hat{i}_y + (z_5 - z_{p_{15}})\hat{i}_z}{l_{15}/2}$$

$$\equiv (l_{E_{15}}, m_{E_{15}}, n_{E_{15}})$$
(32)

The dot product of incidence and edge vectors defines the angle β_k

$$\beta_{k_{15}} = \cos^{-1}(l_{I_{15}} l_{E_{15}} + m_{I_{15}} m_{E_{15}} + n_{I_{15}} n_{E_{15}})$$

$$0 \leq \beta_{k_{15}} \leq \pi/2$$
(33)

Similarly, the dot product of observation and edge vectors gives the angle β_s

$$\beta_{s15} = \cos^{-1}(\ell_{o15} \ell_{E15} + m_{o15} m_{E15} + n_{o15} n_{E15}) \quad (34)$$

where $\pi/2 \leq \beta_{s15} \leq \pi$ in the forward-scattering hemisphere.

To obtain θ_{inc} and θ_{diff} , first construct the direction cosines of the interior bisector of the wedge passing through p_{15} . Calculating the coordinates of points p_{46} and p_{28} in the manner of Equation 27, the bisector is*

$$\begin{aligned} \frac{\bar{B}_{15}}{|\bar{B}_{15}|} &= \frac{\left(\frac{x_{p46} + x_{p28}}{2}\right)\hat{i}_x + \left(\frac{y_{p46} + y_{p28}}{2}\right)\hat{i}_y + \left(\frac{z_{p46} + z_{p28}}{2} - z_{p15}\right)\hat{i}_z}{\sqrt{\left(\frac{x_{p46} + x_{p28}}{2}\right)^2 + \left(\frac{y_{p46} + y_{p28}}{2}\right)^2 + \left(\frac{z_{p46} + z_{p28}}{2} - z_{p15}\right)^2}} \\ &\equiv (\ell_{B15}, m_{B15}, n_{B15}) \end{aligned} \quad (35)$$

The vector \bar{B}_{15} is depicted in Figure 11 along with an intermediate incidence angle θ'_{inc15} and the desired incidence angle θ_{inc15} . Take the dot product of \bar{I}_{15} and \bar{B}_{15} to obtain

$$\begin{aligned} \theta'_{inc15} &= \cos^{-1}(\ell_{I15} \ell_{B15} + m_{I15} m_{B15} + n_{I15} n_{B15}) \\ 0 &\leq \theta'_{inc15} \leq \pi \end{aligned} \quad (36)$$

Referring to the right-angle spherical triangle in Figure 11, the law of cosines gives

$$\begin{aligned} \theta_{inc15} &= \cos^{-1}\left(\frac{\cos \theta'_{inc15}}{\sin \beta_{k15}}\right) \\ \theta &\leq \theta_{inc15} \leq \pi \end{aligned} \quad (37)$$

*Equation 35 applies for a cubical structure only. A more general formulation for computing the angle bisector was later developed. See Appendix II.

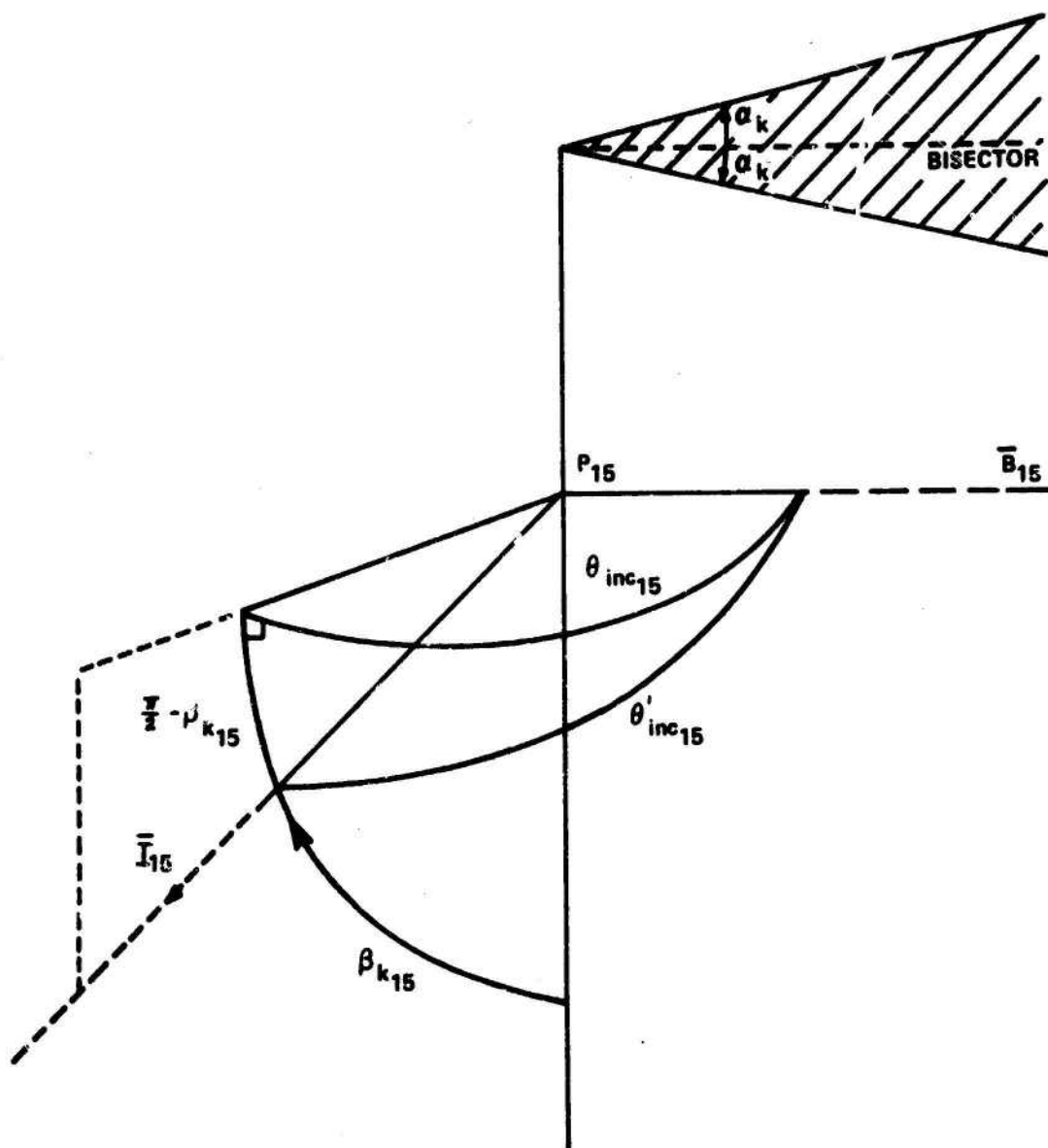


Figure 11 SPHERICAL TRIANGLE FOR INCIDENCE ANGLE

Similar steps lead to the determination of θ_{diff} . Referring to Figure 12, the intermediate observation angle $\theta'_{diff,15}$ is constructed from the dot product of \bar{O}_{15} and \bar{B}_{15} .

$$\theta'_{diff,15} = \cos^{-1}(\bar{O}_{15} \cdot \bar{B}_{15}) = \cos^{-1}(l_{O15} l_{B15} + m_{O15} m_{B15} + n_{O15} n_{B15})$$

$$0 \leq \theta'_{diff,15} \leq \pi$$
(38)

From the right-angle spherical triangle in Figure 12

$$\theta_{diff,15} = 2\pi - \cos^{-1}\left(\frac{\cos \theta'_{diff,15}}{\sin \beta_{S15}}\right)$$

$$\pi \leq \theta_{diff,15} \leq 2\pi$$
(39)

This completes the calculation of mid-point parameters required in the evaluation of diffraction by the finite-length cylinder edge E_{15} . It remains to introduce the polarization convention relating antenna polarization and edge orientation.

In subsection 2.3, we derive expressions for the amplitude and phase of the principal-polarization fields diffracted by an edge on a finite rectangular cylinder. Because of the orthogonality of principal polarizations and the principle of superposition, the diffracted contribution can be calculated for any combination of source antenna polarization, edge orientation, and receiver antenna polarization. We will be concerned with six fixed combinations of source-receiver antenna polarization:

- 1) V/V Transmit Vertical and Receive Vertical
- 2) H/H Transmit Horizontal and Receive Horizontal
- 3) V/LC Transmit Vertical and Receive Left Circular
- 4) H/LC Transmit Horizontal and Receive Left Circular
- 5) V/RC Transmit Vertical and Receive Right Circular
- 6) H/RC Transmit Horizontal and Receive Right Circular

* The roles of "transmitter" and "receiver" may, of course, be interchanged in accordance with the reciprocity principle.

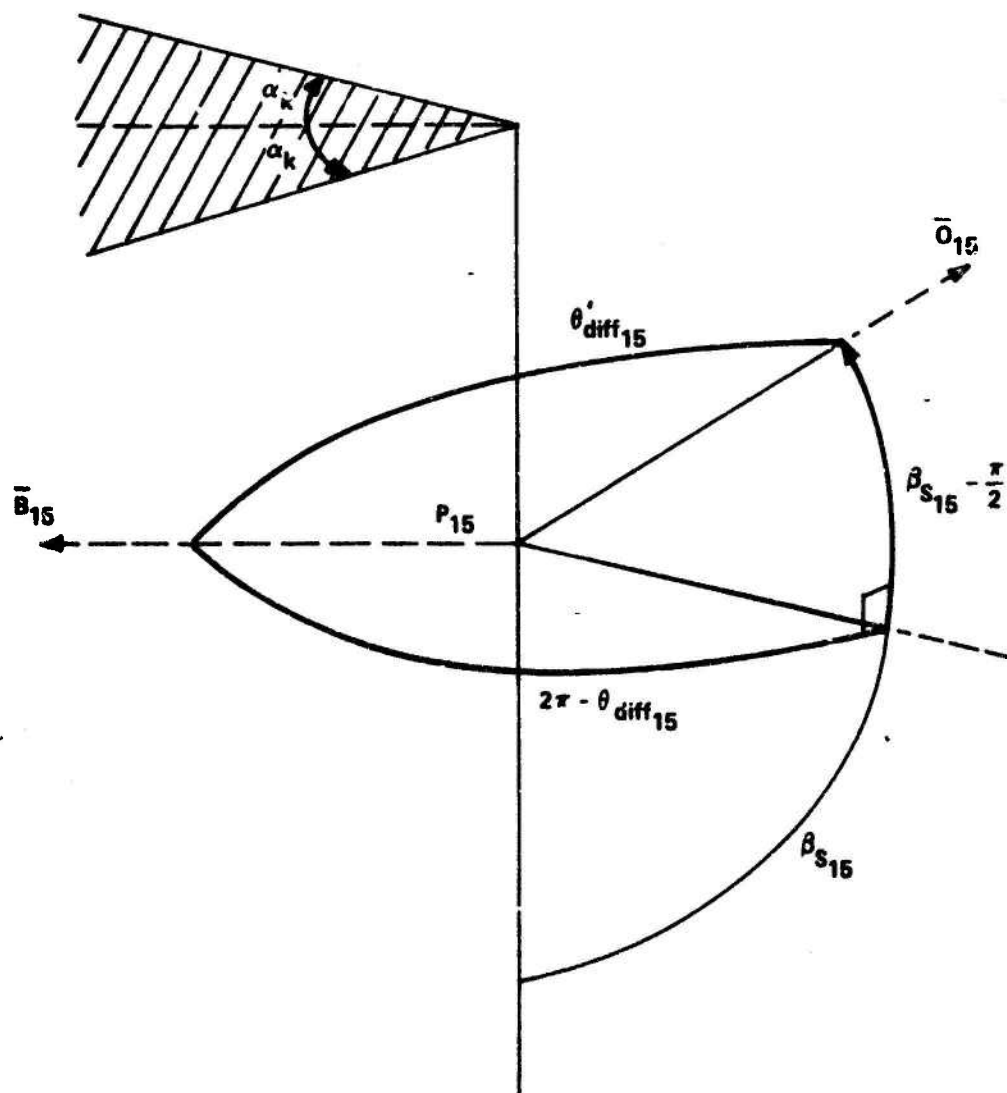


Figure 12 SPHERICAL TRIANGLE FOR OBSERVATION ANGLE

In the vertical polarization case, the E-vector associated with the linearly polarized antenna lies in the plane containing the direction of propagation and the Z-axis of the primary reference system. The horizontal polarization case is orthogonal to the vertical polarization case. Left circular polarization is a counterclockwise wave receding or a clockwise wave approaching. Right circular polarization is the opposite sense to left circular polarization.

Formulas which give the diffraction contribution from an edge for each polarization case are constructed using the polarization scattering matrix (see subsection 2.1.3). It is only necessary to interpret the antenna polarization parameter γ defined in Equations 1 and 2 in terms of edge orientation. Let $\gamma'_t(\gamma'_r)$ be the angle between the z-axis and the normal to the plane containing the incident (observation) vector and the edge. The following relations follow from the polarization convention adopted in subsection 2.1.3.

1) V/V

$$u_{edge} = u_{edge_H} \cos \gamma'_t \cos \gamma'_r + u_{edge_V} \sin \gamma'_t \sin \gamma'_r$$

2) H/H

$$u_{edge} = u_{edge_H} \sin \gamma'_t \sin \gamma'_r + u_{edge_V} \cos \gamma'_t \cos \gamma'_r$$

3) V/LC

$$u_{edge} = u_{edge_H} \frac{\cos \gamma'_t}{\sqrt{2}} + u_{edge_V} \frac{\sin \gamma'_t}{\sqrt{2}} e^{j\frac{\pi}{2}}$$

4) H/LC

$$u_{edge} = u_{edge_H} \frac{\sin \gamma'_t}{\sqrt{2}} + u_{edge_V} \frac{\cos \gamma'_t}{\sqrt{2}} e^{j\frac{\pi}{2}}$$

5) V/RC

$$u_{edge} = u_{edge_H} \frac{\cos \gamma'_t}{\sqrt{2}} + u_{edge_V} \frac{\sin \gamma'_t}{\sqrt{2}} e^{-j\frac{\pi}{2}}$$

6) H/RC

$$u_{edge} = u_{edge_H} \frac{\sin \gamma'_t}{\sqrt{2}} + u_{edge_V} \frac{\cos \gamma'_t}{\sqrt{2}} e^{-j\frac{\pi}{2}} \quad (40)$$

In Equation 40, u_{edge_H} is the horizontal-polarization component of the field solution (where the lower sign is used in Equations 5 or 6). Similarly, u_{edge_V} is the vertical-polarization component of the field solution (where the upper sign is used in Equations 5 or 6). Treating each edge of the obstruction by Equation 40, and summing the contributions from all edges, we obtain the proper diffraction component $\hat{p} \hat{s} \hat{q}$ introduced in Equation 4. It remains to determine the polarization parameters γ'_t, γ'_r .

Figure 13 depicts the geometry for the incidence orientation angle $\beta_{k_{15}}$. First construct the unit vector $\frac{\bar{N}_{I_{15}}}{|\bar{N}_{I_{15}}|}$ which is normal to the plane containing the incidence vector \bar{I}_{15} and the edge vector \bar{E}_{15} :

$$\frac{\bar{N}_{I_{15}}}{|\bar{N}_{I_{15}}|} = \frac{1}{\sin \beta_{k_{15}}} \frac{\bar{E}_{15}}{|\bar{E}_{15}|} \times \frac{\bar{I}_{15}}{|\bar{I}_{15}|} \quad (41)$$

Next obtain the angle between the normal and the z-axis

$$\cos \gamma'_t = \frac{\bar{N}_{I_{15}}}{|\bar{N}_{I_{15}}|} \cdot \hat{e}_z$$

$$\gamma'_t = \cos^{-1} \left\{ \frac{1}{\sin \beta_{k_{15}}} (\ell_{E_{15}} m_{I_{15}} - m_{E_{15}} \ell_{I_{15}}) \right\} \quad (42)$$

Similarly, the observation orientation angle γ'_r involves the unit vector $\frac{\bar{N}_{O_{15}}}{|\bar{N}_{O_{15}}|}$ which is normal to the plane containing the edge vector and the observation vector \bar{O}_{15} . Referring to Figure 14,

$$\frac{\bar{N}_{O_{15}}}{|\bar{N}_{O_{15}}|} = \frac{1}{\sin \beta_{s_{15}}} \frac{\bar{E}_{15}}{|\bar{E}_{15}|} \times \frac{\bar{O}_{15}}{|\bar{O}_{15}|} \quad (43)$$

with the angle between the normal and the z-axis given by

$$\cos \gamma'_r = \frac{\bar{N}_{O_{15}}}{|\bar{N}_{O_{15}}|} \cdot \hat{e}_z$$

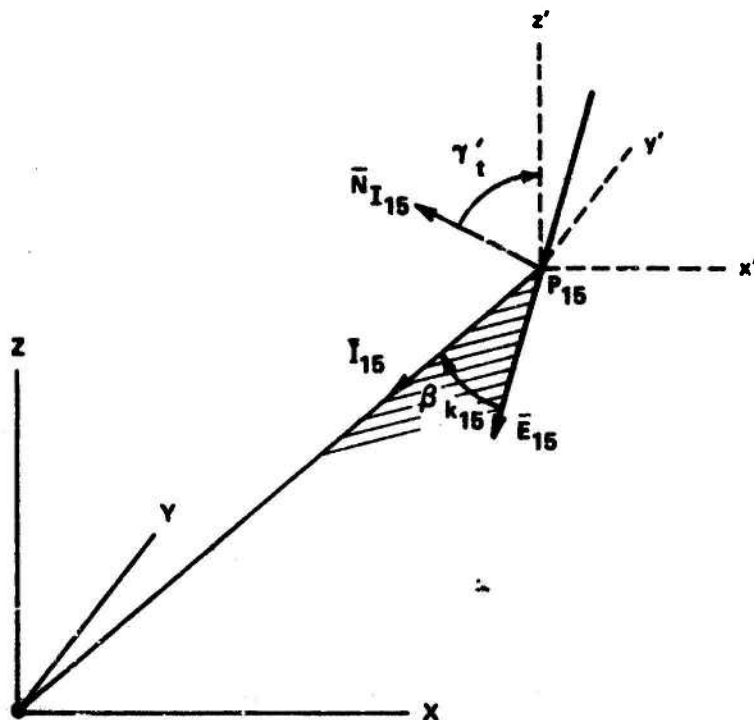


Figure 13 INCIDENCE ORIENTATION ANGLE

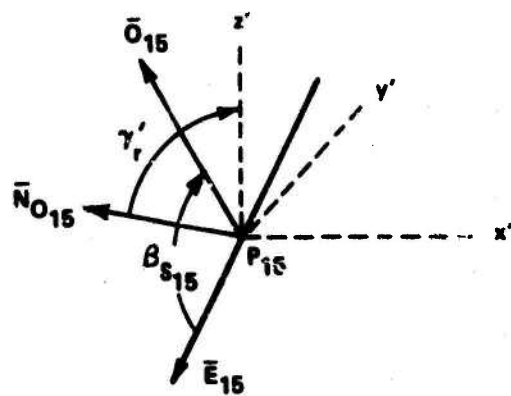


Figure 14 OBSERVATION ORIENTATION ANGLE

so that

$$\gamma_r' = \cos^{-1} \left\{ \frac{1}{\sin \beta_{s15}} (L_{E15} m_{O15} - m_{E15} L_{O15}) \right\} \quad (44)$$

2.4.2 Sample Calculations for Isolated Edges

In this section the final diffraction formulas of subsection 2.3 are combined with the geometrical considerations introduced in subsection 2.4.1. As a step in the checkout of the computer program, the present discussion is limited to the total field around isolated edges on the rectangular cylinder. Section 2.4.3 contains calculations of the total field around the rectangular cylinder, considering all contributing edges.

For simplicity, we choose a uniform square cylinder with side-length 100 feet. (All distances in this section are given in feet unless otherwise noted.) An omnidirectional radiator (source) is located at (0, 0, 50) with wavelength $\lambda = 1.09$ feet (near 1000 MHz). Both vertical or horizontal polarization are considered. The distances separating the building centroid from the source or observation plane are equal ($D_1 = D_2$).

2.4.2.1 Vertical Edge

Consider the total field around a finite vertical edge (specifically the edge with nodes 1 and 5 shown in Figure 10) on a square building placed on a flat earth. Let the vertical edge be 100 in height. By choosing $z_0 = 50$ and $z = 50$, the source, observation elevation and mid-point of the edge lie in a horizontal plane.

Figure 15 is a top view of this horizontal plane when one face of the specified edge is normal to the line joining the source and the y-axis of the observation plane. The separation of both the source and observation plane from the building centroid is taken to be 1000. The continuous curve in Figure 16 is a plot of the total field as a function of y for vertical polarization. For $y \leq 50$, the observation points lie in the shadow of both geometric optics and the singly-diffracted field arising at edge E_{15} . As y increases beyond 50 feet, the diffraction contribution from the isolated vertical edge is

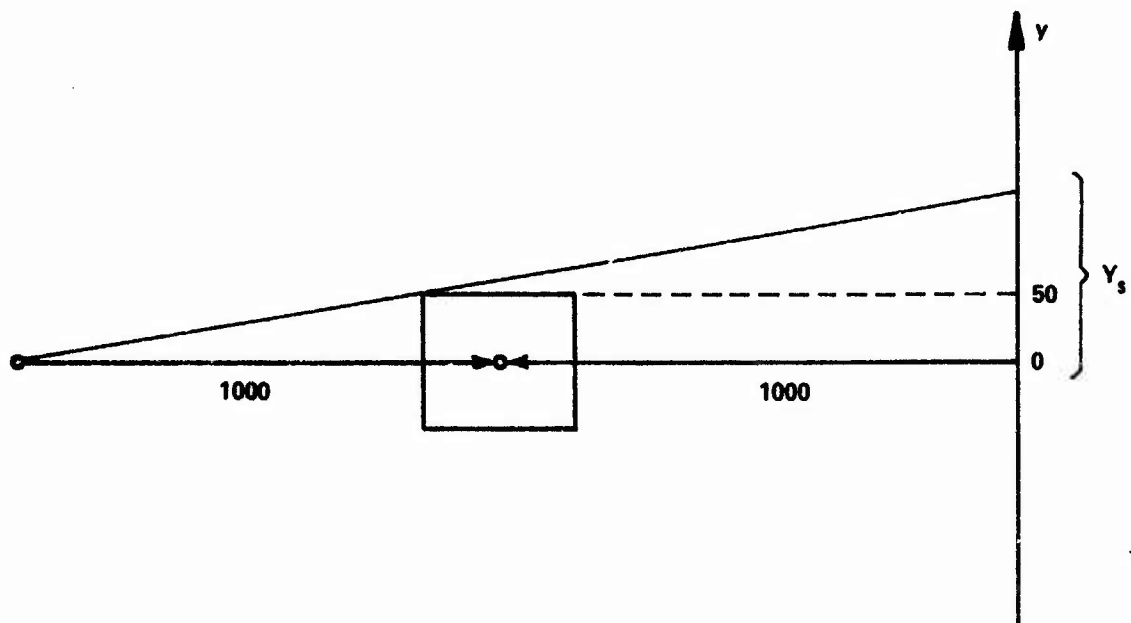


Figure 15 PLAN VIEW OF LAYOUT FOR RECTANGULAR BUILDING

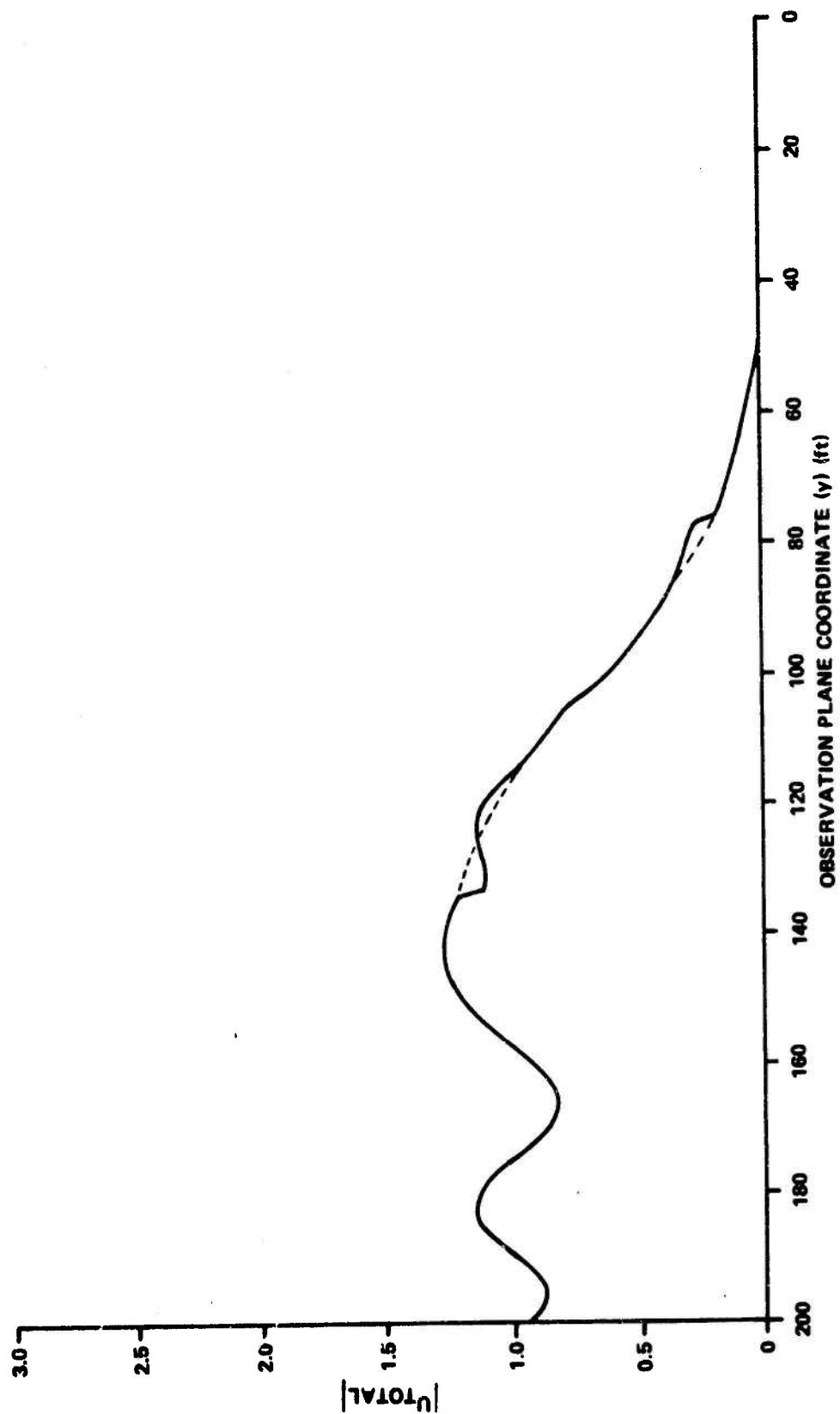


Figure 16 THEORETICALLY CALCULATED TOTAL FIELD SCATTERED FROM
FINITE VERTICAL EDGE

seen. Notice the small discontinuity in field estimates occurring at $y = 76$; at this point calculations switch from GDT to the half-plane formulation. For the assumed configuration, the forward scattering direction corresponds to $y \sim 105$. Half-plane formulas are employed out to $y = 135$, where the discontinuity between these results and those based upon GDT is apparent. For $y > 135$, GDT is used to obtain the familiar oscillation observed in the total field. Finally, the best estimate of fields near discontinuities in the predicted curve is shown as dashed lines. In this instance, errors in the calculations are less than the granularity of the final computer plot.

Figure 17 is a top view of the same horizontal plane where one face of the specified edge lies at 45 degrees with respect to the line joining the source and the y -origin of the observation plane. Figure 18 shows calculations of the total field in the region $0 \leq y \leq 200$ for horizontal polarization. Notice that singly-diffracted fields extend to $y = 0$ for this orientation of the building. The major observation is that discontinuities in predictions are reduced for the nonnormal face case.

2.4.2.2 Horizontal Edge

Next we examine the total field around the isolated horizontal edge E_{56} depicted in Figure 10. Figure 19 shows a side view of the square obstacle when the specified edge lies perpendicular to the line joining the source and the z -axis of the vertical observation plane. Figure 20 is a plot of the magnitude of the total field calculated at observation points along the z -axis, for horizontal polarization. Both geometric optics and the singly diffracted field are completely shadowed by the top of the building for $z \leq 100$ feet. The transition from GDT to the half-plane formulation occurs at $z = 125$ feet, and the switch back to GDT is made at $z = 180$. For $z > 180$, the calculated field exhibits the damped oscillation (with distance) characteristic of the illuminated region.

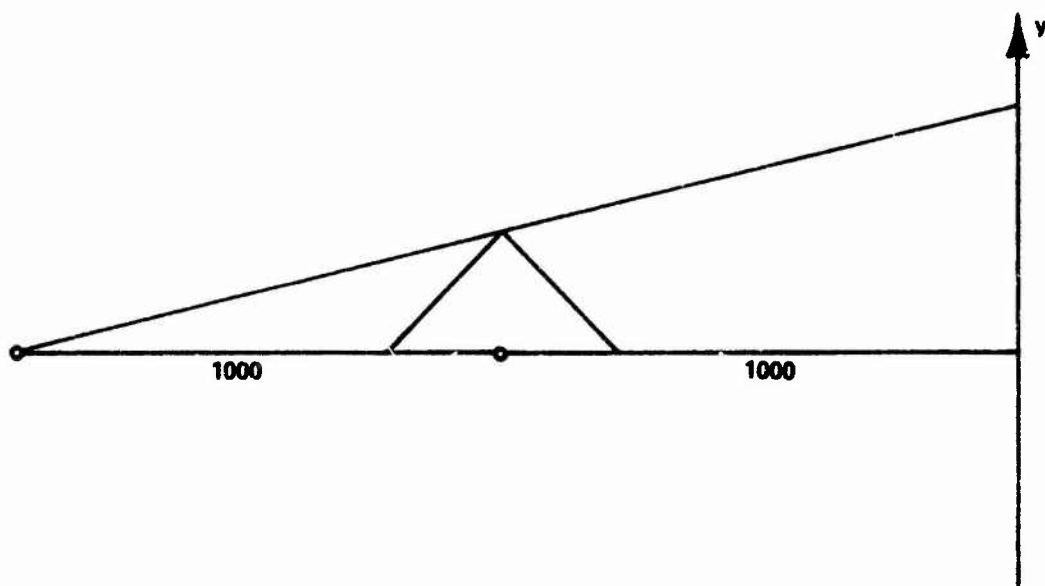


Figure 17 PLAN VIEW OF LAYOUT FOR RECTANGULAR BUILDING

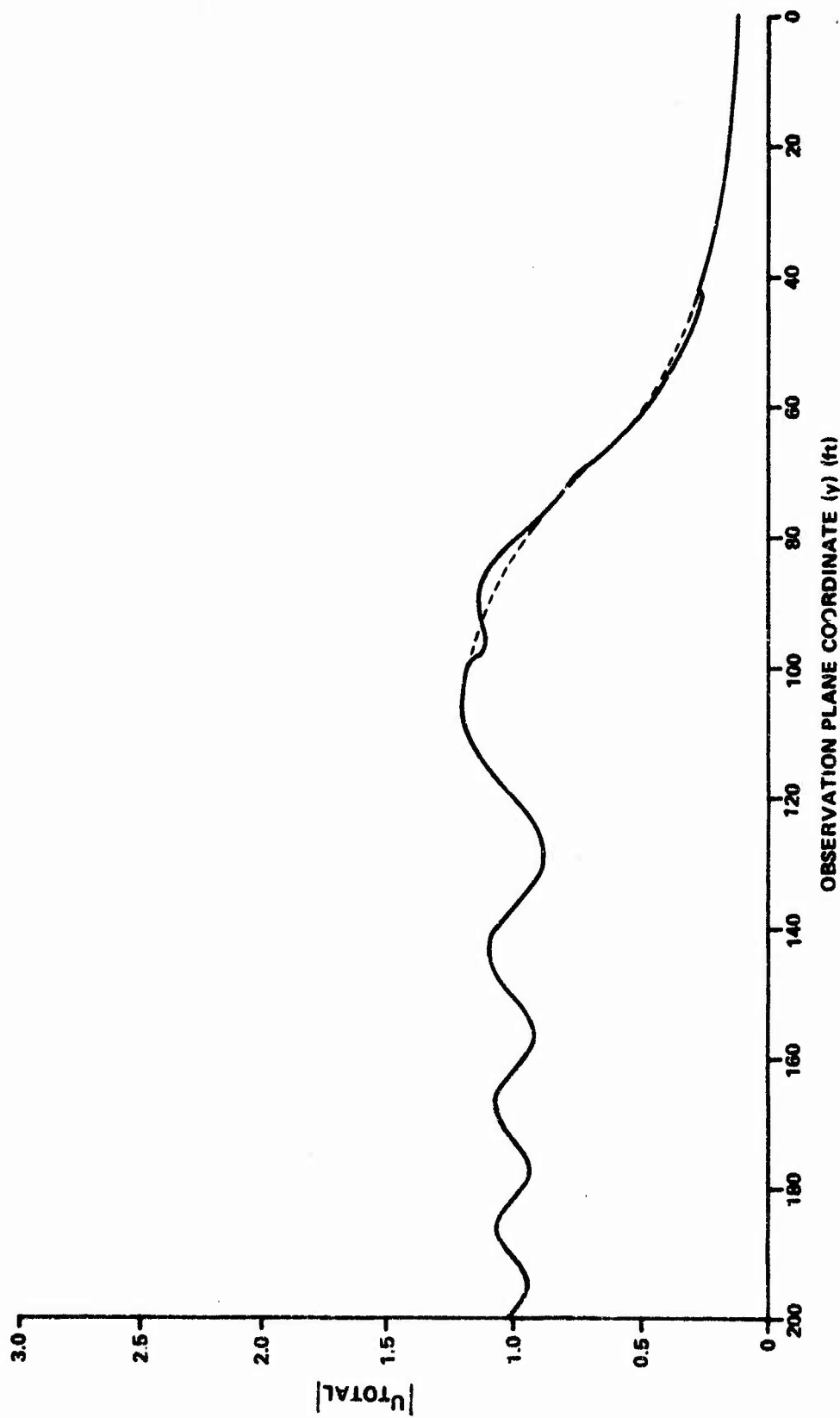


Figure 18 THEORETICALLY CALCULATED TOTAL FIELD SCATTERED FROM
FINITE VERTICAL EDGE

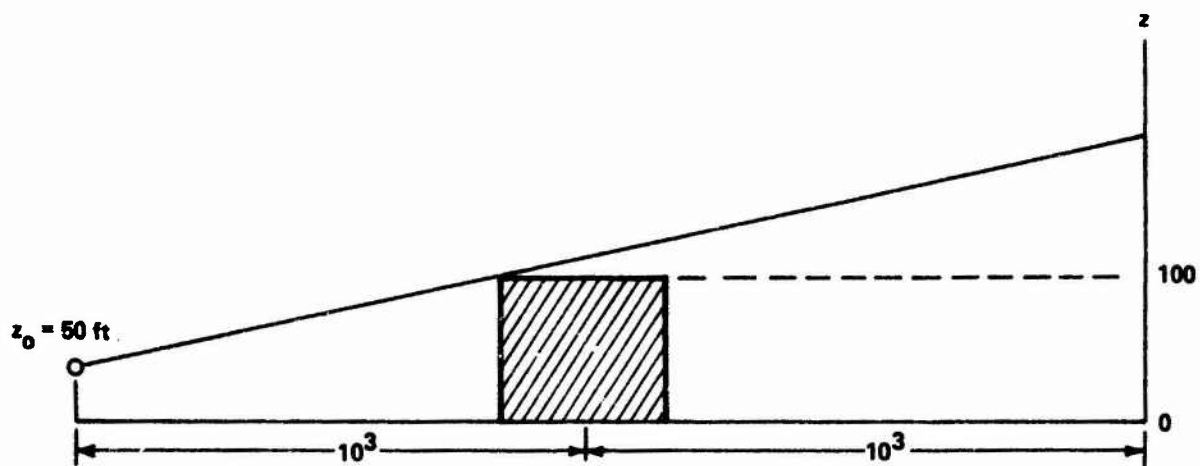


Figure 19 – SIDE VIEW OF SQUARE OBSTACLE

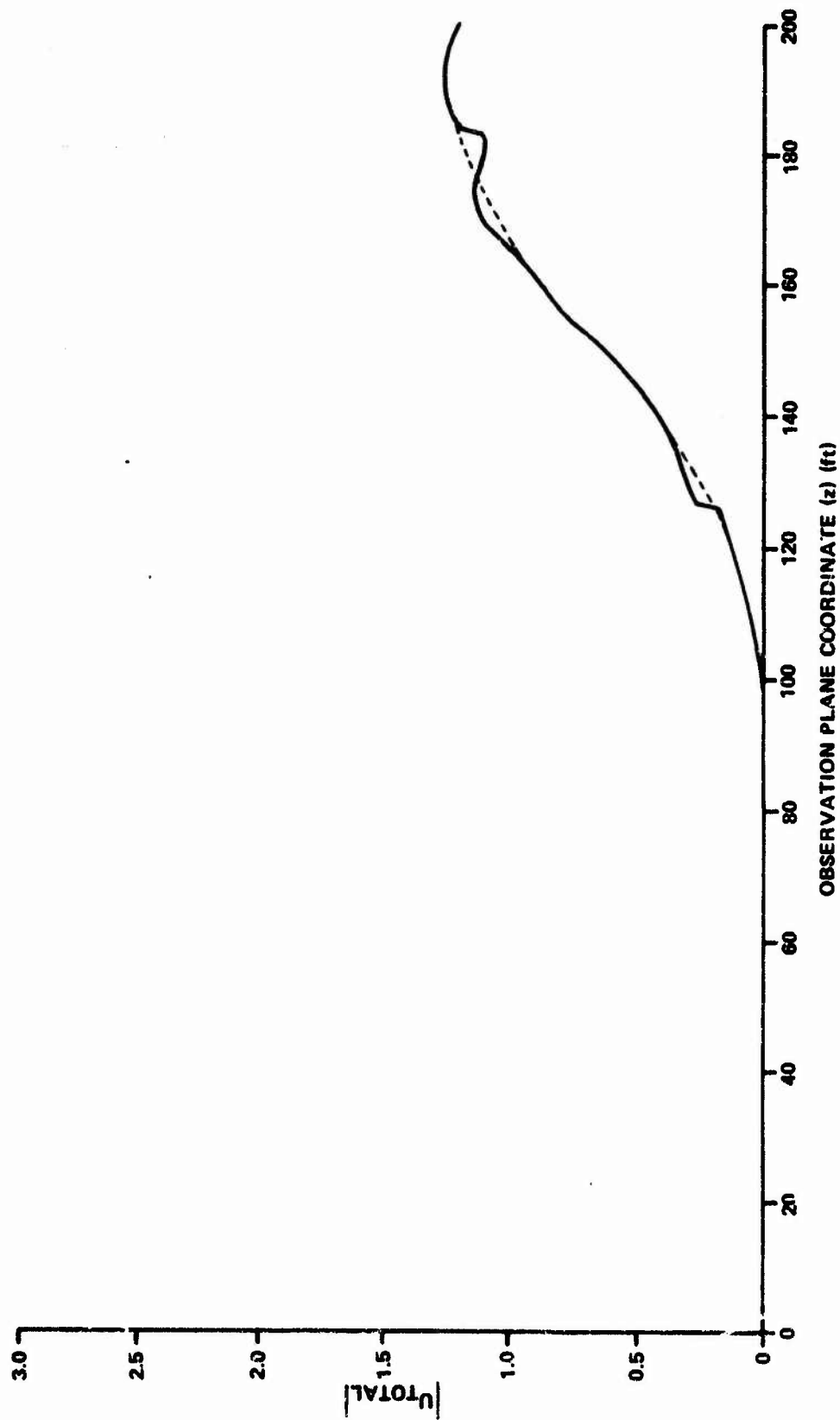


Figure 20 THEORETICALLY CALCULATED TOTAL FIELD SCATTERED FROM
A HORIZONTAL EDGE

2.4.2.3 Comments

The results shown in Figures 16, 18 and 20 are representative of many such calculations for isolated edges which were made to facilitate compilation of the computer program for the rectangular building. These figures illustrate the dependence of edge scattering upon aspect angle, edge orientation and polarization. They also indicate the presence of discontinuities which are sufficiently small so that prediction capability for practical applications is not degraded.

2.4.3 Sample Calculation Considering All Contributing Edges

Examples of a full calculation area presented in Section 3.2 for the rectangular obstruction utilized in the flight test validation. Computer-generated plots are shown which provide dB contours of the field strength relative to the field strength under free-space conditions. In addition, Figures 73, 74, and 75 show lateral plots similar to those presented in the previous section.

2.5 GEOMETRICAL-OPTIC SHADOWING

The computer program developed by Calspan provides the capability of plotting the geometric shadow of spherical, cylindrical and polyhedral obstructions at arbitrary observation planes.

Geometric-optics, valid for vanishing wavelength, predicts that the field within the geometric shadow of an obstruction is identically zero while the field outside the geometric shadow is unperturbed by the obstacle. Obviously, geometric-optics neglects the effects of diffraction.

Experimental field measurements for a helicopter flying within the shadow of a sphere and cylinder are presented in Sections 3.3 and 3.4. It is shown that predictions based upon geometric-optics are not accurate for the conditions of the cases considered.

Section 3

FLIGHT TEST VALIDATION

3.1 GENERAL DISCUSSION

A flight test program was conducted to provide experimental data which could be used to evaluate the accuracy of the predictions provided by the computer program. As noted earlier, the analytic model provides for the calculation of electromagnetic fields diffracted from a rectangular building (of perfect conductivity) with arbitrary dimensions (length, width, height) at an arbitrary orientation with respect to the radar facility. The relative signal level* is calculated, for a given frequency, at arbitrarily chosen (position and number) vertical planes behind the building (perpendicular to a common line through the radar site and the center of the building). The calculation is made in each plane at points spaced closely enough to yield an accurate picture of the perturbed field.

Tests were conducted utilizing a rectangular obstruction. Comparisons between theoretical predictions and the experimental results were made for the rectangular obstruction; very good agreement has been obtained. Spherical and cylindrical obstructions were also investigated in the tests. For the latter two obstruction types, for which diffraction effects are not provided by the computer program, the experimental results are described and compared with simple geometric shadow calculations.

A helicopter was utilized to simultaneously transmit both S-band and VHF signals as it traversed selected flight paths behind the obstacle. Received signals were recorded using ground-based equipment. The aircraft traverses were flown at altitudes varying between 290 to 2200 feet and distances 2650 to 13,000 feet behind the obstructions. The aircraft progress was filmed in the tests. A flashing light in the camera field-of-view, synchronized with event markers on the receiver recorders, served to correlate aircraft position with data records.

*Relative signal level is defined as the ratio of the total field at a point in space with the obstacle present to the field that would exist at that point in the absence of the obstacle.

3.1.1 Preliminary Considerations

At program initiation, an airborne survey in the Buffalo, New York area was undertaken to identify rectangular, cylindrical, and spherical obstructions which could be used for validation and testing purposes. Specific sites were chosen on the basis of accessibility, relative isolation of the structure, and surrounding topography.

Prior to conducting the actual flight tests, a study of each selected site was made. This included the determination of equipment placement and flight test planning to identify landmarks and other navigational aids which were used during the flight tests to establish the various flight profiles. For the rectangular building, the orientation of those buildings as shown on the maps later proved to be inaccurate and thus introduced obliqueness between the desired and actual flight paths (see Section 3.1.5).

Concurrent with the preliminary surveys and flight planning stages, all the equipment associated with the tests was collected, assembled and bench checked to ensure proper operation.

For the tests, a one-way transmission path was employed (i.e., transmission from helicopter to ground). Initially considered was a radar type of measurement which would have resulted in a two-way path, the aircraft being used as a reflector. This would have yielded measurements dependent on the aircraft radar cross section (RCS) (i.e., the aircraft reflection properties). Aircraft RCS is however dependent upon polarization and fluctuates rapidly with time (scintillates) due to aspect angle changes. Therefore, even without an obstruction, the received signal would have varied in amplitude and these variations would mask those due to obstacle diffraction. Thus, a one-way measurement procedure was selected.

The reciprocity theorem of electromagnetics asserts, in effect, that the received signal will remain the same if the relative positions of transmitting and receiving antennas are reversed. Therefore, for ease of accessibility and control, the receiving and recording equipment were based on the ground.

It should be noted, for a two-way transmission path (radar) the dB signal strength changes due to presence of the obstacle shown in subsequent sections would change by a factor of two.

3.1.2 Experimental Procedures

Appropriate S-band transmitting equipment and antennas were installed in the helicopter for the flight tests. The VHF transmission channel utilized the helicopter's onboard transmitter and antenna. Receiving equipment and recorders were allowed to warm-up and stabilize prior to data recording. Dry runs were made to ensure proper operation of all equipment and to verify communication procedures between the aircraft and base.

The microwave receivers were tuned each time during the "approach" phase of the run by adjusting the LO frequency for maximum receiver output. The data run then followed immediately and was recorded. The VHF receiver required no adjustment after initial tuning.

Typical flight test profiles are illustrated in Figure 21 for the case of the rectangular obstruction in which three different obstruction orientations were viewed. For the spherical and cylindrical obstructions only one viewing angle was employed because of the obstruction symmetry. For each orientation, the flight tests included traverses for both horizontally and vertically polarized S-band transmissions as well as simultaneous vertically polarized VHF transmissions. For each of two ranges (three, for the sphere), such as denoted by R1 and R2 in Figure 21, three constant altitude azimuth "cuts" were made. At the beginning and end of each run, the pilot radioed the altitude and air speed of the helicopter. The aircraft altimeter was initially set to zero upon landing at the test site.

After each run calibration tests were performed. A signal generator with a calibrated output attenuator was connected to the respective receivers and the receiver output recorded as a function of signal input level. Calibration records were made in 5 dB steps over the full dynamic range of each receiver.

3.1.3 Instrumentation

The airborne S-band transmitting equipment and antennas were mounted on a plywood board; the entire unit was easily transportable and conveniently installed on the helicopter at the test site. (See Figures 22 through 25.) An RF switch was employed to select either a vertical or

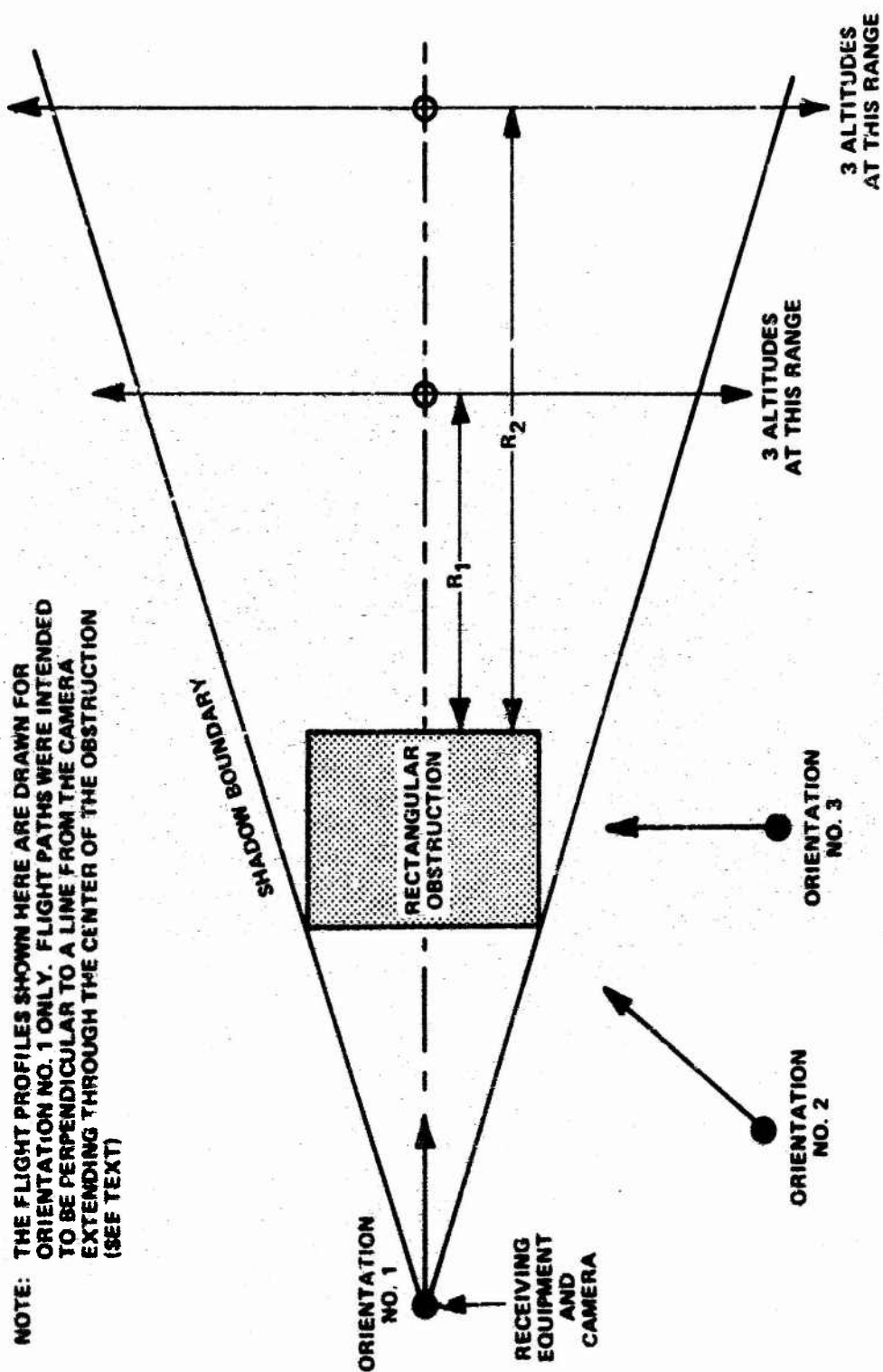


Figure 21 CONCEPTUAL PLAN VIEW OF TEST SITE; TYPICAL TEST PROFILES

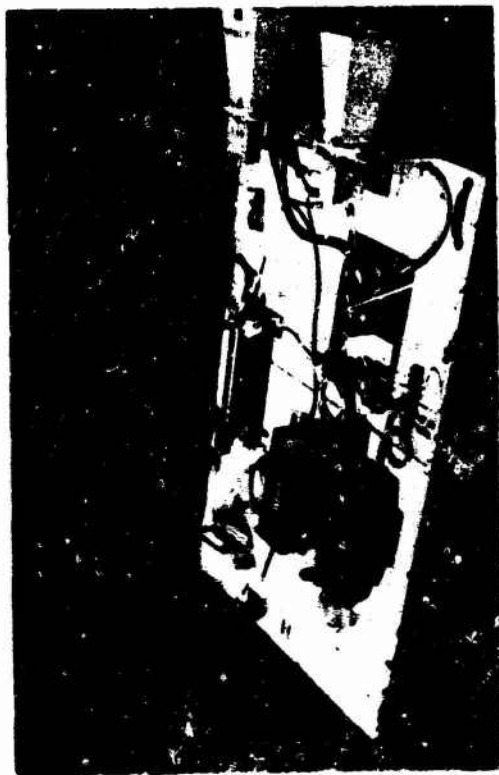


Figure 22 S-BAND TRANSMITTING SYSTEM
(MOUNTED ON PLYWOOD BOARD)



Figure 23 S-BAND TRANSMITTING SYSTEM
(BEING INSTALLED IN HELICOPTER)



Figure 24 S-BAND TRANSMITTING SYSTEM
(HELICOPTER INSTALLATION)



Figure 25 S-BAND TRANSMITTING SYSTEM
(FRONT VIEW)

horizontal polarized transmit horn. Figure 26 shows a block diagram of the microwave and VHF transmitting and receiving equipment.

The microwave transmitter consisted of a solid-state source (Frequency Sources, Type FS14R) operating nominally at 3006 MHz, with a RF power output of 700 mW. The transmitter operated from a well regulated power supply which eliminated, for practical purposes, frequency shift due to input voltage variations. Frequency drift as a function of operating temperature was approximately 50 kHz per degree F, well within limits for these tests. A single-pole double-throw microwave switch was used to select the transmit polarization. The transmit horn antenna gain was 10 dB, the beamwidth approximately 55 degrees. In normal level flight of the helicopter the transmitted beam main lobe axis was in the horizontal plane perpendicular to the main aircraft axis.

The ground based S-band receive terminal consisted of 15 dB gain horn antennas above a ground plane covered with RF absorber, Eccosorb CV3 material, as shown in Figure 27. The antenna beam is deflected up from the horizon by approximately 10 degrees thereby reducing effects of ground reflections. The RF absorber below the receive antenna served to shape the antenna pattern near the horizon plane to further reduce ground reflection effects. All flights were conducted well within the 3 dB azimuth and elevation plane beamwidths (35 degrees and 14 degrees, respectively) of the ground receive antenna.

Each receiver consisted of a low noise TWT amplifier (NF 8.0 dB), a mixer-preamplifier, and a logarithmic post-amplifier and detector. The IF center frequency was 30 MHz and the bandwidth 2 MHz. The IF logarithmic post-amplifier provided a DC output which was proportional to logarithm of the input signal level (dB scale). The outputs of the receivers were recorded on a chart recorder. The sensitivity of each receiver was approximately -100 dBm at the TWT input and the dynamic range was in excess of 60 dB. Photographs of the receiving and recording equipment are shown in Figures 28, 29 and 30.

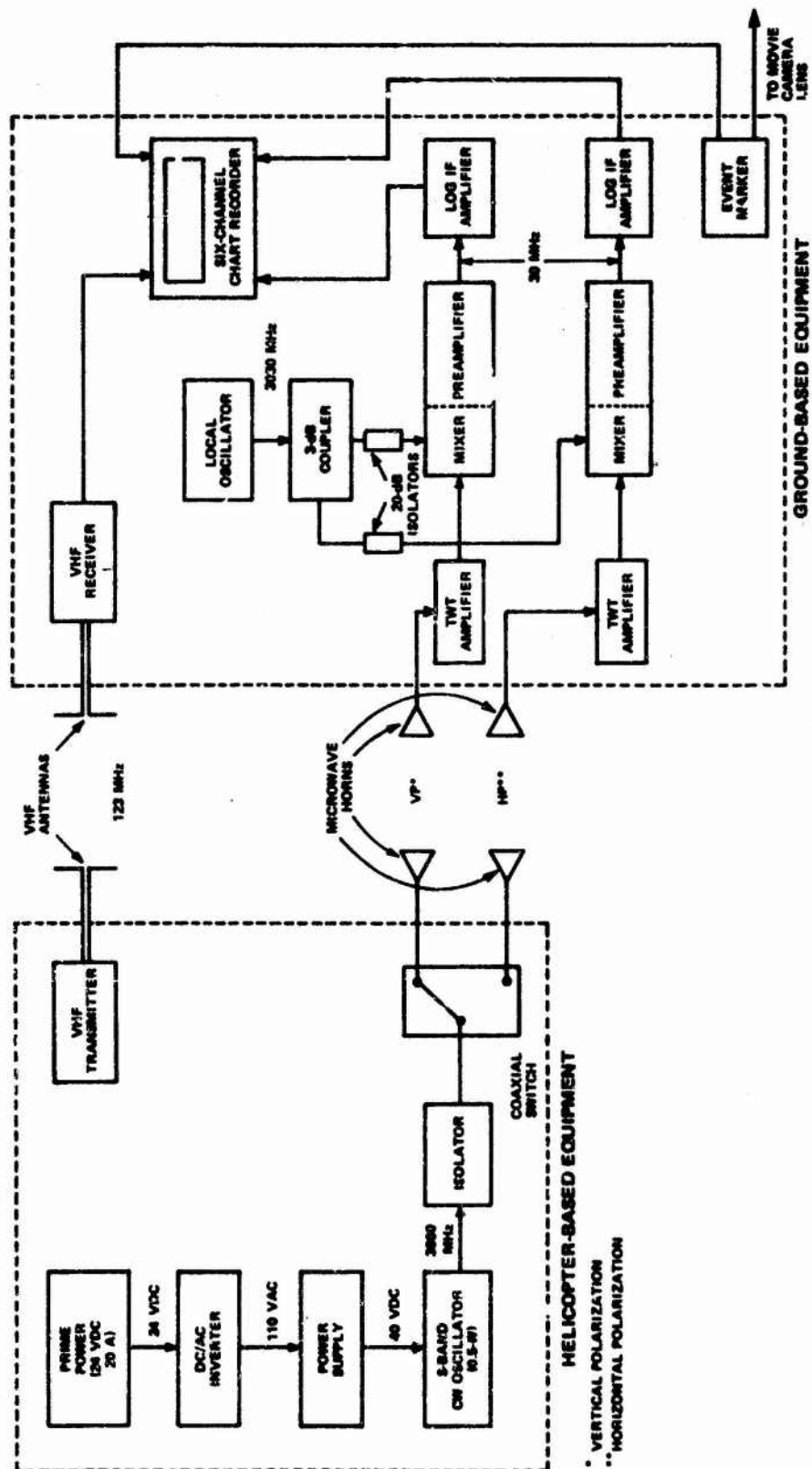


Figure 26 BLOCK DIAGRAM OF EQUIPMENT LAYOUT



Figure 27 S-BAND RECEIVE ANTENNAS



Figure 28 RECEIVING EQUIPMENT



Figure 29 RECEIVING EQUIPMENT



Figure 30 RECORDING EQUIPMENT

The VHF transmission frequency was 123 MHz. The ground based VHF receiver consisted of a NEMS Clarke Type 1501 superheterodyne receiver with sensitivity of -105 dBm and a dynamic range, with AGC, of approximately 60 dB. The AGC voltage was used to measure the received signal level. The transmitting and receiving antennas consisted of quarter-wave ground plane monopoles. The receiving monopole is seen in Figures 31 and 32 which also show a typical configuration of the ground station operation.

3.1.4 Tracking

In order to compare and correlate the measured data with the predicted effects, it was important to be able to relate the aircraft position to the recorded signal amplitude data. For this purpose, a movie camera recorded aircraft flight and position relative to the obstruction on film. For correlation of flight position with signal recordings during data runs, automatic timing signals were fed simultaneously to the chart recorder and a light emitting diode (LED) was placed in the field of view of the camera. The light flashes on the film records could be correlated in the analysis of the data with the timing marks recorded on the chart recorder. The movie camera and the LED are shown in position in Figure 33.

3.1.5 Position Determination and Error Analysis

The motion pictures were analyzed using a framing/analysis projector to determine the position of the helicopter. The geometrical parameters are defined as follows (see diagram)

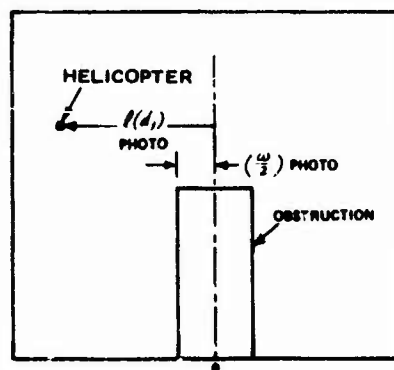




Figure 31 VHF RECEIVING ANTENNA



Figure 32 VHF RECEIVING ANTENNA

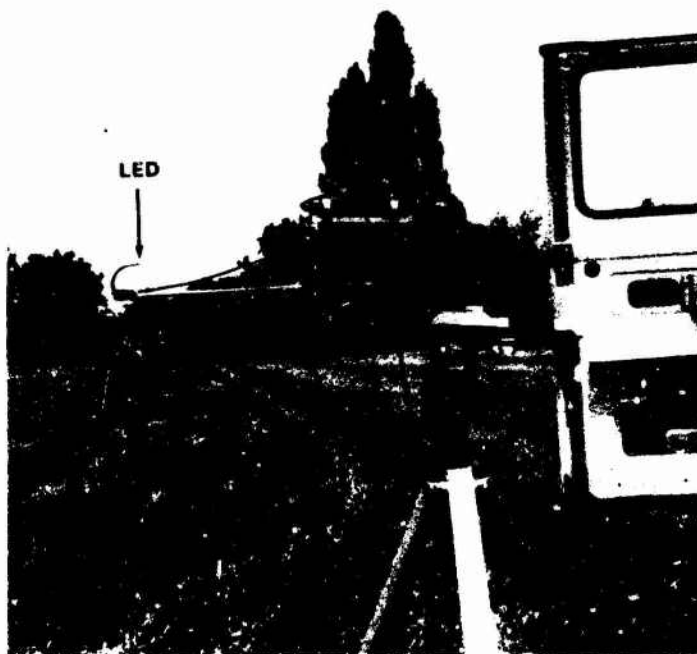


Figure 33 MOVIE CAMERA AND LED

- $\left(\frac{w}{2}\right)_{true}$ is the true half-width of the obstruction
 d_1 is the distance between the camera and plane containing maximum projected dimensions of the obstruction
 d_2 is the distance between the flight path ground track and the plane containing the maximum projected dimension of the obstruction
 $\frac{w}{2}(d_1 + d_2)$ is the projected half-width of the obstruction at a distance*
 $l(d_1 + d_2)$ is the true position of the helicopter*

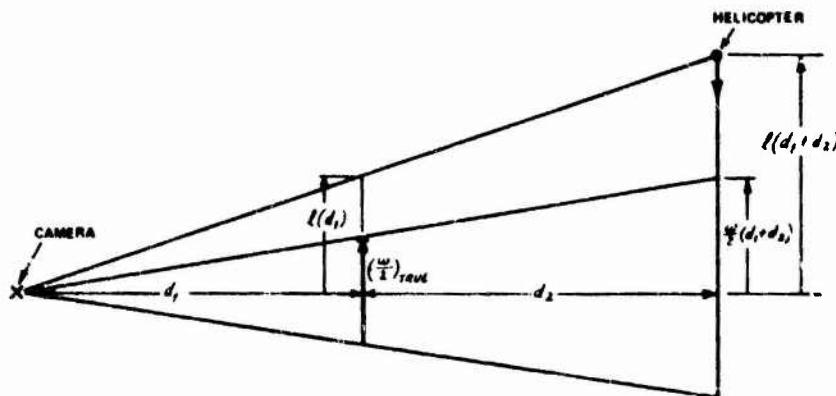
From the laws of similar triangles, we have

$$\frac{l(d_1 + d_2)}{l(d_1)} = \frac{(d_1 + d_2)}{d_1} \quad (45)$$

or

$$l(d_1 + d_2) = \frac{d_1 + d_2}{d_1} \cdot l(d_1) \quad (46)$$

Now, on the film analysis projection screen, onto which an arbitrary, fixed grid was affixed, the following is observed:



* The variable is a function of the argument contained in the parenthesis.

Since

$$\frac{l(d_1)}{l_{photo}(d_1)} = \frac{\left(\frac{w}{2}\right)_{true}}{\left(\frac{w}{2}\right)_{photo}} \quad (47)$$

Then

$$l(d_1) = \frac{\left(\frac{w}{2}\right)_{true}}{\left(\frac{w}{2}\right)_{photo}} \cdot l_{photo}(d_1) \quad (48)$$

where $\left(\frac{w}{2}\right)_{photo}$ and $l_{photo}(d_1)$ are in arbitrary units.

Substituting $l(d_1)$ from Equation 48 into Equation 46 yields

$$l(d_1 + d_2) = \frac{d_1 + d_2}{d_1} \cdot \left(\frac{w}{2}\right)_{true} \cdot \frac{l_{photo}}{\left(\frac{w}{2}\right)_{photo}} \quad (49)$$

Equation 49 formed the basis of the determination of the true position of the helicopter.

Since all of the parameters in Equation 49 are not precisely known, an error analysis was performed to determine the uncertainty in $l(d_1 + d_2)$. The total error, Δl , may be written

$$\Delta l = \frac{\partial l}{\partial d_1} \delta d_1 + \frac{\partial l}{\partial d_2} \delta d_2 + \frac{\partial l}{\partial l_{photo}} \delta l_{photo} + \frac{\partial l}{\partial \left(\frac{w}{2}\right)_{photo}} \delta \left(\frac{w}{2}\right)_{photo} \quad (50)$$

The procedure is straightforward. Typical values used for the errors associated with the parameters are

$$\delta d_1 \sim 0.10 \text{ feet}$$

$$\delta d_2 \sim 20 \text{ to } 40 \text{ feet}$$

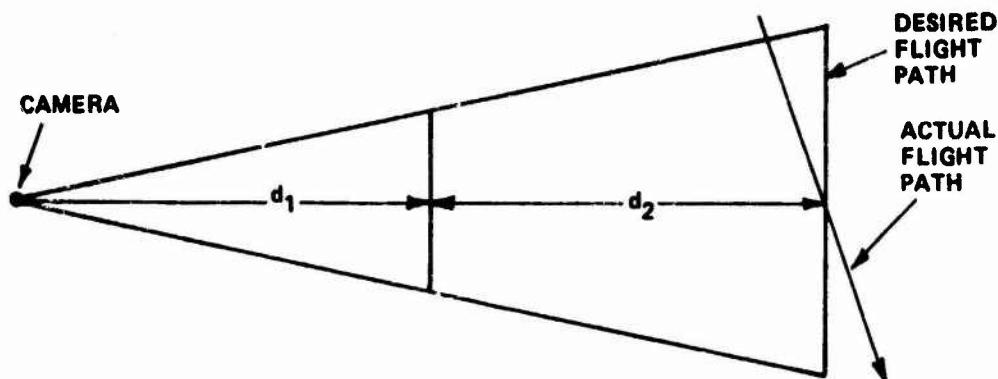
$$\delta l_{photo} \sim 0.05 \text{ (arbitrary units)}$$

$$\delta \left(\frac{w}{2}\right)_{photo} \sim 0.05 \text{ (arbitrary units)}$$

The resultant Δl will be indicated in the data presented in the following sections by a horizontal line associated with a given data point.

Another uncertainty was in the exact altitude of the helicopter. During some runs, an altitude change occurred due to winds, buffeting and other factors. An altitude variation of ± 30 feet from that radioed by the pilot was assumed as typical. This altitude variation was translated into a possible signal amplitude variation by using calculated signal amplitude versus altitude curves. The possible signal amplitude variation due to this is indicated by a vertical bar associated with each data point.

An additional source of uncertainty occurred with respect to tests utilizing the rectangular obstruction. The flight trajectory was somewhat skewed; that is, it was not perpendicular to a line extended from the camera through the center of the obstruction (see diagram below). As a result, in order to use Equation 47, it was necessary to change the value of d_2 to minimize the error in the determination of ℓ . The uncertainty, however, occurred in the computation of predicted signal levels. That is, because the observation plane was constantly changing, it would have been necessary to make a prohibitive number of computer runs. Therefore, only a small number of computer runs were made to cover the range change of the observation plane during the flight tests and linear interpolation on the dB scale was employed between the planes for which calculations were performed. Because the occurrence and positions of interference maxima and minima are very dependent on range, some error due to the interpolation is expected. It may in fact be possible to miss a localized maximum or minimum.



3.2 DIFFRACTION FROM A SPHERICAL OBSTRUCTION

3.2.1 Description of Experimental Layout

An isolated spherical water tank, located on the premises of Moog, Inc., East Aurora, New York was selected for the spherical obstruction for which diffraction experiments were performed. Photographs of the tank are shown in Figure 35. Dimensional information of the experimental configuration is contained in Figure 34.

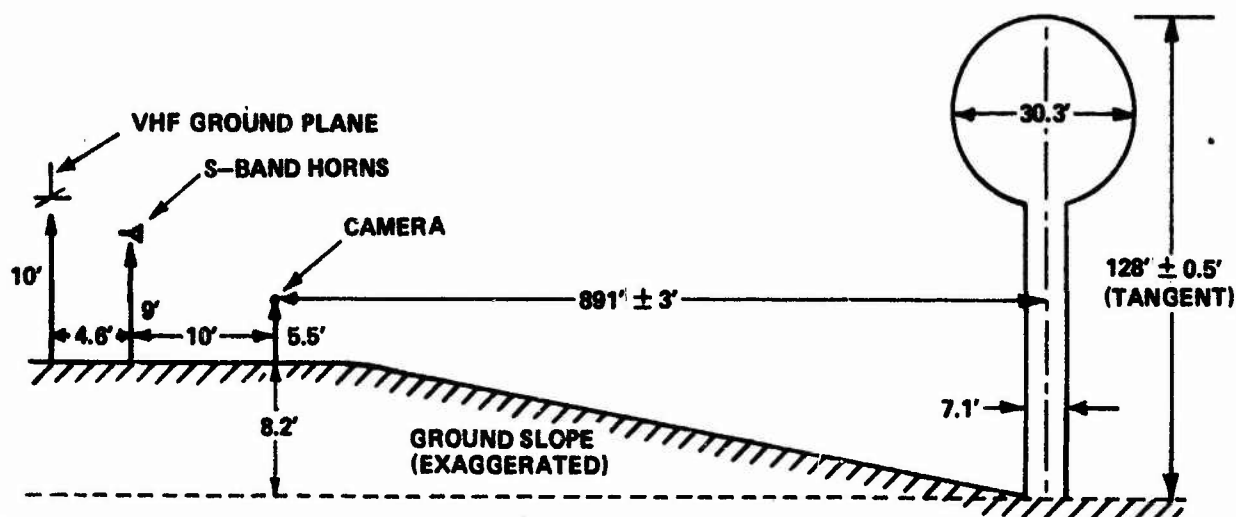


Figure 34 | EXPERIMENTAL SET-UP FOR SPHERE DIFFRACTION STUDY

A description of the equipment utilized to conduct the experiment and the experimental procedures employed have been presented in Section 3.1.

3.2.2 Scope of Tests Performed

Table 1 shows the scope of tests performed including the various ranges, altitudes and polarizations along with definition of the corresponding test number. For all tests, only vertical polarization was utilized in the VHF measurement, whereas both horizontally and vertically polarized signals were recorded at S-band.



**TAKEN FROM APPROXIMATE POSITION OF MOVIE
CAMERA; LOOKING WEST**



(LOOKING NORTHWEST)

**Figure 35 SPHERICAL WATER TANK USED AS TEST OBJECT (LOCATED IN
EAST AURORA, NEW YORK)**

Table I
SPHERICAL OBSTRUCTION
SCOPE OF TESTS PERFORMED

A. RANGE FROM OBSTACLE: 2850 \pm 72 feet
 HEIGHT OF PROJECTION OF SPHERE TOP: 439 \pm 9 feet
 HEIGHT OF PROJECTION OF SPHERE BOTTOM: 313 \pm 6 feet

TEST NUMBER	AVERAGE** ALTITUDE (ft AGL)	S-BAND POLARIZATION (f = 3006 MHz)	VHF POLARIZATION (f = 123.4 MHz)	POSITION (AS SEEN BY CAMERA)	RESULTS SHOWN IN FIGURE
M111	540	V	V	ABOVE SHADOW TOP	36
M112		H	V		
M121	500	V	V	GRAZING SHADOW TOP	37
M122		H	V		
M131	290	V	V	WITHIN CYLINDRICAL SUPPORT SHADOW	38
M132		H	V		
M141	437	V	V	WITHIN SPHERE SHADOW	39
M142		H	V		

B. RANGE FROM OBSTACLE: 5700 \pm 72 feet
 HEIGHT OF PROJECTION OF SPHERE TOP: 815 \pm 9 feet
 HEIGHT OF PROJECTION OF SPHERE BOTTOM: 591 \pm 6 feet

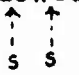
TEST NUMBER	AVERAGE** ALTITUDE (ft AGL)	S-BAND POLARIZATION (f = 3006 MHz)	VHF POLARIZATION (f = 123.4 MHz)	POSITION (AS SEEN BY CAMERA)	RESULTS SHOWN IN FIGURE
M211	700	V	V	WITHIN SPHERE SHADOW	40
M212		H	V		
M221	921	V	V	ABOVE SPHERE SHADOW	41
M222		H	V		
M231	532	V	V	WITHIN CYLINDRICAL SUPPORT SHADOW	42
M232		H	V		

C. RANGE FROM OBSTACLE: 10,600 \pm 72 feet
 HEIGHT OF PROJECTION OF SPHERE TOP: 1,421 \pm 9 feet
 HEIGHT OF PROJECTION OF SPHERE BOTTOM: 1,029 \pm 6 feet

TEST NUMBER	AVERAGE** ALTITUDE (ft AGL)	S-BAND POLARIZATION (f = 3006 MHz)	VHF POLARIZATION (f = 123.4 MHz)	POSITION (AS SEEN BY CAMERA)	RESULTS SHOWN IN FIGURE
M311	1545	V	V	ABOVE SHADOW TOP	43
M312		H	V		
M321	1325	V	V	WITHIN SPHERE SHADOW	44
M322		V	V		
M331	1000	V	V	WITHIN CYLINDRICAL SUPPORT SHADOW	45
M332		H	V		

* REFERENCED TO S-BAND HORNS' POSITION
 ** \pm 30 feet. ALTIMETER SET TO ZERO AT INSTRUMENTATION SITE.

3.2.3 Experimental Results

Figures 36 through 45 show recorded signal level (dB relative to no obstruction) as a function of distance along the flight path. The centerline of the water tank is taken to be at the origin. Positive numbers denote positions to the right of the centerline. On each figure is a drawing showing the water tank and the relative flight path altitude. The numbers on the flight path arrow indicate the helicopter altitude* at the beginning and end of a test run. The geometric shadow of the spherical obstruction is denoted by the dashed lines. Other coordinate positions are also indicated on the recordings; the error ranges associated with the indicated positions are also shown. For cases when the flight path is such that the helicopter is shadowed by the water tank, the boundaries of the shadow region are denoted by .

Both S-band ($f = 3006$ MHz) and VHF ($f = 123.4$ MHz) data are presented. The reference signal level of 0 dB was chosen to correspond to the relatively unperturbed signal level at helicopter positions along the test flight path quite far from the water tank. The signal level (dB) shown are for one-way transmission. For a two-way path (e.g., radar), the dB change would increase by a factor of two.

The calculation of diffraction effects from spherical obstructions was not within the scope of the present program. We note, for the present, that basic creeping wave diffraction analysis indicates that when horizontal polarization (HP) is employed, the major contribution to the observed signal occurs from a horizontal plane through the obstacle; and, similarly, for a vertically polarized signal, major effects are caused by vertical plane cuts through the obstacle. Thus, more interference effects are expected for the horizontally polarized signal than the vertically polarized signal since the cylindrical support effectively disrupts one component of the VP signal. More detailed analyses would have to be performed to provide an accurate description of the scattering. The flight test results presented here could be used for comparison with results of such a theoretical model of diffraction effects.

* +30 feet; altimeter set to zero at test site.

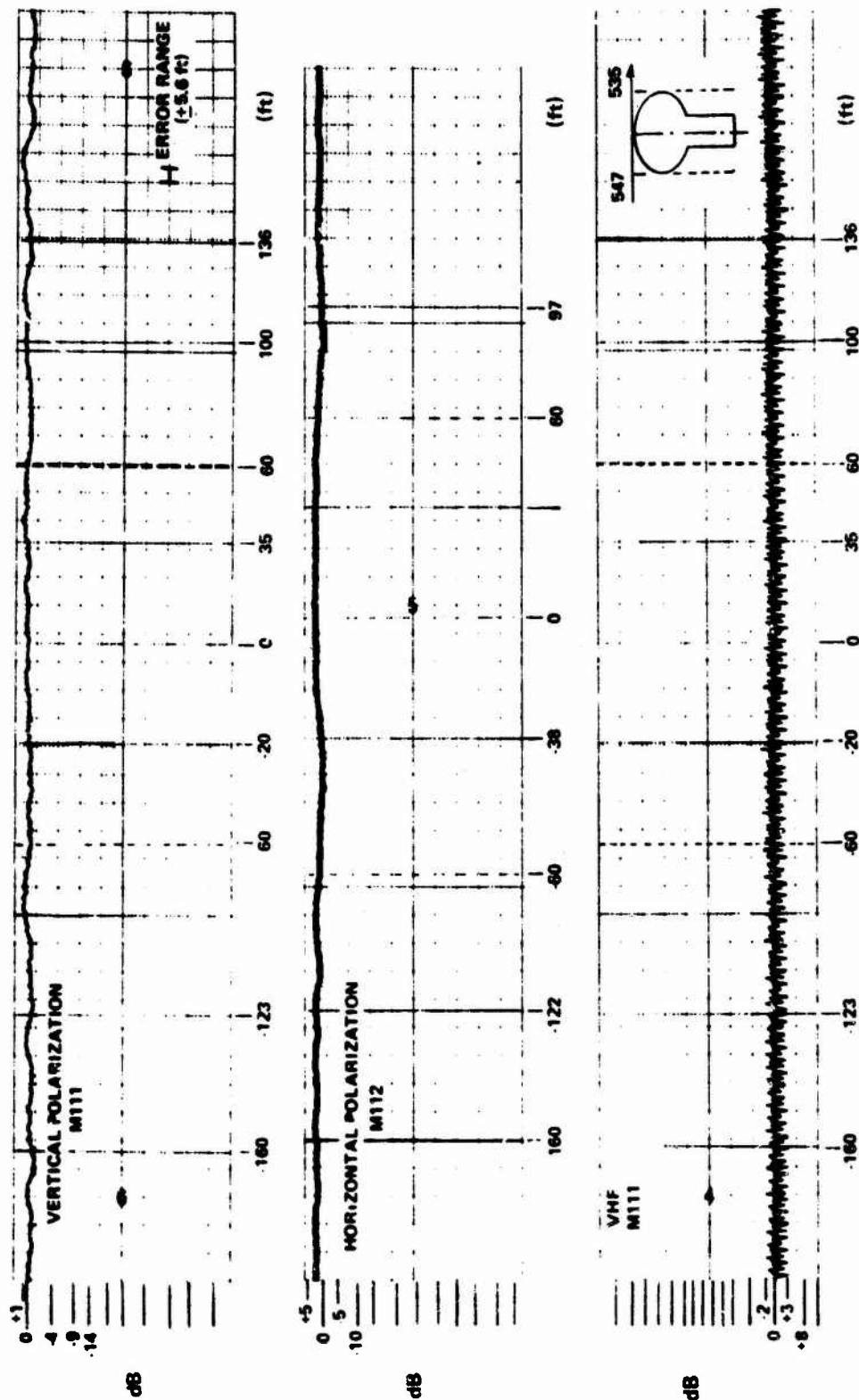


Figure 36 RELATIVE SIGNAL STRENGTH VS DISTANCE FROM TEST CENTERLINE
FOR SPHERICAL WATER TANK; $d_1 = 891$ FT, $d_2 = 2650$ FT, ALTITUDE =
540 FT

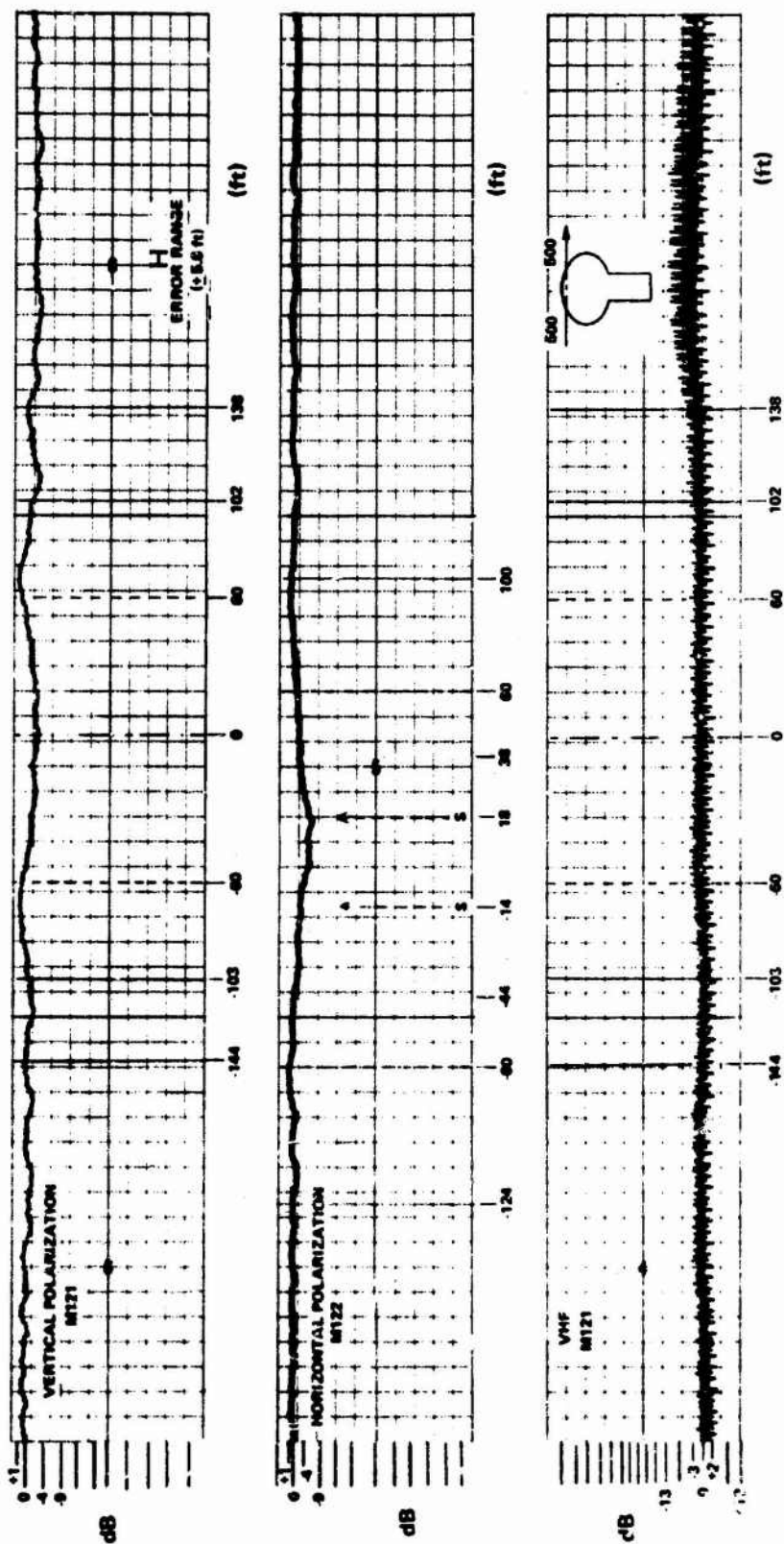


Figure 37 RELATIVE SIGNAL STRENGTH VS DISTANCE FROM TEST CENTERLINE
FOR SPHERICAL WATER TANK; $d_1 = 891$ FT, $d_2 = 2650$ FT, ALTITUDE =
500 FT

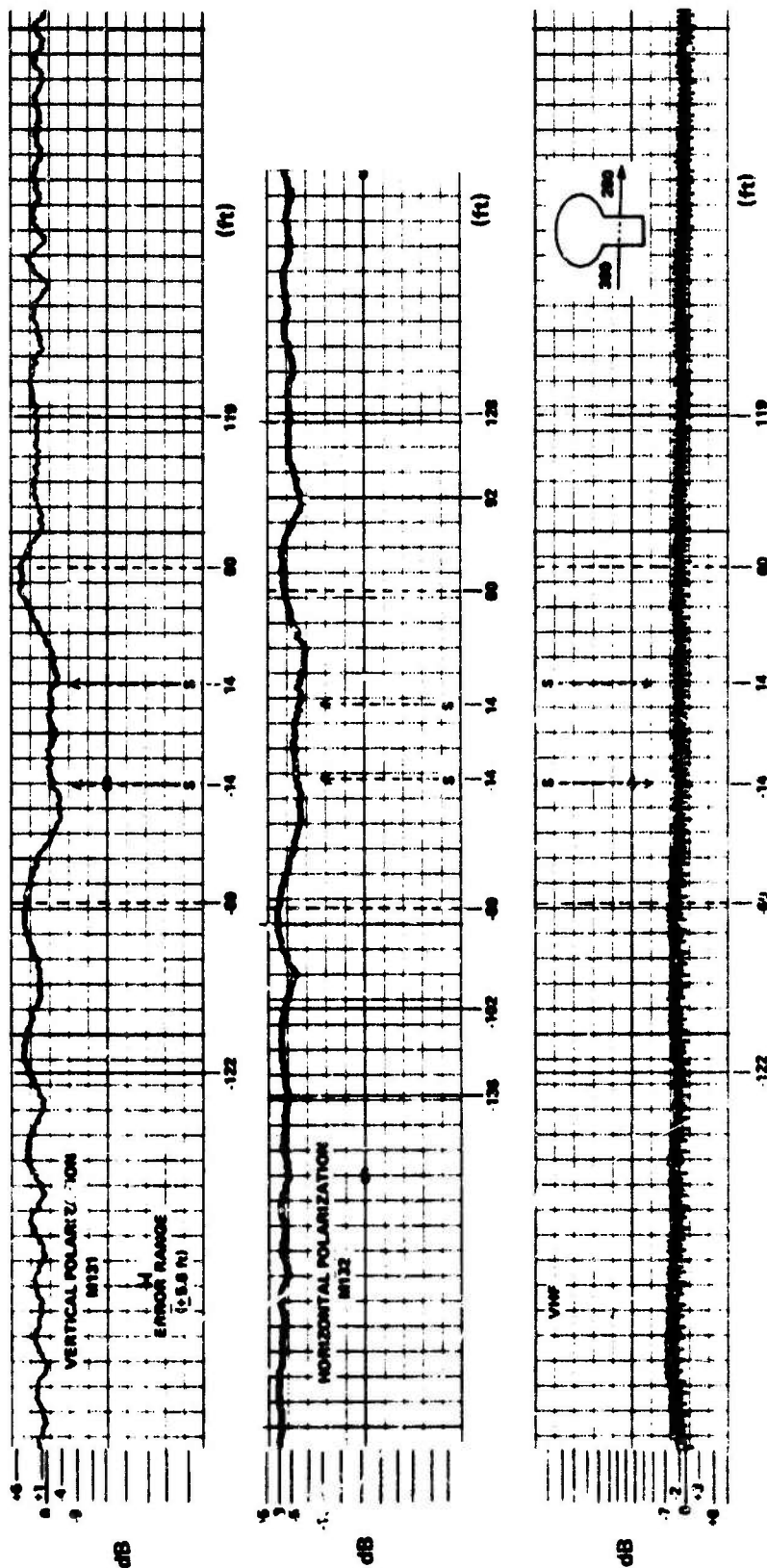


Figure 38 RELATIVE SIGNAL STRENGTH VS DISTANCE FROM TEST CENTERLINE
FOR SPHERICAL WATER TANK; $d_1 = 891$ FT, $d_2 = 2650$ FT, ALTITUDE =
290 FT

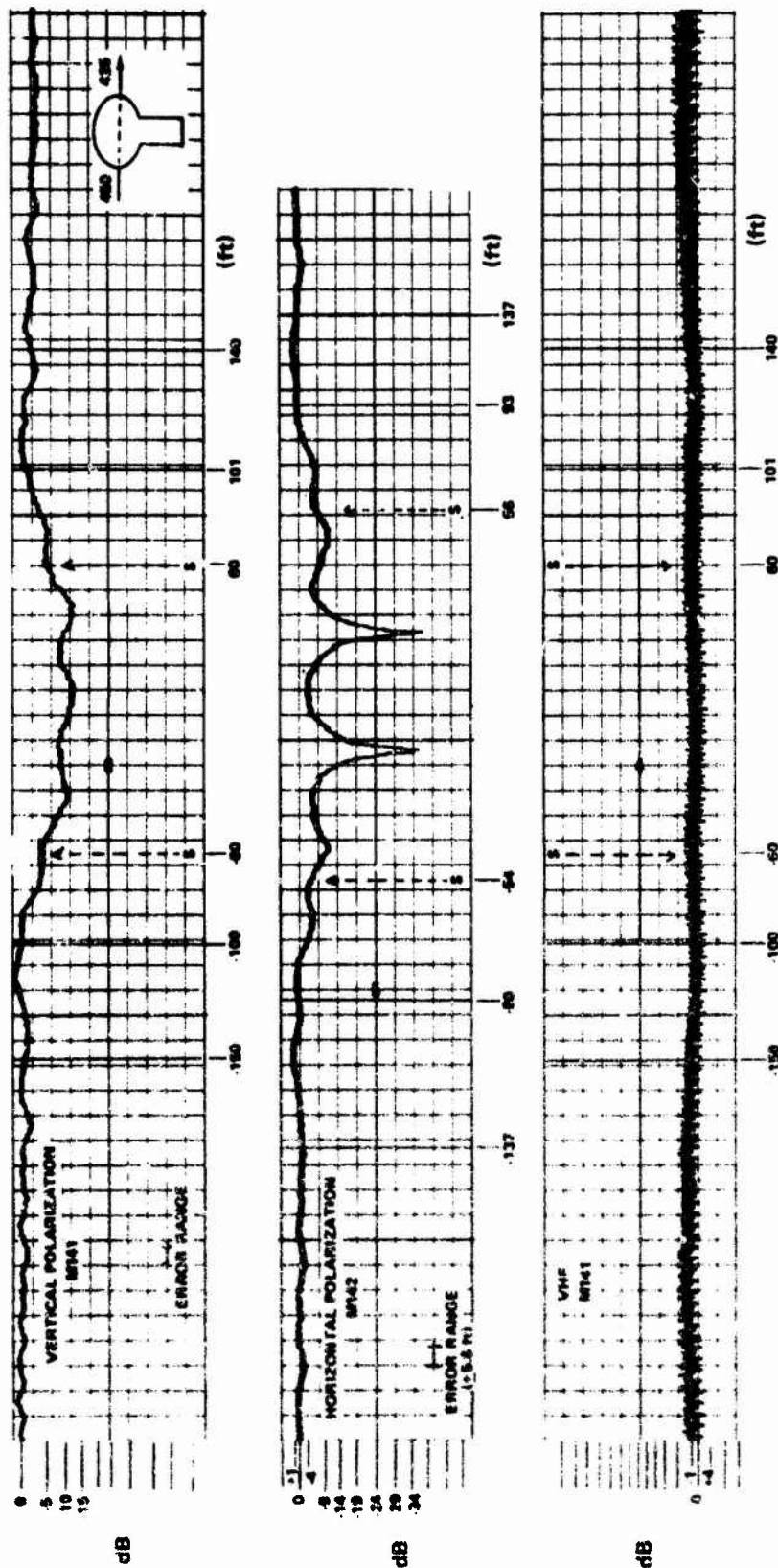


Figure 39 RELATIVE SIGNAL STRENGTH VS DISTANCE FROM TEST CENTERLINE
 FOR SPHERICAL WATER TANK: $d_1 = 891$ FT, $d_2 = 2850$ FT, ALTITUDE =
 437 FT

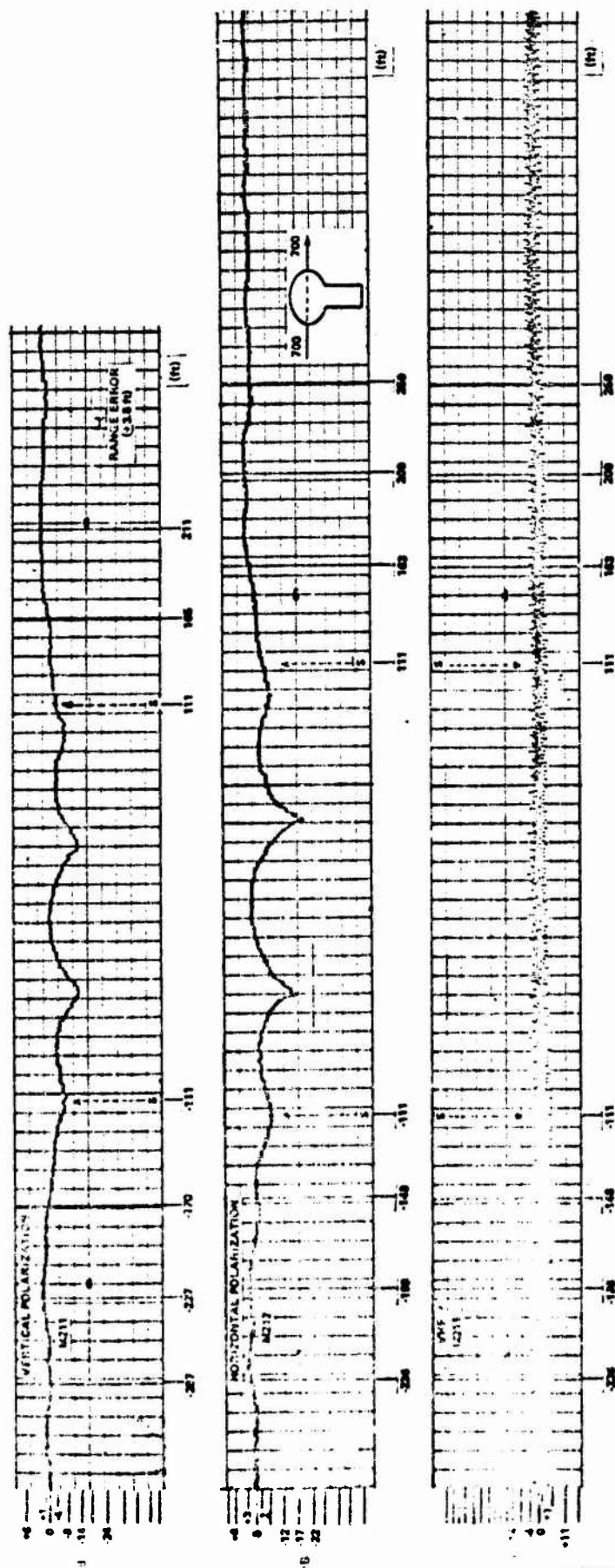


Figure 40 RELATIVE SIGNAL STRENGTH VS
DISTANCE FROM TEST CENTERLINE
FOR SPHERICAL WATER TANK; $d_1 =$
881 FT, $d_2 = 8700$ FT, ALTITUDE =
700 FT

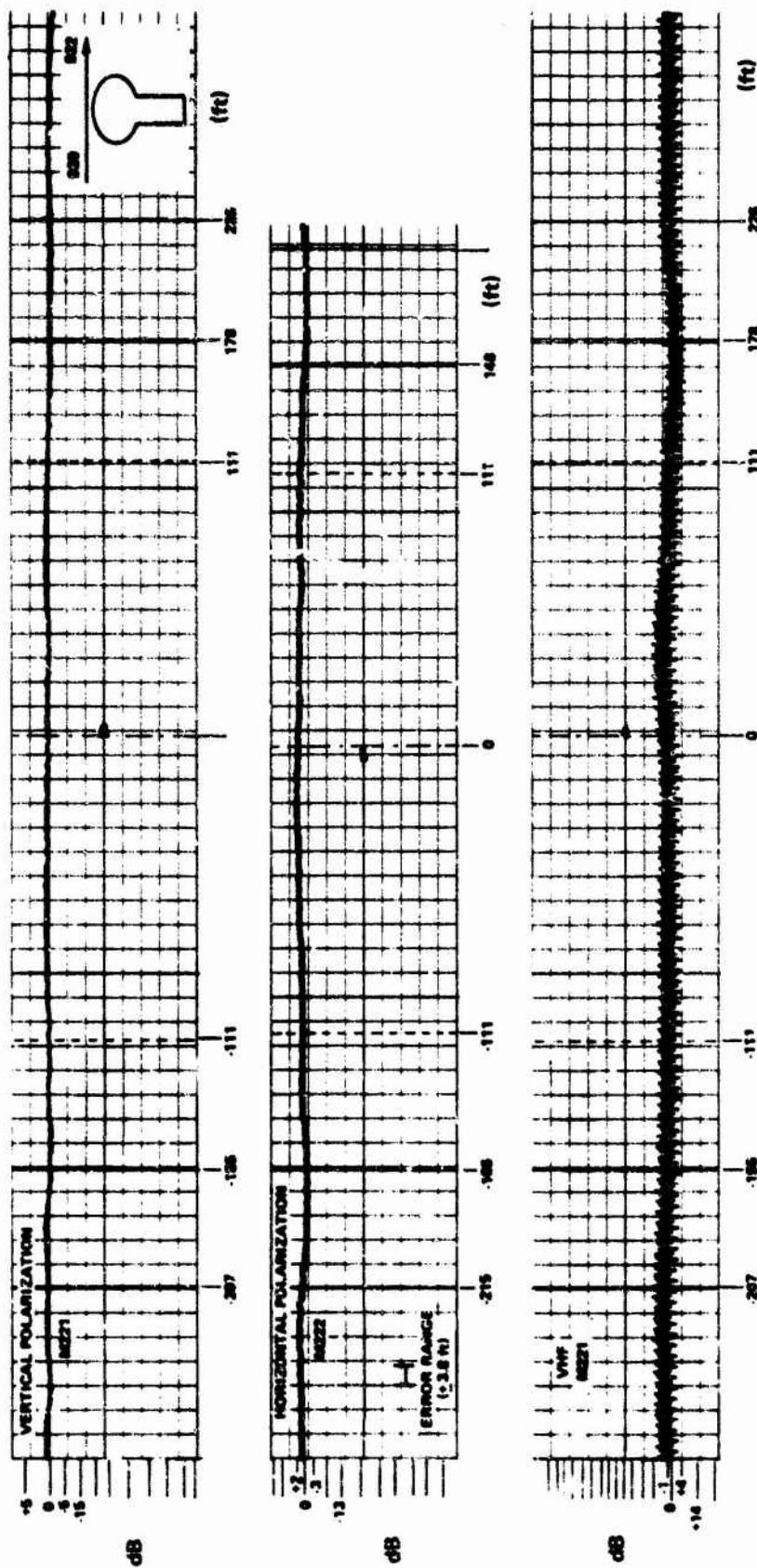


Figure 41 RELATIVE SIGNAL STRENGTH VS DISTANCE FROM TEST CENTERLINE
FOR SPHERICAL WATER TANK; $d_1 = 891$ FT, $d_2 = 5700$ FT, ALTITUDE =
921 FT

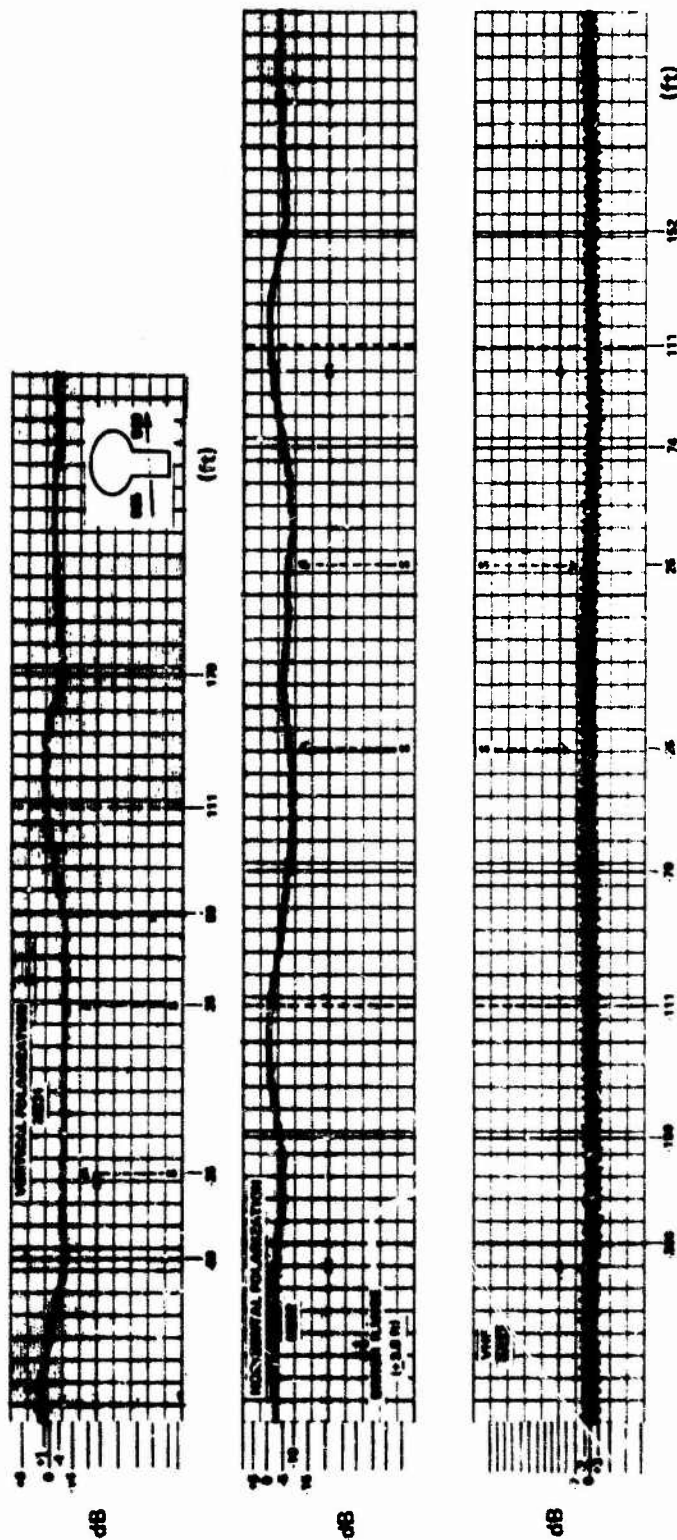


Figure 42 RELATIVE SIGNAL STRENGTH VS DISTANCE FROM TEST CENTERLINE
FOR SPHERICAL WATER TANK; $d_1 = 85.1$ FT, $d_2 = 5700$ FT, ALTITUDE =
532 FT

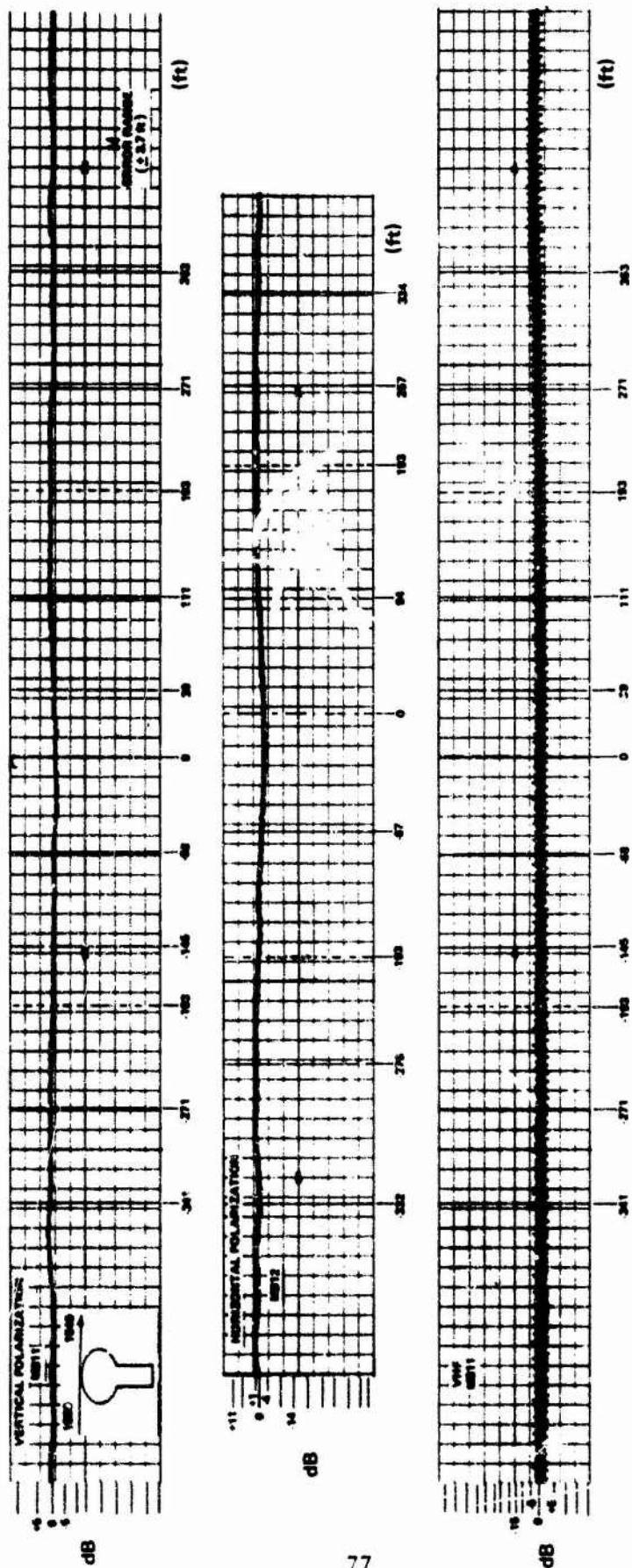


Figure 43 RELATIVE SIGNAL STRENGTH VS DISTANCE FROM TEST CENTERLINE
FOR SPHERICAL WATER TANK; $d_1 = 891$ FT, $d_2 = 10,600$ FT, ALTITUDE =
1545 FT

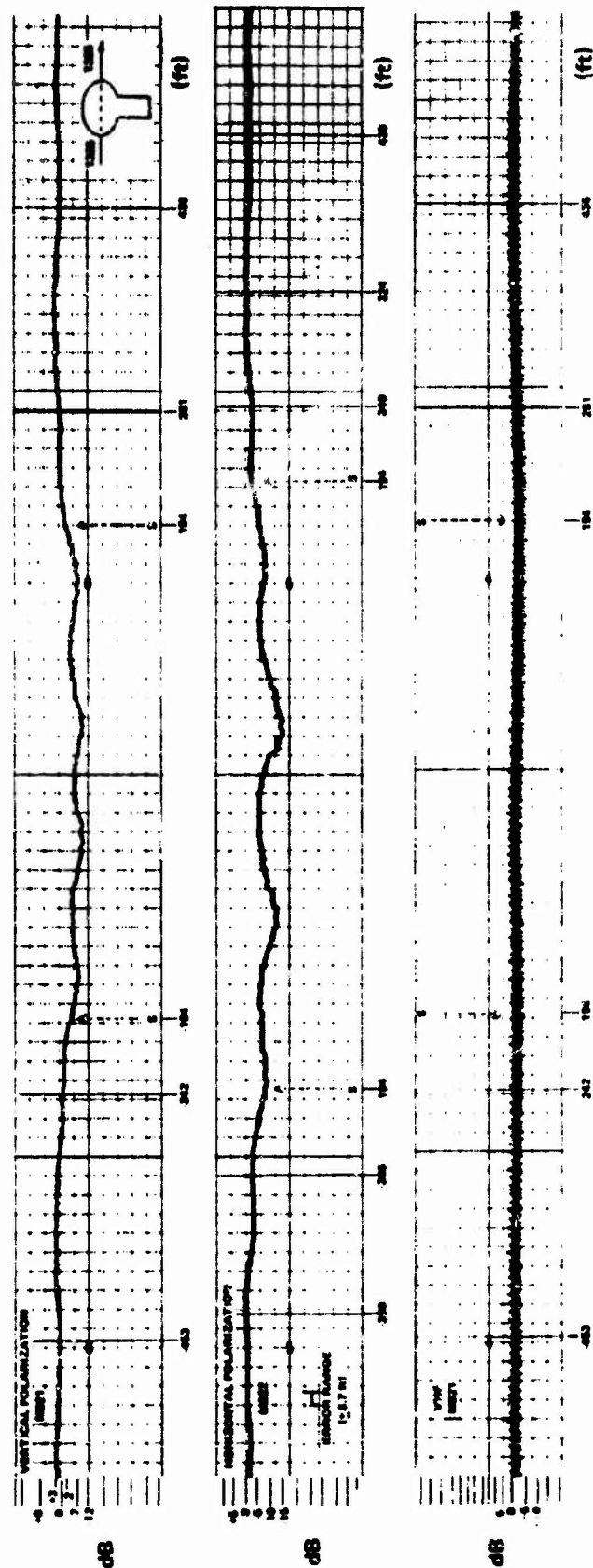


Figure 44 RELATIVE SIGNAL STRENGTH VS DISTANCE FROM TEST CENTERLINE
FOR SPHERICAL WATER TANK; $d_1 = 891$ FT, $d_2 = 10,600$ FT,
ALTITUDE = 1325 FT

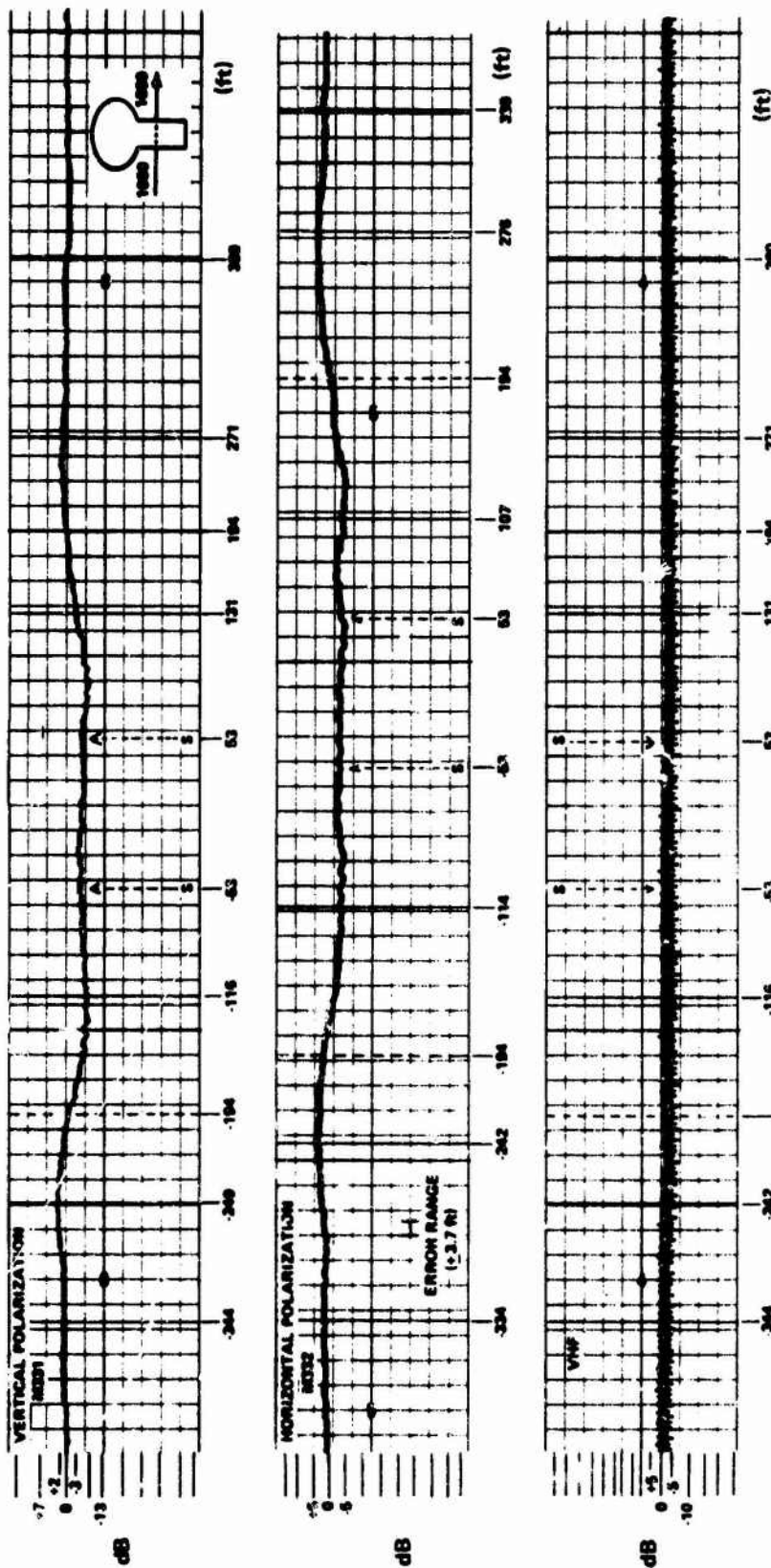


Figure 45 RELATIVE SIGNAL STRENGTH VS DISTANCE FROM TEST CENTERLINE
FOR SPHERICAL WATER TANK; $d_1 = 891$ FT, $d_2 = 10,600$ FT,
ALTITUDE = 1000 FT

Additionally, we note that, if geometrical optics is assumed to be valid, the field would be equal to the unperturbed field everywhere except within the geometric shadow when the field would vanish. As will be shown later, the predictions of geometrical optics are not very accurate.*

Results for tests M111 and M112 are shown in Figure 36. For these runs, the flight path was above the projected shadow of the water tank. The vertically and horizontally polarized signal levels varied by only about 1 dB throughout the test run. A noise-like modulation can be seen on the VHF signal. This modulation occurred on every VHF signal recorded during the flight test program. The period of the modulation, upon close inspection of the data trace, corresponds to a frequency of 3050 cycles (revolutions) per minute. The helicopter engine speed was nominally 3100 rpm. Because the engine drives various electrical generators, it is probable that the modulation originates in the power supply to the VHF transmitter.

The average VHF level may be obtained by drawing a line representing the average of the fluctuations. It is noted that, in Figure 3b, the average VHF signal remained virtually constant during the test run.

Figure 37 shows results for a lower altitude trajectory; in test M121, the flight path just grazed the top of the shadow; whereas, in test M122, the flight path fell somewhat below the top of the shadow. In both M121 and M122, the average VHF signal changes by about 1 dB throughout the run and doesn't appear to be influenced by the water tank. However, both the VP and HP S-band signals do appear to exhibit level changes that are due to the presence of the tank. For the vertically polarized case (M121), maxima (> 1 dB) occur just before and just after the sphere shadow boundaries while a minimum of -2 dB occurs when the helicopter is directly over the top. For the HP case, the signal level, after reaching a maximum of about $+1$ dB, decreases to about -6 dB when the helicopter is shadowed by the sphere.

Tests M131 and M132 were flown at an altitude of 290 feet; the trajectory was such that the helicopter was shadowed by the cylindrical support. The S-band perturbations caused by the structure are clearly shown in Figure 38. Interference maxima and minima occur within the vicinity of the obstruction and are visible beyond four sphere diameters

* Geometrical optics would provide a reasonable estimate of the field at a range, R , from the obstacle such that $R \ll d^2/\lambda$, where d is the characteristic length or diameter of the sphere. At VHF, d^2/λ equals 113 feet while at S-band, d^2/λ equals 2743 feet, for the sphere.

(or 20 cylinder support diameters) away from the obstruction. For the HP case, variations occur which change the signal level from +1 dB to a maximum of +4 dB at the sphere shadow boundaries at ± 60 feet. The signal level then decreases to a low of -4 dB prior to the helicopter's entering the cylinder shadow. When the helicopter is within the shadow, the signal level increases to about 0 dB. A slight dip to -2.5 dB occurs at the cylinder centerline. The pattern is quite symmetrical as is expected.

For the HP case, the features are generally the same as described above. The peak that occurs near the sphere shadow is at +1 dB while the minimum which occurs just before the cylinder shadow is at -9 dB. At aircraft positions of -87.3 feet and +89.9 feet, minima of -6.3 and -7.5 dB occur, respectively.

The average VHF signal remains relatively constant throughout both runs at a level of about -2 dB.* In run M132, there is a unexplained decrease in level to about -7 dB at positions between 60 and 90 feet. It is believed that this signal level change is not due to scattering from the obstacle.

Results for a flight path through the center of the spherical shadow (Runs M141 and M142) are shown in Figure 39. The sphere shadow boundaries occur at ± 60 feet. For the VP case, the signal level begins to decrease near -120 feet, roughly twice the sphere shadow width; a local minimum of -13.8 dB occurs at the obstacle centerline. At the shadow boundaries, the signal is down 5 dB.

The outstanding feature of the VP case is the large maximum which occurs when the helicopter is directly behind the obstacle; the signal level increases to -2.5 dB from a low of -36 dB at two points within the shadow. It appears, as before, that major perturbations occur out to distances approximately equal to twice the shadow boundary half-width. The larger variations seen in the HP case relative to the VP case are explainable from creeping wave diffraction theory, as previously discussed in this section.

*It was sometimes difficult to determine the precise 0 dB (no perturbation) level. The VHF signal exhibited slow linear changes even when far from the obstruction. It is probable that the slowly-varying change in level is due to the influence of the helicopter body on the VHF antenna resulting in a non-omnidirectional VHF pattern. An independent measurement of the VHF antenna pattern was not made.

The VHF signal level remains virtually unchanged; VHF communications would not be affected by the obstacle.

The second set of measurements was performed for a helicopter-to-obstacle range of 5700 feet. Table 1 gives test details and Figures 40, 41 and 42 show results.

Figure 40 gives results for a flight path within the sphere shadow. For both M211 and M212, the VHF signal undergoes very little change. Both the VP and HP signals have broad peaks (0 dB) at the center of the shadow. The minima within the shadow are -14 dB in the VP case and -17 dB in the HP case. As before, it appears that perturbations are significant out to distances approximately equal to twice the shadow boundary half-width.

The trajectory in Figure 41 (Runs M221, M222) is well above the obstruction. The VHF and both S-band signals (vertical and horizontal polarizations) remain constant throughout the run.

Results for a flight path through the cylindrical support (Runs M231, M232) are shown in Figure 42. Peaks in signal level (+1 dB) occur before the helicopter reaches the sphere shadow boundary (-11 feet). The signal level is -5 dB on the shadow boundary for both VP and HP cases. The HP case exhibits larger signal variations and a local maximum occurs within the shadow.

The VHF signal remains relatively unchanged although there appears to be a slight decrease in level (to -2 dB) when the helicopter is in the shadow.

Data for the third set of measurements with the spherical obstruction are shown in Figures 43, 44, and 45. In Figure 43, the flight path was above the shadow top. Perturbation to VHF and both S-band signals is negligible.

A flight path through the center of the shadow is shown in Figure 44. For both VP and HP cases, a local maximum of -6 dB occurs in the center of the shadow. Three interference cycles occur within the shadow region for both cases. The VHF signal is unaffected, except for a slight decrease of level to -2 dB near the center of the shadow.

In Figure 45, results for a flight path through the cylindrical support are shown. Both VP and HP S-band signals exhibit the same features. Just before and just after the shadow boundaries (± 194 feet), peaks in the signal (+2 dB) occur. The level within the shadow region is approximately -3 dB. The VHF signal level is virtually unaffected.

3.2.4 Conclusions

For all cases considered, the VHF signal level is, for practical purposes, unaffected by the presence of the spherical water tank. The ratio of sphere diameter to wavelength for these tests was 92 at S-band and 3.8 at VHF.

For flight paths above or just grazing the shadow top, the S-band signals are not significantly affected by the obstruction. However, for flight paths into the shadow region, significant perturbations do occur. Although maxima occur within the shadow region, the signal level is generally much less than the unperturbed level. Variations in signal level occur beyond the shadow region. Perturbations of from 1 to 4 dB were evident for aircraft distances out to approximately twice the shadow boundary half-width. The horizontally polarized S-band signal exhibited greater fluctuations than the vertically polarized case.

It is obvious that a simple geometric optics prediction would be grossly in error for the test conditions run. As noted earlier, theoretical techniques for analyzing the diffraction from shapes of this type do exist and these could be developed for addition to the computer program.

3.3 DIFFRACTION FROM A CYLINDRICAL OBSTRUCTION

3.3.1 Description of Experimental Layout

The experimental measurements of diffraction from a cylindrical obstruction were performed using a large, isolated cylindrical water tank which is located in Corfu, New York. Figures 46 and 47 show several photographs of the tank. An elevation view of the experimental configuration is shown in Figure 48

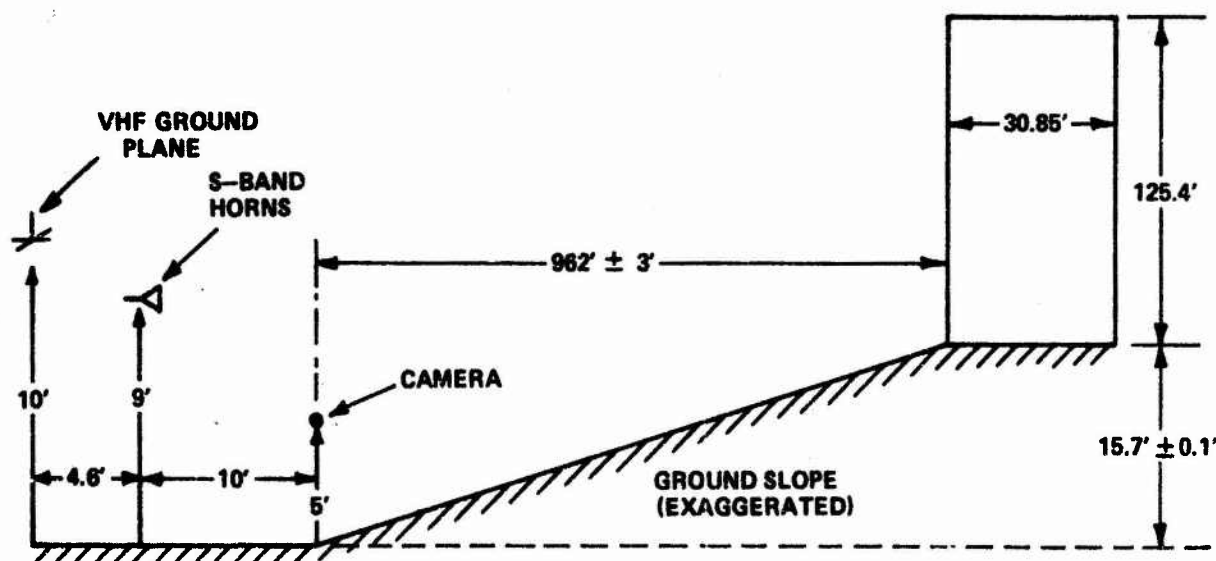
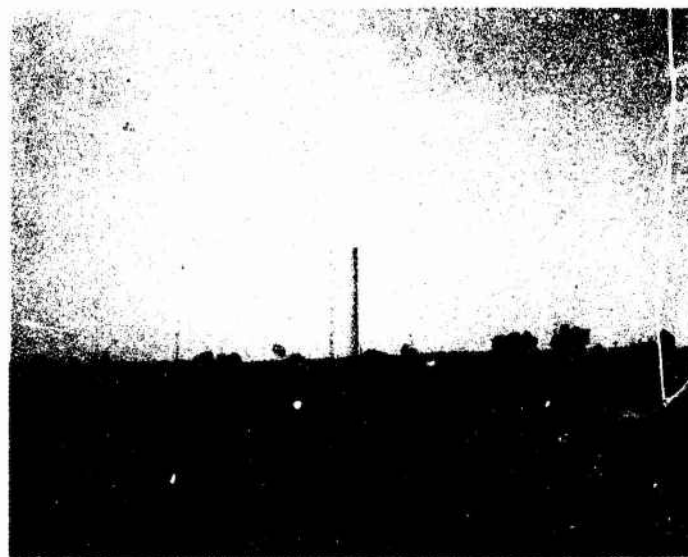
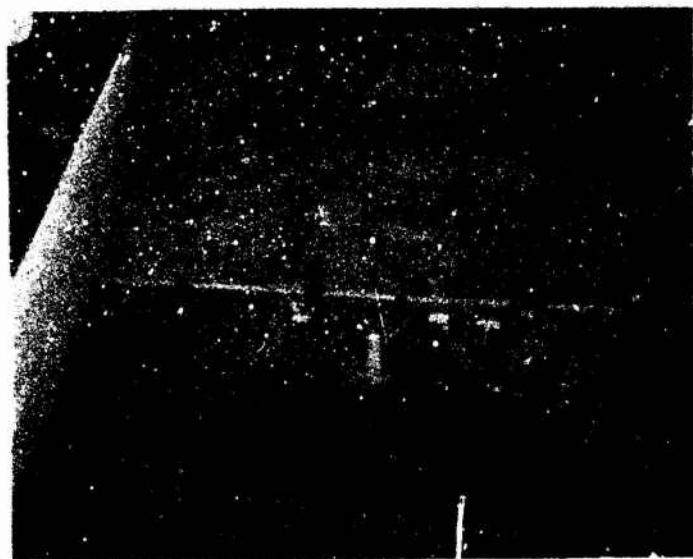


Figure 48 EXPERIMENTAL SETUP FOR CYLINDER DIFFRACTION STUDY

A description of the equipment utilized to conduct the experiment and of the experimental procedures employed were presented in Section 3. . .

3.3.2 Scope of Tests Performed

Table 2 describes the flight tests performed with the cylindrical obstruction. On the day of the flight test, a haze developed (after testing had begun) which decreased visibility considerably both for the pilot and for the ground crew. For this reason, it was necessary to limit the testing at the farthest range to only one altitude. Ranges, altitudes and polarizations pertinent to each test are shown in the table along with corresponding test numbers.



**Figure 46 CYLINDRICAL WATER TANK USED AS TEST OBJECT (LOCATED
IN CORFU, NEW YORK)**

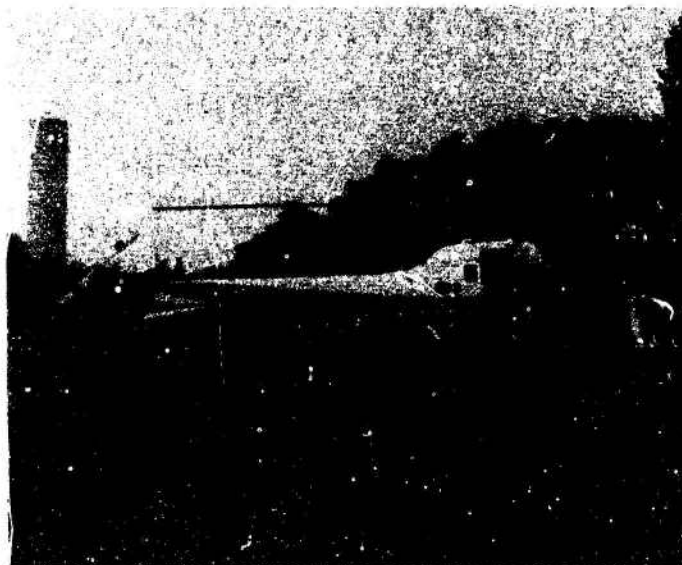


**Figure 47 CYLINDRICAL WATER TANK
(TWO VIEWS)**

Table II
CYLINDRICAL OBSTRUCTION
SCOPE OF TESTS PERFORMED

A. RANGE FROM OBSTACLE: 6300 ± 30 feet
HEIGHT OF PROJECTION OF CYLINDER TOP:* 990 ± 14 feet

TEST NUMBER	AVERAGE** ALTITUDE (ft AGL)	S-BAND POLARIZATION (f = 3006 MHz)	VHF POLARIZATION (f = 123.4 MHz)	POSITION (AS SEEN BY CAMERA)	RESULTS SHOWN IN FIGURE
C111	1125	V	V	ABOVE SHADOW BOUNDARY TOP	49
C112		H	V		
C121	775	V	V	WITHIN CYLINDER SHADOW	50
C122		H	V		
C131	390	V	V	NEAR BOTTOM OF CYLINDER SHADOW	51
C132		H	V		

B. RANGE FROM OBSTACLE: 13,300 ± 80 feet
HEIGHT OF PROJECTION OF CYLINDER TOP:* 1,943 ± 17 feet

TEST NUMBER	AVERAGE** ALTITUDE (ft AGL)	S-BAND POLARIZATION (f = 3006 MHz)	VHF POLARIZATION (f = 123.4 MHz)	POSITION (AS SEEN BY CAMERA)	RESULTS SHOWN IN FIGURE
C221	1000	V	V	WITHIN CYLINDER SHADOW	52
C222		H	V		

OTHER TEST RUNS IN THIS SERIES WERE NOT POSSIBLE BECAUSE OF POOR VISIBILITY CONDITIONS.

* REFERENCED TO S-BAND HORNS' POSITION

** ± 30 feet, ALTIMETER SET TO ZERO AT INSTRUMENTATION SITE.

3.3.3 Experimental Results

The recorded S-band and VHF signals are presented in Figures 49 through 52. The dB signal level changes shown are for one-way transmission.* The first set of measurements was for a range of 6300 feet between the obstruction and helicopter flight path. Figure 49 shows results for a flight path above the top of the cylinder shadow. Both VP and HP S-band signals are virtually unperturbed.

The VHF signal exhibits a noise believed to be caused by an improper electrical ground. (This noise was not the same as that described on page 80.) The average VHF signal was unaffected by the obstruction, however.

Figure 50 (Run C121) shows the measured VP signal level for a flight path within the region of shadowing by the cylindrical obstruction, again at a range of 6300 feet. The vertically polarized signal exhibited variations of about ± 3 dB out to beyond four shadow boundary half-widths. Beginning at about -185 feet relative to the plane containing the ground-based receiving antenna and the tank symmetry axis, the signal level began to decrease. Within the shadow region (± 116 feet), the diffracted field was quite symmetrical. A broad local maximum (-5 dB) occurred following the first minimum within the shadow. The level then reached a minimum of -30 dB and near the center of the shadow, the signal level was approximately -20 dB. Note also that two smaller local maxima occurred near the center of the shadow region.

As we have previously seen, "major" diffraction effects seem to occur within a region extending out to twice the shadow boundary half-width (± 232 feet).

During Run C122, the recorder gain was not properly adjusted to compensate for the lower output from the HP receiver; and, hence, the full dynamic range needed to record the signal level within the shadow boundary

*For a two-way path (e. g., radar), the dB level would change by a factor of two.

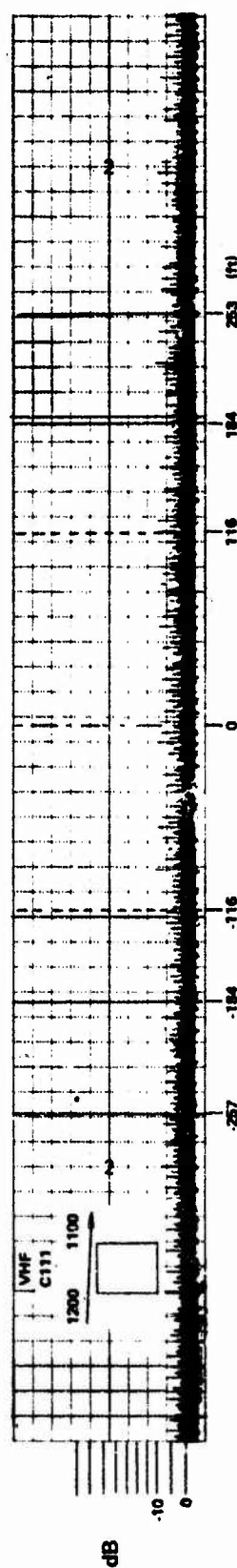


Figure 49 RELATIVE SIGNAL STRENGTH vs DISTANCE FROM TEST CENTERLINE FOR CYLINDRICAL WATER TANK; $d_1 = 962$ FT, $d_2 = 6300$ FT, ALTITUDE = 1125 FT

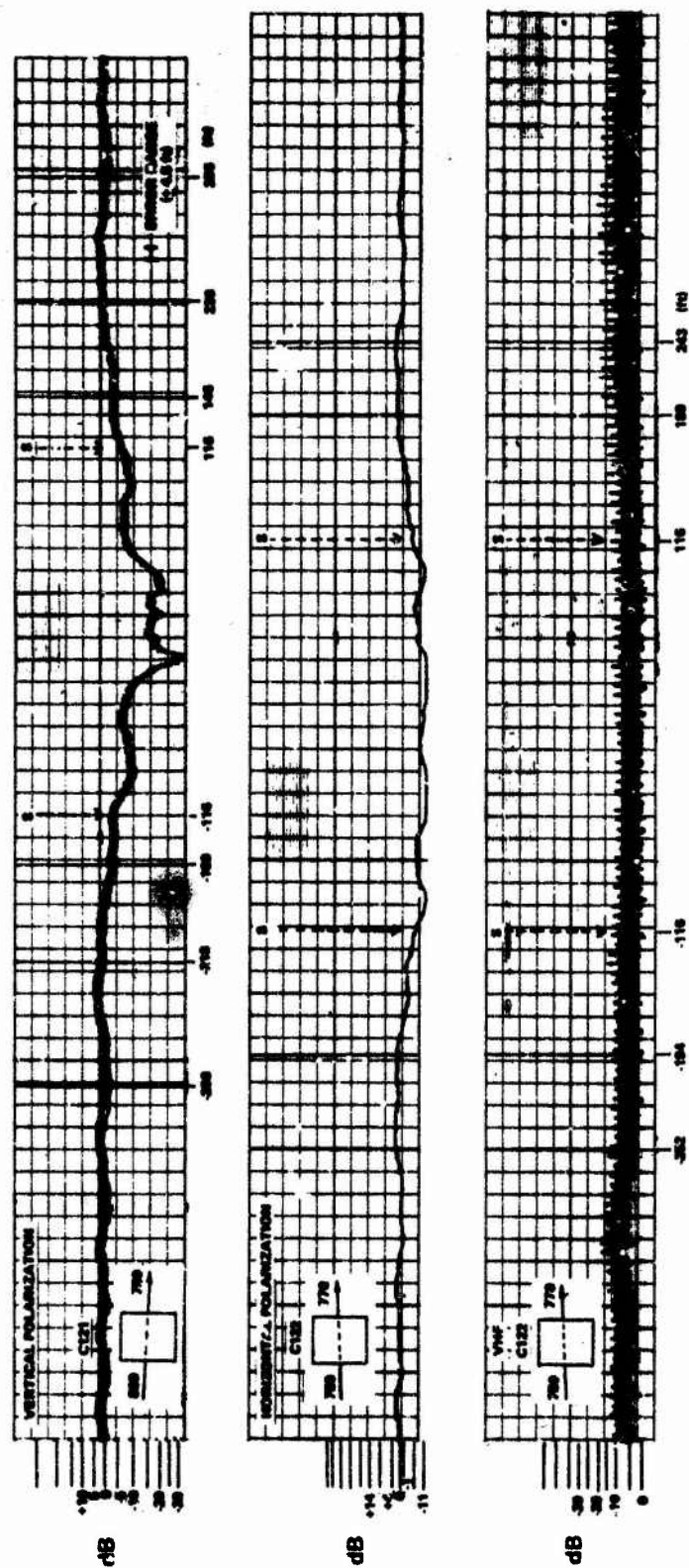


Figure 50 RELATIVE SIGNAL STRENGTH vs DISTANCE FROM TEST CENTERLINE FOR CYLINDRICAL WATER TANK; $d_1 = 962$ FT, $d_2 = 6300$ FT, ALTITUDE = 7715 FT

was not provided. There are some features however that were preserved. Following small changes in amplitude, the signal level began to decrease at about -194 feet. At the shadow boundary, the level was about -5 dB (roughly the same value as for the VP case). Three maxima are seen to occur within the shadow boundaries. The central maximum within the shadow reached a level of -10 dB.

The VHF signal decreased slowly and reached a minimum of -8 dB when situated at -306 feet (i. e., to the left of the obstacle). The signal then increased in level to a maximum of 0 dB (the unperturbed value) behind the water tank. Upon leaving the shadowed region, the signal again began to decrease to about -7.5 dB, reaching that level at a position of around 336 feet. Further analysis would be required to determine whether the indicated behavior is due to the presence of the obstacle or whether the result is due to ground effects, antenna pattern changes, or other causes.

The results are shown in Figure 51 for Tests C131 and C132, during which relatively low altitude flight paths were flown. The VP signal level changes encountered here were similar to those of the previous VP test, but the null at the center of the shadow (see C121) was absent. At the shadow boundaries, the signal level was -5 dB. The deep nulls within the shadow reached -30 dB and the broad peak at the center of shadow reached -9 dB. For the HP case (C132), sufficient dynamic range to view the signal nulls within the shadow was not provided, due to improper gain adjustments previously described. At the shadow boundaries, the signal level is approximately -5 dB. Small amplitude changes (± 3 dB) occurred at positions away from the obstruction.

Considering both C131 and C132, the VHF signal exhibits a scalloped pattern which appears throughout the extent of the run. There appeared to be a slight increase in average VHF signal level when the helicopter was within the obstruction shadow. In some regions, the VHF level dropped to -10 dB. Detailed analysis would be required to assess the effects of ground reflections, antenna pattern effects, and the effect of the obstruction itself to determine the source of the VHF signal fluctuations.

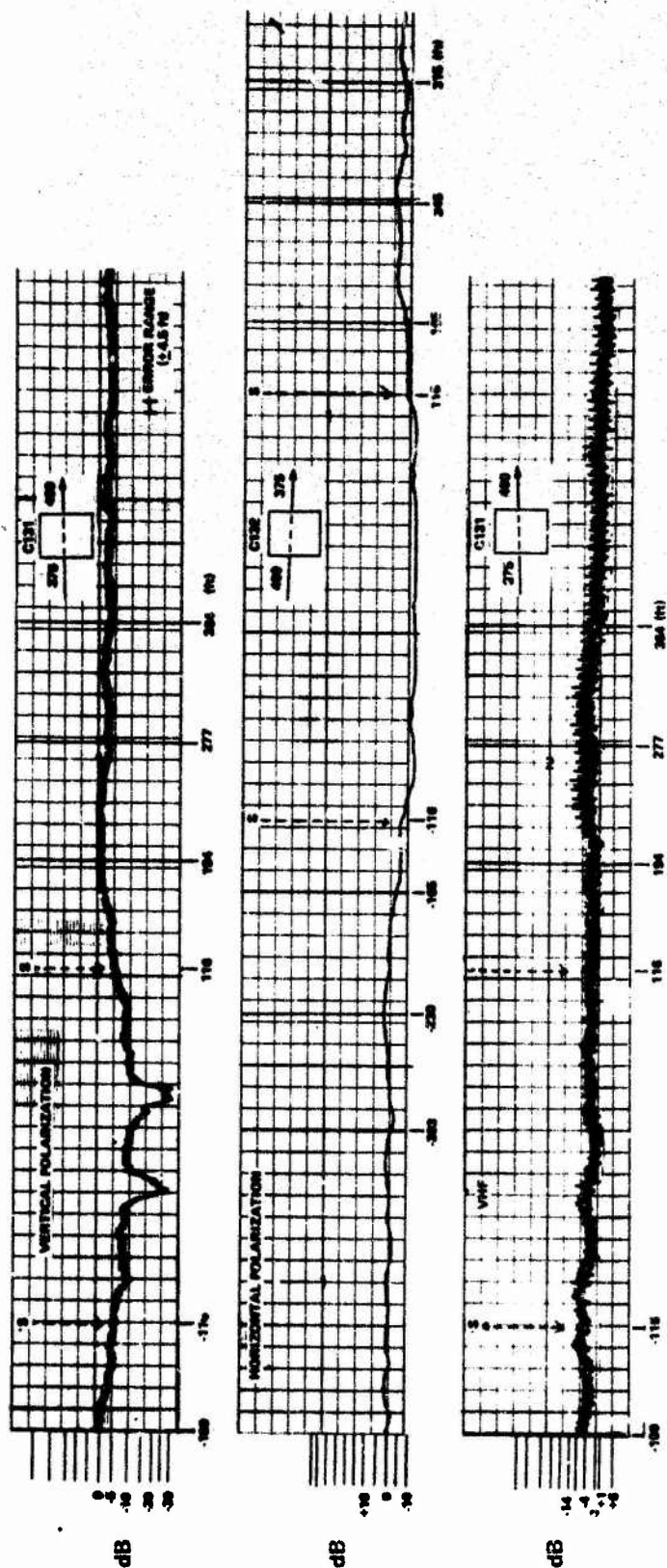


Figure 51 RELATIVE SIGNAL STRENGTH vs DISTANCE FROM TEST CENTERLINE FOR CYLINDRICAL WATER TANK; $d_1 = 962$ FT, $d_2 = 6300$ FT, ALTITUDE = 390 FT

A second set of runs was attempted for an obstacle-to-helicopter range of 13,300 feet. However, due to extremely bad visibility conditions, results for only one altitude were obtained. These results are shown in Figure 52. The HP receiver channel was adjusted to provide sufficient dynamic range for these runs.

The signal level for both the VP and HP cases remained below -5 dB when the helicopter was within the shadow of the cylindrical water tank. The HP signal showed three broad maxima within the shadow; the deepest null was at -27 dB. The VP signal also showed the two broad peaks, each within the outer third of the shadow region. Closer to the center of the shadow, the VP signal also showed the two broad peaks, each within the outer third of the shadow region. Closer to the center of the shadow, the VP signals fluctuated more than the HP signal did. The deepest null for the VP case reached -26 dB.

For both cases, perturbations due to the obstruction occurred out to distances approximately equal to twice the shadow boundary half-width. Variations of about ± 3 dB in the VHF signal level occurred throughout the run.

3.3.4 Conclusions

For flight paths within the shadow region of the cylindrical obstacle, both S-band signals (VP and HP) exhibited significant loss (-25 dB). Because two-way transmission (radar) would entail losses equal to twice those measured, it is very likely that an aircraft would not be visible to a radar when the aircraft was in the shadow region of the obstruction utilized for our test. Signal level perturbations generally occurred for aircraft positions within approximately twice the shadow boundary half-width of the obstacle.

During some of the runs, the VHF signal level varied by 10 dB and this change occurred prior to entry into the shadow region. Behind the shadow, the VHF level generally increased. The source of this signal level variation was not firmly established.

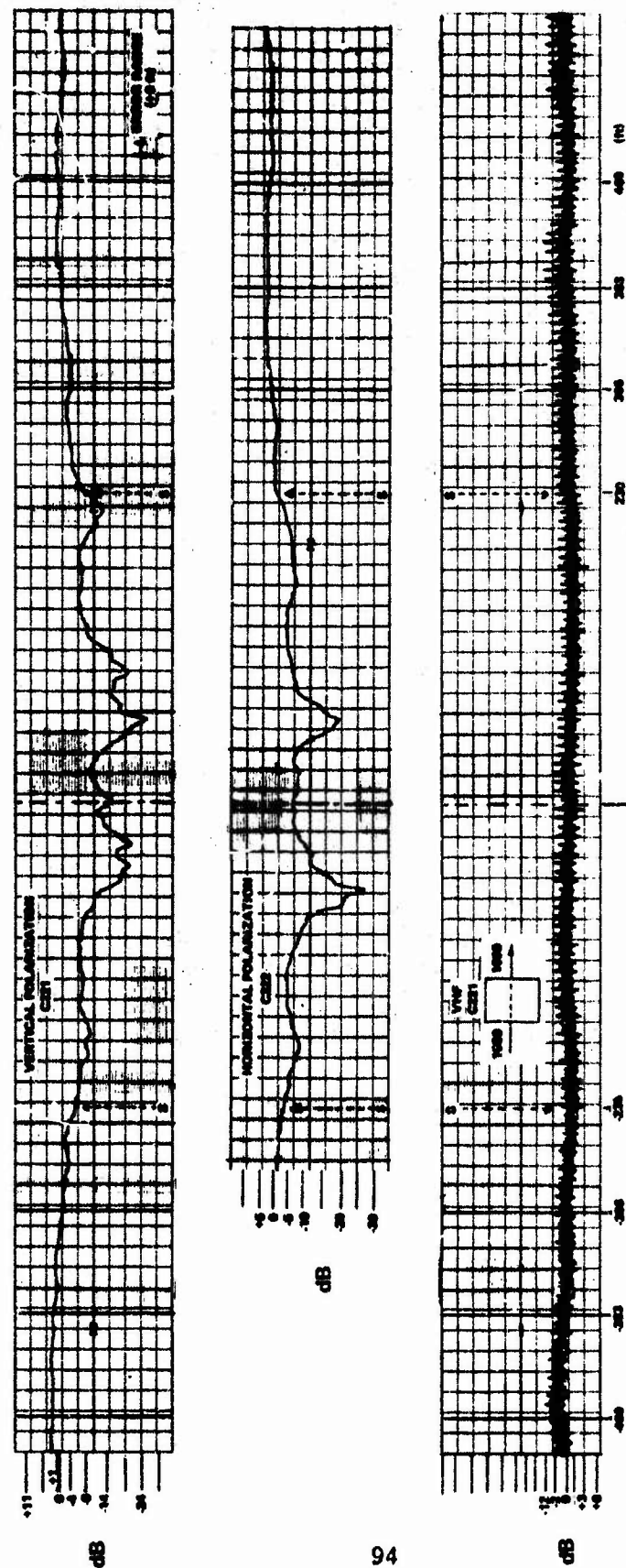


Figure 52 RELATIVE SIGNAL STRENGTH vs DISTANCE FROM TEST CENTERLINE FOR CYLINDRICAL WATER TANK; $d_1 = 962$ FT, $d_2 = 13,300$ FT, ALTITUDE = 1000 FT

A simple geometric optics prediction would overestimate the amount of loss within the shadow and underestimate the loss in regions outside of but near the shadow boundary.

Theoretical techniques for analyzing diffraction from cylindrical structures are available and this capability could be added to the computer program.

3.4 DIFFRACTION FROM A RECTANGULAR OBSTRUCTION

Rectangular obstructions selected for the flight tests, which closely approximate the theoretical model utilized in the computer program, were the water intake gate buildings located on the Robert Moses Parkway near Niagara Falls, New York. Figures 53 and 54 show aerial photographs of the buildings. Certain features of the site are evident. Firstly, the buildings are isolated from each other and from other obstructions. Also, test flight paths were over the water area where relative freedom from other obstructions prevailed. Barely visible in Figure 54 are three towers and a bridge which possibly caused some multipath effects in the VHF channel during some of the measurements. Figure 55, looking east, shows a number of towers which may also have had an effect upon the VHF results. The ground equipment was based on the northern side of the expressway as indicated in Figure 54.

Both of the buildings were utilized, in different tests, to attain the three orientations desired. The east building provided a "look" at a broad face (B-series) from the location marked (1). From the same location, the west building provided a look at an intermediate angle (A-series). To provide a look at the narrow face of a rectangular building (N-series), the receiving van was moved eastward to location (2) until the desired view of the west building was obtained.

The faces of the buildings are all metal and set on concrete foundations. Figures 56 through 59 are photographs of the buildings. Certain deviations from the theoretical model are evident. First of all, the top of each building is peaked, not flat. Additionally, eight vertical aluminum ribs or fins protrude from the broad faces and top of the building. Finally, the broad faces of the building are constructed of stainless steel panels which

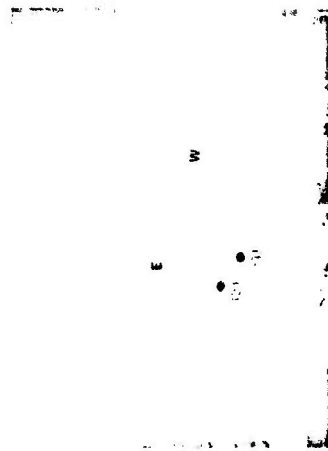


Figure 54 AERIAL VIEW OF NIAGARA INTAKE GATE BUILDINGS LOOKING SOUTHEAST

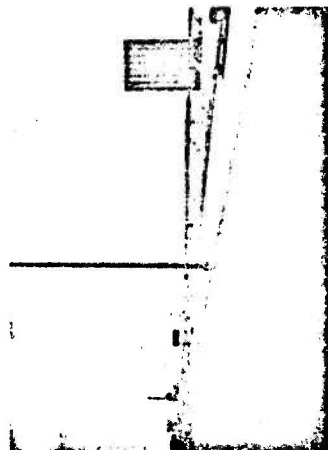


Figure 53 AERIAL VIEW OF NIAGARA INTAKE GATE BUILDINGS LOOKING NORTHWEST

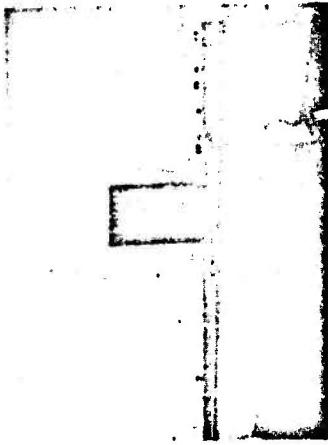


Figure 56 PHOTOGRAPH OF NIAGARA INTAKE GATE BUILDINGS

Figure 55 BRIDGE AND TOWERS: POSSIBLE SOURCES OF VHF MULTIPATH

NOTE:
FIGURES 56 THROUGH
59 ILLUSTRATE THE
FIN STRUCTURE AND
THE PEAKED ROOF



Figure 57 PHOTOGRAPH OF NIAGARA INTAKE GATE BUILDINGS



Figure 58 PHOTOGRAPH OF NIAGARA INTAKE GATE BUILDINGS

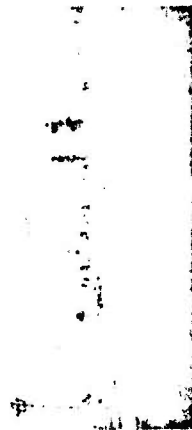


Figure 59 PHOTOGRAPH OF NIAGARA INTAKE GATE BUILDINGS

Preceding page blank

97

Preceding page blank

not perfectly flat, but have a shallow faceted pattern. It is not expected that the facets are of major importance. For the B-series, the facets in view of the receiver are shielded from the airborne transmitter. For the N-series, the fins shadow the facets and form a periodic structure. The possible effects of this are discussed in the N-series section. For the A-series, it is believed that the fins were of much more importance than the facets in affecting scattering from the structure.

The effects of the nonflat roof and of the fins on the roof have not been specifically isolated or assessed.

Despite these differences between the theoretical model and the experimental obstruction, the following sections demonstrate that good agreement between theoretical predictions and experimental results has been obtained.

3.4.1 Comparison Between Theory and Experiment

3.4.1.1 Broad Face View (B-series)

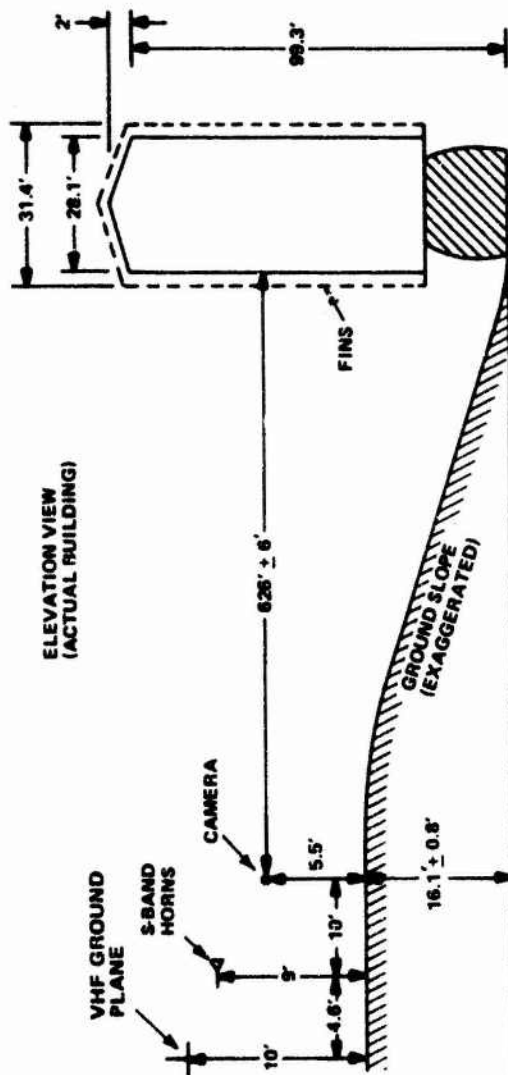
3.4.1.1.1 Description of Experimental Layout

Figure 60 shows both plan and elevation views of the experimental configuration for the B-series tests. All relevant distances and dimensions are noted on the figure. The plan view was plotted using the developed computer program and is one of the outputs provided.

3.4.1.1.2 Scope of Tests Performed and Data Reduction

Table 3 shows the scope of tests performed at this orientation. For both Group A and Group B, the range from the obstacle is given, not as a single number, but as an extent of variation. This resulted from having a flight path which was oblique to the test centerline.* Having an oblique flight path somewhat complicated the comparison of experimental and theoretical data (see Section 3.1.5).

* Defined as a horizontal line from the receive horns extending through the center of the obstruction and terminating at the observation plane.



NOTE: BUILDING HEIGHT (FLAT ROOF)
OF 101 ft ASSUMED IN COMPUTER
MODEL.

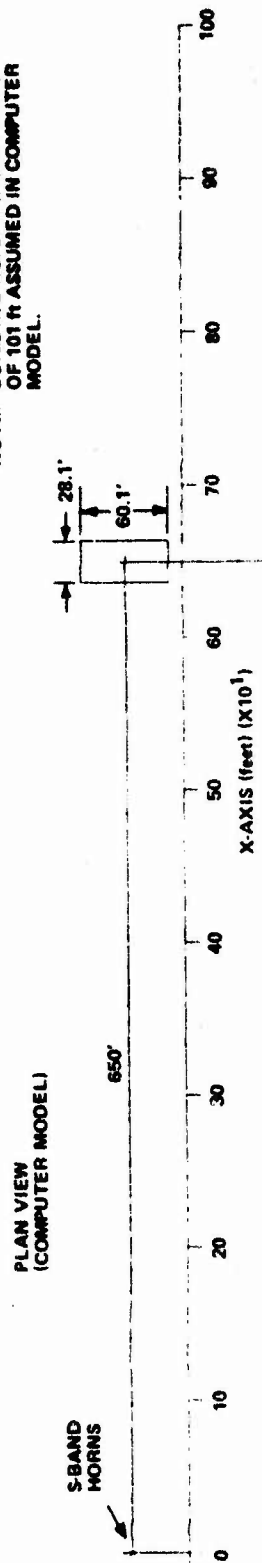


Figure 60 EXPERIMENTAL LAYOUT FOR B-SERIES

Table III
RECTANGULAR OBSTRUCTION, B-SERIES
SCOPE OF TESTS PERFORMED

A. RANGE FROM OBSTACLE: 4120 TO 4400 ft¹
HEIGHT OF PROJECTION OF OBSTACLE TOP:^{*2} 570 ft

TEST NUMBER	AVERAGE** ALTITUDE (ft AGL)	S-BAND POLARIZATION (f = 3006 MHz)	VHF POLARIZATION (f = 123.4 MHz)	RESULTS SHOWN IN FIGURE
B111	655	V	V	67
B112		H	V	
B121	950	V	V	68
B122		H	V	
B131	400	V	V	69
B132		H	V	

B. RANGE FROM OBSTACLE: 8250 TO 8760 ft¹
HEIGHT OF PROJECTION OF OBSTACLE TOP:^{*3} 1068.8 ft

TEST NUMBER	AVERAGE** ALTITUDE (ft AGL)	S-BAND POLARIZATION (f = 3006 MHz)	VHF POLARIZATION (f = 123.4 MHz)	RESULTS SHOWN IN FIGURE
B211	1150	V	V	70
B212		H	V	
B221	1650	V	V	71
B222		H	V	
B231	650	V	V	72
B232		H	V	

^{*} REFERENCED TO S-BAND HORNS' POSITION

^{**} ± 30 feet ; ALTIMETER SET TO ZERO AT INSTRUMENTATION SITE.

1. RESULT OF OBLIQUE FLIGHT PATH.
2. CALCULATED AT 4120 ft.
3. CALCULATED AT 8250 ft.

Figures 61 through 66 show computer-generated plots of dB contours for vertical and horizontal polarization (S-band) and for VHF (vertical polarization). Indicated on the plots are the altitudes associated with specific test runs. These plots were not used to provide the comparison data; such data were obtained from the computer printout of the normalized signal level (in dB) at a specific observation plane of interest. Only one observation plane is shown for each of the two major range changes. We note, however, that computer data was obtained at several observation planes within the range variations shown for both Groups A and B.

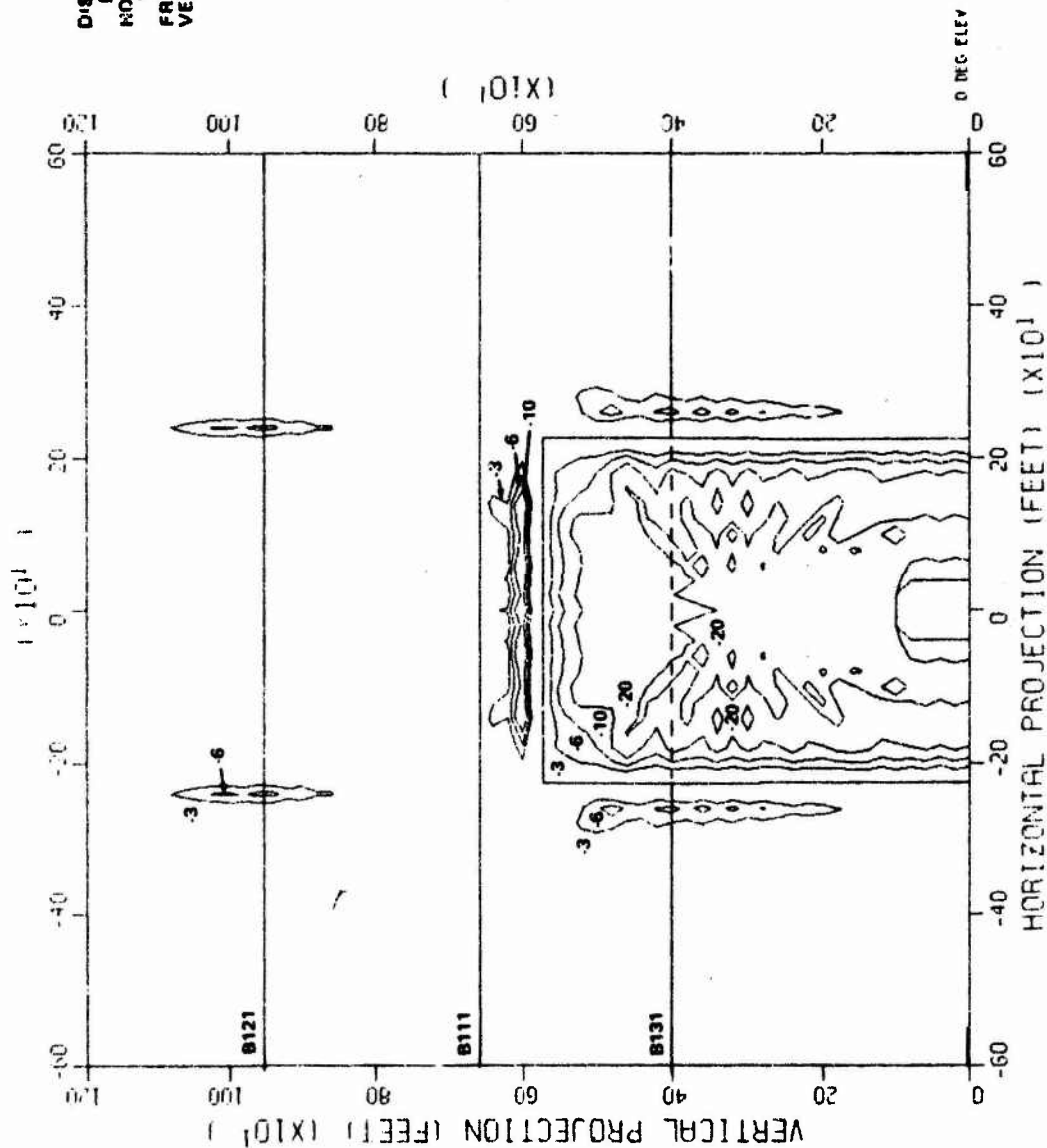
Figures 61 through 66 also indicate that the aircraft altitude did not remain constant but changed during the course of some of the runs. The altitude lines shown in the figures are connected between the values reported by the pilot at the beginning (left side of figure) and end (right side of figure) of a given run.

3.4.1.1.3 Experimental and Theoretical Data Comparison (B-Series Tests)

The flight test and theoretical data for the B-series tests are shown in Figures 67 through 72. The VHF signal was recorded for both S-band passes (horizontal and vertical polarization); only one recording is presented because the data are similar.

The theoretical data is denoted in the figures by a cross (+). The length of the vertical line represents the uncertainty in signal level resulting from an uncertainty in altitude; the horizontal line represents an uncertainty in helicopter position (see Section 3.1.5 for further details). The aircraft speed was assumed to be constant when it was shielded behind the obstruction from view of the camera. This assumption was needed to determine the helicopter's position.

In Figure 67, very good agreement is evident for both polarizations of the S-band signal. The VHF signal, on the left side of the building, is scalloped and appears to be from 5 to 10 dB lower than the predicted values. This region represents the beginning of the run where several potential VHF multipath sources exist, such as a bridge and several towers. It is also possible that ground and/or water reflections may account for the result (see Figure 55). Further into the run, agreement becomes much better.



DISTANCE TO PROJECTION
PLANE IS 4120 ft
HORIZON CORRESPONDS
TO ORIGINATE - 0 feet
FREQUENCY - 3002.0 MHz
VERTICAL POLARIZATION

Figure 61 FLIGHT PATHS, B1X1-SERIES, S-BAND, VERTICAL POLARIZATION

DISTANCE TO PROJECTION
PLANE IS 4120 ft
HORIZON CORRESPONDS
TO ORIGINATE - 6 feet
FREQUENCY - 3008.0 MHz
HORIZONTAL POLARIZATION

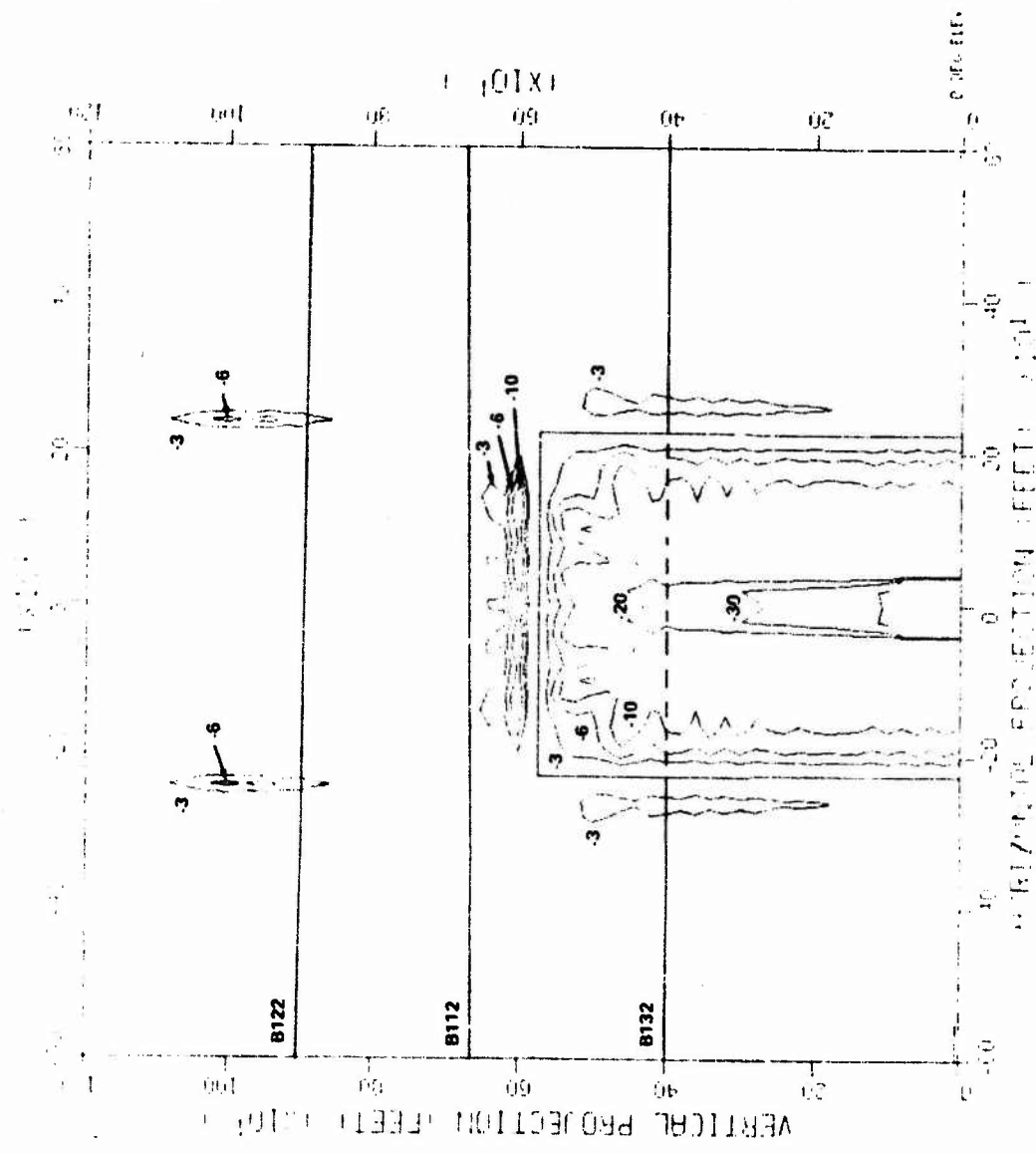
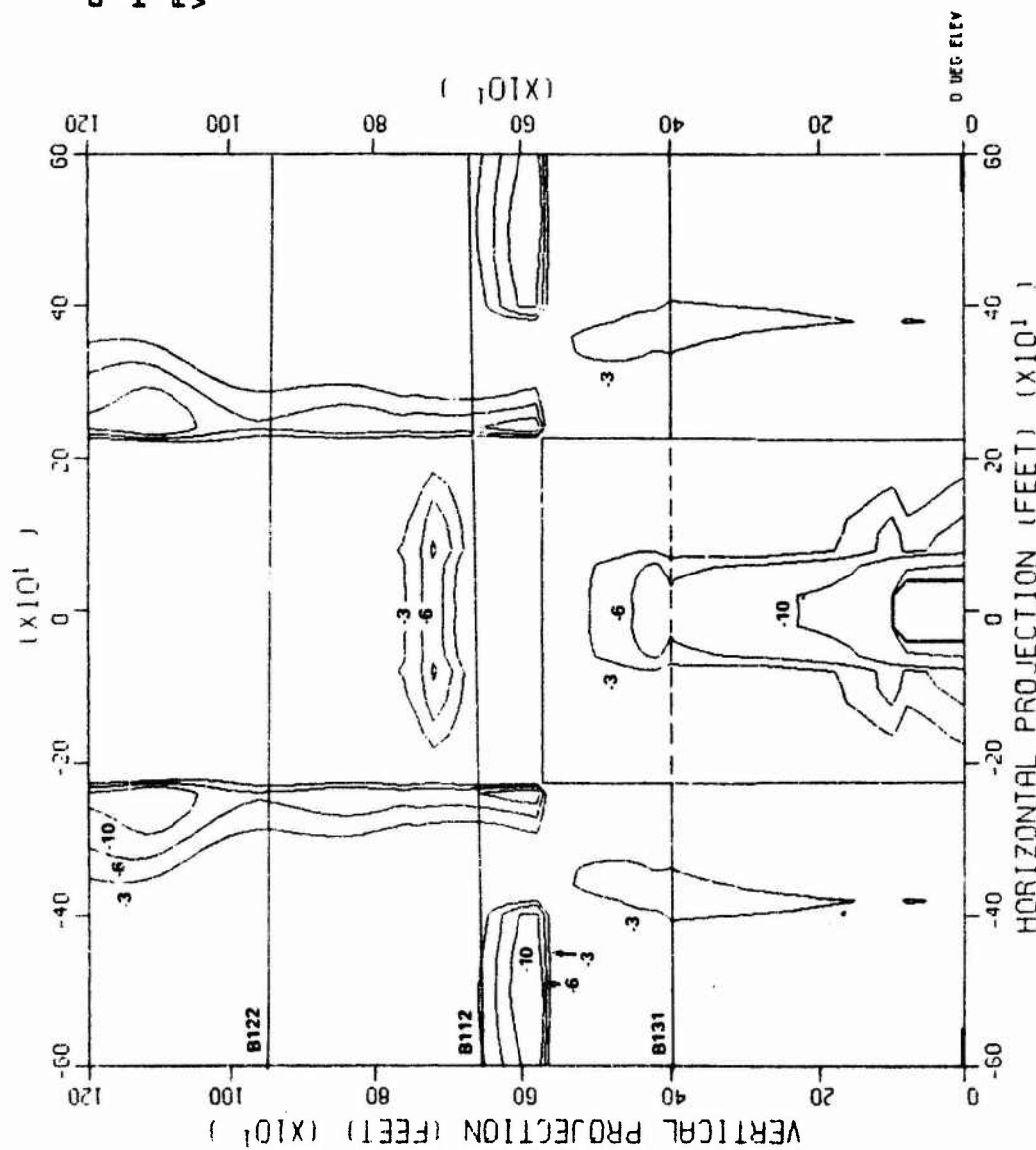


Figure 62 FLIGHT PATHS, B1X2-SERIES, S-BAND, HORIZONTAL POLARIZATION

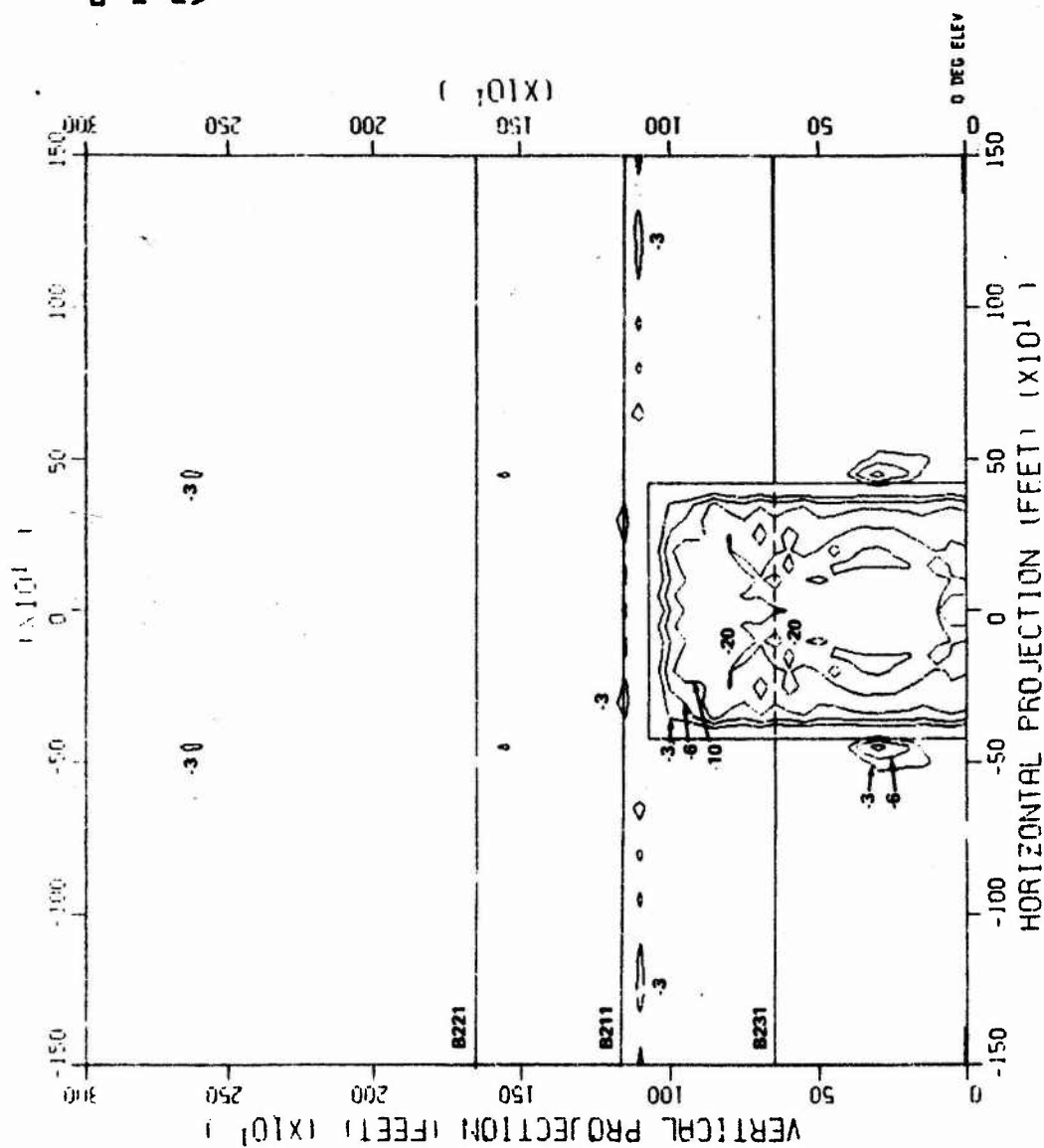
Reproduced from
best available copy.



DISTANCE TO PROJECTION
PLANE IS 4120 ft
HORIZON CORRESPONDS
TO ORIGINATE - 0 feet
FREQUENCY " 123.4 MHz
VERTICAL POLARIZATION

Figure 63 FLIGHT PATHS, B1XY-SERIES, VHF, VERTICAL POLARIZATION

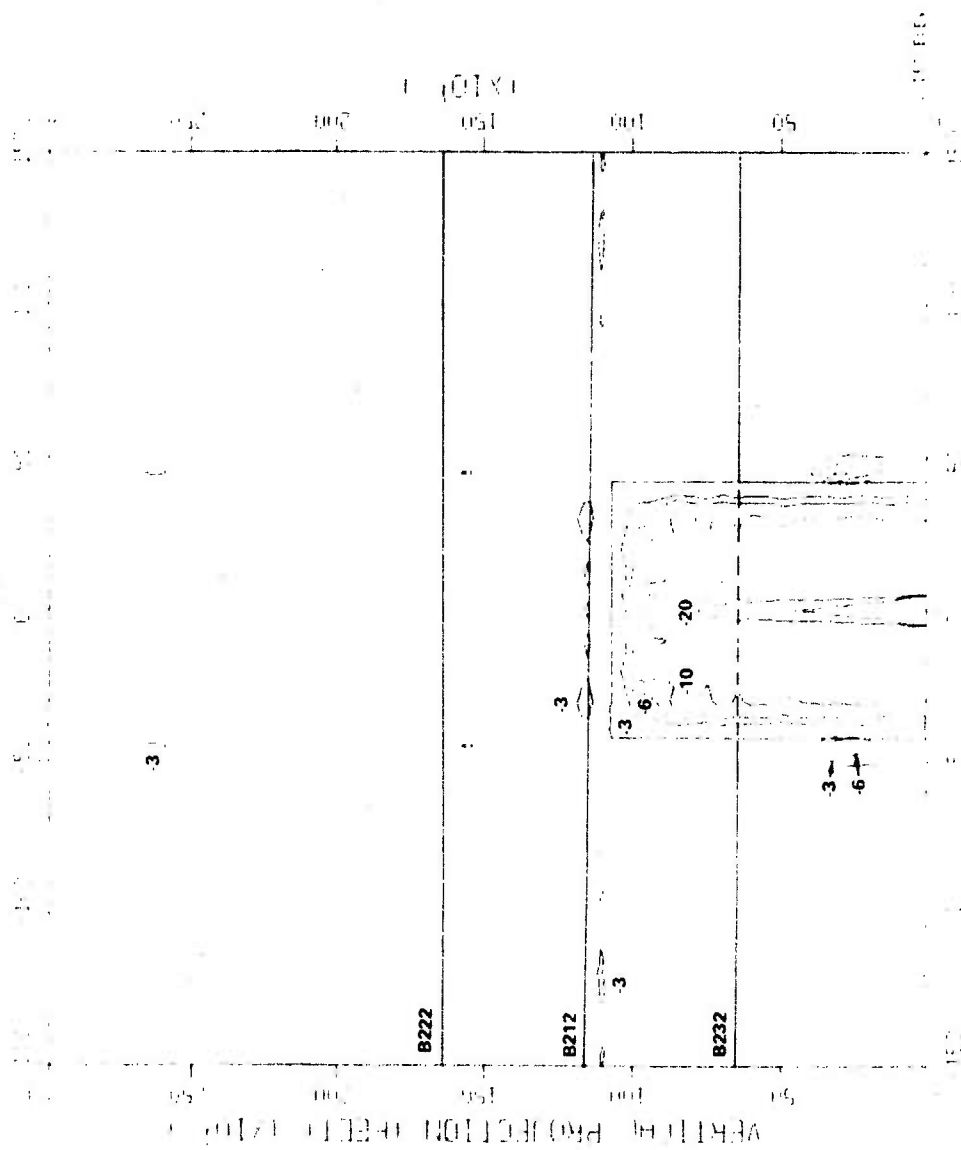
Reproduced from
best available copy.



DISTANCE TO PROJECTION
PLANE IS 8250 ft
HORIZON CORRESPONDS
TO ORIGINATE = 0 feet
FREQUENCY = 3000.0 MHz
VERTICAL POLARIZATION

Figure 64 FLIGHT PATHS, B2X1-SERIES, S-BAND, VERTICAL POLARIZATION

DISTANCE TO PROJECTION
PLANE IS 8250 ft
HORIZON CORRESPONDS
TO ORDNATE = 0 feet
FREQUENCY = 3006.0 MHz
HORIZONTAL POLARIZATION



Reproduced from
best available copy.

Figure 65 FLIGHT PATHS, B2X2-SERIES, S-BAND, VERTICAL POLARIZATION

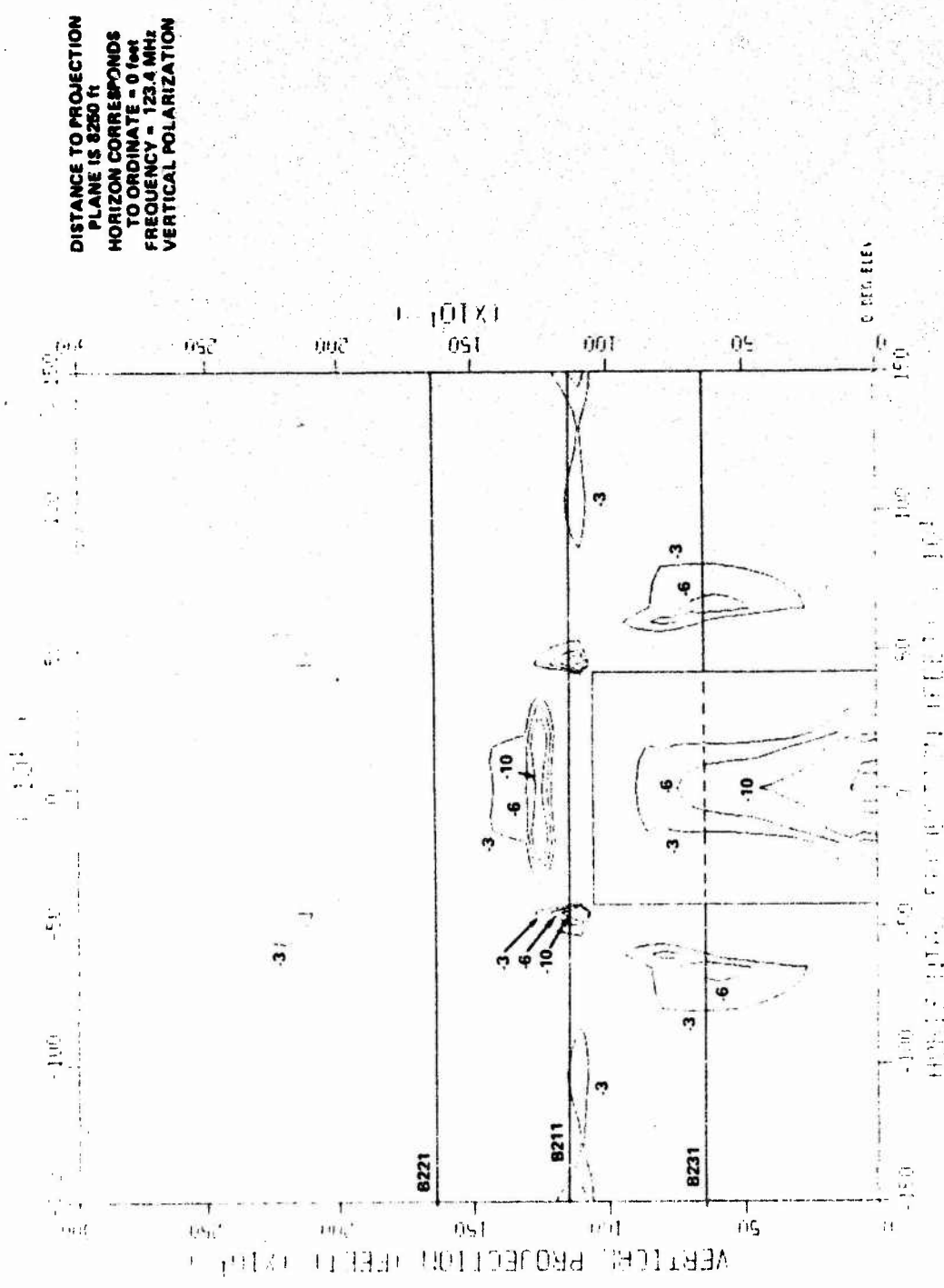


Figure 66 FLIGHT PATHS, B2XY-SERIES, VHF, VERTICAL POLARIZATION

Reproduced from best available copy.

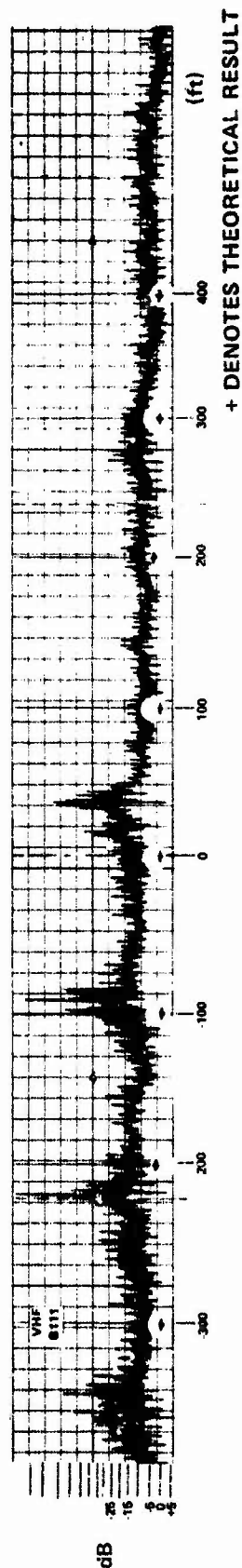
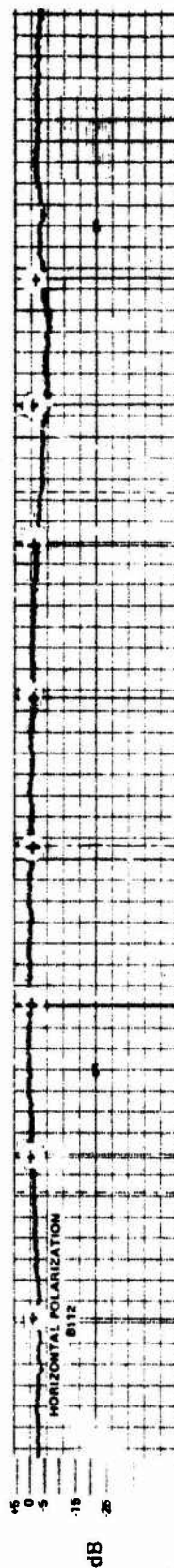
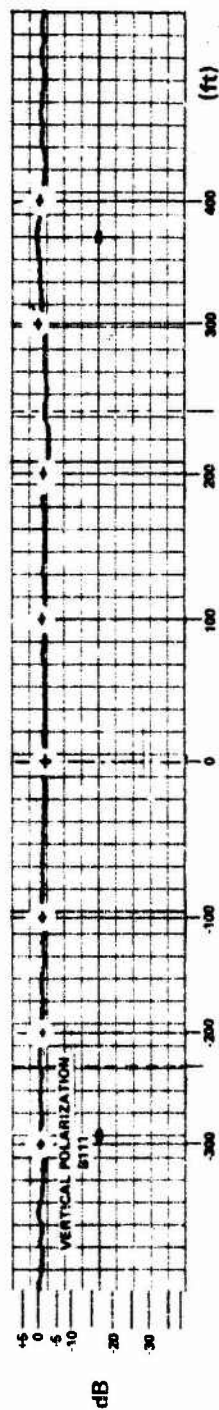


Figure 67 COMPARISON BETWEEN THEORY AND EXPERIMENT, RELATIVE SIGNAL STRENGTH vs DISTANCE FROM TEST CENTERLINE, RUNS B111 AND B112; $d_1 = 650$ FT, $d_2 \approx 4200$ FT, ALTITUDE ≈ 655 FT

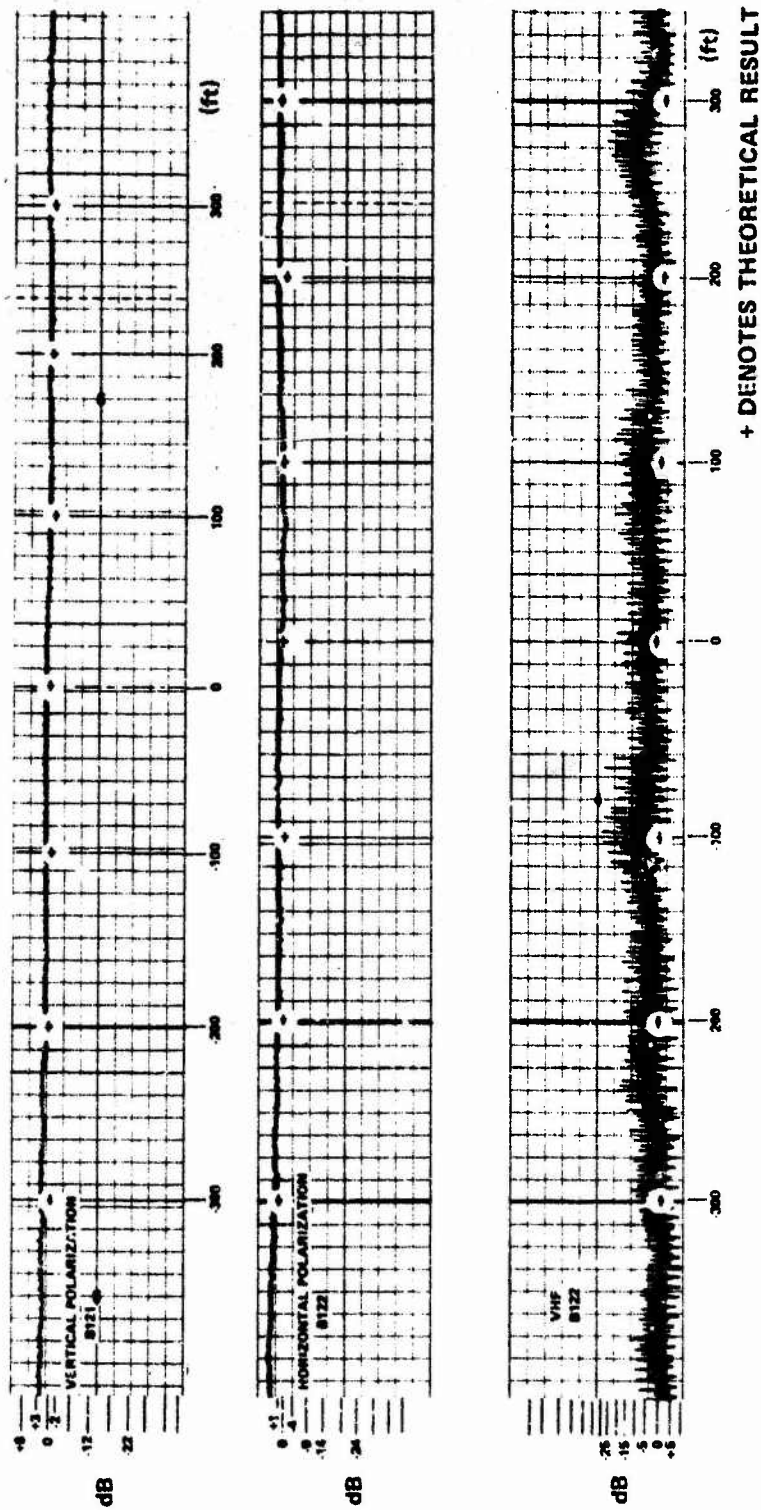


Figure 68 COMPARISON BETWEEN THEORY AND EXPERIMENT, RELATIVE SIGNAL STRENGTH vs DISTANCE FROM TEST CENTERLINE, RUNS B121 AND B122;
 $d_1 = 650$ FT, $d_2 \approx 4200$ FT, ALTITUDE ≈ 950 FT

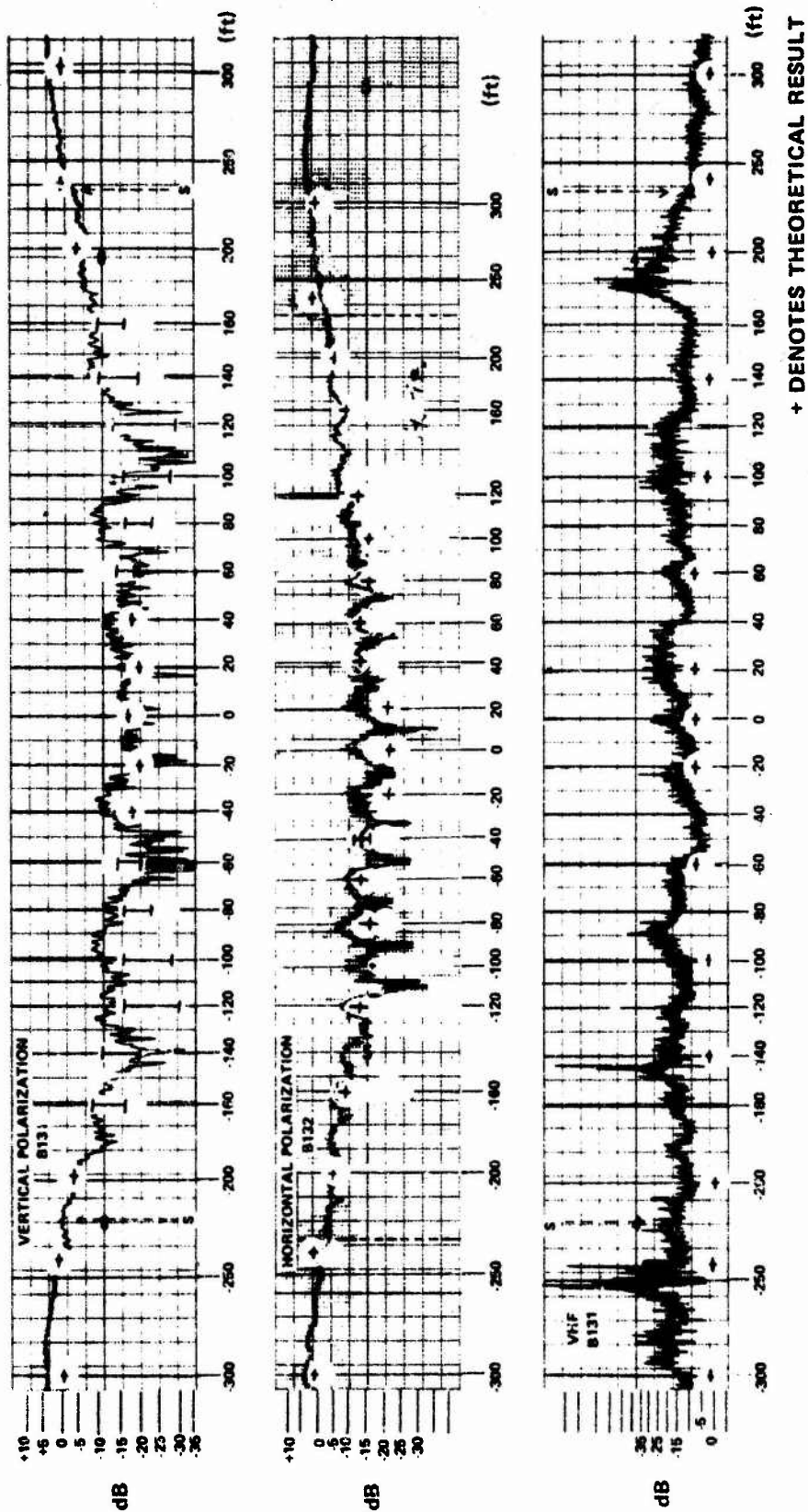
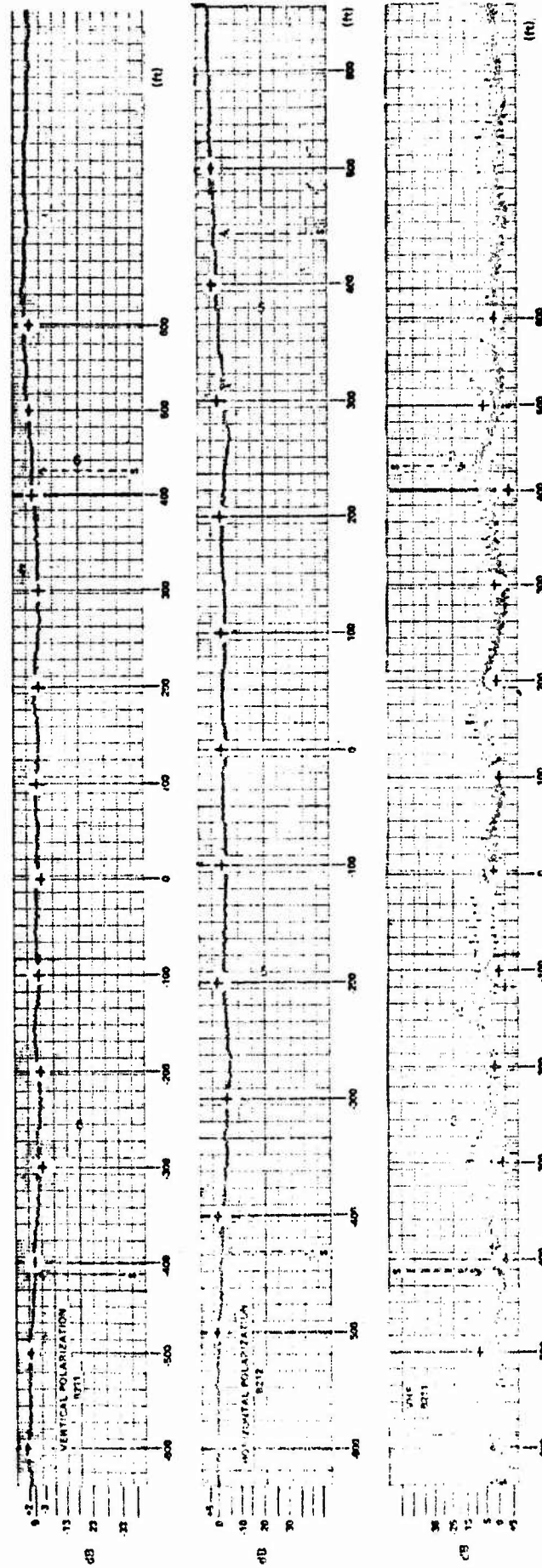


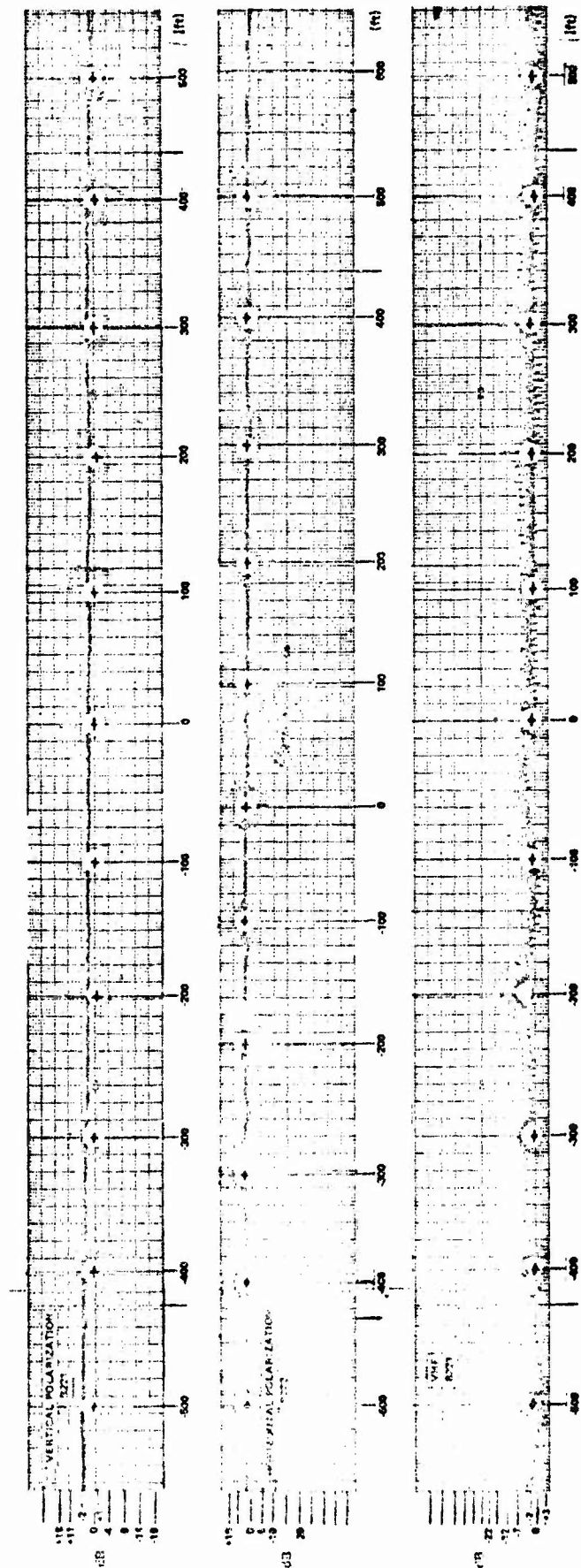
Figure 69 COMPARISON BETWEEN THEORY AND EXPERIMENT, RELATIVE SIGNAL STRENGTH vs DISTANCE FROM TEST CENTERLINE, RUNS B131 AND B132; $d_1 = 650$ FT, $d_2 \approx 4200$ FT, ALTITUDE ≈ 400 FT



+ DENOTES THEORETICAL RESULTS

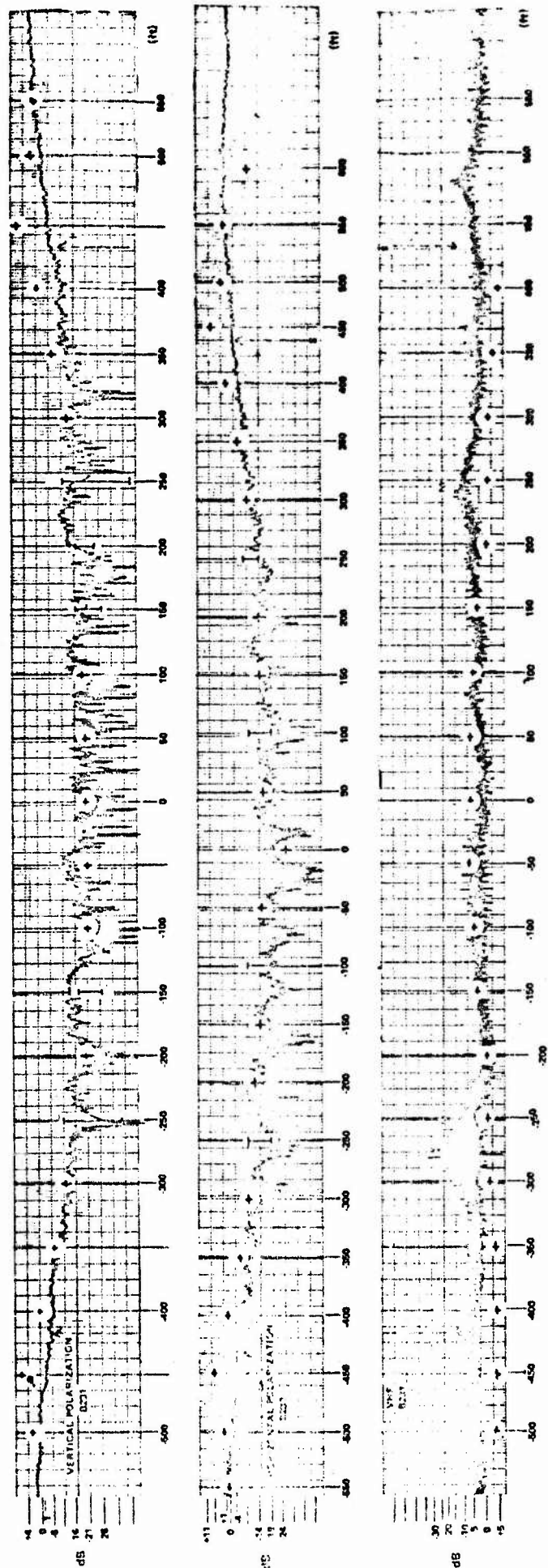
Preceding page blank

Figure 70 COMPARISON BETWEEN THEORY
AND EXPERIMENT, RELATIVE
SIGNAL STRENGTH vs. DISTANCE
FROM TEST CENTERLINE, RUNS
B211 AND B212; $d_1 = 650$ FT,
 $d_2 \approx 8500$ FT, ALTITUDE ≈ 1150 FT



Preceding page blank

Figure 71 COMPARISON BETWEEN THEORY AND
EXPERIMENT, RELATIVE SIGNAL
STRENGTH vs. DISTANCE FROM TEST
CENTERLINE, RUNS B221 AND B222;
 $d_1 = 650$ FT, $d_2 = 8500$ FT,
ALTITUDE ≈ 1650 FT



• DE NOTES THEORETICAL RESULTS

Preceding page blank

Figure 72 COMPARISON BETWEEN THEORY AND EXPERIMENT, RELATIVE SIGNAL STRENGTH vs. DISTANCE FROM TEST CENTERLINE, RUNS B231 AND B232; $d_1 = 650$ FT., $d_2 = 8500$ FT. ALTITUDE ≈ 8500 FT.

Runs B121 and B122 (Figure 68) were for an altitude of 950 feet; good agreement was obtained for all recorded signals.

The next set of traverses was at an altitude of 400 feet. Runs B131 and B132 are shown in Figure 69. The S-band predictions agree reasonably well with recorded data. It is noted, however, that not every peak or null has been predicted. This may be partially due to the fact that the observation (geometric) plane range changed linearly because of the oblique flight path. The theoretical predictions were of necessity obtained for a set of discrete observation planes. Because of the relatively short wavelength (10 cm) it is expected that interference effects (superposition of incident and scattered fields) will be sensitive to small changes in the observation point. To illustrate this, Figures 73, 74 and 75 show the variation in signal level as a function of range (from the center of the obstruction) for the three orientations of the rectangular building. It is noted that the location of minima and maxima is dependent upon range. Other factors, such as the deviation of the building from the theoretical model, could possibly account for minor discrepancies.

The VHF signal shown in the Figure 69 (Run B131) shows the scalloped effect seen on previous data. The average level appears to be about 10 dB lower than expected (for the incoming flight). The reference level of 0 dB was taken as the average signal level reached on the right side of the recording (at the end of the run). The gradual change in level occurring as the helicopter flew its traverse was also noted during tests with the cylinder and sphere. This could possibly be due either to the pattern of the VHF monopole mounted on the underside of the helicopter or to ground effects.

Flight test and theoretical data for the second range (Figure 70) are shown in Figures 70, 71 and 72. At an altitude of about 1160 feet (Figure 70), good agreement is obtained for all signals recorded. Runs B221 and B222, shown in Figure 71, were performed at an altitude of 1650 feet, well above the top of the shadow. Recognizing that the 0 dB reference level for the vertically polarized S-band signal should have been set slightly higher, good agreement is evident. The VHF signal exhibited scalloping during the incoming phase of the flight but agreement in the right half of the recording is excellent.

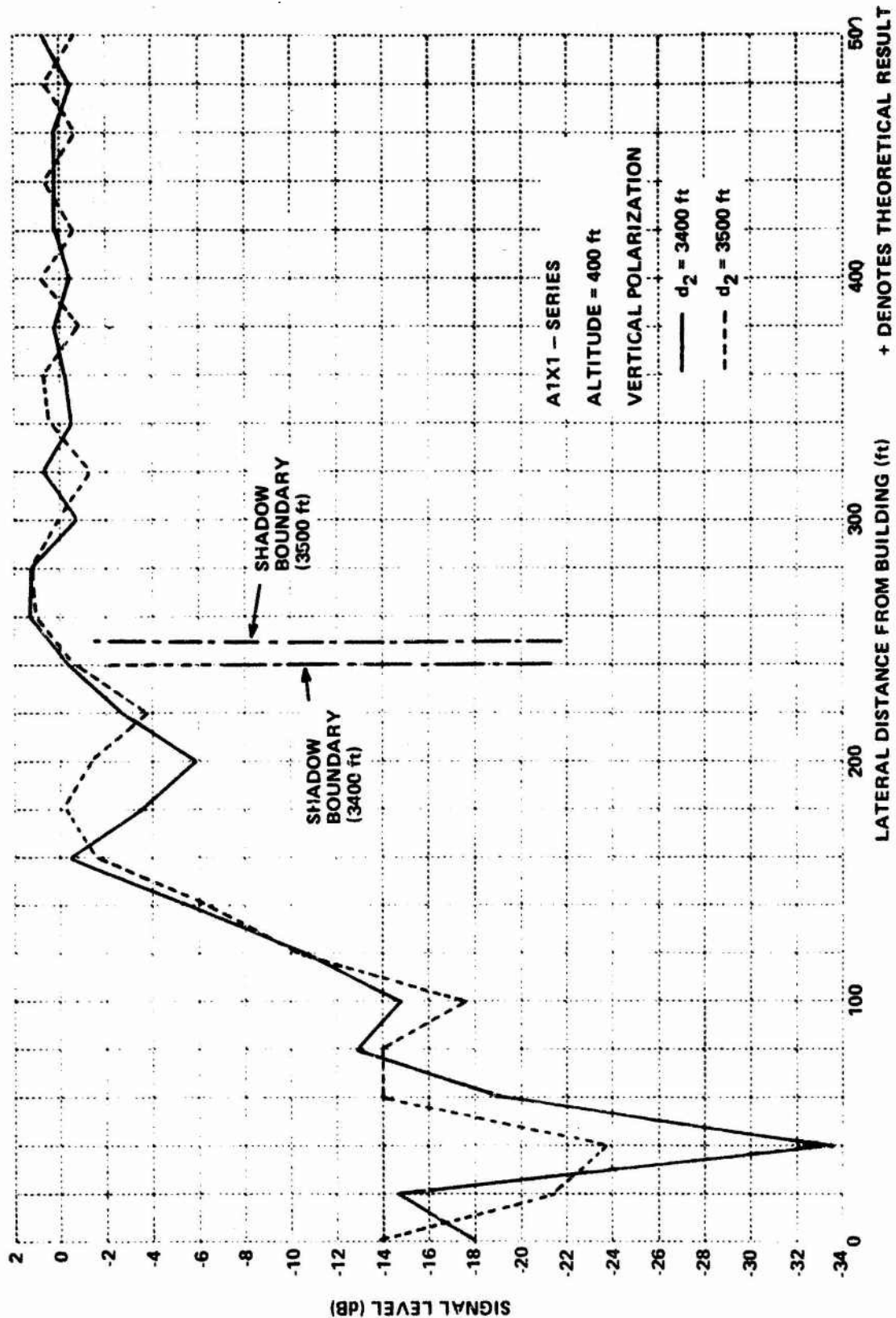


Figure 74 LEVEL VARIATION AS A FUNCTION OF RANGE, A1X1-SERIES

Figure 72 gives results for an altitude of 650 feet, where flight into the obstruction shadow occurred (Runs B231 and B232). For both the vertically and horizontally polarized signals, agreement between the experimental results and theoretical predictions is quite good except in the region just outside the shadow boundaries. A peak in the signal level is predicted whereas the measured signal decreased monotonically resulting in about a 10 dB difference between the measured and the predicted signal levels in this region.

The predicted signal level peak arises from the Q-factor (see equation 19, Section 2.3.2). At large distances between source and obstruction, the obstruction is illuminated by a nearly planar phase front giving rise to focusing in the direction of a line from the source to the center of the edge. The reason that the peaks did not appear in the flight test may be due to several factors. For the particular obstacle orientation and aircraft altitude employed during those runs, the theoretical model should provide a good representation. Because agreement between theory and experiment is very good for runs which do not intersect the shadow boundary, it may be that the formulation utilized in the region around the shadow boundary (and to connect the GDT theories on both sides of the shadow boundary) is incomplete. Further investigations would be required to establish the cause of this discrepancy.

The predicted and measured VHF signal levels agree within the central portion of the shadow region but from about ± 300 feet "outward" the measured signal is 5 to 8 dB lower than expected. This difference is probably due to ground effects and/or a deviation of the airborne antenna pattern from omnidirectional.

3.4.1.2 Arbitrary Angle View (A-Series)

3.4.1.2.1 Description of Experimental Layout

Figure 76 shows both plan and elevation views of the experimental configuration for the A-series tests. Relevant distances and dimensions are noted on the figure. The plan view was plotted using the computer program developed on this project.

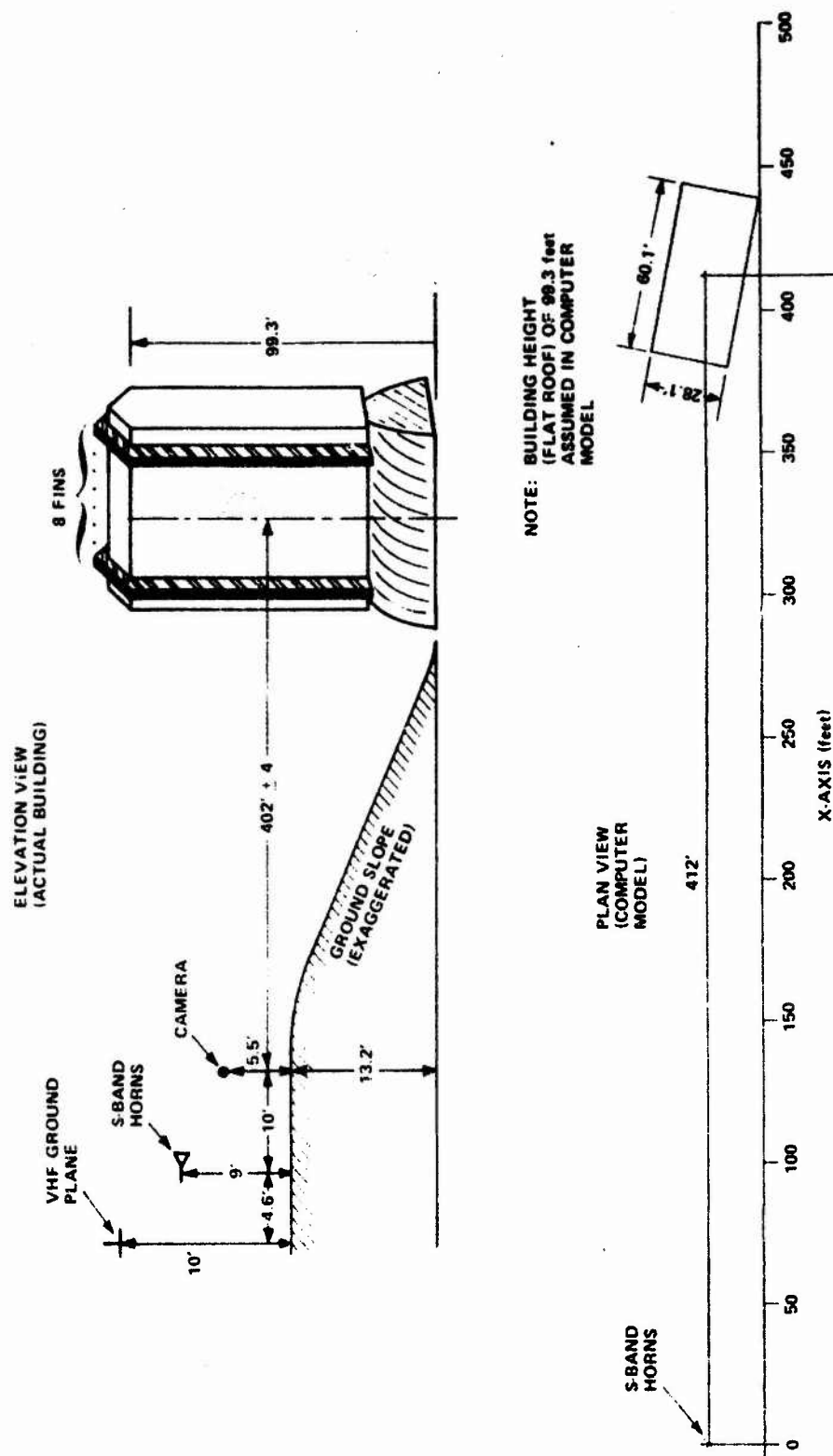


Figure 76 EXPERIMENTAL LAYOUT FOR A-SERIES

3.4.1.2.2 Scope of Tests Performed

Table 4 describes the tests performed at this obstacle orientation. The actual flight path was not perpendicular to the line extended between the ground terminal and the obstruction; thus, the distance to the observation plane varied linearly during the test runs. The consequences of this are discussed in detail in Section 3.4.1.1.

Figures 77 through 82 show an overview of the tests performed. Data corresponding to maximum and minimum distance of the observation plane from the obstacle are shown along with the flight path altitudes associated with a given test number. The initial and final altitudes indicated are those reported by the pilot.

When analyzing the film record for this series, the vertical center line of the front face of the building was arbitrarily established as the zero distance reference for the horizontal axis (abscissa). The computer runs, however, employed the center of the projection of the obstacle as the reference. For correspondence, the theoretical data was shifted 50 feet to the left for the closer range and 110 feet to the left for the farther range. The abscissa for the plots has been shifted to correspond to the data records.

Also denoted on Figure 77 are important reference lines for the building. These are labeled a, b, c, and d and correspond to identically labeled lines on the data recordings.

3.4.1.2.3 Experimental and Theoretical Data Comparison (A-Series Tests)

Flight test and theoretical data for the A-series tests are shown in Figures 83 through 88. The horizontal and vertical extent of the data "points" show the uncertainty in signal level due to possible aircraft altitude and lateral position variations.

For Runs A111 and A112, the helicopter altitude was 1500 feet, which placed the flight path above the obstruction shadow. The chosen plotting scale utilized for computer predictions inadvertently limited the altitude at

Table IV
RECTANGULAR OBSTRUCTION, A-SERIES
SCOPE OF TESTS PERFORMED

A. RANGE FROM OBSTACLE: 3300 TO 3850 ft¹
HEIGHT OF PROJECTION OF OBSTACLE TOP:^{*2} 756.3 ft

TEST NUMBER	AVERAGE** ALTITUDE (ft AGL)	S-BAND POLARIZATION (f = 3006 MHz)	VHF POLARIZATION (f = 123.4 MHz)	RESULTS SHOWN IN FIGURE
A111	1500	V	V	83
A112		H	V	
A121	900	V	V	84
A122		H	V	
A131	400	V	V	85
A132		H	V	

B. RANGE FROM OBSTACLE: 6850 TO 7700 ft¹
HEIGHT OF PROJECTION OF OBSTACLE TOP:^{*3} 1460.4 ft

TEST NUMBER	AVERAGE** ALTITUDE (ft AGL)	S-BAND POLARIZATION (f = 3006 MHz)	VHF POLARIZATION (f = 123.4 MHz)	RESULTS SHOWN IN FIGURE
A211	2200	V	V	86
A212		H	V	
A221	1000	V	V	87
A222		H	V	
A231	500	V	V	88
A232		H	V	

* REFERENCED TO S-BAND HORNS' POSITION

** ± 30 ft; ALTIMETER SET TO ZERO AT INSTRUMENTATION SITE.

1. RESULT OF OBLIQUE FLIGHT PATH
2. CALCULATED AT 3300 ft
3. CALCULATED AT 6850 ft

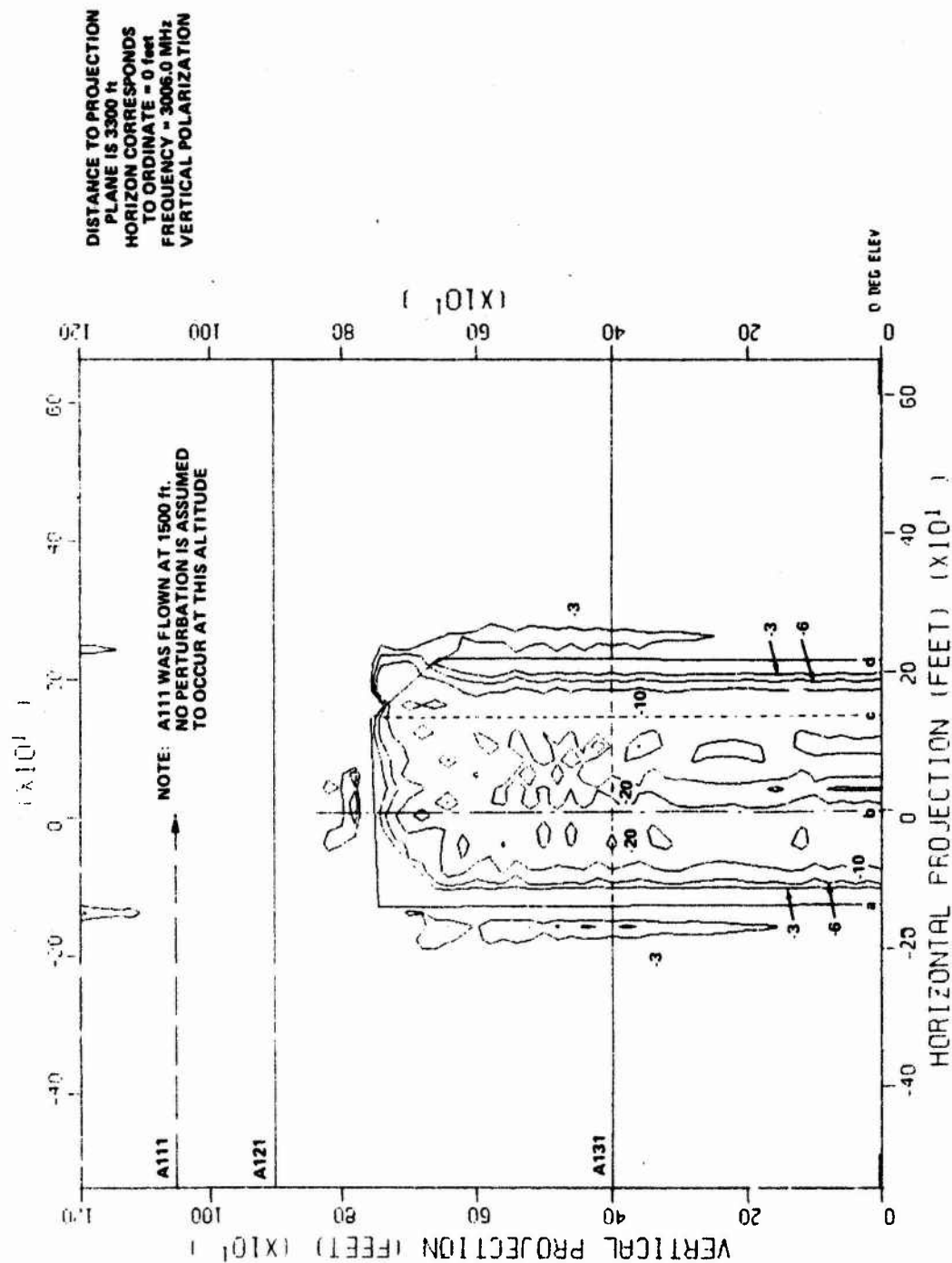


Figure 77 FLIGHT PATHS, A1X1-SERIES, S-BAND, VERTICAL POLARIZATION

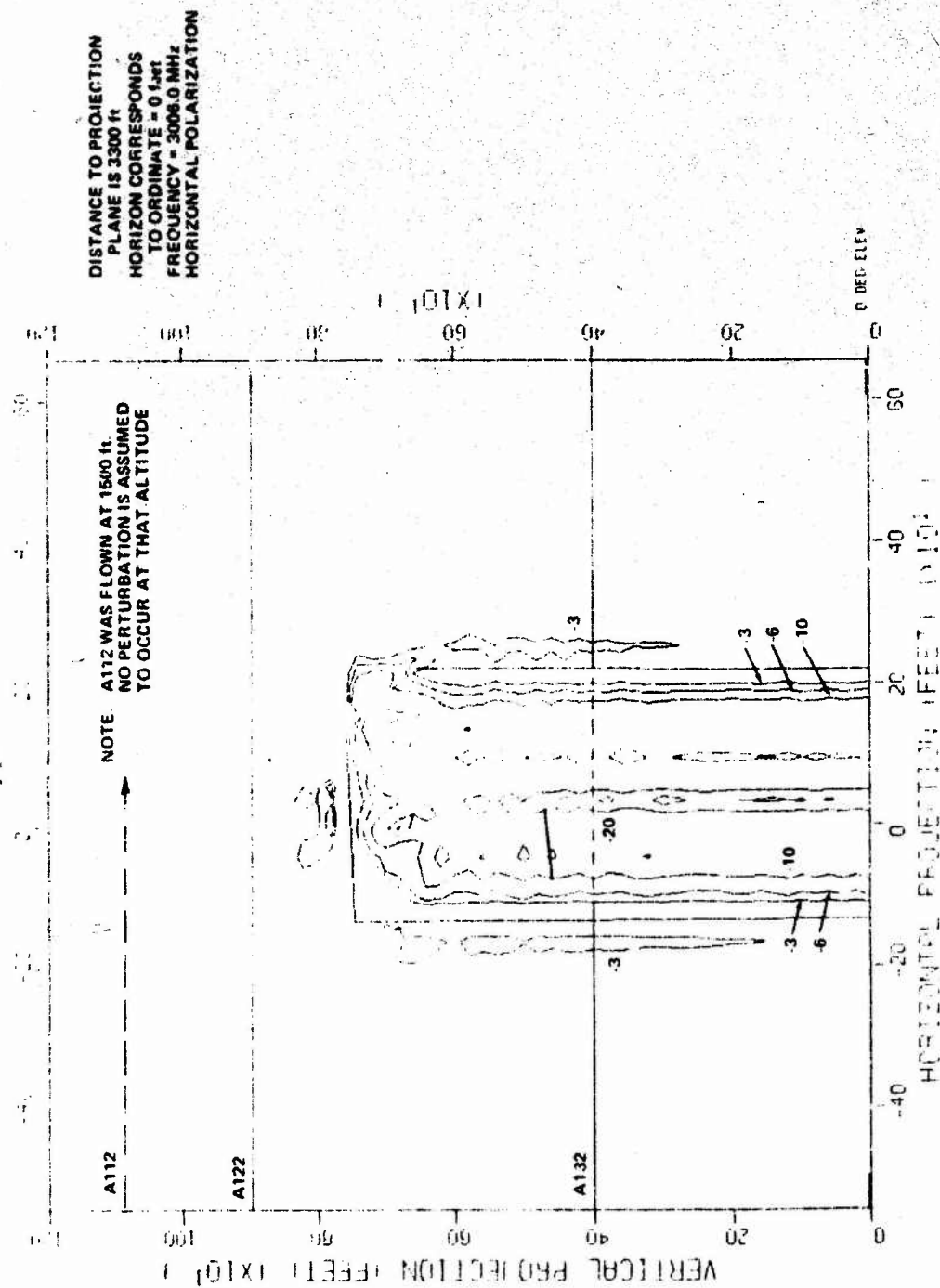


Figure 78 FLIGHT PATHS, A1X2-SERIES, S-BAND, HORIZONTAL POLARIZATION

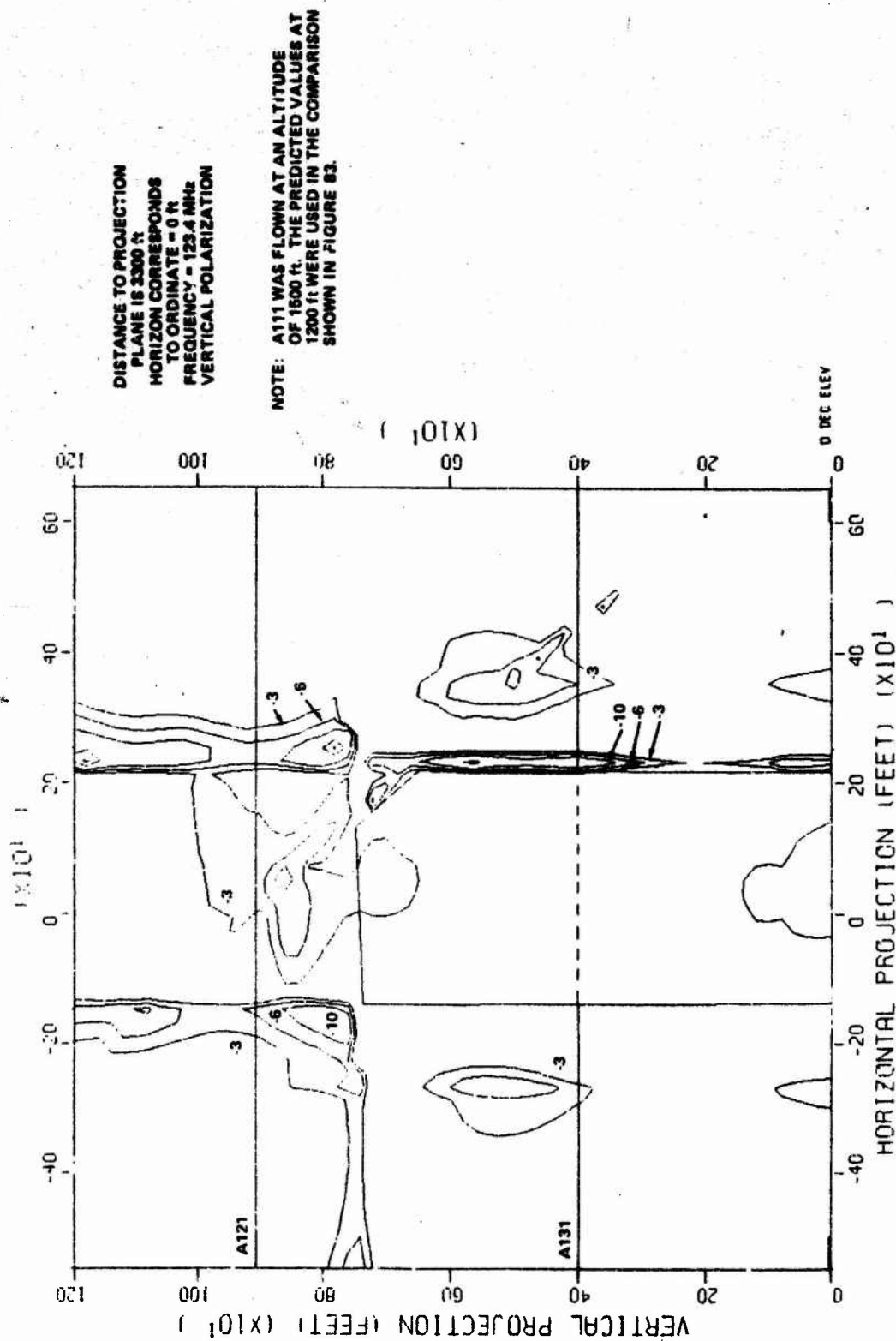


Figure 79 FLIGHT PATHS, A1XY-SERIES, VHF, VERTICAL POLARIZATION

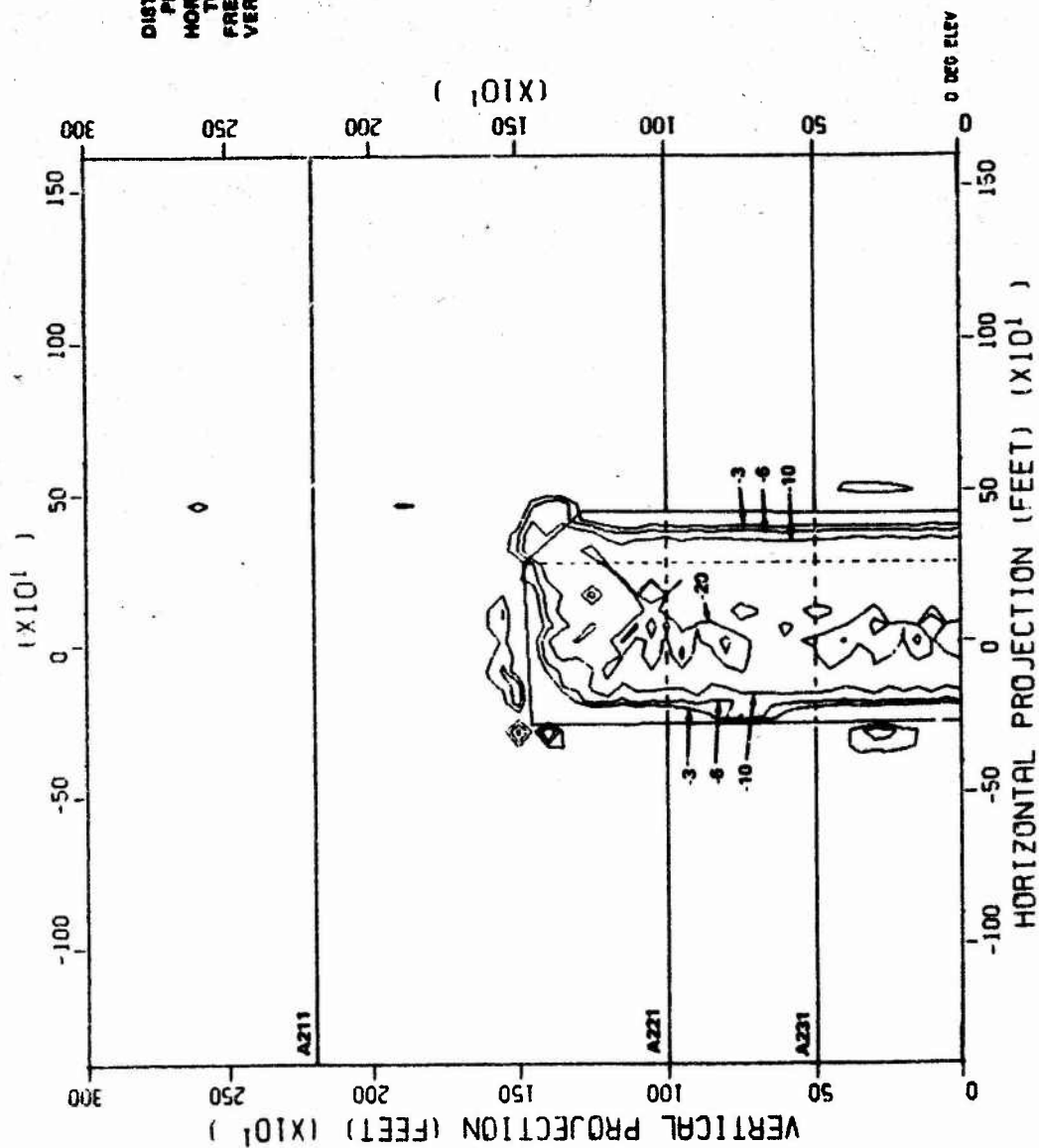
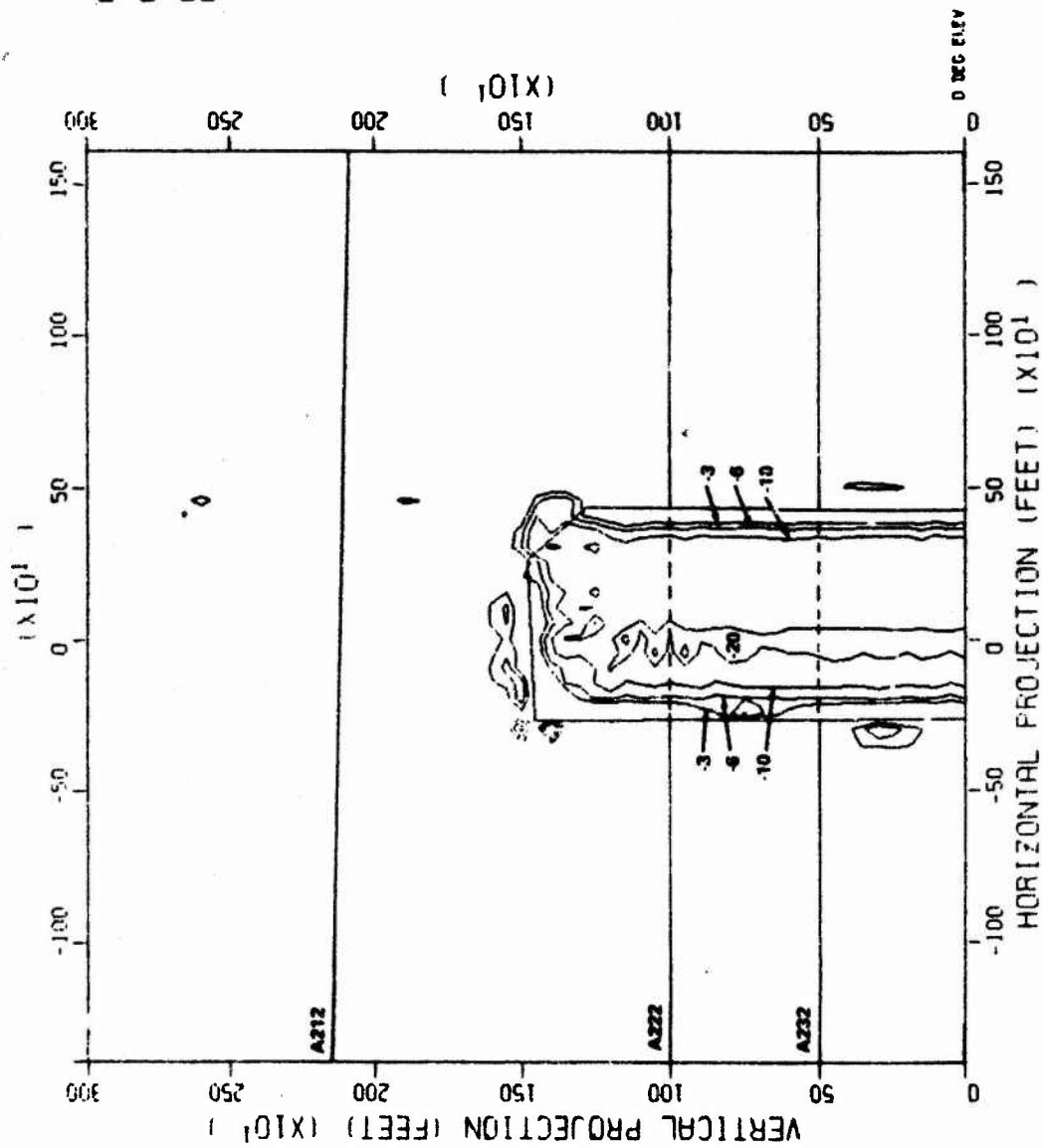


Figure 80 FLIGHT PATHS, A2X1-SERIES, S-BAND, VERTICAL POLARIZATION



DISTANCE TO PROJECTION
PLANE IS 6850 ft
HORIZON CORRESPONDS
TO ORDNATE - 6 feet
FREQUENCY - 3000.0 MHz
HORIZONTAL POLARIZATION

Figure 81 FLIGHT PATHS, A2X2-SERIES, S-BAND, VERTICAL POLARIZATION

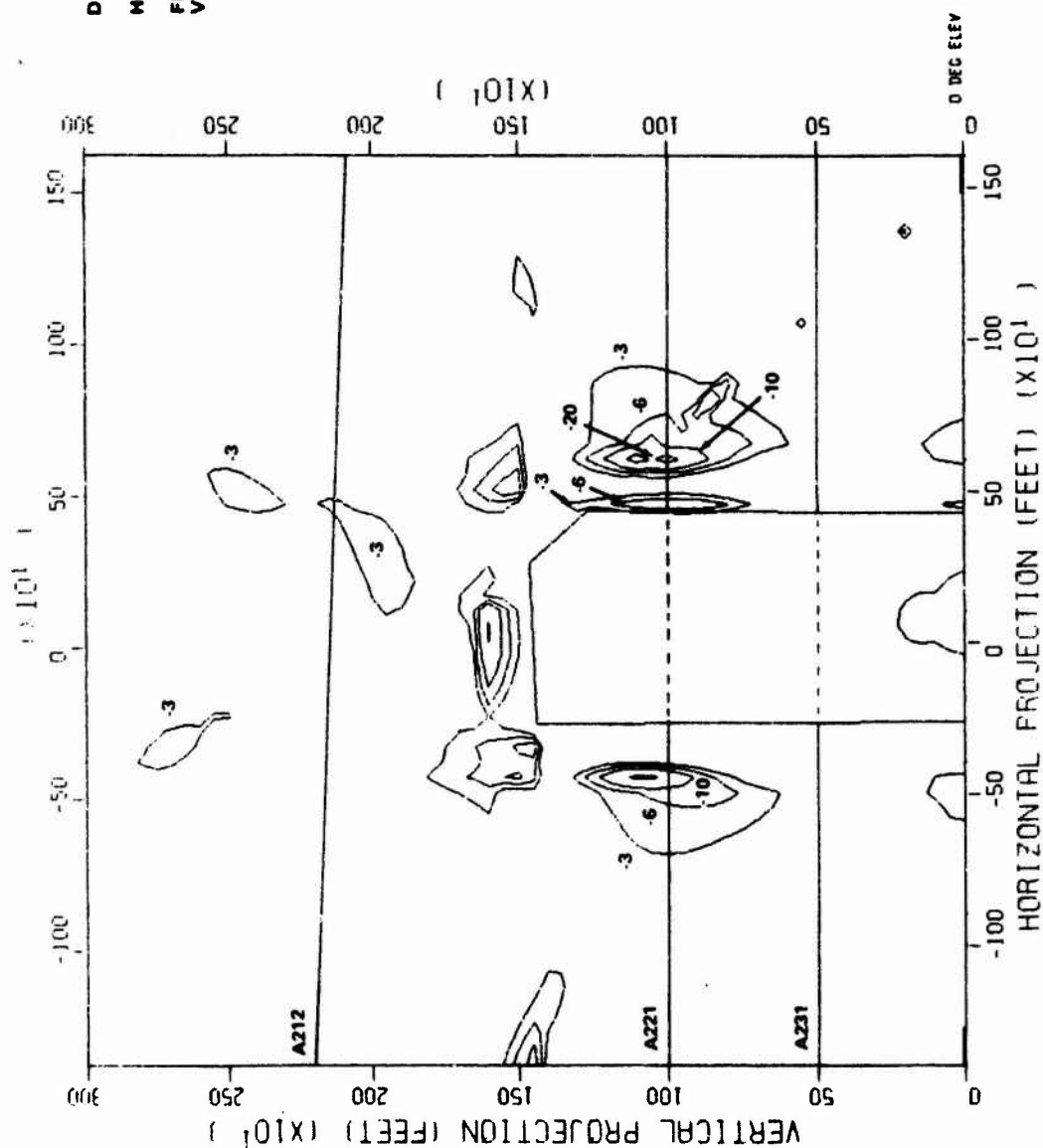


Figure 82 FLIGHT PATHS, A2XY-SERIES, VHF, VERTICAL POLARIZATION

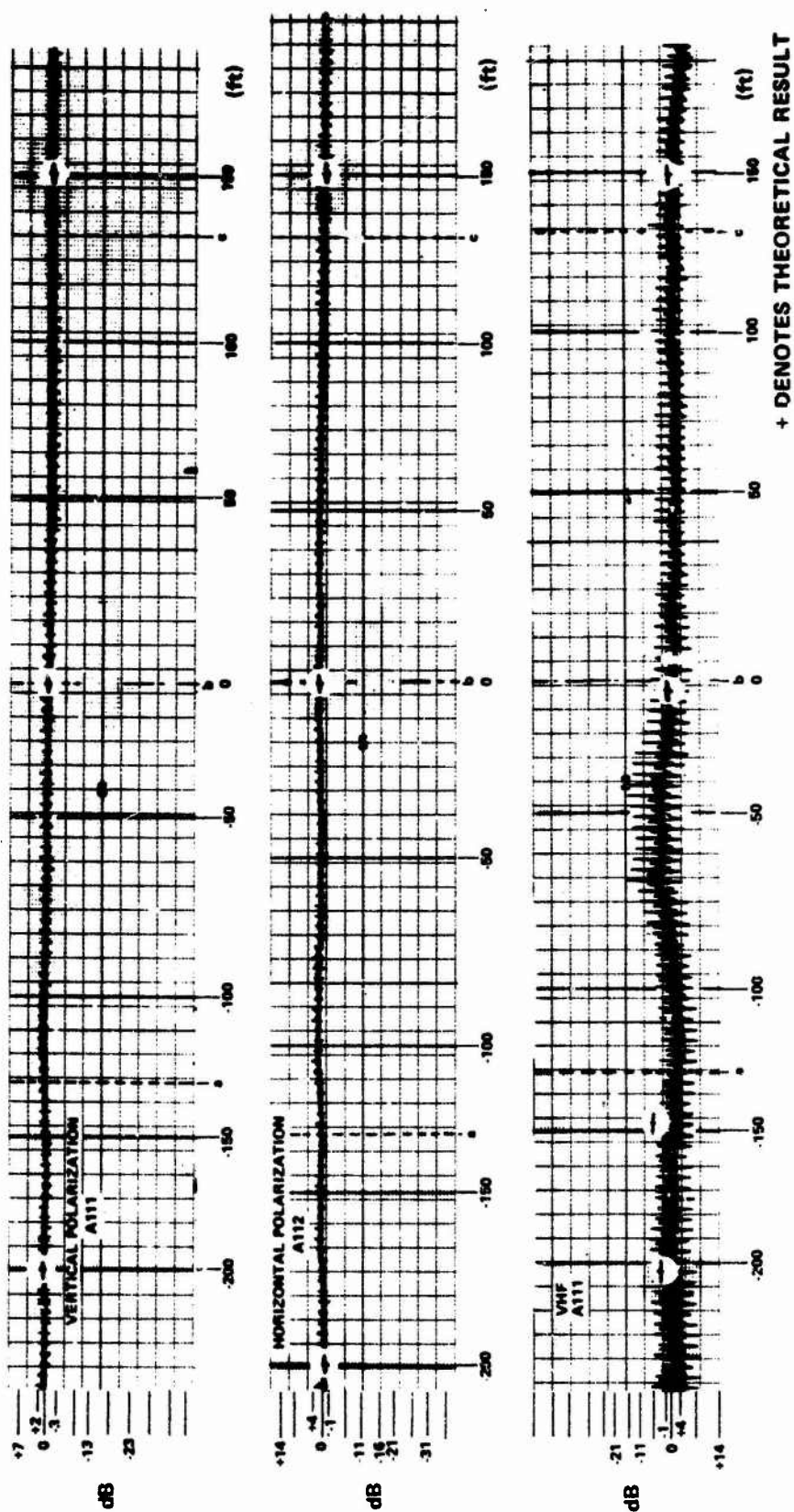


Figure 83 COMPARISON BETWEEN THEORY AND EXPERIMENT, RELATIVE SIGNAL STRENGTH vs DISTANCE FROM TEST CENTERLINE, RUNS A111 AND A112;
 $d_1 = 412$ FT, $d_2 \approx 3300$ FT, ALTITUDE ≈ 1500 FT

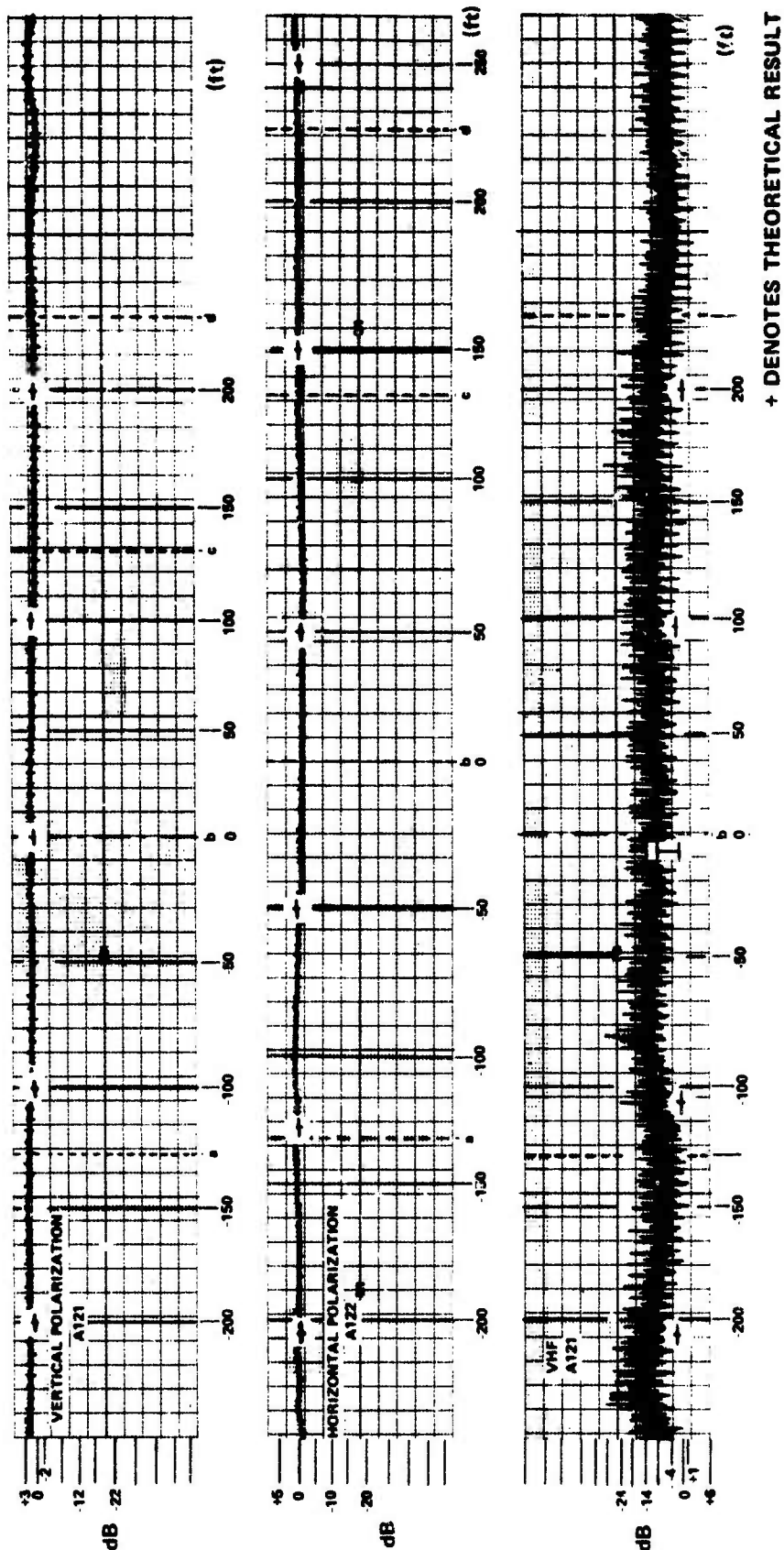


Figure 84 COMPARISON BETWEEN THEORY AND EXPERIMENT, RELATIVE SIGNAL STRENGTH
 vs DISTANCE FROM TEST CENTERLINE, RUNS A121 AND A122; $d_1 = 412$ FT,
 $d_2 \approx 3300$ FT, ALTITUDE ≈ 900 FT

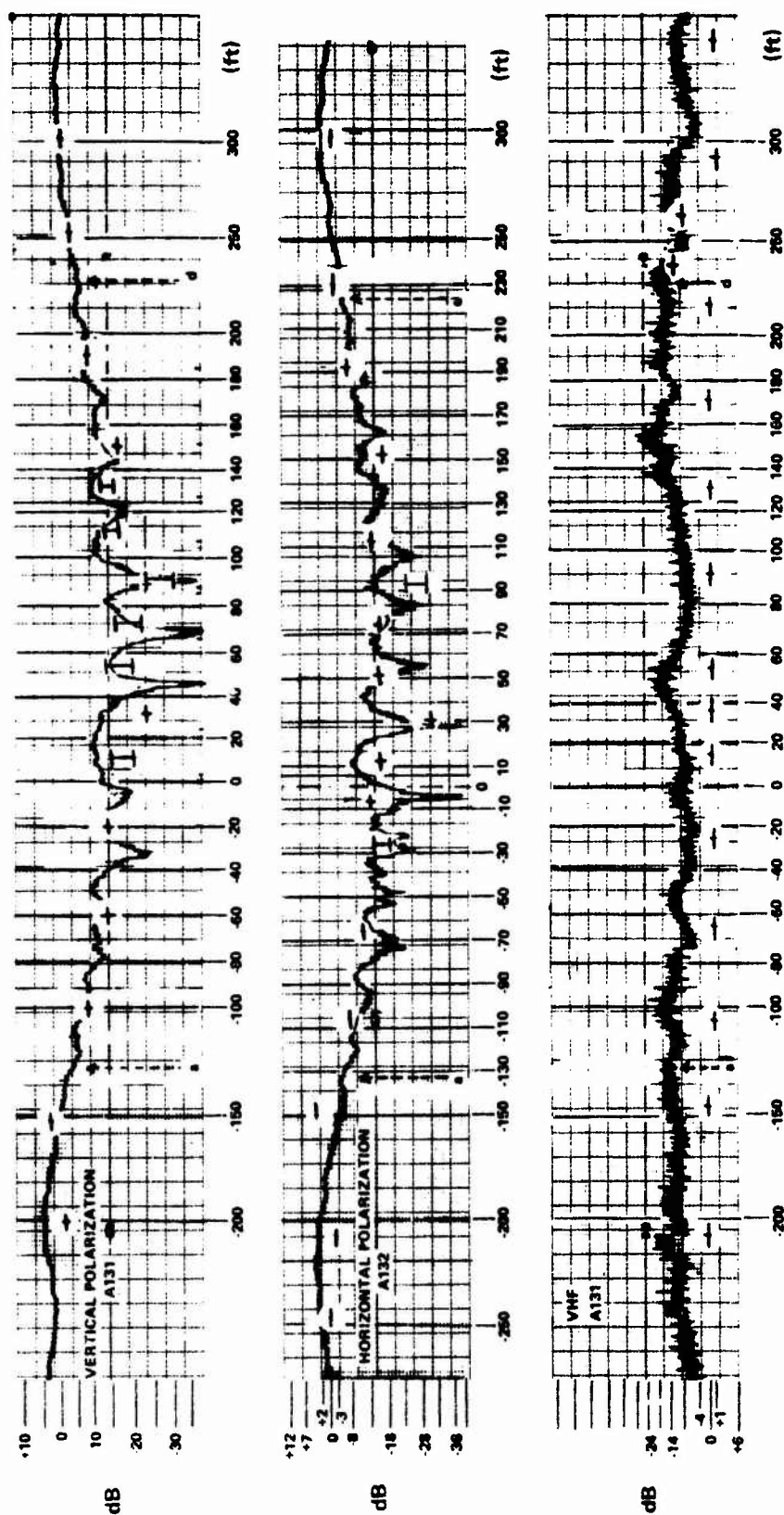


Figure 85 COMPARISON BETWEEN THEORY AND EXPERIMENT, RELATIVE SIGNAL STRENGTH
vs DISTANCE FROM TEST CENTERLINE, RUNS A131 AND A132; $d_1 = 412$ FT,
 $d_2 \approx 3300$ FT, ALTITUDE ≈ 400 FT

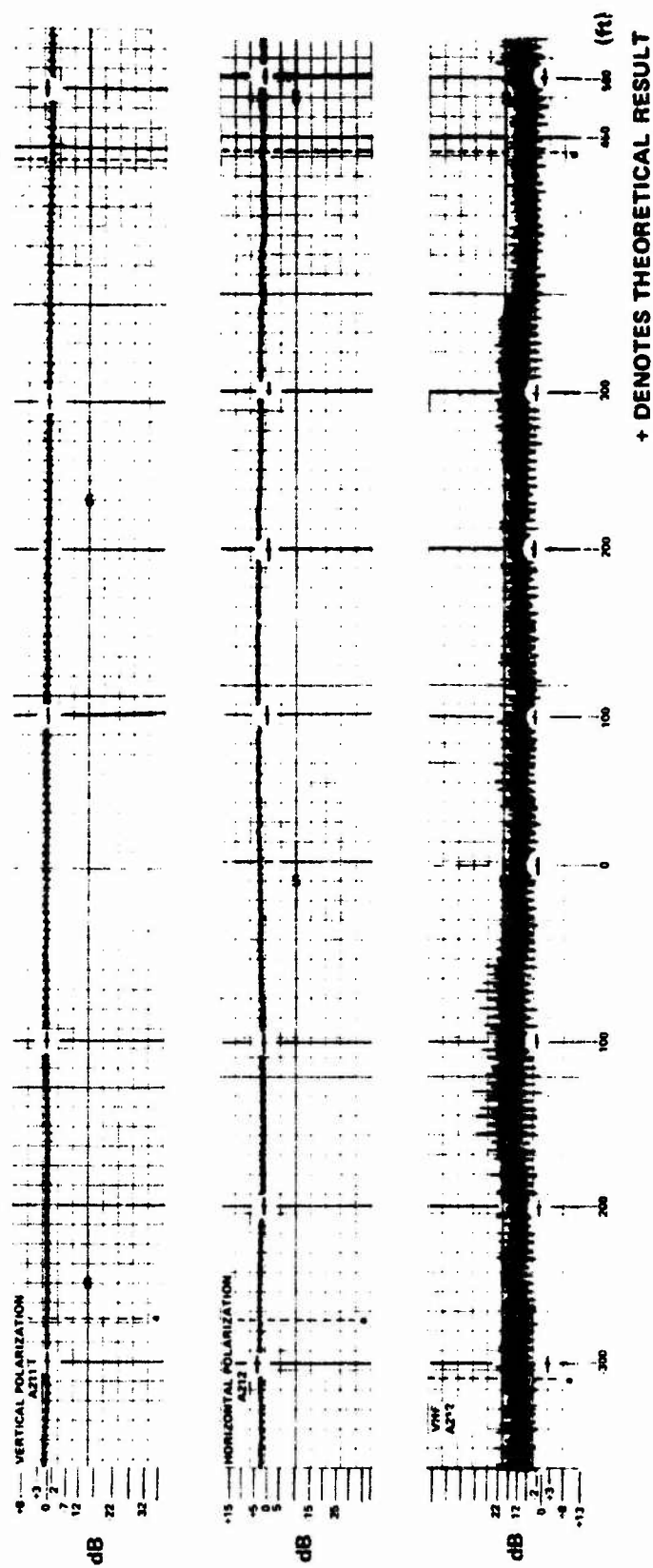


Figure 86 COMPARISON BETWEEN THEORY AND EXPERIMENT, RELATIVE SIGNAL STRENGTH
vs DISTANCE FROM TEST CENTERLINE, RUNS A211 AND A212; $d_1 = 412$ FT,
 $d_2 \approx 6850$ FT, ALTITUDE ≈ 2200 FT

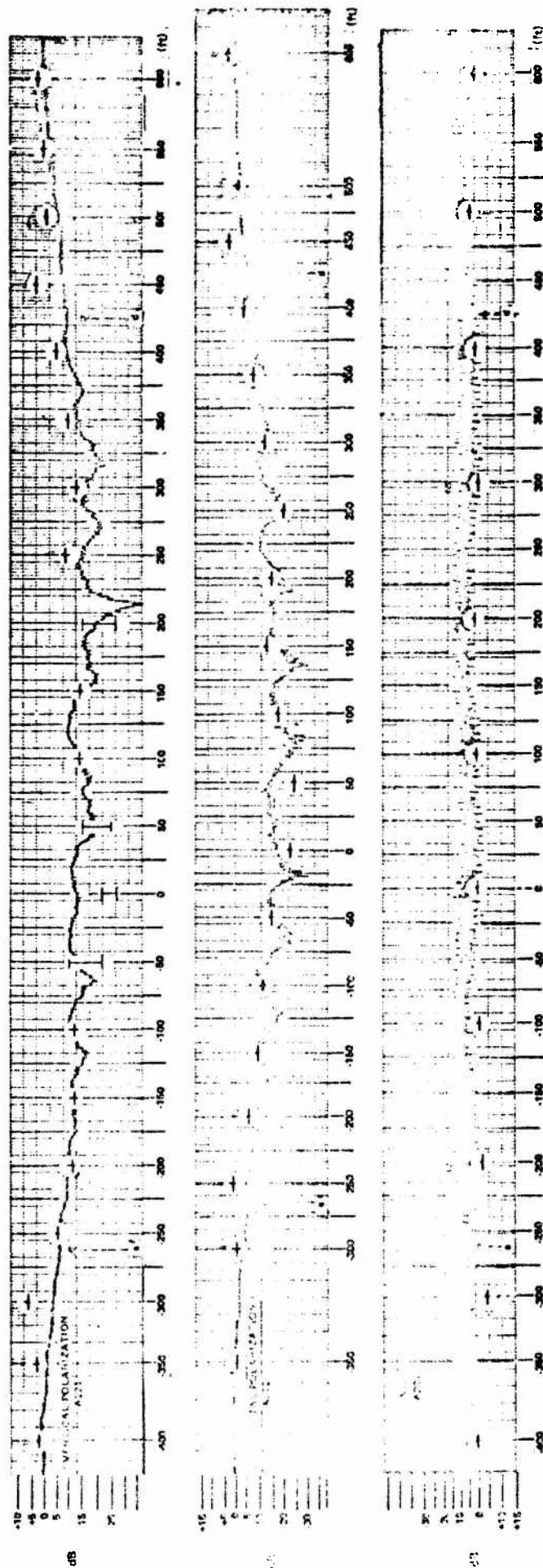
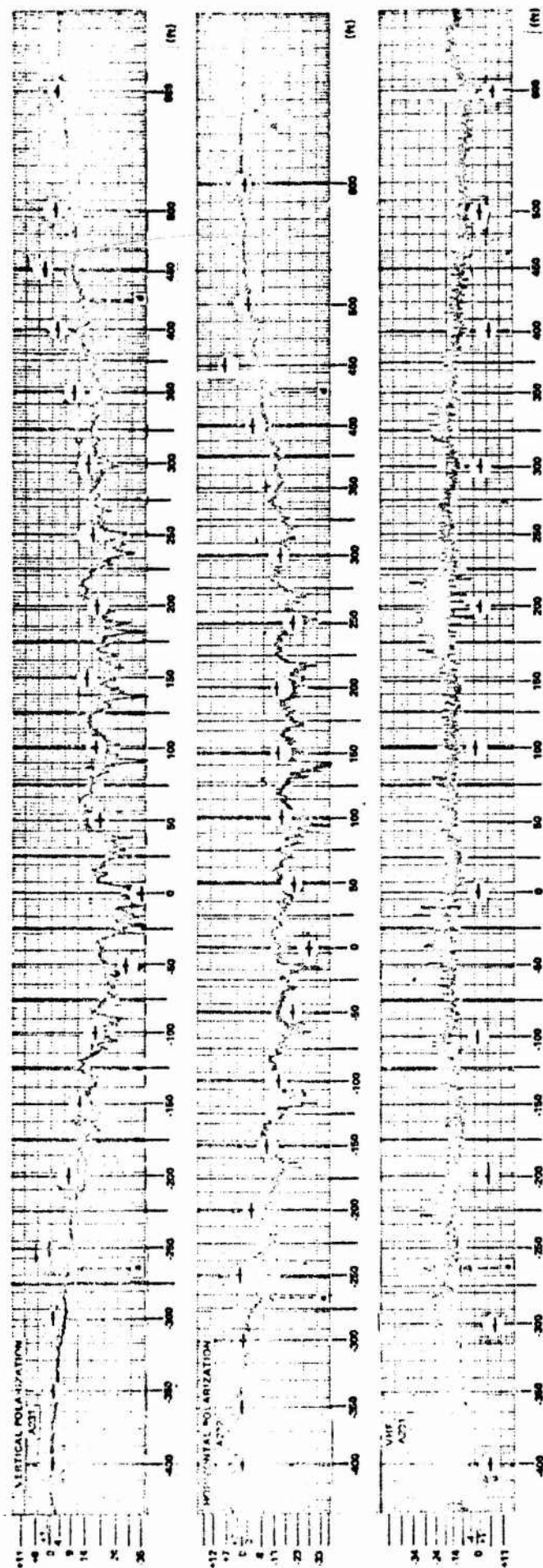


Figure 87 COMPARISON BETWEEN THEORY AND EXPERIMENT, RELATIVE SIGNAL STRENGTH vs. DISTANCE FROM TEST CENTERLINE, RUNS A221 AND A222.
 $d_1 = 412$ FT, $d_2 = 6350$ FT,
 ALTITUDE ≈ 1000 FT



+ DENOTES THEORETICAL RESULTS

Figure 88 COMPARISON BETWEEN THEORY AND EXPERIMENT, RELATIVE SIGNAL STRENGTH vs. DISTANCE FROM TEST CENTERLINE, RUNS A231 AND A232; $d_1 = 412$ FT, $d_2 = 6850$ FT, ALTITUDE ≈ 600 FT

which calculations were made to 1200 feet. Although calculations at 1500 feet were not available, it was felt that the 1200 foot altitude would provide results that would reasonably approximate the true situation. Predictions for all three cases are in good agreement with the experimental results. The VHF signal does, however, exhibit a decrease in level in the region of -50 feet. An additional computer run would have had to be made to see if theory predicts this. It was felt that the expense of doing that was not justified since there is much other data available for VHF comparisons.

Runs A121 and A122 (Figure 84) were performed for an altitude of 900 feet, also above the top of the geometric shadow projection. Agreement between S-band predictions, both for VP and HP is excellent. The VHF signal is lower than predicted by about 5 dB. It is possible that the 0 dB reference level* should have been set "higher" on the recording which would bring the theoretical and experimental data into closer agreement. For the A-series obstacle orientation and flight trajectories, the towers, that possibly caused multipath effects in the B-series tests, are not considered to be significant scatters.

Figure 85 shows results for Runs A131 and A132. The aircraft passed through the geometric shadow of the building on these runs. S-band agreement is quite good. Because of the oblique flight path, it was not expected that every peak or null within the shadow would be predicted from the discrete set of observation planes utilized. For example, in Run A131, at -200 feet, a null is predicted whereas a peak was recorded. The discrepancy is about 7 dB. In Run A132, a similar result is obtained near -200 feet. Also, a peak is predicted at -150 feet which does not appear on the recording.

Good agreement is obtained for the VHF signal if the reference level of the calculated points is raised by about 10 dB. The null that is predicted just outside of line d does not appear on the recording.

* Judged to be where perturbations do not occur in signal level.

Preceding page blank

The next set of figures show results for an observation plane range of approximately 7000 feet. Runs A211 and A212, at an altitude of 2200 feet, provided trajectories over the top of the geometric shadow. S-band agreement is quite good; VHF agreement is good provided the 0 dB reference is moved "upward" one major division, or about 5 dB.

Figures 87 and 88 show results for flight trajectories within the geometric shadow; the helicopter altitudes were 1000 feet and 500 feet, respectively. In Run A221, peaks just outside the shadow boundaries (lines a and d) are predicted for the vertically polarized signal but were not experimentally observed. The same is true for the horizontally polarized signal in Run A222. Otherwise, the predicted S-band signal agrees quite well with experimental results. The VHF predictions are in fairly good agreement with results in most places. A sharp decrease in level is predicted in the region between 600 and 700 feet (see Figure 82). Such a decrease does occur between 550 and 600 feet. It is known that the spatial distribution of the diffraction field is sensitive to the angular orientation of the building and it is probable that the assumed angle is slightly in error.

Figure 88 shows data from Runs A231 and A232 taken at an aircraft altitude of 500 feet. Peaks are predicted near the shadow boundary but do not appear in the experimental data for both VP and HP S-band signals. Agreement is otherwise quite good. For the VHF signal, a shift in the average level brings the results into fairly good agreement.

3.4.1.3 Narrow Face View (N-Series)

3.4.1.3.1 Description of Experimental Layout

Figure 89 shows both plan and elevation views of the experimental configuration for this series of tests. Relevant information is shown.

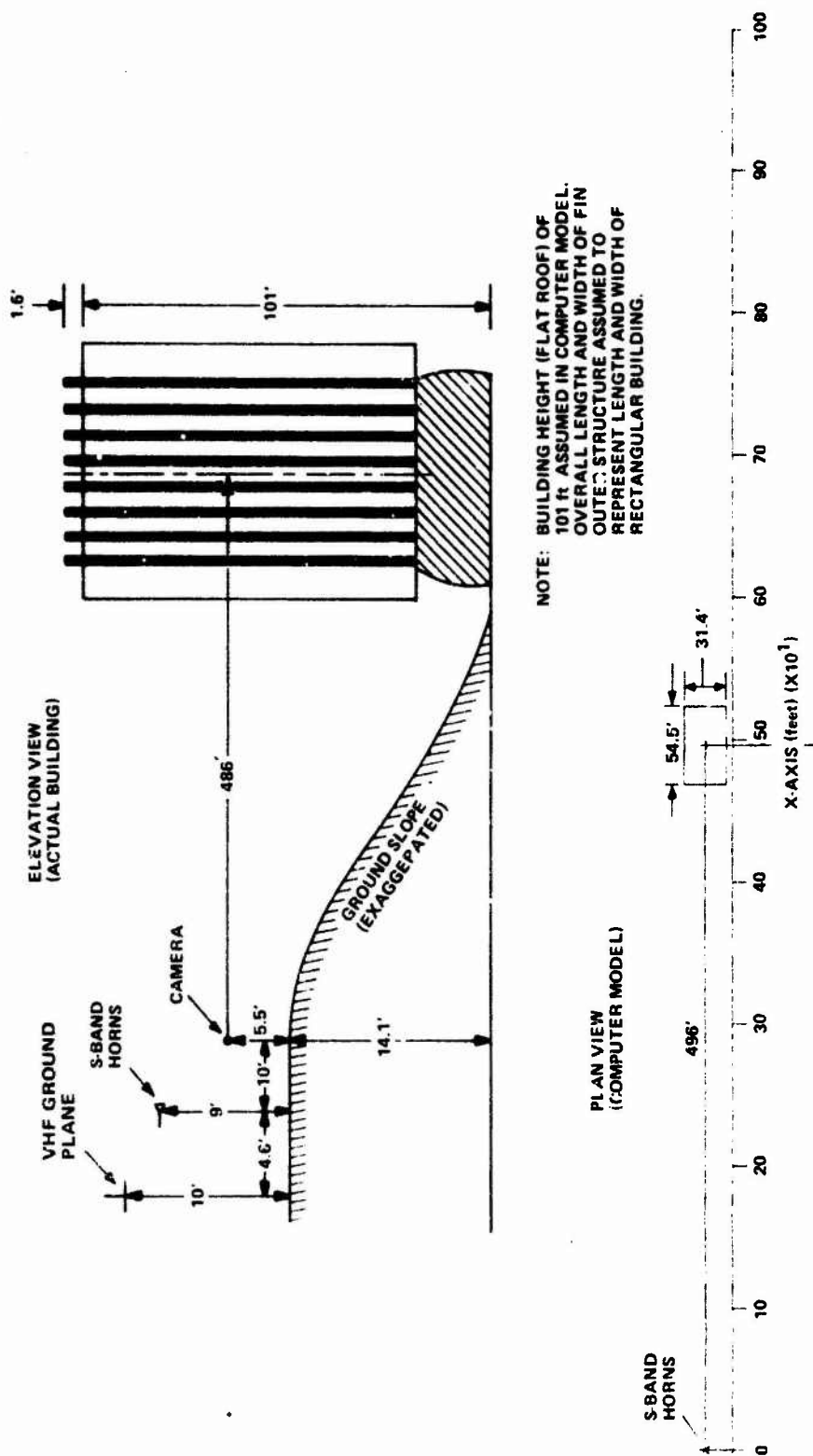


Figure 89 EXPERIMENTAL LAYOUT FOR N-SERIES

3.4.1.3.2 Scope of Tests Performed

Table 5 describes the tests performed for the narrow face series. The flight path was only slightly oblique, thus the change in the observation plane range was not as large as it was for the two previous series.

Figures 90 through 95 show an overview of the tests performed.

3.4.1.3.3 Experimental and Theoretical Data Comparison (N-Series Tests)

Results for the narrow face view series are contained in Figures 96 through 101. Excellent agreement is shown for Runs N111 and N112 for VP, HP, and VHF signals. For Runs N121 and N122, agreement is again excellent. The VHF signal is noted to be asymmetrical, contrary to what is expected for the symmetrical obstacle configuration. The asymmetry is probably due to multipath and/or a non-omnidirectional VHF antenna pattern.

The final set of runs for the closer range is shown in Figure 98. The aircraft altitude of 400 feet provided a trajectory within the shadow of the obstruction. Agreement between the theoretical predictions and the experimental S-band results is quite good. It is noted that peaks in signal level are predicted near the shadow boundaries; as before, the peaks do not appear in the experimental results. The measured VHF signal level exhibited variations during the test; between -200 and -80 feet, and again between 120 and 200 feet. The exact cause of the level changes is not known but may be due to multipath or possibly due to the fins protruding from the building.

Test runs at a distance of approximately 8000 feet between the observation plane and the obstruction are shown in Figures 97, 100 and 101. Figures 93 and 94 show that the trajectories of N211 and N212 pass through very localized contours of -3 to -6 dB decreases in signal level. These points are shown on the figures. The measured data does not, however, show these decreases. The -3 dB contours have a vertical extent of 150 feet,

Table V
RECTANGULAR OBSTRUCTION, N-SERIES
SCOPE OF TESTS PERFORMED

A. RANGE FROM OBSTACLE: 3300 TO 3400 ft¹
HEIGHT OF PROJECTION OF OBSTACLE TOP:^{*2} 633.5 ft

TEST NUMBER	AVERAGE** ALTITUDE (ft AGL)	S-BAND POLARIZATION (f = 3006 MHz)	VHF POLARIZATION (f = 123.4 MHz)	RESULTS SHOWN IN FIGURE
N111	981	V	V	96
N112		H	V	
N121	755	V	V	97
N122		H	V	
N131	400	V	V	98
N132		H	V	

B. RANGE FROM OBSTACLE: 8000 TO 8350 ft¹
HEIGHT OF PROJECTION OF OBSTACLE TOP:^{*3} 1418.3 ft

TEST NUMBER	AVERAGE** ALTITUDE (ft AGL)	S-BAND POLARIZATION (f = 3006 MHz)	VHF POLARIZATION (f = 123.4 MHz)	RESULTS SHOWN IN FIGURE
N211	2200	V	V	99
N212		H	V	
N221	1670	V	V	100
N222		H	V	
N231	888	V	V	101
N232		H	V	

* REFERENCED TO S-BAND HORNS' POSITION

** ± 30 ft; ALTIMETER SET TO ZERO AT INSTRUMENTATION SITE

1. RESULT OF OBLIQUE FLIGHT PATH
2. CALCULATED AT 3300 ft
3. CALCULATED AT 8000 ft

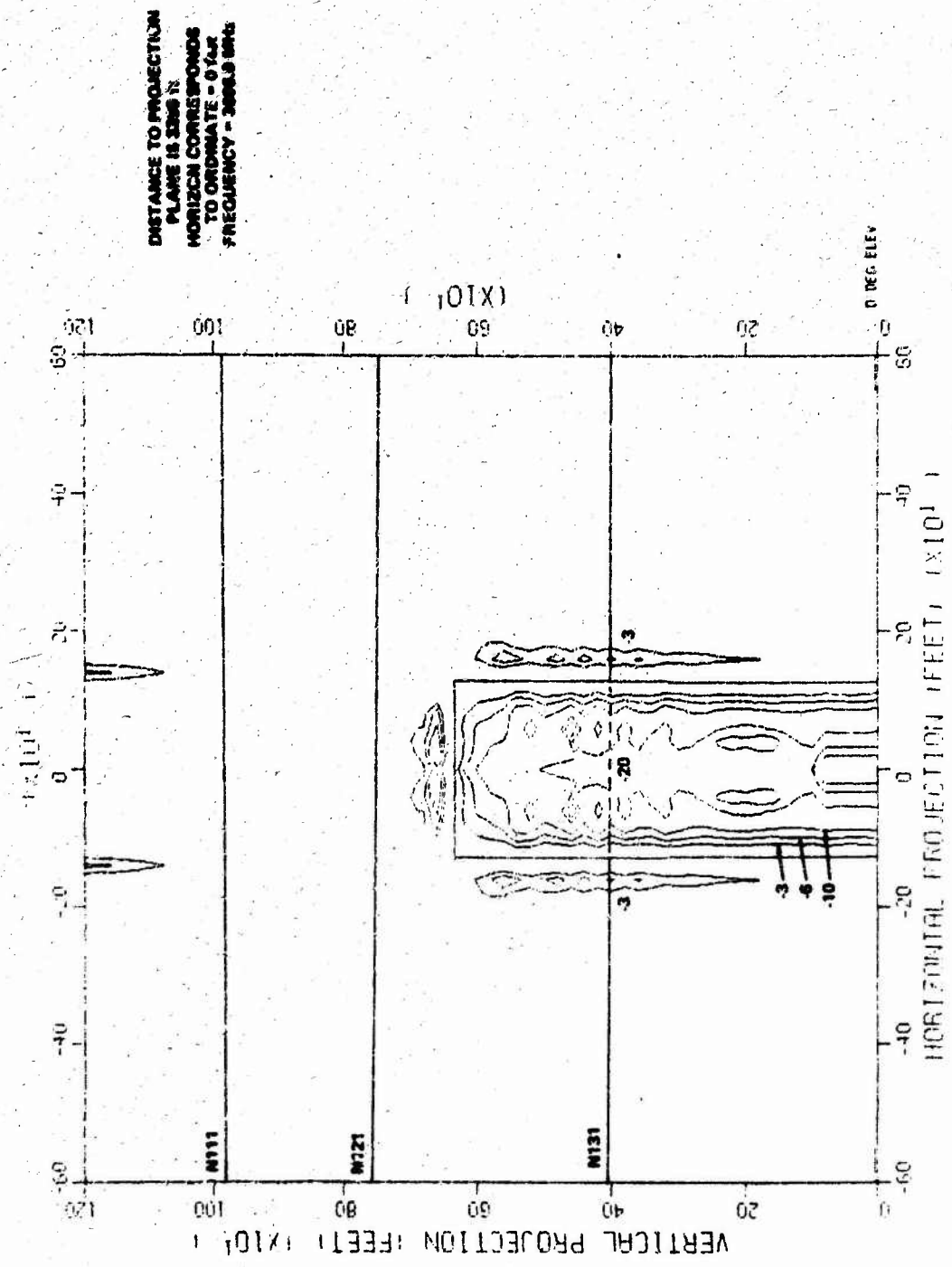


Figure 90 FLIGHT PATHS, N1X1-SERIES, S-BAND, VERTICAL POLARIZATION

147

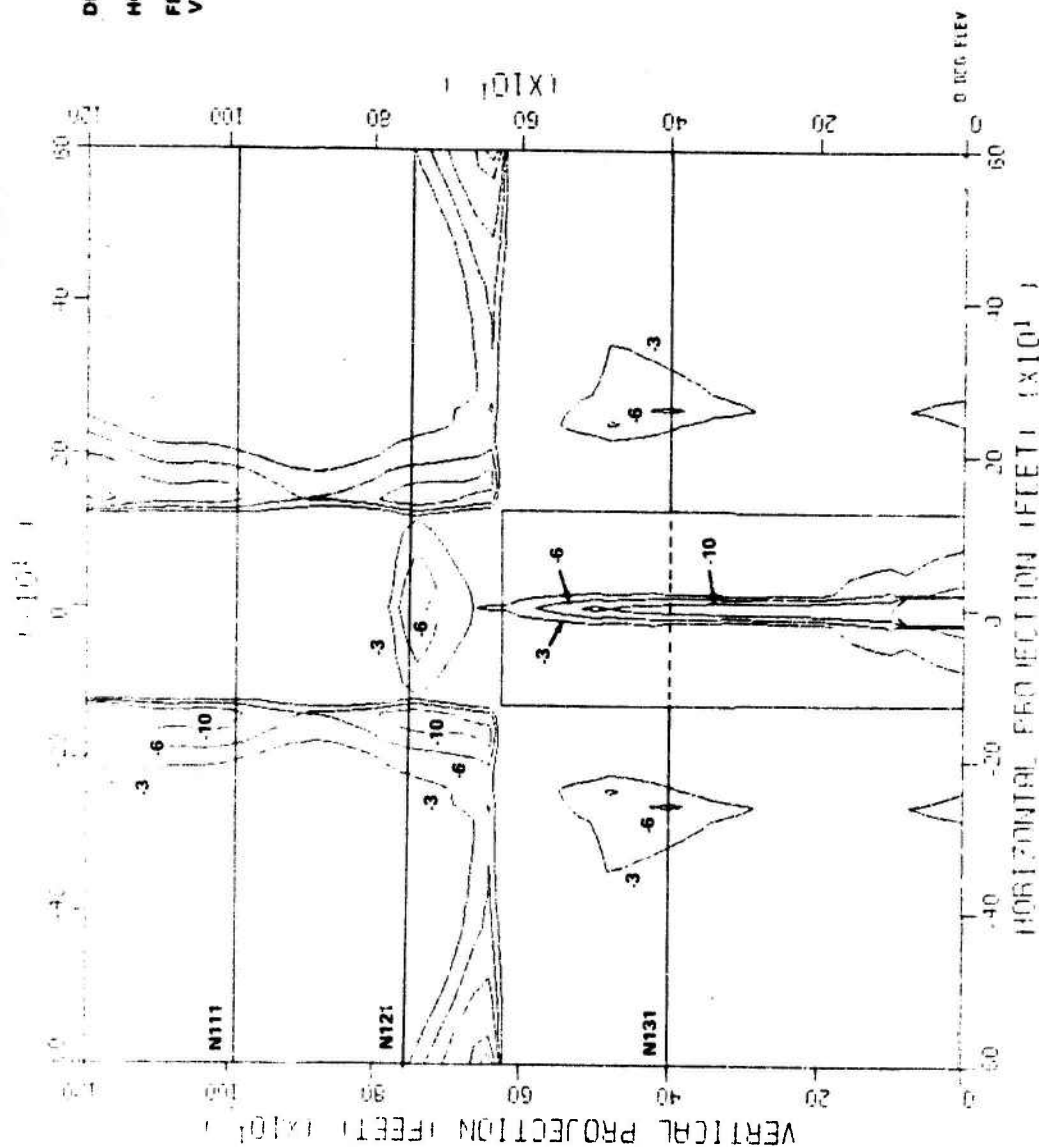


Figure 92 FLIGHT PATHS, N1XY-SERIES, VHF, VERTICAL POLARIZATION

Reproduced from
best available copy.

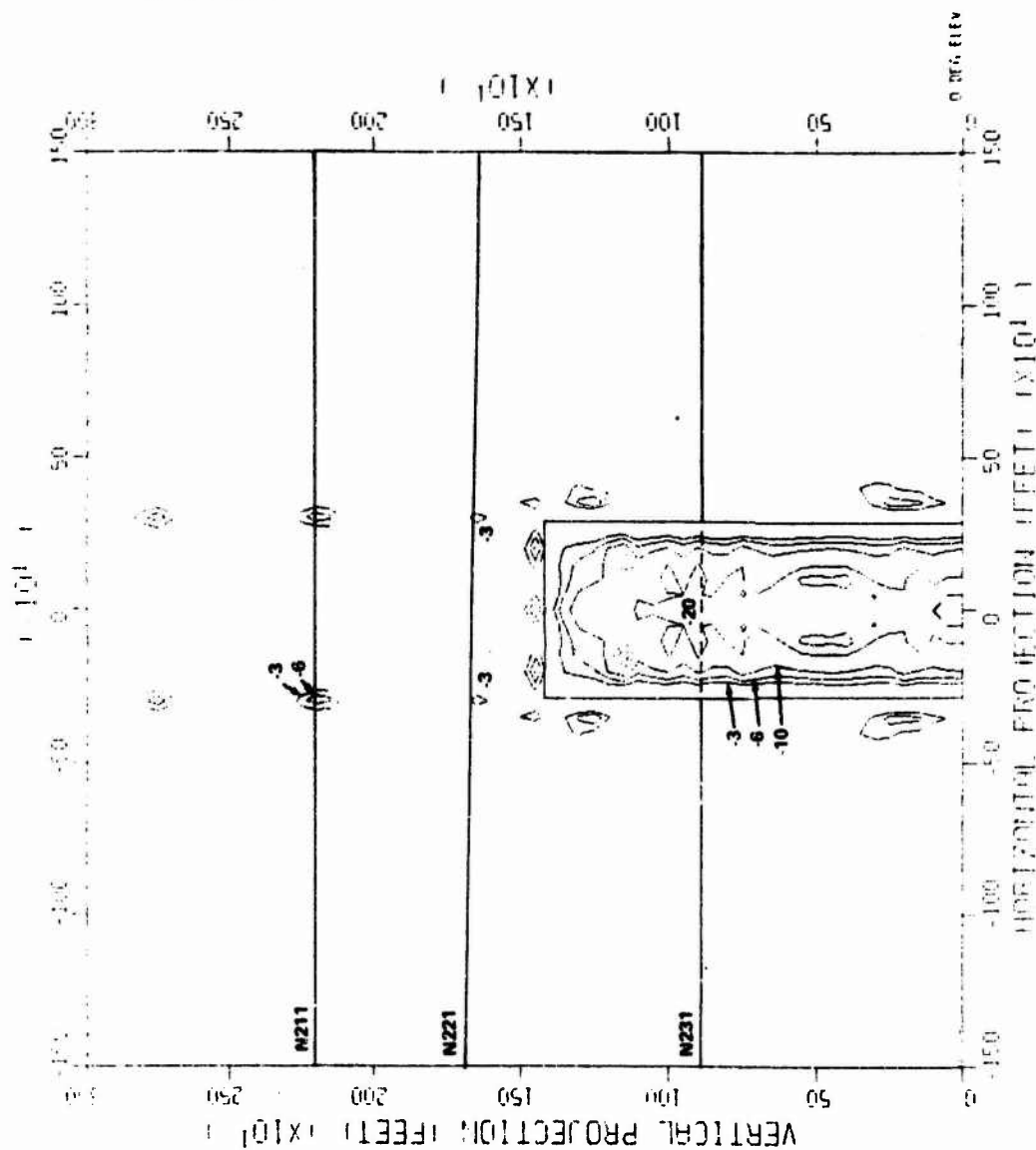


Figure 93 FLIGHT PATHS, N2X1-SERIES, S-BAND, VERTICAL POLARIZATION

Reproduced from
 best available copy.

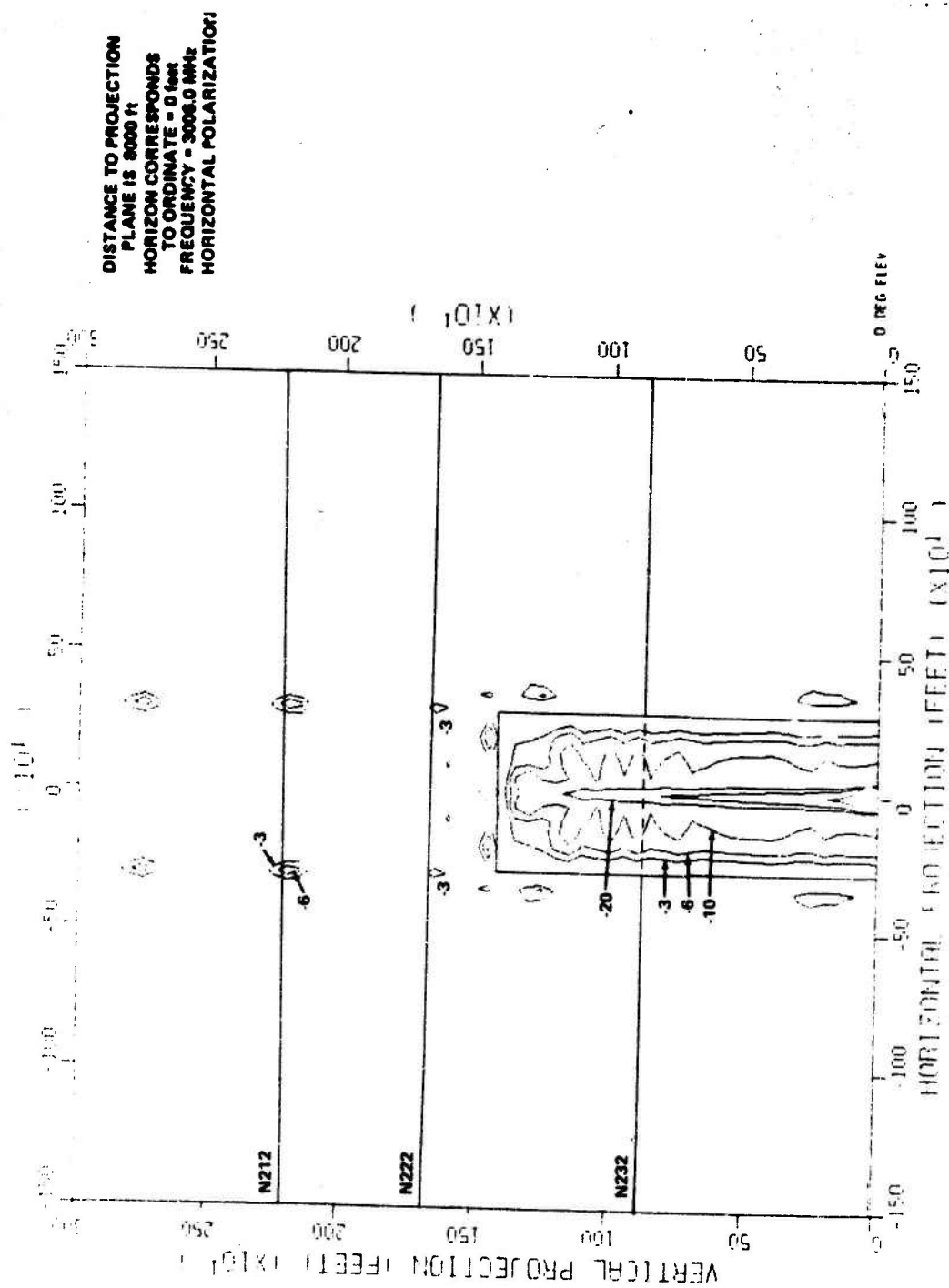
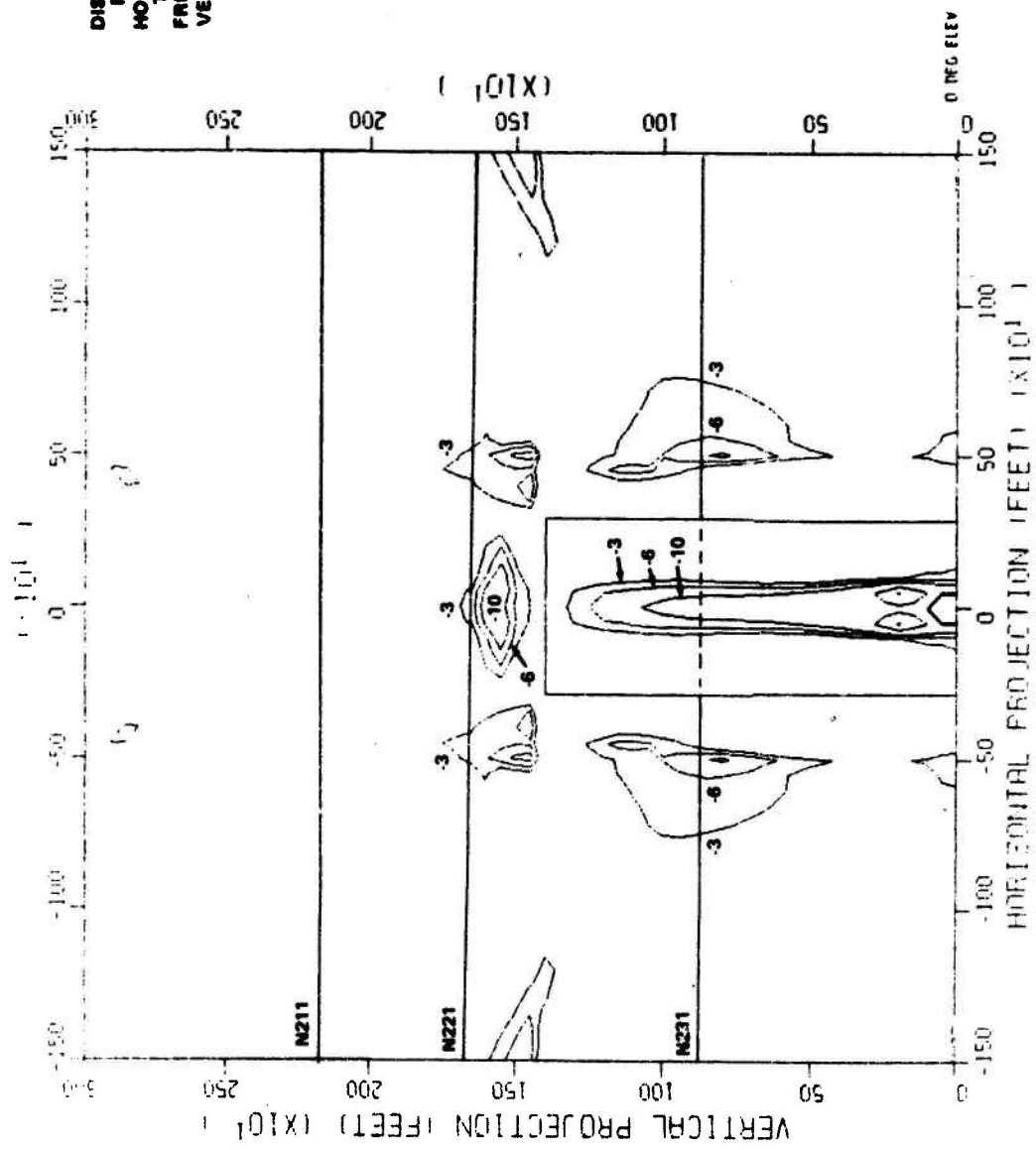


Figure 94 FLIGHT PATHS, N2X2-SERIES, S-BAND, HORIZONTAL POLARIZATION

Reproduced from
best available copy.



DISTANCE TO PROJECTION
PLANE IS 8000 ft
HORIZON CORRESPONDS
TO ORIGINATE - 0 feet
FREQUENCY = 123.4 MHz
VERTICAL POLARIZATION

Reproduced from
best available copy.

Figure 95 FLIGHT PATHS, N2XY-SERIES, VHF, VERTICAL POLARIZATION

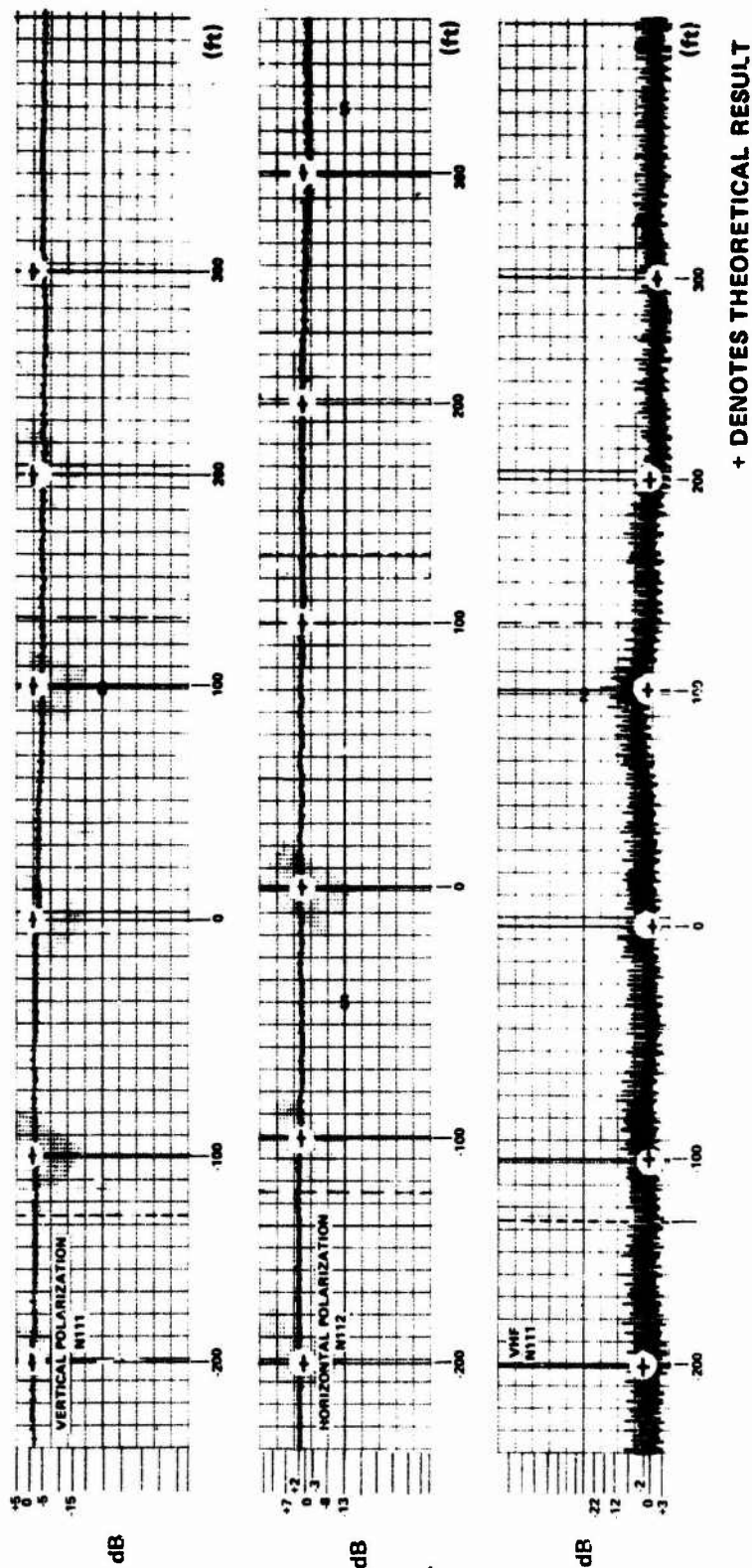


Figure 96 COMPARISON BETWEEN THEORY AND EXPERIMENT, RELATIVE SIGNAL STRENGTH
vs DISTANCE FROM TEST CENTERLINE, RUNS N111 AND N112; $d_1 = 496$ FT, $d_2 \approx 3300$ FT,
ALTITUDE ≈ 991 FT

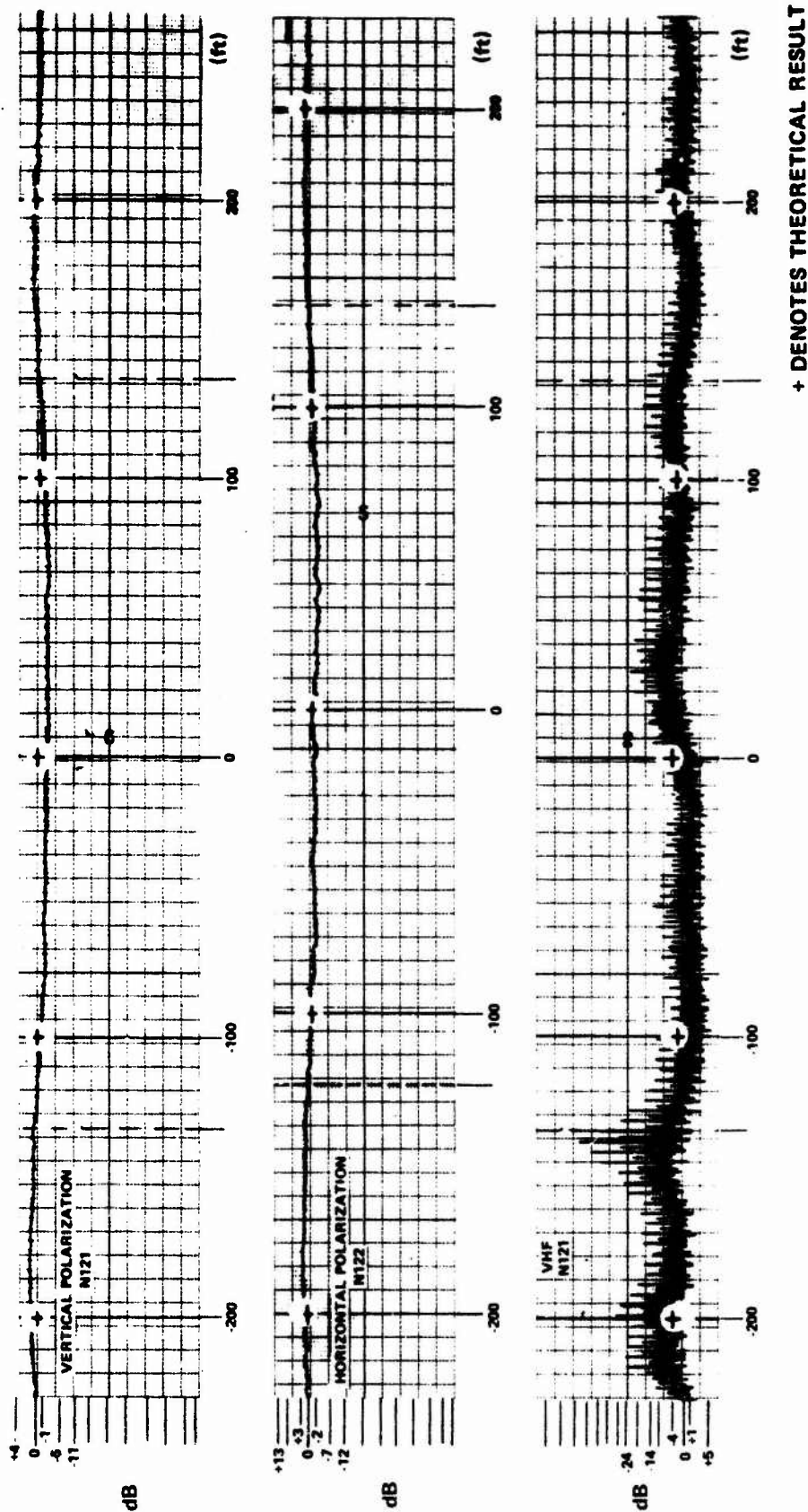
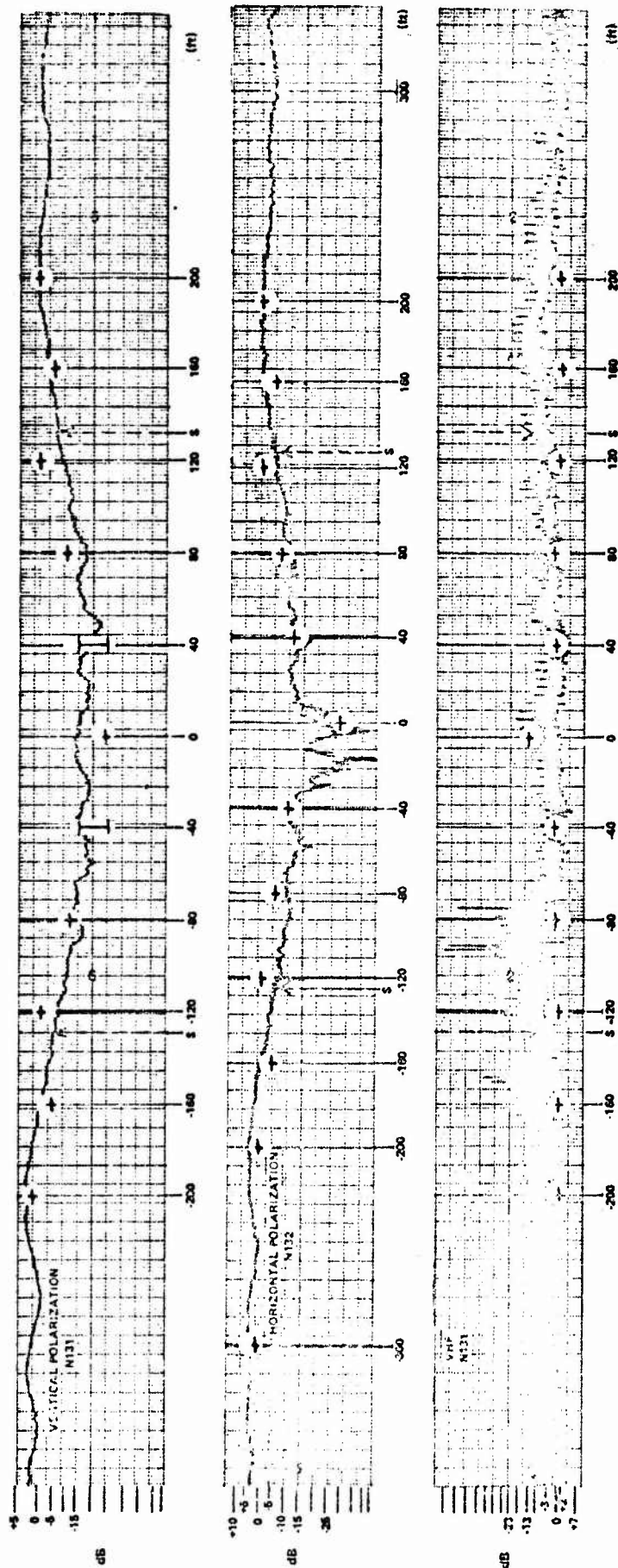


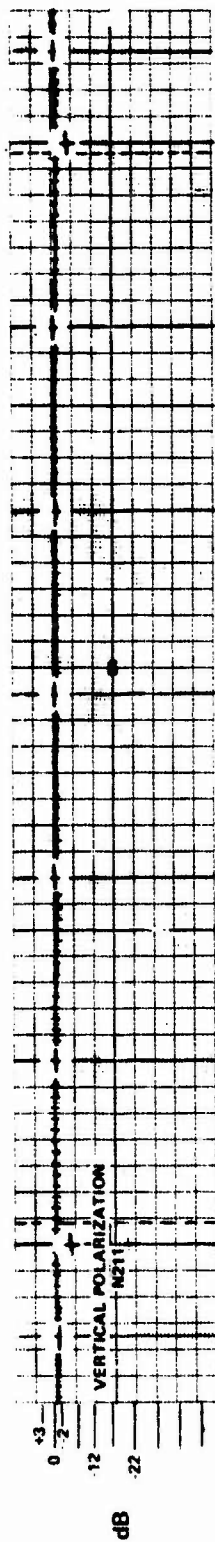
Figure 97 COMPARISON BETWEEN THEORY AND EXPERIMENT, RELATIVE SIGNAL STRENGTH
vs DISTANCE FROM TEST CENTERLINE, RUNS N121 AND N122; $d_1 = 496$ FT, $d_2 \approx 3300$ FT,
ALTITUDE ≈ 755 FT



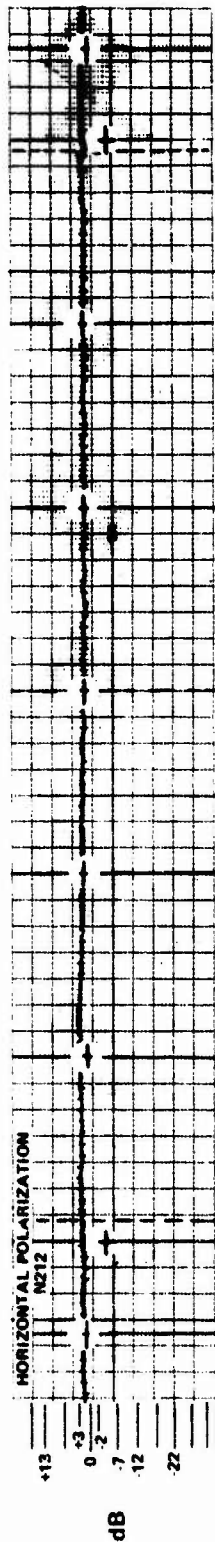
+ DENOTES THEORETICAL RESULTS

Preceding page blank

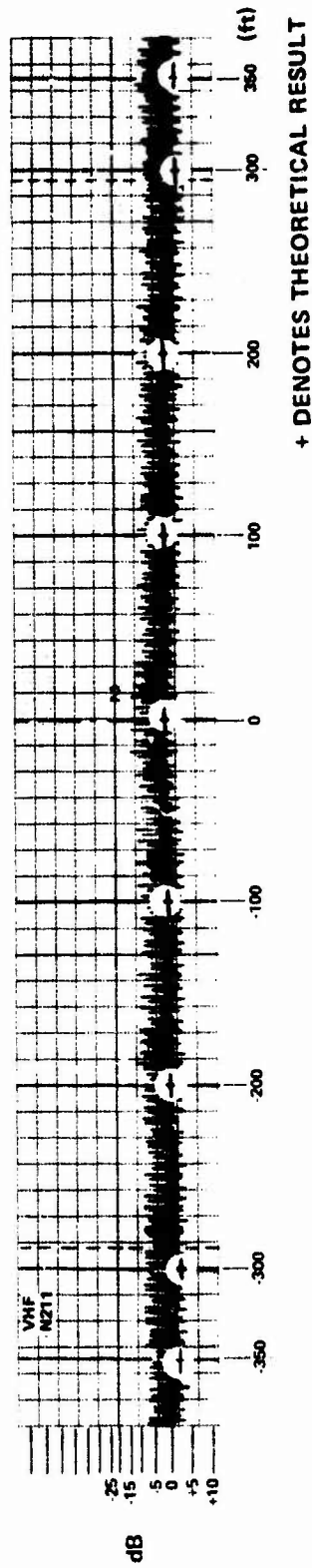
Figure 98 COMPARISON BETWEEN THEORY AND EXPERIMENT, RELATIVE SIGNAL STRENGTH VS. DISTANCE FROM TEST CENTERLINE, RUNS N131 AND N132; $d_1 = 496$ FT, $d_2 = 3300$ FT, ALTITUDE ≈ 400 FT



dB



dB



+ DENOTES THEORETICAL RESULT

Figure 99 COMPARISON BETWEEN THEORY AND EXPERIMENT, RELATIVE SIGNAL STRENGTH
vs DISTANCE FROM TEST CENTERLINE, RUNS N211 AND N212; $d_1 = 496$ FT,
 $d_2 \approx 8000$ FT, ALTITUDE ≈ 2200 FT

Preceding page blank

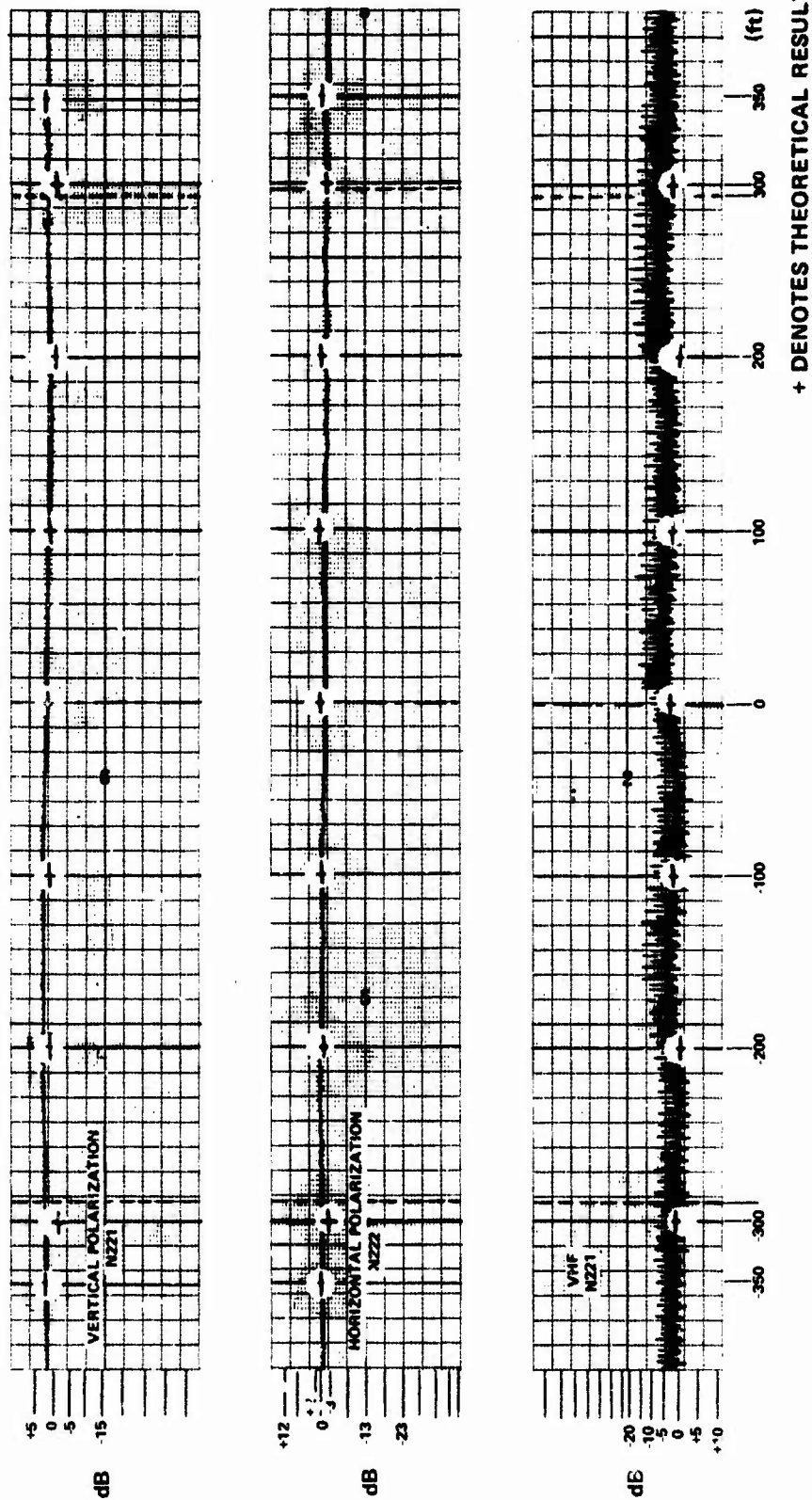


Figure 100 COMPARISON BETWEEN THEORY AND EXPERIMENT, RELATIVE SIGNAL STRENGTH
vs DISTANCE FROM TEST CENTERLINE, RUNS N221 AND N222; $d_1 = 496$ FT,
 $d_2 \approx 8000$ FT, ALTITUDE ≈ 1670 FT

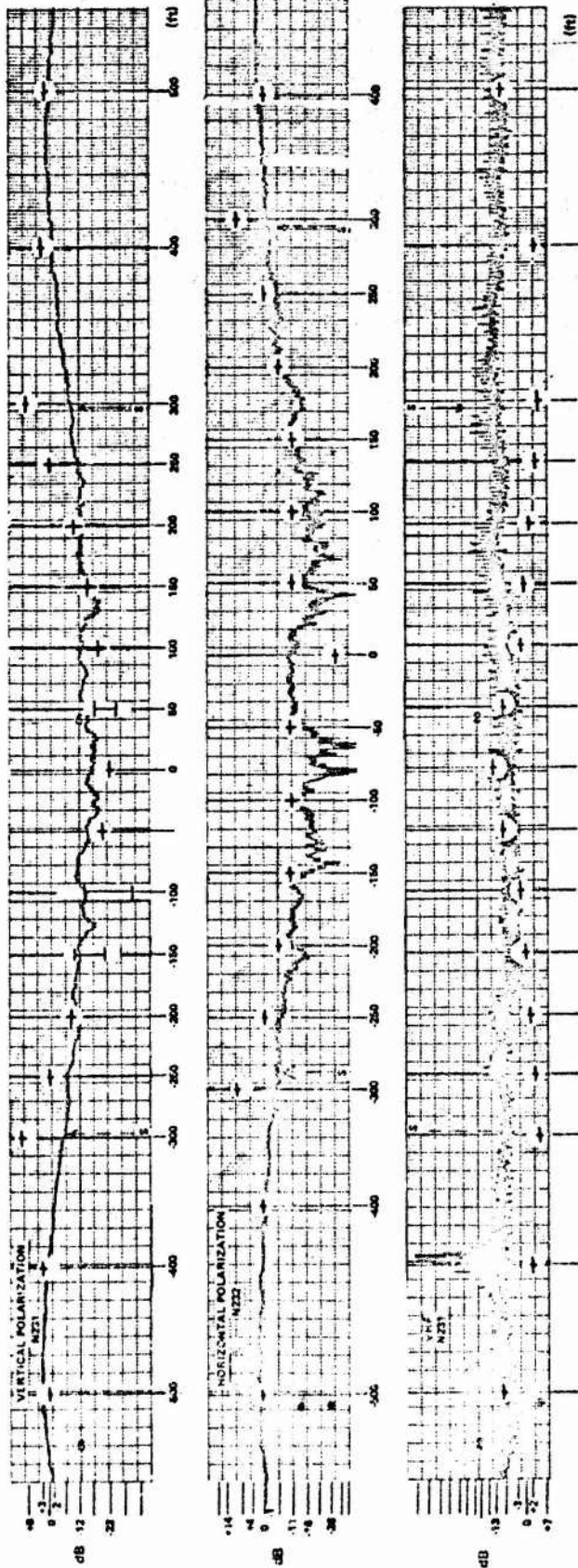
and it is not likely that an altitude error could have caused missing the regions. Therefore, it is suggested that the discrepancy is due to the differences between the idealized model assumed in the computer program and the actual building which, as has been pointed out, has metallic fins which protrude from its sides and top.

The trajectories of Runs N221 and N222 were again above the top of the geometric shadow. The extent of the -3 dB S-band contour shown in Figures 93 and 94 is about 50 feet. Corresponding decreases do not appear on the recordings. Otherwise, agreement is very good. The VHF results are likewise in good agreement.

The final set of runs is shown in Figure 101. Large peaks in signal level at $+300$ feet are predicted for the S-band case but were not observed during the test. It is felt that model differences are again the cause of this effect. Agreement within the shadow region is good. Within ± 15 feet, single order diffraction takes place from only the roof of the building. The difference between theory and experiment within this region is probably due to differences between the idealized model and the actual finned and peaked roof.

For the VHF case, differences between theory and experiment appear to correspond to those observed for a within-the-shadow trajectory for the nearer range (see Run N131). Where increases in VHF signal level are predicted (e. g., +6 dB at $+300$ feet), the recorded signal was generally less than 0 dB with a trend toward an increase in level near the center of the shadow.

It is likely that the fins on the building are the major causes of the differences observed between flight test data and theory. The spacing between the fins is approximately 8 feet which is also equal to the VHF wavelength; thus, strong interference effects due to multiple scattering are likely to be present.



Preceding page blank

• DENOTES THEORETICAL RESULTS

Figure 101 COMPARISON BETWEEN THEORY AND EXPERIMENT, RELATIVE SIGNAL STRENGTH VS DISTANCE FROM TEST CENTERLINE, RUNS N231 AND N232, $d_1 = 486$ FT, $d_2 \approx 8000$ FT, ALTITUDE ≈ 889 FT

3.4.2 Conclusions

In general, good agreement between theoretical predictions and experimental results for all three orientations of the rectangular building has been obtained.

The S-band results are particularly good (generally within 2 dB). One difference (on the order of 7 dB) was the appearance of peaks in predicted signal level near the shadow boundaries. Such peaks were not experimentally observed.* It was noted previously that, for the assumed theoretical model, the peaks result from the "focusing effect" of edges being illuminated by nearly planar phase fronts. Deviations of the actual building from the model could possibly account for the difference, although for the B-series, where the theoretical model is a good representation of the actual building (for low altitude, within-the-shadow flights), the difference still exists. It is possible that the analytical method of combining GDT and half-plane formulas might be a contributing source of the predicted signal peaks. The shadow boundary formulation is discussed in Section 2.3.5

The analytical methods employed in the shadow boundary region should be reexamined to determine if the predicted peaks in signal level near the shadow boundary are the result of approximations employed in the theoretical development.

It was noted that the average VHF signal level appeared to change gradually during the test runs. It is likely that a nonomnidirectional airborne VHF antenna pattern was the cause of this signal level variation. Thus it was sometimes difficult to choose the no-perturbation or 0 dB reference level. In many cases, it appears that a shift in this reference level is all that would be required to bring VHF results, on the average, into fairly good agreement with predictions.

Scalloping also appeared on many recorded VHF signals. The scalloping is probably attributable to ground reflections and/or multipath from towers and a bridge in the vicinity of the test object. For lower frequency

* Interestingly, peaks just outside the shadow boundaries were experimentally observed during the sphere tests.

signals, normally accompanied by wide beamwidth (if not omnidirectional) antenna patterns, multipath effects can become significant. Improvements in the calculated data could be made in this case by incorporating into the computer program ground reflection effects.

Finally, it is again noted that, for the N-series, metallic fins protrude from the sides and top of the building. The spacing between the fins is 8 feet which is also approximately equal to the VHF wavelength. Thus, interference effects are expected to be present. Therefore, some of the differences between the theoretical and experimental results could be attributed to the differences between the idealized theoretical model and the actual structure.

Section 4

CONCLUSIONS

For the rectangular building, agreement between the experimental S-band flight test data and predicted behavior of signal levels was very good, generally within 2 dB of each other. One discrepancy was that predicted peaks of about 7 dB in signal level at points near the shadow boundaries were not experimentally observed. Although there are physical arguments which deem the appearance of those peaks credible, it is also possible that they result from the use of certain approximate methods utilized in providing transition between shadow boundary and geometric diffraction theory analytic formulations.

The easiest and fastest way of resolving this would be to conduct a scale model experiment where there would be no differences between assumed and actual obstacle properties. If the peaks still do not appear, the more involved procedure of reevaluating the analytical procedures should be undertaken.

The VHF signal exhibited scalloping and other level changes which, it is felt, were not caused by diffraction from the obstacle under test. These signal variations are attributed to ground refractions, other multipath phenomena, and possibly, a nonomnidirectional airborne VHF antenna pattern. Because the recorded VHF signal was not constant, even for helicopter positions far from the obstacles, it was sometimes difficult to determine the no-perturbation or 0 dB reference level. In many cases, good agreement between theory and experiment can be obtained by merely uniformly shifting the reference level assumed in the data reduction by an appropriate amount.

The effects of ground reflections and antenna pattern effects can be incorporated into the computer program; this would provide a more accurate model of the electromagnetic configuration.

Measurements of S-band and VHF signals were also made utilizing spherical and cylindrical obstructions. No theoretical predictions were made for these cases, other than simple geometric optics as provided in the computer. Interestingly, peaks in signal level appeared near the shadow boundaries for many of the sphere tests; they were absent for the cylinder.

For both the sphere and cylinder, S-band signal level perturbations (on the order of from 2 to 4 dB, one-way) extended out to approximately twice the distance of the shadow boundary projection. Within the shadow region, the signal level was generally much less than the free-space field, although for both the sphere and cylinder a signal peak of typically -3 dB was present over a fairly large region in the center of the geometric shadow. In summary, geometric-optical predictions based on the line-of-sight overestimate the signal loss within the shadow and underestimate the loss outside the shadow.

A study program can be performed to develop appropriate theories that would accurately take into account diffraction contributions for spherical and cylindrical obstructions. Such theories could be easily incorporated into the present computer program. Theoretical predictions could be compared with the experimental results already obtained.

REFERENCES

1. Van de Hulst, H.C., Light Scattering by Small Particles, New York, Wiley (1957).
2. Abramowitz, M. and I.A. Stegun, Handbook of Mathematical Functions, Applied Mathematics Series, 55, Gov't Printing office (1964).
3. Bechtel, M.E. and R.A. Ross, "Radar Scattering Analysis," Research Information Series, CAL Report No. ER/RIS-10, August 1966, Calspan Corporation, Buffalo, New York

Appendix I

EVALUATION OF THE Q-FACTOR

1.0 INTRODUCTION AND SUMMARY

The appendix presents an analysis of the effects of illumination and observation of a scattering edge at angles not normal to the edge. Effects of moderate amounts of phase-front curvature are accounted for through the use of a fresnel-integral formulation.

The Q-factor calculation is comprised of two subroutines, one called after the incidence direction and related information has been computed and another called for each observation point of interest. The second subroutine is thus called hundreds or thousands of times for each call of the first subroutine which now includes computations that need only be performed once for each incidence angle.

This appendix describes the computational procedures, gives flow charts for the two subroutines, and demonstrates the accuracy of the analysis in certain limiting cases.

2.0 LARGE CURVATURE OF INCIDENT WAVEFRONTS

For very long edges and very short radar wavelengths, incident wave curvature is treated by considering the edge as a collection of shorter edges; it must be recognized that the diffraction coefficient, which is ignored here except as a factor to be supplied from another subroutine, will in fact differ slightly for each of the shorter edges; this effect is expected to be of minor importance and is not being accounted for in the overall diffraction program because it would greatly increase computation time and complexity.

Let us consider the distance from the source point to each point on the scattering edge; the geometry is shown in Figure 102.

Preceding page blank

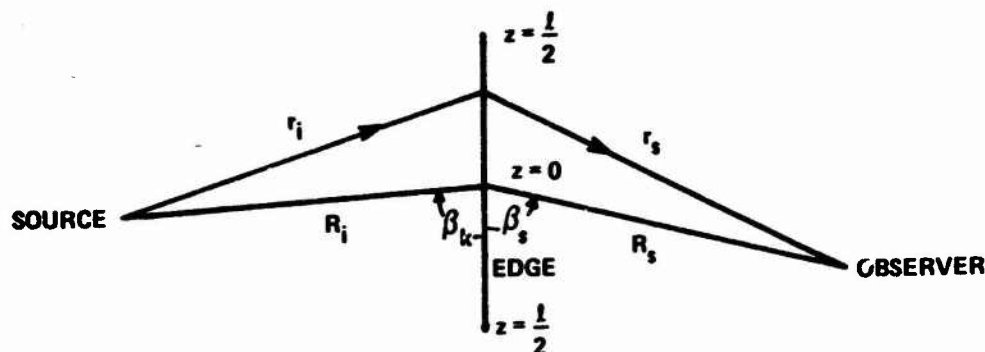


Figure 102 BASIC EDGE GEOMETRY

The distance is given by the approximation

$$r_i = R_i + z \cos \beta_k + \frac{1}{2} \left(\frac{z^2}{R_i} \right) \sin^2 \beta_k - \frac{1}{2} \left(\frac{z^3}{R_i^2} \right) \cos \beta_k \sin^2 \beta_k - \frac{1}{8} \left(\frac{z^4}{R_i^3} \right) \sin^2 \beta_k (1 - 5 \cos^2 \beta_k) \quad (51)$$

where the variables are as shown in Figure 102. Because the distance appears in a phase term, any terms that change it by a significant fraction of a wavelength will have an effect on the integration necessary to determine the diffracted field, u_p , i.e.,

$$u_p = \left(\frac{T(\theta)}{i\pi R_s} \right) \left(\frac{u'_0}{R_i \sqrt{4\pi}} \right) \underbrace{v \int_{-\frac{l}{2}}^{\frac{l}{2}} e^{ik(r_i + r_s)} dz}_Q \quad (52)$$

where

$T(\theta)$ = diffraction coefficient supplied from another portion of computer program,

u'_0 = incident field amplitude, and

$v = \sin \beta_k \sin \beta_s$

and other variables are shown in Figure 102.

Efforts to evaluate the integral of equation (52) suggest that a direct integration for phase functions involving powers of z above the second are impractical. Suppose, instead, that we break up the edge into shorter

subsections, each of them short enough so that only phase terms through z^2 need be incorporated. Now we can evaluate the integral as a sum of integrals, each of them over a length of edge short enough to permit use of the Fresnel-integral solution to equation 52 under the assumption that and higher-order terms are negligible. This approach does complicate the logic of the computer program, but it appears to be the best way to handle excessively large amounts of phase-front curvature.

The first problem is to establish the best way in which to break up the edge into sufficiently short segments. In Figure 103 is shown the geometry for the case in which there are five segments on the edge. In general, the program allows for up to 15 segments; only odd numbers of segments are used because then the midpoint of the middle segment is also the midpoint of the total edge. We are supplied with R_{i_3} , R_{s_3} , β_{k_3} , and β_{s_3} from a previous subroutine. These parameters are the ones we normally use, since normally only one segment is needed (i.e., $N = 1$). In the N -segment case, the subscripts on the parameters supplied are $n_m = (N + 1/2)$. We must compute all of the quantities R_{i_n} , R_{s_n} , β_{k_n} and β_{s_n} for use in the integration which has now become

$$Q = \sqrt{v} \int_{-\frac{\ell}{2}}^{\frac{\ell}{2}} e^{-ik(r_i + r_s)} dz = \sum_{n=1}^N \left(\frac{R_{i_{nm}}}{R_{i_n}} \right) \left(\frac{R_{s_{nm}}}{R_{s_n}} \right) e^{ik(R_{i_n} - R_{i_{nm}})} e^{ik(R_{s_n} - R_{s_{nm}})} \quad (53)$$

where

$$Q_n = V_n \int_{-\frac{\ell}{2N}}^{\frac{\ell}{2N}} e^{-ikz(\cos\beta_{k_n} + \cos\beta_{s_n}) - ikz^2 \left(\frac{\sin^2\beta_{k_n}}{2R_{i_n}} + \frac{\sin^2\beta_{s_n}}{2R_{s_n}} \right)} dz \quad (54)$$

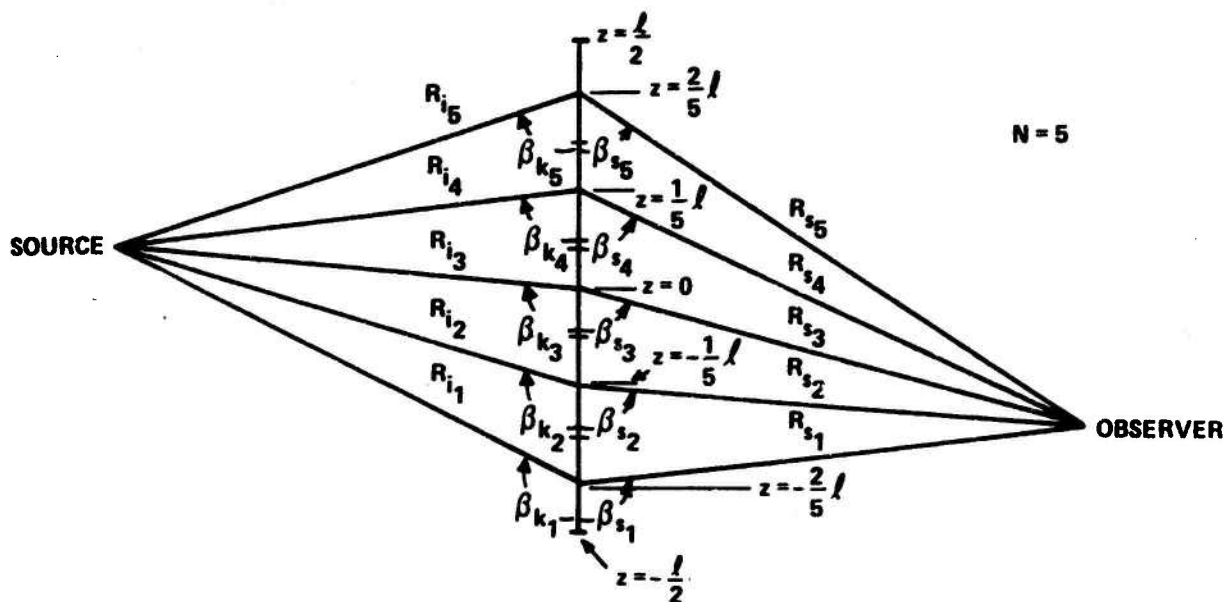


Figure 103 SUBDIVISION OF EDGE INTO SHORTER SEGMENTS

In equation 53, the summation contains ratios of ranges to compensate for the varying distances of the edge segments from the source and the receiver; range effects are neglected for the various elements in the integration along the edge, but in the case of a very long edge, for which N exceeds unity, it seems reasonable to include range-correction factors for the segments. The phase factors shown in equation 53 are very important, because they are (approximately) accounting for the large amount of phase curvature that makes it inaccurate to evaluate Q with a single integration. Thus we have reduced the phase variation within the integrand by subdividing the edge and now must account for that phase curvature by using appropriate phase shifts for the contributions of the segments of the edge. Obviously this approach can yield only approximate results: N must approach infinity for Q to approach the correct value. It does seem quite certain, however, that the accuracy obtained using the present approach will be more than adequate for the intended application.

The next question that must be considered is how to determine the number of segments to be used. Consider equation 51, which gives the distance to a point located z units from the center of the line segment of interest. Also, assume we have a single segment for the moment. Then, if we are to be able to use the approximation involving the removal of z^3 and higher-order terms from equation 51, we must have a negligible phase shift contribution from these terms; that is,

$$\left| \frac{l^3}{16R_i^2\lambda} \sin^2\beta_k \left[\cos\beta_k + \frac{l}{8R_i} (1 - 5\cos^2\beta_k) \right] \right| \ll 1 \quad (55)$$

is required if these terms are to be dropped. Replacing $1/16\lambda$ by $k/100$, since k is available in the program, we can rewrite the criterion as

$$\left| \frac{k l^3}{R_i^2} \sin^2\beta_k \left[\cos\beta_k + \frac{l}{8R_i} (1 - 5\cos^2\beta_k) \right] \right| \ll 100 \quad (56)$$

In the program, we require that the quantity on the left-hand side be less than 10, noting that this approach is conservative since the amount of correction is generally much less than the value shown in the left side of inequality 56 since that quantity is computed for the worst case of $z = l/2$. The computational approach is simple: we compute the left-hand side of inequality 56. If this quantity is less than 10, we set $N = 1$ and proceed as before. If the quantity is greater than 10, we set $N = 3$, replace l by $l/3$, and recompute the left-hand side of the inequality. Note that l is cubed so the resulting quantity is only of the order of $1/27$ of its previous value. Again the inequality is tested. The procedure continues until either an N is found such that the inequality is satisfied or else $N = 15$, the maximum value allowed in the present program. Values of N greater than 15 would occur only for such a long edge and such a close radiator that many other assumptions in our general approach would also fail, so this limitation is not a severe one in terms of operational capability. In any case, very large values of N would lead to greatly increased computation times.

Note that this establishment of N is based only on the source-to-edge distance; if the source is far from the edge and the receiver is close to the edge, $N = 1$ will be used. If both source and receiver are close to the edge, the breakdown will still be effected and the method will lead to valid results. Note that the only real effect of breaking the edge down into a set of N shorter edges is to improve the accuracy of the phase terms of the integrand so that the Fresnel-integral results will be valid. The penalty in computer time lies in the necessity to evaluate N different Q_n values and to add these Q_n values, with appropriate amplitude and phase adjustment, to obtain the overall Q value for a given combination of incidence and observation angles. Note that we choose N by making computations on successively shorter and shorter sections of edge centered on the center of the overall edge and that further checks, using sections near the ends of the overall edge, could be made but are not necessary since the values obtained near the ends would differ but little from those at the center, and, in any case, we are only trying to satisfy, in a general way, inequality 56.

Once N has been established, it is necessary to compute other parameters for later use. If $N = 1$, very little computation is necessary in the first subroutine, $Q1$, which is called only once for each incidence angle (see Section 3). If N exceeds unity, the quantities R_{l_n} and β_{k_n} must be computed for the N values of n ; these computations are made in subroutine $Q1$. For each observation point, R_{s_n} and β_{s_n} must be computed in subroutine $Q2$, which is called once for each observation point (see Section 5). Because we will only have $N > 1$ for relatively short source-to-edge distances, we can compute the distance to the center of each segment of the edge straightforwardly from the law of cosines, viz.

$$R_{l_n} = \left[R_{l_{nm}}^2 - R_{l_{nm}} \left(\frac{l}{N} \right) (N+1-2n) \cos \beta_{k_{nm}} + \left(\frac{l}{2N} \right)^2 (N+1-2n)^2 \right]^{\frac{1}{2}} \quad (57)$$

where $R_{l_{nm}}$, the distance to the center of the overall edge, is available from a previous subroutine, as is $\beta_{k_{nm}}$, the angle at the center of the overall edge; $(l/2N)(N+1-2n)$ is simply the amount by which the center

of the n^{th} edge segment is offset from the center of the overall edge (see Figure 103). The incidence angles could be solved for but they are really not needed: what are needed are the sines and cosines of these angles, quantities that are found from the formulas

$$\sin \beta_{k_n} = \frac{R_{i_{nm}} \sin \beta_{k_{nm}}}{R_{i_n}} \quad (58)$$

and

$$\cos \beta_{k_n} = \frac{R_{i_{nm}} \cos \beta_{k_{nm}} - \frac{l}{2N} (N+1-2n)}{R_{i_n}} \quad (59)$$

Since all of the quantities required in equations 58 and 59 are already available, computation of the required sines and cosines is very rapid. Finally, we compute in QQ1 the (complex) constants required in equation 54,

$$F = \frac{R_{i_{nm}}}{R_{i_n}} e^{ik(R_{i_n} - R_{i_{nm}})} \quad (60)$$

For the distances and angles from the edge segments to the receiver, formulas essentially identical to equations 57 through 59 are used in subroutine QQ2. The only modification required there is one that (for the $N > 1$ situation) is necessitated by the fact that the distances to the receiver may be very great and thus may lead to errors in the square-root computation in equation 58; in addition, elimination of the square root operation can save time. Therefore, the values of $R_{s_{nm}}$ greater than 30,000 meters we use a series approximation to equation 57,

$$R_{s_n} = R_{s_{nm}} - \left(\frac{l}{2N}\right)(N+1-2n) \left[\cos \beta_{s_{nm}} - \frac{\sin^2 \beta_{s_{nm}} \left(\frac{l}{2N}\right)(N+1-2n)}{2R_{s_{nm}}} \right] \quad (61)$$

which provides good accuracy in short computation times, the latter consideration being very important in a subroutine called as many times as QQ2 is

3.0 SUBROUTINE QQ1

Subroutine QQ1 computes certain quantities that will be needed later in the program. Inputs to QQ1 are

AK	=	wave number ($= 2\pi/\lambda$) (meters ⁻¹)
AL	=	length of (overall) edge (meters)
RSP	=	range from source to center of edge (meters) ($= R_{inm}$ in discussion in Section 2)
BETAK	=	angle line of sight makes with edge (radians) ($= \beta_{knm}$ in discussion in Section 2)

which are determined in earlier subroutines. As indicated in Section 2, the primary purpose of subroutine QQ1 is to establish N, the number of segments into which the edge is to be subdivided, and to compute other quantities for later use.

Outputs from subroutine QQ1 are

RJ (J)	=	range from center of J'th segment to source (meters) ($= R_{in}$ for n'th segment in Section 2)
SNBETK (J)	=	$\sin \beta_{kn}$ in Section 2 (equation 58)
CSBETK (J)	=	$\cos \beta_{kn}$ in Section 2 (equation 59)
CFACT (J)	=	normalization factor F (equation 61)
NSG	=	number of segments (N in Section 2)
AX	=	AL/NSG (meters)

The basic flow within subroutine QQ1 is shown in Figure 104. Note that if $N = 1$, the usual situation, most of the subroutine is bypassed and relatively few computations need be made. The indices J in the quantities defined above range from 1 to NSG. All of the computations in this subroutine were discussed, and appropriate equations were given, in Section 2.

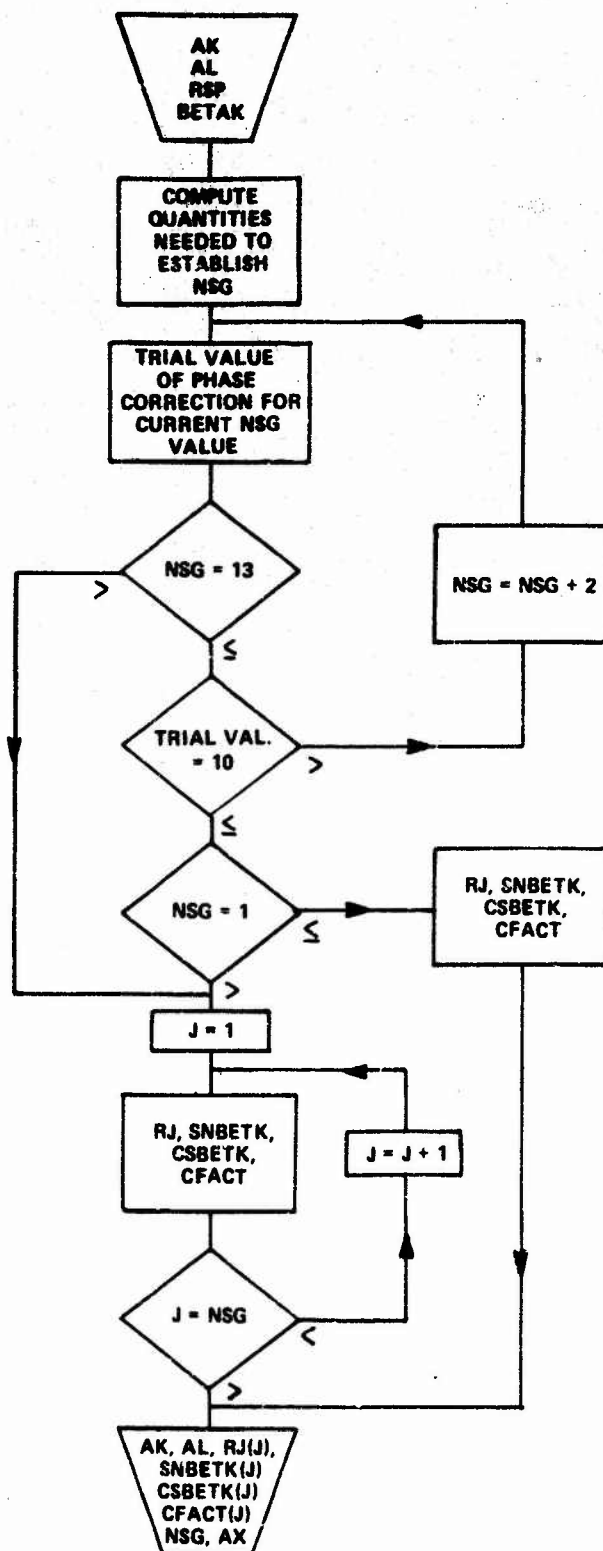


Figure 104 FLOW DIAGRAM FOR SUBROUTINE QQ1

4.0 MODIFIED ASYMPTOTIC APPROXIMATIONS TO FRESNEL-INTEGRAL EXPRESSIONS

The most important part of the evaluation of the Q factor is the integration indicated in equation 54. By restricting the maximum length of the edge segments, we assure that the use of terms only up to order z^2 is a valid approximation. We can perform the integration exactly and obtain

$$Q_n = V_n \sqrt{\frac{\pi}{2a_n}} e^{i \frac{b_n^2}{a_n}} \left[\left\{ C(Y_n + Z_n) - C(Y_n - Z_n) \right\} - i \left\{ S(Y_n + Z_n) - S(Y_n - Z_n) \right\} \right] \quad (62)$$

where

$$Y_n = b_n \sqrt{\frac{2}{\pi a_n}}$$

$$Z_n = \frac{l}{n} \sqrt{\frac{a_n}{2\pi}}$$

$$a_n = \frac{k}{2} \left(\frac{\sin^2 \beta_{kn}}{R_{kn}} + \frac{\sin^2 \beta_{sn}}{R_{sn}} \right)$$

$$b_n = \frac{k}{2} (\cos \beta_{kn} + \cos \beta_{sn})$$

and we use the Fresnel integrals

$$C(z) = \int_0^z \cos\left(\frac{\pi}{2} t^2\right) dt \quad (63)$$

$$S(z) = \int_0^z \sin\left(\frac{\pi}{2} t^2\right) dt \quad (64)$$

Direct evaluation of Q_n using standard subroutines for the Fresnel integrals is used for small Y and Z values, * but if these values become very large, as they may, overflows can occur in the computer. If either argument is less than 5, we use the IBM subroutine directly, as before, to evaluate equation 62. The argument supplied to this subroutine must be $\frac{\pi}{2} x^2$

* In subsequent discussions of evaluation of the Fresnel-integral expressions, the subscript n's are omitted; note that all such evaluations are performed independently for each n value required.

rather than x because of the different definition they have used for the Fresnel integrals. Note that the algebraic sign of the Fresnel integrals is lost (because of the squaring of the argument before the subroutine is called); provision therefore has to be made to give the computed Fresnel integrals the same signs as the original arguments.

We have developed an accurate asymptotic form that can be used for arguments as small as 5. This expansion is based upon the asymptotic expansion given at the bottom of page 322 of Reference 2, i. e.,

$$\begin{aligned} \frac{C(x)}{S(x)} \sim 0.5 \pm \left(0.3183099 - \frac{0.0968}{x^4} \right) \frac{\frac{\sin\left(\frac{\pi}{2}x^2\right)}{\cos\left(\frac{\pi}{2}x^2\right)}}{x} \\ - \left(0.10132 - \frac{0.154}{x^4} \right) \frac{\frac{\sin\left(\frac{\pi}{2}x^2\right)}{\cos\left(\frac{\pi}{2}x^2\right)}}{x^3} \end{aligned} \quad (65)$$

where the upper signs and functions are used for $C(x)$, and the lower signs and functions, for $S(x)$; the error is less than 3×10^{-7} for greater than 5. Using these asymptotic expansions in equation 62 and doing considerable algebraic juggling, we obtain the form

$$\begin{aligned} Q_n = V_n \sqrt{\frac{\pi}{2a}} \left[\frac{1}{\sqrt{2}} FRT e^{i\frac{b^2}{a}} + e^{-i\frac{a}{x}\left(\frac{L}{N}\right)^2} \left\{ \left[(CF1 + CF2) \sin(ARG) - (CF3 - CF4) \cos(ARG) \right] \right. \right. \\ \left. \left. + i \left[(CF1 - CF2) \cos(ARG) + (CF3 + CF4) \sin(4RG) \right] \right\} \right] \end{aligned} \quad (66)$$

where

$$\begin{aligned} AC1 &= 0.3183099 \\ AC2 &= 0.10132 \\ AC3 &= 0.0968 \\ AC4 &= 0.154 \end{aligned}$$

YPZ	=	Y + Z
YMZ	=	Y - Z
FRT	=	sgn (YPZ) = sgn (YMZ)
YPZC	=	YPZ ³
YMZC	=	YMZ ³
YPZF	=	YPZ ⁴
YMZF	=	YMZ ⁴
CF1	=	(AC1-AC3/YPZF)/YPZ
CF2	=	(AC1-AC3/YMZF)/YMZ
CF3	=	(AC2-AC4/YPZF)/YPZC
CF4	=	(AC2-AC4/YMZF)/YMZC
ARG	=	πYZ

and other variables are as previously defined. Variables in the list above are the same ones used in computer subroutine QQ2. The first term will generally be zero (i. e., FRT = 0), in which case the first phase factor need not be computed. This formulation is the basic one used in subroutine QQ2, discussed in the next section.

Note that only two sines and two cosines will normally be required for those cases in which the first term does not appear. Computation time is therefore less than is required for use of the IBM subroutines, since their subroutine CS must be called twice, requiring a sine and a cosine computation each time, plus a sine and a cosine for the exponential in front of equation 62.

When the distances from the edge to the source and the observer become very large, $N = 1$ and the conventional far-field result is obtained; this expression is

$$Q \sim lV \text{sinc}(bl) \quad (67)$$

In Section 6 we demonstrate that our computer program does, in fact, yield results approaching equation 67 using equation 66. Because it appears very unlikely that equation 67 will be a legitimate approximation in the situations of interest on this project, we have not included provisions for computing Q from equation 67, although this equation is obviously much better

computationally. If later usage of the program should be desired for diffraction from relatively short edges at great distances (to both source and receiver), it will be relatively easy to include a provision for using this approximation.

5.0 SUBROUTINE QQ2

This subroutine is called once for each observation angle. The inputs to the subroutine are AK, AL, RJ(J), SNBETK(J), CSBETK(J), CFACT(J), NSG, and AC, all of which are obtained from subroutine QQ1, plus RPO and BETAS, the quantities $R_{s_{nm}}$ and $\beta_{s_{nm}}$ discussed in Section 2. The latter two variables are obtained from a geometry subroutine preceding Q₂.

The basic flow of subroutine QQ2 is shown in Figure 105. If NSG is not unity, the ranges and angles to the edge segments must be computed using equations analogous to equations 57 through 61 of Section 2. Then the basic quantities necessary to compute the Fresnel integrals are computed. Depending upon YPZ and YMZ, either the exact formulation (equation 62) or the asymptotic formulation (equation 66) is used. When NSG > 1, the basic computations and Fresnel-integral computations must be repeated NSG times and the results appropriately summed to obtain Q, the desired output of QQ2.

6.0 CHECKOUT OF COMPUTER PROGRAM SUBROUTINES

In this section we consider some basic checks that have been made.

First, consider the fact that when the smaller of YPZ and YMZ exceeds 5, subroutine QQ2 switches from Equation 62 to Equation 66 as its basis for computing Q. It is desirable that the transition be smooth to avoid the introduction of discontinuities in the output at such a point. Although the approximation used in equation 66 is very accurate, the equation is obviously very different from equation 62; further, examination of the IBM subroutine CS indicates that a quite different asymptotic expansion is used there because they switch to the asymptotic form at (their) argument value of 4, corresponding to our argument 1.596. Consequently, good agreement between these very

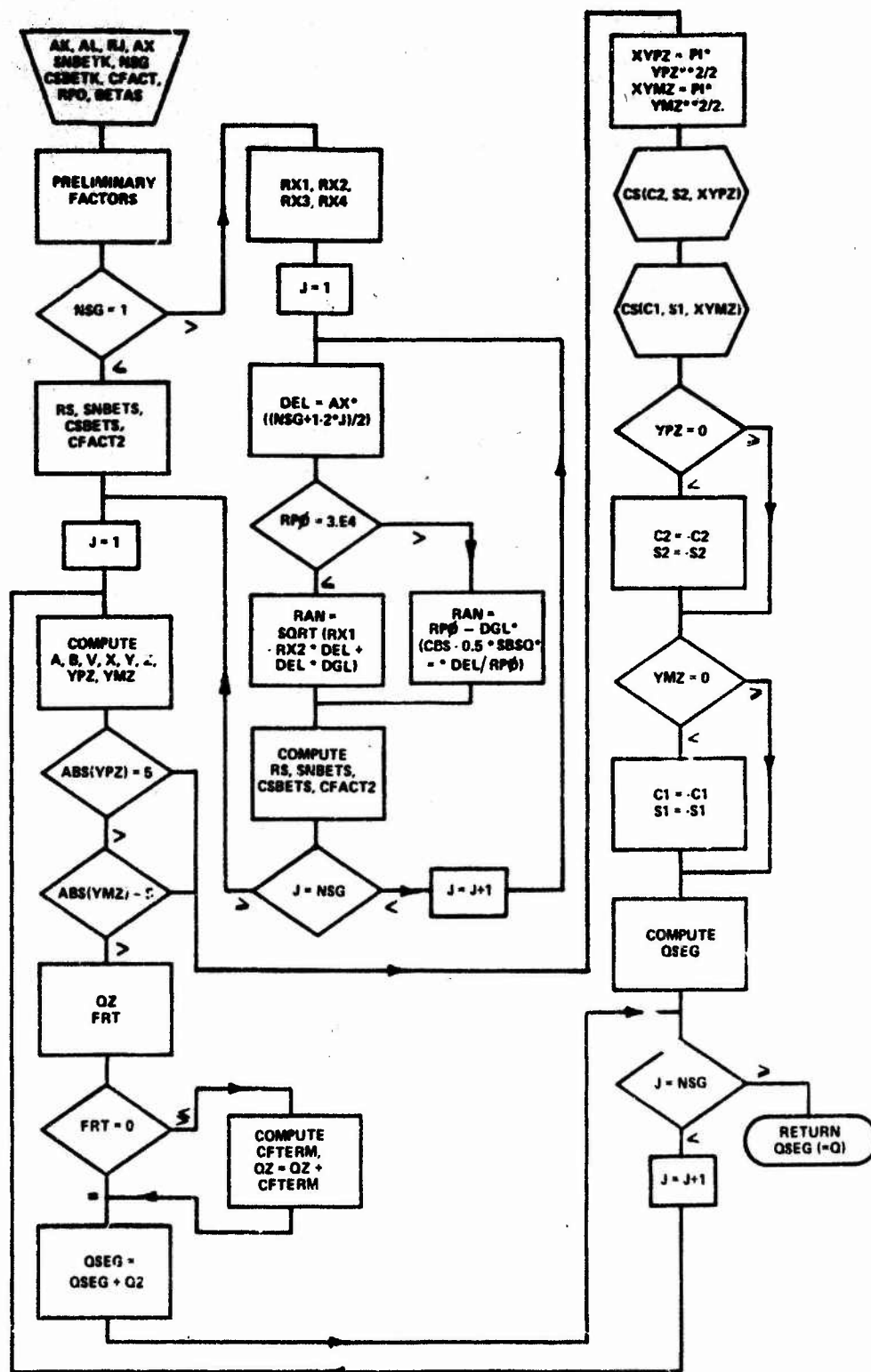


Figure 105 FLOW DIAGRAM FOR SUBROUTINE QQ2

different forms suggests very strongly that both formulations are working correctly. In Figure 106 is shown the Q value for a particular example having $N = 1$; the small circles correspond to values computed from equation 62, and the crosses, to values computed from equation 66. It is obvious that the two formulations are leading to results that agree very well, because the lines through the computed points are very smooth.

For situations in which the edge must be subdivided into segments the behavior of Q becomes quite complex because we effectively have a near-field situation in which the field behavior cannot be computed simply. It is therefore very difficult to establish the validity of the program in this situation. We have made some trial runs leading to $N = 3$ and have shown that the program logic is able to function in this case. Transition regions in which the Fresnel-integral computations switch from equation 62 to equation 66 seem to behave properly (in the $N > 1$ case, it is possible to use one of these formulations for some of the segments and the other formulation for other segments).

Finally, we have made a check run for distances great enough to satisfy equation 67 very closely. For an edge 300 feet long and an X-band radar ($\lambda = 0.1$ foot), Q was computed for normal incidence and observation at angles very near normal; it was assumed that source and receiver were each 10^9 feet from the edge. Even at this very great distance, a small imaginary part was obtained for Q (although certainly not a large enough contribution to be of practical concern); errors in the real part are very small as well. The results obtained, as shown in Table VI, verify that the computer program does yield results in close agreement with the far-zone approximation but only if very great distances are involved. For the same parameters as were used here but ranges to source and receiver of 10^7 feet, the approximation is fairly good in general form but significant errors do exist in the real part; in addition, the imaginary part then starts to become significant. For distances of 10^6 feet, still a considerable distance in the context of the present application, the approximation becomes quite poor; not only are the real parts of Q poorly predicted, but the imaginary parts become comparable in magnitude to the real parts, whereas the imaginary

Table VI
COMPARISON OF COMPUTED Q VALUES
WITH FAR-ZONE APPROXIMATION

Observation Angle (rad)	$Q_{\text{far zone}}$	
1.5707960	91.440023	91.439468 - i0.043088991
1.5708952	78.769011	78.847198 - i0.032505315
1.5709944	46.852322	46.977310 - i0.006677389
1.5710936	10.879805	10.995770 - i0.019518994
1.5711432	-3.559492	-3.467960 - i0.028038964

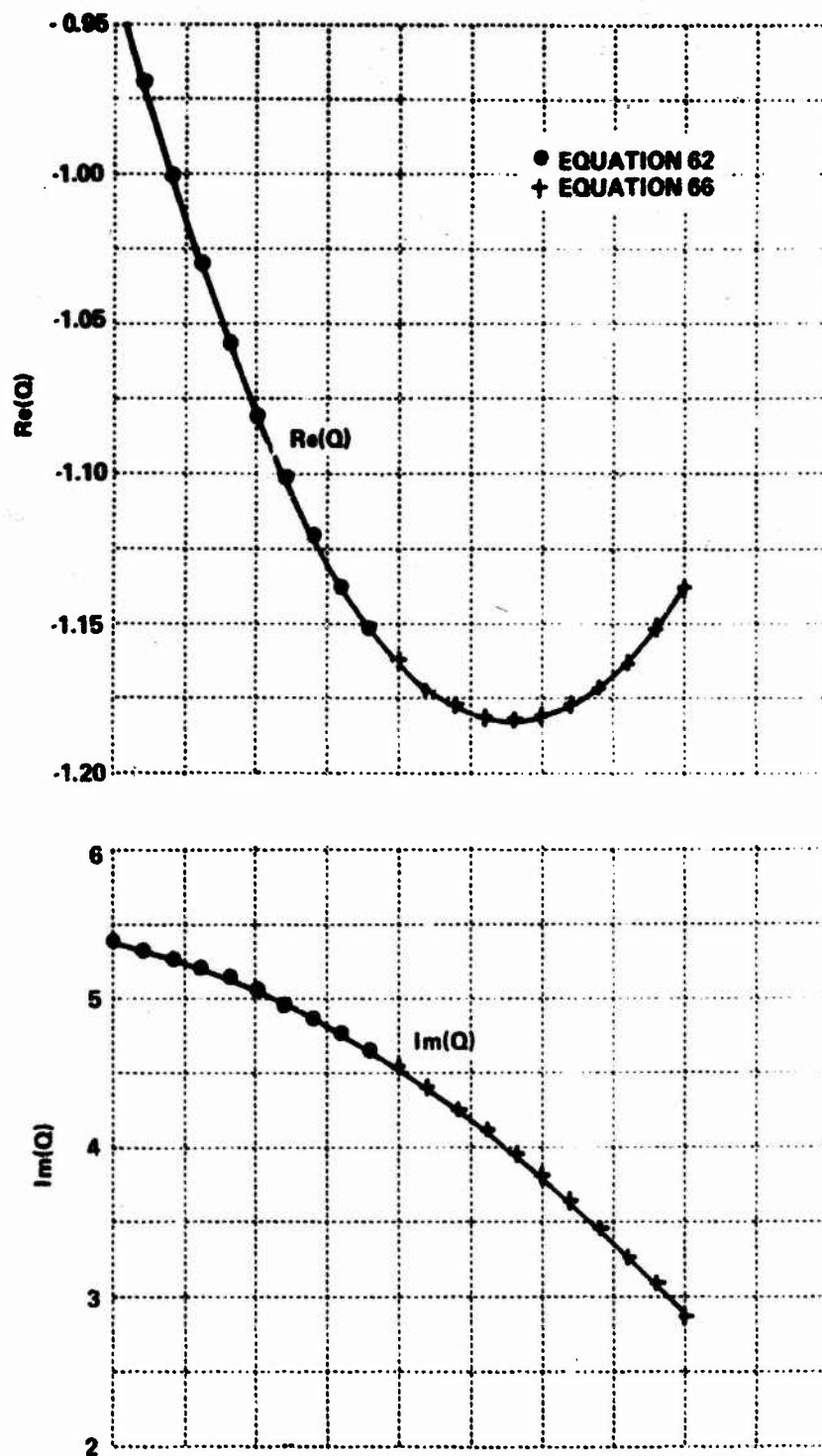


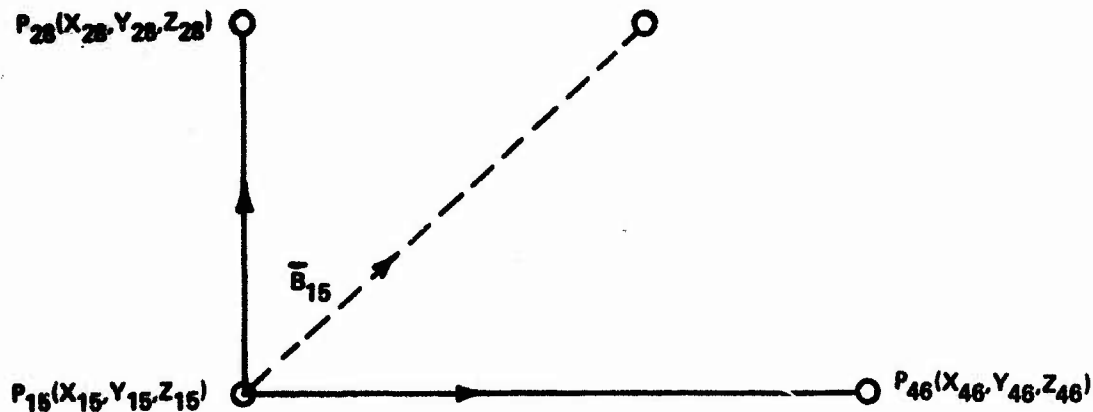
Figure 106 EXAMPLE OF CONTINUITY OF Q AT TRANSITION BETWEEN EQUATIONS 62 AND 66

parts are zero under the approximation of equation 67. For shorter edges and/or longer wavelengths, of course, the approximation can be satisfactory at shorter distances.

Appendix II

REFORMULATION OF BISECTOR COMPUTATION

Utilizing the notation in the figure below, the equations shown below provide a more general formulation for calculating an angle bisector.



$$\begin{aligned} \frac{\vec{P}_{1528}}{|\vec{P}_{1528}|} &= \frac{(X_{P_{28}} - X_{P_{15}})\hat{x} + (Y_{P_{28}} - Y_{P_{15}})\hat{y} + (Z_{P_{28}} - Z_{P_{15}})\hat{z}}{\sqrt{(X_{P_{28}} - X_{P_{15}})^2 + (Y_{P_{28}} - Y_{P_{15}})^2 + (Z_{P_{28}} - Z_{P_{15}})^2}} \\ &= (\ell_{P_{1528}}, m_{P_{1528}}, n_{P_{1528}}) \end{aligned}$$

$$\begin{aligned} \frac{\vec{P}_{1546}}{|\vec{P}_{1546}|} &= \frac{(X_{P_{46}} - X_{P_{15}})\hat{x} + (Y_{P_{46}} - Y_{P_{15}})\hat{y} + (Z_{P_{46}} - Z_{P_{15}})\hat{z}}{\sqrt{(X_{P_{46}} - X_{P_{15}})^2 + (Y_{P_{46}} - Y_{P_{15}})^2 + (Z_{P_{46}} - Z_{P_{15}})^2}} \\ &= (\ell_{P_{1546}}, m_{P_{1546}}, n_{P_{1546}}) \end{aligned}$$

$$\begin{aligned} \frac{\vec{B}_{15}}{|\vec{B}_{15}|} &= \frac{(\ell_{P_{1528}} + \ell_{P_{1546}})\hat{x} + (m_{P_{1528}} + m_{P_{1546}})\hat{y} + (n_{P_{1528}} + n_{P_{1546}})\hat{z}}{\sqrt{2}} \\ &= (\ell_{B_{15}}, m_{B_{15}}, n_{B_{15}}) \end{aligned}$$